Atomic-Level Analysis of Oxygen Exchange Reactions on Ceria-based Catalysts

by

Ethan Lee Lawrence

A Dissertation Presented in Partial Fulfillment
of the Requirements for the Degree
Doctor of Philosophy

Approved May 2019 by the
Graduate Supervisory Committee:

Peter Crozier, Chair
Jerry Lin
Jingyue Liu
William Petuskey

ARIZONA STATE UNIVERSITY

August 2019

ABSTRACT

Non-stoichiometric oxides play a critical role in many catalytic, energy, and sensing technologies, providing the ability to reversibly exchange oxygen with the ambient environment through the creation and annihilation of surface oxygen vacancies. Oxygen exchange at the surfaces of these materials is strongly influenced by atomic structure, which varies significantly across nanoparticle surfaces. The studies presented herein elucidate the relationship between surface structure behaviors and oxygen exchange reactions on ceria (CeO_2) catalyst materials. *In situ* aberration-corrected transmission electron microscopy (AC-TEM) techniques were developed and employed to correlate dynamic atomic-level structural heterogeneities to local oxygen vacancy activity.

A model Ni/CeO_2 catalyst was used to probe the role of a ceria support during hydrocarbon reforming reactions, and it was revealed that carbon formation was inhibited on Ni metal nanoparticles due to the removal of lattice oxygen from the ceria support and subsequent oxidation of adsorbed decomposed hydrocarbon products. Atomic resolution observations of surface oxygen vacancy creation and annihilation were performed on CeO_2 nanoparticle surfaces using a novel time-resolved *in situ* AC-TEM approach. Cation displacements were found to be related to oxygen vacancy creation and annihilation, and the most reactive surface oxygen sites were identified by monitoring the frequency of cation displacements. In addition, the dynamic evolution of CeO_2 surface structures was characterized with high temporal resolution AC-TEM imaging, which resulted in atomic column positions and occupancies to be determined with a combination of spatial precision and temporal resolution that had not previously been achieved. As a result, local lattice

expansions and contractions were observed on ceria surfaces, which were likely related to cyclic oxygen vacancy activity. Finally, local strain fields on CeO_2 surfaces were quantified, and it was determined that local strain enhanced the ability of a surface site to create oxygen vacancies. Through the characterization of dynamic surface structures with advanced AC-TEM techniques, an improvement in the fundamental understanding of how ceria surfaces influence and control oxygen exchange reactions was obtained.

To Robin, my wife, best friend, and biggest supporter.

ACKNOWLEDGMENTS

First and foremost, I would like to extend my deepest gratitude to Dr. Peter Crozier, who has provided invaluable guidance and instruction for my professional development as well as treasured advice for my personal growth. Throughout the years, his continued and unwavering support has undoubtedly shaped my past, present, and future, and for that I am forever grateful.

I would also like to acknowledge all of the past and present members of the Crozier research group who have helped me in countless ways over the years. In particular, I would like to thank Dr. Will Bowman, Dr. Benjamin Miller, Dr. Qianlang Liu, and Dr. Barnaby Levin, each of whom has supervised my research, shared their experiences, and mentored me beyond what was necessary or expected. They have each led by example for what an exemplary doctoral student should be, and I hope to become a role model as each of them has been to me. Every member of the Crozier research group has made me feel welcomed and supported throughout my research career, and for that I am thankful.

Throughout my time at ASU, I have interacted with and relied upon many staff members to assist with my experiments. I would like to thank Dr. Shery Chang, Dr. Katia March, Karl Weiss, Ken Mossman, and Fred Pena for their willingness to always answer my questions and provide assistance when facing a challenge. My research would not have been possible without their expertise and assistance.

I would also like to thank my parents, in-laws, and other family members for always believing in me and providing support over the years. Most importantly, I want to thank

my wife, Robin, for enduring the long journey that this Ph.D. has been and for always encouraging me to push forward to the finish.

I would like to acknowledge the funding supplied by the National Science Foundation's Department of Material's Research (DMR-1308085), as well as the ASU Dean's Fellowship. In addition, I would like to acknowledge the use of the microscopes at ASU's John M. Cowley Center for High Resolution Electron Microscopy. Finally, I acknowledge travel and conference support provided by the Microscopy Society of America and ASU's School for Engineering of Matter, Transport and Energy.

TABLE OF CONTENTS

Page

CHAPTER Page

CHAPTER Page

CHAPTER Page

LIST OF TABLES

Table Page

LIST OF FIGURES

Figure Page

Figure Page

Figure Page

1 Introduction

1.1 Motivation

Economic growth, as measured by gross domestic product (GDP), is strongly correlated to energy demand. The world's GDP is expected to double by 2040, resulting in a predicted 28% increase in global energy demand (U.S. Energy Information Administration, 2017). Unfortunately, this energy demand increase will rely heavily on carbon-intensive fossil fuels such as coal and oil. An estimated 16% increase in CO_2 emissions is expected by 2040 due to increased fossil fuel consumption (U.S. Energy Information Administration, 2017). Over the past several decades, an increase in the atmospheric CO_2 concentration due to human influence has caused a gradual warming of the planet, as shown in Figure 1.1 (Stocker, 2014; Rogelj et al., 2019). Further human-induced global warming is believed to cause additional effects such as the melting of glaciers, rising sea levels, and more frequent extreme weather conditions. Not only will these adverse effects cause severe ecological changes but may also cause mass population displacement and resource scarcity. To address these concerns, the 2015 Paris Agreement aims to join all nations in 'pursuing efforts to limit temperature increase to 1.5°C above pre-industrial levels' through reduced greenhouse gas emissions (Horowitz, 2016). Consequently, mitigation of climate change through the development of low-carbon energy technologies and improvements in the energy efficiency of existing technologies is of crucial importance.

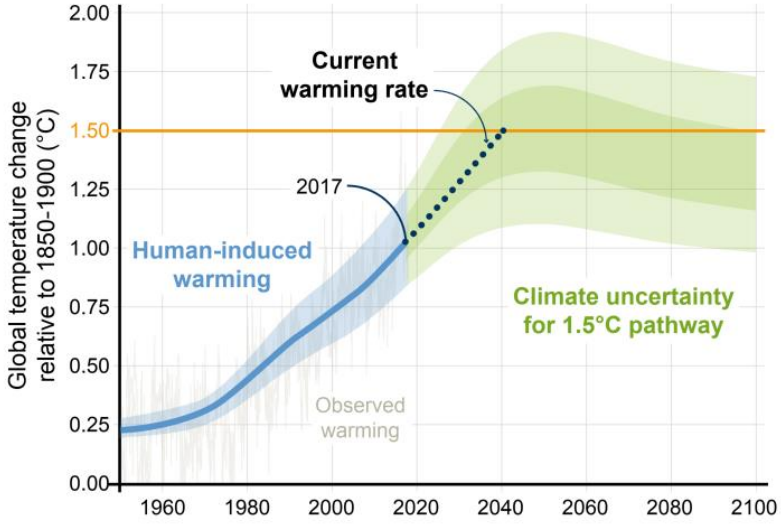

Figure 1.1. Human-induced global temperature change. At the current warming rate, the global temperature is estimated to reach 1.5°C around 2040. The green shaded '1.5°C pathway' provides an optimistic model if CO_2 emissions are reduced immediately and reach zero by 2055. Figure from (Rogelj et al., 2019).

Significant efforts have been made towards the implementation of carbon-neutral technologies, and concerns over CO_2 emissions have greatly expanded the use of renewable energy sources in recent years. Renewables are currently the fastest-growing energy source in the world, growing at a rate of 2.3%/year, whereas fossil fuels such as natural gas (1.4%/year), petroleum and other liquids (0.7%/year), and coal (0.1%/year) all experience much slower growth rates (U.S. Energy Information Administration, 2017). However, fossil fuels are still predicted to account for 77% of the world's energy consumption in 2040 – further necessitating the need for low-carbon energy technology development and making the complete replacement of fossil fuels with renewable sources unrealistic (U.S. Energy Information Administration, 2017). Natural gas is a cleaner, less carbon-intensive energy source compared to coal and other liquid fuels, making it an attractive reduced-CO_2 emission energy source. Due to an abundant supply and rising production, natural gas

consumption is projected to increase by 42% in 2040 (U.S. Energy Information Administration, 2017). With such pronounced growth of renewables and natural gas use, there is a pressing need for technical advancements to improve efficiencies, reduce cost, and optimize functionality.

Heterogenous catalysis is of paramount importance for many carbon-intensive energy and chemical synthesis technologies. The use of a catalyst to reform natural gas into olefins (e.g. C_1-C_4) or hydrogen produces chemical feedstocks for many critical processes, including petrochemical and ammonia synthesis. The main component of natural gas, methane, is often reformed into syngas, a mixture of hydrogen and carbon monoxide, and is used to produce ammonia, methanol, gasoline, and other synthetic liquid fuels (Ghoneim et al., 2016). Common catalytic transformation pathways include steam reforming, dry reforming, partial oxidation, and autothermal reforming (Rostrup-Nielsen, 1993; Liu et al., 2010). Hydrogen is considered a promising clean energy carrier for the future due to its negligible CO_2 emissions at point of usage and high energy content (Dincer, 2012; Dincer & Acar, 2015; Cormos et al., 2014) and is often used as a fuel for various types of fuel cells. A major challenge of developing a sustainable hydrogen economy is its inherent reliance on fossil fuels for hydrogen production and the subsequent CO_2 emissions that are released during reforming processes. Consequently, innovative catalysts and processes are being explored to minimize energy consumption and capture CO_2 emissions while increasing efficiency and stability (Nikolaidis & Poullikkas, 2017; Miller et al., 2016). For example, directly reforming natural gas in solid oxide fuel cells (SOFCs) can greatly increase energy conversion efficiencies and produce a highly concentrated CO_2 flue stream for simple CO_2 capture; however, technical difficulties related to catalyst deactivation must

still be overcome (Gür, 2016). Future improvements in catalyst efficiency, cost, and stability promise to lead towards more sustainable low-carbon energy technologies.

Oxygen exchange reactions underpin many of the energy conversion processes that are important for renewable energy, environmental pollutant remediation, chemical synthesis, and other technologies. For instance, during SOFC operation, gaseous oxygen is reduced to oxygen ions at the cathode, which then diffuse through a solid oxide electrolyte to oxidize fuel molecules at the anode (Adler, 2004). Catalytic membrane reactors also rely on oxygen exchange and transport to perform both gas separation and catalytic processes (Sunarso et al., 2008), with applications such as oxidative coupling of methane to ethane and/or ethene (Nozaki & Fujimoto, 1994; Zeng et al., 1998), partial oxidation of methane to syngas (Pei et al., 1995; Yang et al., 2005), selective oxidation of ethane/propane to ethene/propene (Akin & Lin, 2002; Cavani et al., 2007; Takht Ravanchi et al., 2009; Dalmon et al., 2007), and CO_2 separation and capture (Lingling Zhang et al., 2012: 2). Oxygen exchange takes place at a gas-solid interface and involves both oxygen reduction and oxidation, which are complex, multistep processes (Kilner et al., 1996; Kamiya et al., 2000; Adler, 2004; De Souza, 2006; Armstrong et al., 2013). Kinetically, oxygen incorporation and removal is often the rate-limiting step in technological applications (Adler et al., 2007; Tsipis & Kharton, 2008; Lei Wang et al., 2012; Geffroy et al., 2017; De Souza, 2017; Bouwmeester et al., 1994), and it is therefore desirable to design materials that maximize the oxygen exchange rate.

Electroceramic oxides are used for a wide range of oxygen exchange applications and often have fluorite or perovskite structures (Alcock, 1993). Oxygen transport occurs

via thermally-activated oxygen vacancy hopping, and aliovalent cation doping of these ceramics is used to introduce and manipulate oxygen vacancies. Accordingly, the transport properties are 'tunable', and selective doping of the material can result in electronic, ionic, or mixed ionic-electronic conduction (MIEC). Based on the efficiency with which MIEC oxides can incorporate, transport, and release oxygen, considerable efforts have focused on the research and development of MIECs for solid electrolytes and electrodes, gas separation membranes, selective oxidation catalysts, and resistive memory devices (Sunarso et al., 2008; Adler et al., 2007; De Souza, 2017; Geffroy et al., 2017; Gu et al., 2018). High temperatures are often required for these applications; however, there is a desire to move to lower operating temperatures to improve stability and reduce cost. Consequently, materials systems that maintain high-temperature device performance while at lower operating temperatures are being extensively explored (Brett et al., 2008; Wachsman & Lee, 2011; Sadykov et al., 2013).

CeO_2 (ceria) and ceria-based materials have a well-known ability to switch Ce oxidation state while maintaining structural integrity, allowing a facile, reversible conversion to a nonstoichiometric oxide during oxygen exchange and transport processes. Ceria's unique properties have made it a technologically important material for three-way catalysts for automotive exhaust emission control, solid electrolytes and electrodes for fuel cells, reforming of hydrocarbons, water-gas shift reactions, oxygen separation membranes, and photocatalytic water splitting applications (Trovarelli, 1996, 2002; Trovarelli & Llorca, 2017; Aneggi et al., 2016; Melchionna & Fornasiero, 2014; Montini et al., 2016; Sun et al., 2012). The relatively facile oxygen exchange and transport abilities of ceria-based materials have made them ideal candidates for various low-temperature (LT)

applications, including LT-SOFCs (Wachsman & Lee, 2011; Gao et al., 2016), steam reforming of methane (Angeli et al., 2015, 2014), and selective oxidation of ethane/propane (Gärtner et al., 2013; Park et al., 2018; Zhang et al., 2017). Interestingly, and despite the obvious technological importance, a detailed understanding of how ceria affects and regulates catalytic oxygen exchange and transport processes is still not well established.

The overarching goal of the work presented here is to develop an atomic-level, fundamental understanding of how ceria-based materials influence and control oxygen exchange processes, a critical component for the continued development of energy-related, catalytic technologies. Properties of CeO_2 that affect surface exchange reactions are discussed in detail in the following sections. Surface atomic structures regulate the incorporation and release of oxygen, necessitating the use of atomic-level, *in situ* techniques, such as transmission electron microscopy (TEM), to probe the material's functionality. Furthermore, the development and implementation of advanced transmission electron microscopy techniques presented here may be generally applied to other electroceramic oxide systems relevant to oxygen exchange applications.

1.2 Oxygen Exchange

Oxygen exchange occurs at a gas-solid interface and involves both oxygen reduction and oxidation. The incorporation of oxygen from the gas phase into the solid requires four general steps: O_2 adsorption, molecular dissociation, electron transfer, and incorporation of adsorbed O into surface oxygen vacancies. The release of oxygen from the solid occurs in reverse order: extraction of O from the lattice, electron transfer, recombination into an O_2 molecule, and desorption of O_2. Although these simple reaction

steps are generally agreed upon for mixed-conducting oxides, there is no agreement as to the exact series or simultaneity of the elementary reaction steps or which step is rate determining (Adler et al., 2007; De Souza, 2017). Adopting Kröger-Vink notation (Kröger & Vink, 1956), the oxygen reduction reaction can be written as:

Adsorption: $$O_{2(gas)} + S_{(ad)} \rightleftarrows O_{2(ad)} \quad (1.1)$$

Dissociation: $$O_{2(ad)} + 4e' + 2S_{(ad)} \rightleftarrows 2O''_{(ad)} \quad (1.2)$$

Incorporation: $$2O''_{(ad)} + 2V_O^{\cdot\cdot} \rightleftarrows 2O_O^X \quad (1.3)$$

where O_2 is diatomic oxygen, O is an oxygen atom, V is a surface oxygen vacancy, S is a surface site, and (ad) is the adsorbed state of the species. Although the four-electron transfer step is included in Equation (1.2) for simplicity, it is uncertain if this is correct and charge transfer may occur in various amounts in other elementary reaction steps (Adler et al., 2007). A simplified schematic of oxygen incorporation into ceria is shown as an example in Figure 1.2.

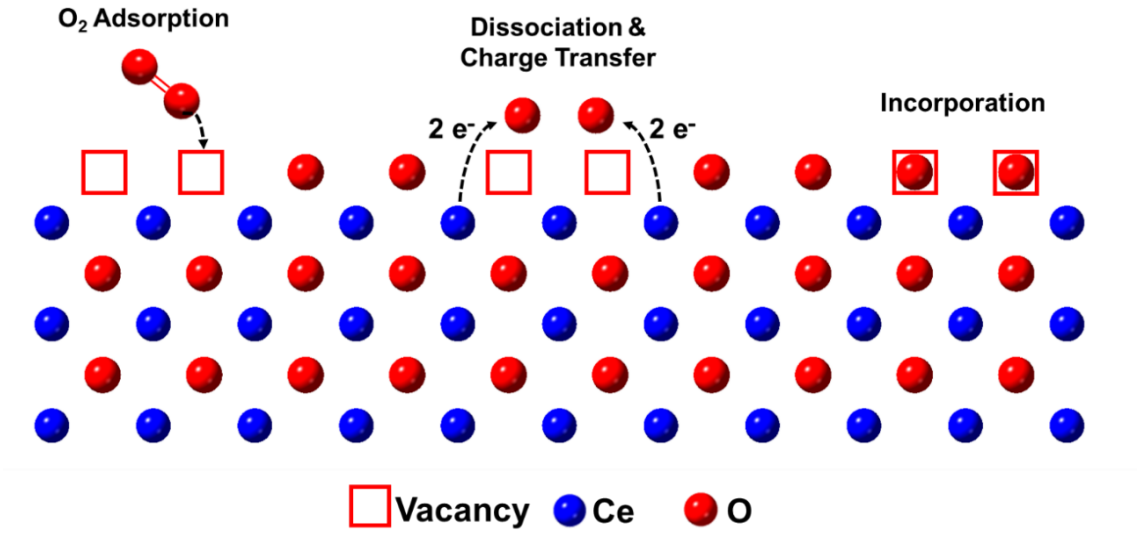

Figure 1.2. Schematic of the general steps of oxygen incorporation into a ceria surface.

The exchange flux of the dynamic equilibrium between oxygen molecules in the gas phase and oxygen in the solid is described by the surface exchange coefficient, *k*. This single parameter aims to characterize the overall surface exchange kinetics that result from the complex interplay between the many possible reaction steps and many possible intermediate species that may be associated with adsorption, dissociation, charge transfer, or incorporation. Although values of *k* are routinely determined for fluorite and perovskite oxides using isotope exchange and ion beam analysis, this metric is unable to reveal the surface exchange mechanism. There have been several studies aimed at deriving universal atomistic expressions for the surface exchange coefficient on mixed-conducting oxides (De Souza, 2006, 2017; Adler et al., 2007; Kilner et al., 1996); however, these quantitative descriptions lack the ability to indicate the exact surface exchange mechanism or explicitly determine the rate-limiting step. In fact, Adler *et al.* concluded that "In all likelihood, the true mechanism(s) cannot be determined without a more definitive determination of the

nonlinear kinetics and incorporation of independent information about the surface structure and relevant reactive intermediates." (Adler et al., 2007).

Another equally important material's parameter useful for describing oxygen exchange reactions is the oxygen vacancy formation energy (E_a), which is defined as:

$$E_a = E_{Defective} - E_{Bulk} + \frac{1}{2}\mu_{O_2} \quad (1.4)$$

where $E_{Defective}$ is the total energy of the system with an oxygen vacancy, E_{Bulk} is the energy of the system without the vacancy, and μ is the chemical potential of an oxygen molecule. The chemical potential term depends on the oxygen partial pressure, so oxygen-rich and oxygen-poor conditions can be used to determine limiting cases (Han et al., 2018; Sun et al., 2017; Paier et al., 2013). It is generally assumed that the oxygen vacancy formation energy is a good descriptor of the oxidizing power of the oxide (Aryanpour et al., 2013; Trovarelli & Llorca, 2017); that is, a lower energy of vacancy formation means a better oxidant. Experimental information to directly elucidate the vacancy formation energy is limited, mainly due to the lack of high purity samples necessary for detailed, and often complex, experiments (Tanaka et al., 2002). Consequently, theoretical calculations of the vacancy formation process have been the main analysis technique. Calculations have provided beneficial insights into defect formation processes; however, they are not always predictive. Depending on the calculation method, supercell size, vacancy location/concentration, and other input parameters, results can vary dramatically and may even lead to an incorrect conclusion (Han et al., 2018; Agarwal & Metiu, 2016; Tanaka et al., 2002; Migani et al., 2010a; Kullgren et al., 2012). Hence, theoretical calculations are

relied upon for a qualitative assessment, and general trends in calculations are used to analyze trends in experimental data. For example, calculations predicted that oxygen vacancy formation energy on ceria is surface dependent, establishing that the redox activity of ceria depends on the types of exposed crystal facets (Sayle et al., 1994; Conesa, 1995; Zhou et al., 2005).

1.3 CeO_2 (ceria)

Ceria's ability to reversibly exchange oxygen with the surrounding environment through a $Ce^{4+/3+}$ oxidation state change has been the focus of several decades of research and is a principal reason for the widespread use of ceria-based materials in a variety of industrial applications (Trovarelli, 2002, 1996; Montini et al., 2016). Ceria can form a series of nonstoichiometric CeO_x compositions (with $1.5 \leq x \leq 2$), resulting in a wide range of electrical, optical, and catalytic properties. The material's properties can be readily tuned by using aliovalent doping to introduce oxygen vacancies, nanostructuring to expose specific crystal facets, or by forming metal-CeO_2 interfaces through deposition of various metals. These structural-modification approaches provide powerful tools for the precise tailoring of ceria at the atomic level, allowing application-specific properties to be engineered. The following sections will discuss these structural-modification approaches and how they influence the catalytic oxygen exchange properties of ceria-based materials.

1.3.1 Structural Properties

CeO_2 adopts the fluorite structure with a face-centered cubic unit cell (space group $Fm\bar{3}m$) consisting of Ce^{4+} cations bonded to eight nearest-neighbor oxygen atoms and each O^{2-} anion is tetrahedrally bonded to four nearest-neighbor cerium atoms as shown in Figure 1.3. The removal of O^{2-} anions from the CeO_2 lattice results in reduced, nonstoichiometric ceria, or CeO_x, where $1.5 \leq x \leq 2$, and is accompanied by an oxidation state change from Ce^{4+} to Ce^{3+} (Bevan, 1955). To maintain charge neutrality, two trivalent Ce ions are necessary for each oxygen vacancy. Using Kröger-Vink notation (Kröger & Vink, 1956), the defect chemistry of O^{2-} removal can be written as:

$$2Ce_{ce}^{X} + O_{O}^{X} \leftrightarrow 2Ce'_{ce} + V_{O}^{\cdot\cdot} + \frac{1}{2}O_{2(gas)} \tag{1.5}$$

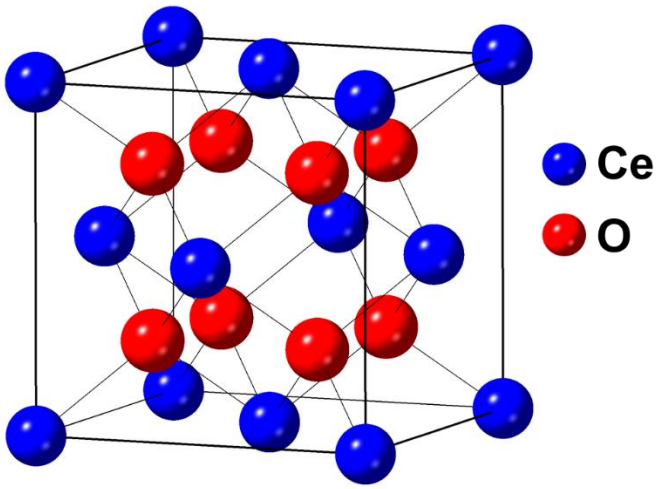

Figure 1.3. The cubic fluorite structure of CeO_2.

Reduction of CeO_2 at elevated temperatures and low oxygen pressures results in a variety of oxygen-deficient, nonstoichiometric oxides, as shown in the phase diagram of

CeO_x in Figure 1.4a (Bevan, 1955; Körner et al., 1989; Panlener et al., 1975; Ricken et al., 1984; Niu et al., 2015; Adachi & Imanaka, 1998). The so-called α phase, which is a disordered nonstoichiometric fluorite-related phase, has been shown to be stable at high temperatures and occurs in a range of CeO_x composition from $1.714 < x < 2$ with a random distribution of oxygen vacancies (Bevan, 1955; Bevan & Kordis, 1964; Panlener et al., 1975). The lattice parameter increases as the amount of oxygen vacancies increases (x decreases in CeO_x) due to unbalanced forces acting on neighboring cerium atoms when an oxygen vacancy is introduced, as shown in Figure 1.4b (Brauer et al., 1960; Chiang et al., 1993; Mogensen, 2000; Muhich, 2017). At lower temperatures, the α phase can transform into a series of ordered, fluorite-related phases with the generic formula Ce_nO_{2n-2m}, such as Ce_6O_{11} (β phase), Ce_9O_{16} (ζ phase), and $Ce_{11}O_{20}$ (δ phase) (Kümmerle & Heger, 1999; Zinkevich et al., 2006); however, these phases are still debated in the literature due to their complexity and uncertainty of phase relationships (Trovarelli, 2002; Aneggi et al., 2016). At high degrees of reduction (CeO_x with $1.5 < x < 1.714$), the phase diagram is dominated by the body-centered cubic-type C or bixbyite $Ce_2O_{3+\delta}$ phase (σ phase) (space group *Ia3*), which is formed with a combination of three fluorite-like unit cells (Tsunekawa, Sivamohan, et al., 1999). Furthermore, the thermodynamically stable form of fully reduced ceria, A-type hexagonal Ce_2O_3 (θ phase) (space group *P321*), has been suggested to decrease the reversibility of the redox process due to its lower reactivity toward oxygen in air at room temperature (Perrichon et al., 1994).

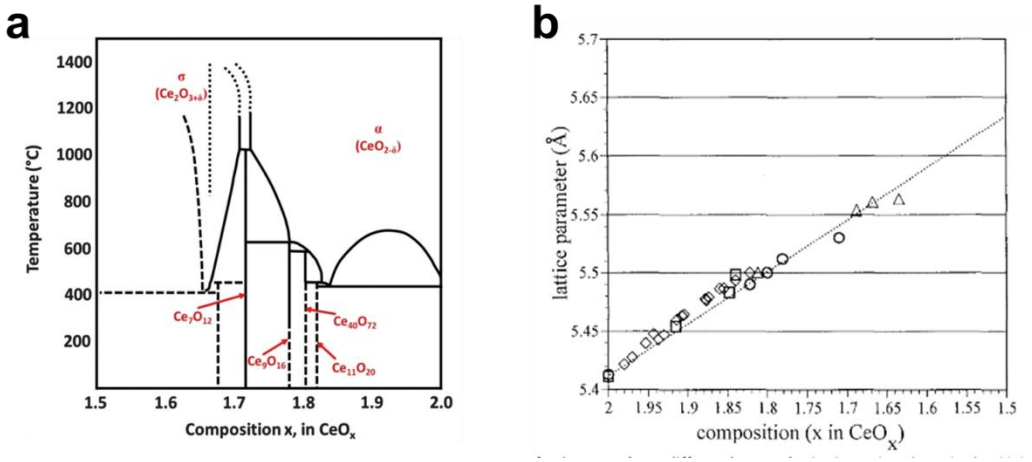

Figure 1.4. (a) Phase diagram of CeO_x. Figure from (Niu et al., 2015). (b) Lattice expansion at different degrees of CeO_x reduction. Figure from (Trovarelli, 2002).

1.3.2 Defects and Transport Properties

As discussed in the previous section, the ceria crystal structure can tolerate a high level of atomic disorder/oxygen vacancy defects, and the organization of these defects plays a key role in the properties of the material. Oxygen vacancies can be introduced in ceria either by reduction or by doping. In the first case, so-called intrinsic vacancies are formed when the removal of oxygen is facilitated by the solid's reaction with the surrounding reducing environment and is represented by Equation (1.5). When aliovalent dopants are incorporated into the crystal lattice, so-called extrinsic oxygen vacancies are induced to maintain charge neutrality. The presence, concentration, and mobility of these lattice defects determine the electronic and ionic conductivity properties of the material.

Ceria displays both electronic and ionic conduction, and both channels of charge transport are important in typical applications (Shoko et al., 2011). The degree of mixed ionic-electronic conductivity strongly depends on temperature, oxygen partial pressure,

and the presence of dopants. Each of these variables affects the charge carrier concentration, which are primarily electrons, holes, and oxygen vacancies for CeO_x. The total electrical conductivity is comprised of electronic and ionic contributions. When pure (undoped) CeO_2 undergoes reduction at low oxygen partial pressures and elevated temperatures, electronic and ionic charge carriers are generated by the reduction of cerium ions and formation of oxygen vacancies. Electronic conduction in reduced pure ceria occurs through the formation of small polarons, where an electron is localized at a given lattice site (Ce^{3+}), and a thermally-activated small polaron hopping process causes ceria to behave as an n-type semiconductor (Tuller & Nowick, 1977; Naik & Tien, 1978; Shoko et al., 2011). Ionic conduction occurs via a thermally-activated diffusion of oxygen ions into oxygen vacancies. In reduced pure ceria, ionic conductivity is a negligible contribution to the total conductivity and electronic conduction dominates, even at elevated temperatures (Trovarelli, 2002; Mogensen et al., 1994). For applications that require high ionic conductivity, such as solid oxide electrolytes, the relative ionic contribution to total conductivity must be dramatically increased and aliovalent dopants are used to increase the concentration of extrinsic oxygen vacancies. Substitutional dopants whose ionic radii are close to that of Ce generally induce high ionic conductivities, as their introduction causes the least perturbation of the crystal lattice (Trovarelli, 2002; Bishop et al., 2012; Butler et al., 1983). Accordingly, Gd^{3+}, Sm^{3+}, and Ca^{2+} are commonly used to improve ionic conductivity in ceria-based materials (Eguchi et al., 1992; Bowman et al., 2015, 2017).

1.3.3 Reducibility

The reducibility of ceria is defined as the tendency to release oxygen or donate it to an adsorbed species through a consequent change in oxygen vacancy concentration and is an essential characteristic for catalytic applications (e.g. automotive emissions-control catalysts). Oxygen vacancy formation energies are typically used as a descriptor for an oxide's reducibility (Ruiz Puigdollers et al., 2017). A separate but related functionality is the oxygen storage capacity (OSC), which is the amount of oxygen that can be reversibly extracted and recovered during a particular reaction. In general, there are two categories of OSC: total OSC and dynamic OSC (Li et al., 2019). The total OSC is the total amount of mobile oxygen available on the surface and in the bulk of the catalyst, which is related to ceria's ability to serve as an oxygen buffer for redox reactions. In comparison, the dynamic OSC consists of only the most reactive and readily available oxygen atoms and vacancies, which are mainly located at the surface, and is more closely related to ceria's ability to support and directly catalyze redox reactions (de Leitenburg et al., 1996; Huang & Beck, 2014). Generally, many studies in the literature do not explicitly state if they are measuring total or dynamic OSC and instead just define their measurement as "OSC". This has resulted in inconsistent values and understandings of OSC as the reader is left to interpret the underlying results on their own. A recent review has addressed this issue by examining the influencing factors of OSC measurements such as measurement technique, pretreatment, aging and calcination temperature, surface area, and reductant gas (Li et al., 2019). Although OSC is related to and often used as a descriptor for catalytic activity, there is no definitive and quantitative correlation between the two (Li et al., 2019). However, it is well established that the energetics of oxygen vacancy formation are substantially

reduced compared to bulk materials with a decrease in ceria particle size to the nanoscale, leading to higher OSC and improvements in redox properties (Trovarelli & Llorca, 2017; Sun et al., 2012; Melchionna & Fornasiero, 2014). Consequently, the facile formation, migration, and annihilation of oxygen vacancies on ceria nanoparticles has attracted a lot of attention due to improvements in reducibility.

The size, shape, surface composition, and surface atomic arrangement of ceria nanoparticles can all influence the reducibility, and the manipulation of these properties provides an avenue to 'tune' the catalytic properties. In general, there are three conceptual approaches to improving the reducibility of ceria nanoparticles: aliovalent doping to introduce extrinsic vacancies, nanostructuring to preferentially expose certain crystal facets, and metal deposition to form metal-ceria interfaces that exhibit unique properties. These approaches can be employed independently or in combination to tailor the catalytic properties for specific reactions, and details of each approach are discussed in subsequent sections.

1.3.4 Effect of Dopants

A wide variety of dopants can form solid solutions with the fluorite structure of CeO_2, and Gd^{3+}, Sm^{3+}, Pr^{3+}, and Ca^{2+} are the most commonly used solutes for oxygen exchange applications (Montini et al., 2016). Doping ceria with aliovalent cations can significantly improve ionic conductivity as a result of increasing the oxygen vacancy concentration. Lower dopant concentrations produce lower vacancy concentrations and ionic conductivities; however, high dopant concentrations can lead to deleterious defect-

vacancy interactions such as clustering or vacancy ordering (Ou et al., 2008; Andersson et al., 2006), so an intermediate dopant concentration is often used to maximize conductivity (Mogensen, 2000; Bishop et al., 2012). The ionic conductivity for ceria doped with Gd, Sm, Pr, and Ca has been measured at 800°C as a function of dopant concentration and is shown in Figure 1.5 (Bishop et al., 2012). For each dopant, the ionic conductivity decreases past an optimum concentration, which varies between ~8-22%. Gd and Sm exhibit the highest overall ionic conductivity as they have the most similarly sized ionic radius to Ce (Eguchi et al., 1992), and are therefore the most commonly used dopants for ceria solid electrolytes and electrodes.

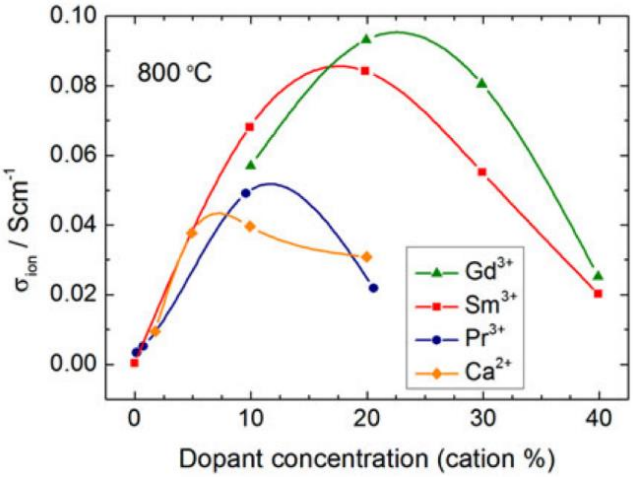

Figure 1.5. Ionic conductivity measured at 800°C as a function of dopant concentration for different ceria solid solutions. Figure from (Bishop et al., 2012).

As SOFCs and oxygen separation applications have trended towards lower operating temperatures to reduce cost and improve efficiencies, the use of doped ceria materials has been widely adopted (Sadykov et al., 2013). The most broadly used doped ceria material, $Ce_{1-x}Gd_xO_{2-x/2}$ (GDC), inherently improves the reducibility of ceria by increasing the concentration of surface exchange sites by introducing oxygen vacancies.

GDC yields higher ionic conductivity than the typically used yttria-stabilized zirconia (YSZ) for low-temperature SOFC electrolytes (Jacobson, 2010; Wachsman & Lee, 2011; Kilner & Burriel, 2014; Kharton et al., 2001) and is also known to inhibit carbon deposition by oxidizing carbon species on its surface with oxygen from the lattice (Ta-Jen Huang et al., 2005; Kubota et al., 2017). The oxygen exchange properties of GDC have been extensively studied using isotopic exchange techniques (Lane & Kilner, 2000; Ruiz-Trejo et al., 1998; Manning et al., 1996; Steele, 1994; De Souza, 2017). The activation energy for surface exchange was shown to decrease for temperatures below 650°C, suggesting a change in mechanism of oxygen adsorption or change of surface composition or atomic arrangement. Segregation of Gd to the surface of GDC has been observed (Lei et al., 2002; Borchert et al., 2005; Sato, 2015; Li et al., 2011), and Kilner *et al.* has suggested that a high concentration of surface segregated dopant cations would change the number of oxygen vacancies or change the local electronic structure, resulting in different surface exchange properties (Ruiz-Trejo et al., 1998). Doped ceria has also been shown to enhance and stabilize the surface concentration of Ce^{3+}, even under relatively oxidizing conditions, and these reactive sites may be responsible for the high surface exchange activity observed for doped ceria (Chueh et al., 2012).

1.3.5 Nanostructured Ceria

The controlled synthesis, characterization, and application of nanostructured CeO_2 has attracted extensive interest over the past few decades, and several reviews have highlighted the recent progress (Trovarelli & Llorca, 2017; Melchionna & Fornasiero, 2014; Sun et al., 2012; Wu & Overbury, 2015; Tang & Gao, 2016; Ta et al., 2013).

Researchers can precisely control the CeO_2 surface atomic arrangements by preferentially exposing certain crystal facets, which changes the oxygen release/uptake characteristics and strongly affects the catalytic properties. The origin of ceria's unique surface-dependent characteristics lies in the variation of the (111), (110), and (100) surfaces, which are the three most thermodynamically stable low index surfaces and have surface energies (eV) of 0.68, 1.01, and 1.41, respectively (Nolan, Grigoleit, et al., 2005). Therefore, the (111) surface is the most stable, followed by the (110) surface, and the least stable (100) surface. Each surface has a lower coordination number than bulk CeO_2 (4 for oxygen and 8 for cerium atoms). Figure 1.6 provides top, side, and perspective views of each type of surface. The bulk terminated (111) surface consists of a repeating O-Ce-O tri-layer structure with an oxygen terminating surface and results in a charge neutral surface with one coordinative unsaturated site for both Ce and O, meaning that only one adsorbate can link to these sites (Mullins et al., 2013). Likewise, the (110) surface is a charge neutral surface due to a stoichiometric balance of Ce and O in each plane, resulting in one and two coordinative unsaturated sites for oxygen and cerium, respectively. The (100) surface consists of a repeating O-Ce-O-Ce structure which causes a net dipole moment perpendicular to the surface and two coordinative unsaturated sites for both Ce and O atoms.

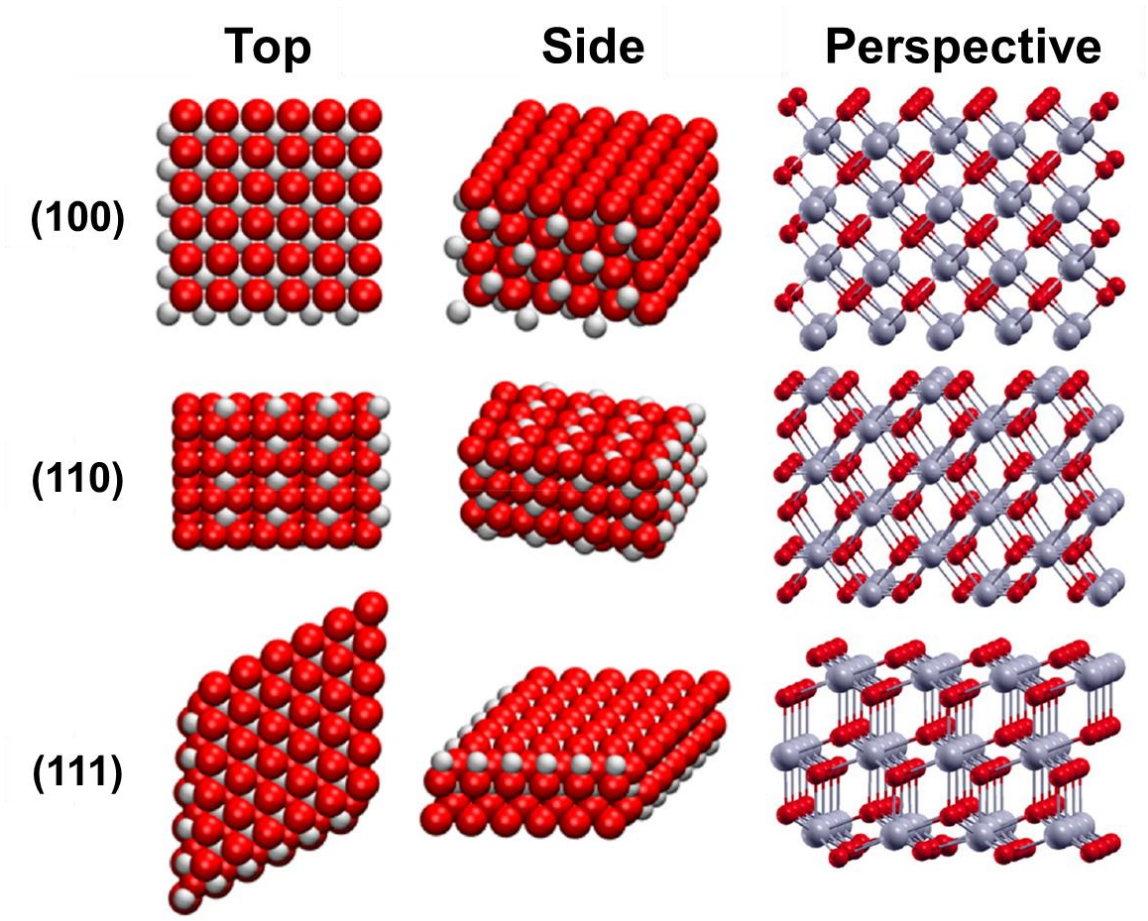

Figure 1.6. Top, side, and perspective views of CeO_2 (100), (110), and (111) surfaces. Gray and red spheres represent Ce and O atoms, respectively. Figure from (Trovarelli & Llorca, 2017).

The (111), (110), and (100) CeO_2 surfaces show surface-dependent reduction characteristics, which were first predicted by theoretical calculations (Sayle et al., 1994; Conesa, 1995) and later confirmed experimentally (Zhou et al., 2005). As briefly discussed in Section 1.2., calculations of oxygen vacancy formation energy (E_a) can be a simple yet powerful predictor for catalytic activity on ceria nanoparticles (Aryanpour et al., 2013). Nolan *et al.* has determined oxygen vacancy formation energies of 2.60 eV, 1.99 eV, and 2.27 eV for (111), (110), and (100) surfaces, respectively (Nolan, Parker, et al., 2005). Although numerical results vary between other theoretical studies, the overall trend of

oxygen vacancy formation energy remains the same – E_a: (111) > (100) > (110) (Nolan et al., 2006; Sayle et al., 1994; Conesa, 1995; Paier et al., 2013; Skorodumova et al., 2004; Baudin et al., 2000). The strong predictive nature of the oxygen vacancy formation energy for catalytic activity has led to theoretical modeling becoming ubiquitous in nanostructured ceria studies (Bruix & Neyman, 2016, 2019).

In addition to surface type, the size of the nanoparticle also influences the surface chemistry of ceria. For ceria nanoparticles below ~10 nm, a significant increase in lattice constant compared to bulk CeO_2 was observed by both Tsunekawa *et al.* and Zhou and Huebner, and the lattice relaxation was attributed to an increased concentration of Ce^{3+} ions at the surface (Tsunekawa, Sahara, et al., 1999; Tsunekawa, Sivamohan, et al., 1999; Zhou & Huebner, 2001). Additional studies demonstrated that a large surface to volume ratio on small CeO_2 nanoparticles exposed a significant amount of low coordinated surface sites, which ultimately induced oxygen vacancies and formed CeO_{2-x} while maintaining the fluorite lattice (Dutta et al., 2006; Hailstone et al., 2009; Deshpande et al., 2005). Theoretical modeling studies have investigated the oxygen vacancy formation energy as a function of CeO_2 nanoparticle size. Migani *et al.* calculated oxygen vacancy formation energies for $(CeO_2)_n$ for n from 20 to 140 and found that the specific location of the oxygen atom strongly influenced the energy for removal (Migani et al., 2010a, 2010b). The lowest energy for vacancy formation was obtained for removing an open two coordinate oxygen atom at the intersection of (100)/(111)-type facets, and a large variability (~2 eV) was found for various surface sites. Furthermore, Migani *et al.* calculated a dramatic size-dependent reduction in oxygen vacancy formation energy, suggesting that certain sizes would produce a minimum in energy. As shown in Figure 1.7, the energy required to

remove an oxygen atom from a ~2 nm ceria nanoparticle is substantially lower than an extended, bulk surface or a 1 nm sized particle (Migani et al., 2010a; Trovarelli & Llorca, 2017). The size and surface dependent oxygen removal characteristics strongly motivate the precisely controlled synthesis of CeO_2 nanoparticles to ultimately tune the catalytic properties.

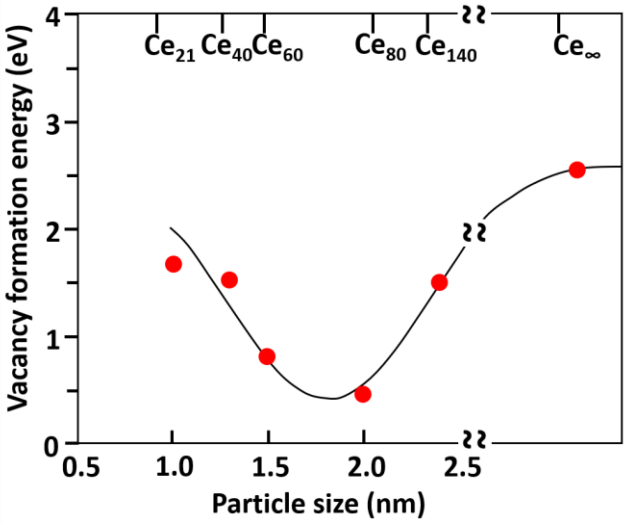

Figure 1.7. Size-dependent oxygen vacancy formation energy for different ceria nanoparticles. Data is from (Migani et al., 2010a; Bruix & Neyman, 2016). Figure adapted from (Trovarelli & Llorca, 2017).

Synthesis of nanostructured ceria occurs through the kinetic control of the nucleation and growth rates of high surface energy crystal faces to overcome the thermodynamically favored low energy faces. CeO_2 nanoparticles typically crystallize in polyhedral geometries due to the isotropic nature of the cubic fluorite structure, resulting in octahedral or truncated octahedral shapes with (111) and (100) facets (Wang & Feng, 2003; Tan et al., 2011; Manli Zhang et al., 2014; Florea et al., 2013; Yan et al., 2008; Migani et al., 2012). Hydrothermal, precipitation, sol-gel, surfactant-assisted, and other synthesis techniques have been used to modify the surface anisotropy and change the

growth rate of the crystal in different directions, producing ceria nanostructures with various morphologies, including cubes, rods, octahedra, wires, tubes, and spheres (Lin & Chowdhury, 2010; Sun et al., 2012). The crystal morphology can be controlled with several synthesis parameters, such as pressure, temperature, pH, solvent, concentration, and characteristics of precursors and additives. Typically used cerium precursors include cerium(III) nitrate hexahydrate [$Ce(NO_3)_3 \cdot 6H_2O$], cerium(III) sulfate hydrate [$Ce_2(SO_4)_3 \cdot xH_2O$], ammonium cerium nitrate [$(NH_4)_2Ce(NO_3)_6$], and cerium chloride ($CeCl_3$) (Mai et al., 2005; Zhou et al., 2005; Gonghua Wang et al., 2013; Pahari et al., 2011; Schneider et al., 2011; Wang et al., 2010). Capping agents, in the form of organic/inorganic additives, and the use of templates are frequently utilized to selectively block certain crystal growth directions and promote the growth of specific surfaces to produce various morphologies (Yang & Gao, 2006; Zhang et al., 2007; Dang et al., 2010; Pan et al., 2008; Fuentes et al., 2008). The main drawback of template or capping agent techniques is the need to remove the additive after synthesis, which can adversely affect the surface reactive sites and introduce impurities (Dengsong Zhang et al., 2012). Consequently, when clean CeO_2 surfaces are needed, template/surfactant free methodologies are preferred.

One of the simplest techniques used to produce nanostructured ceria without templating or additive agents is a hydrothermal synthesis method (Yuan et al., 2009; Yan et al., 2008; Yang et al., 2007, 2009). In this method, a cerium salt is dissolved in water in the presence of a base (NaOH, KOH, or NH_3), and the resulting solution is heat treated in an autoclave. Different morphologies can be produced with various combinations of cerium salt concentration, counterion, pH, temperature, and time of autoclave heat treatment. Anisotropic intermediates during the hydrothermal process or precursor

counterions acting as capping agents can both promote crystal growth in certain directions, resulting in nanostructured ceria (Mai et al., 2005; Wu et al., 2008; Wang et al., 2010). A schematic illustration for the hydrothermal synthesis of nanorods and nanocubes using NaOH as the base is shown in Figure 1.8a. When a cerium precursor is dissolved into a high pH NaOH solution, $Ce(OH)_3$ nuclei precipitate and transition into rod shaped nanocrystals (Mai et al., 2005; Ming Lin et al., 2012). Depending on the nature of the precursor/counterion, the surface free energies and growth rates of certain facets are modified to produce the desired final shape. As shown in Figure 1.8a, when a cerium precursor with chloride ions is used, the formation of nanorods is favored whereas a nanocube shape is favored when nitrate ions are present in the cerium precursor (Wu et al., 2008). Furthermore, the base concentration and temperature of the hydrothermal treatment play major roles in determining the final nanostructured shape, and a morphological phase diagram of CeO_2 nanoparticles, nanorods, and nanocubes is shown in Figure 1.8b. Modified hydrothermal synthesis procedures have also been used to produce flower-like nanorod assemblies, nanowires, octahedra, and hollow nanocubes and nanospheres (Chen et al., 2008; Ji et al., 2012; Yu et al., 2008; Yan et al., 2008; Yang et al., 2010; Liu et al., 2013). The wide variety of possible morphologies demonstrates the versatility of the hydrothermal synthesis method.

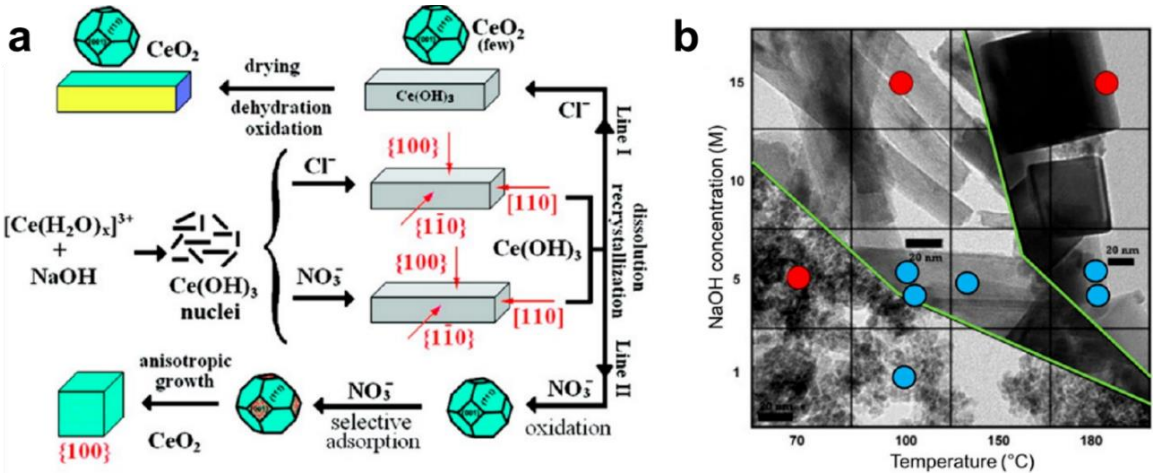

Figure 1.8. (a) Schematic illustration for the hydrothermal synthesis of nanorods and nanocubes. Figure from (Wu et al., 2008). (b) Morphological phase diagram of CeO_2 after hydrothermal treatment. Figure from (Trovarelli & Llorca, 2017) with red circle data from (Torrente-Murciano et al., 2013) and blue circles are data taken from literature.

The most widely investigated morphologies of nanostructured CeO_2 are octahedra, cubes, and rods, mainly due to their shape-dependent catalytic properties and relative shape stability under various conditions (Wu & Overbury, 2015). Transmission electron microscopy (TEM) has been used to extensively characterize the structural properties of CeO_2 octahedra, cubes, and rods (Zhang et al., 2018), and TEM images as well as schematic illustrations of octahedra, cubes, and rods are provided in Figure 1.9. CeO_2 octahedra are composed of eight (111) facets (Figure 1.9a) whereas truncated octahedra (Figure 1.9d) also include six small (100) facets (Manli Zhang et al., 2014; Yan et al., 2008; Wu et al., 2010; Wu, Li, Mullins, et al., 2012). Both octahedra and truncated octahedra are dominated by low surface energy (111) surfaces, and representative low and high resolution TEM (HRTEM) images of octahedra are shown in Figure 1.9g,j. In comparison, CeO_2 nanocubes are ideally enclosed by six (100) facets as shown in Figure 1.9b. However, the ideal nanocube shape is rarely observed in the literature due to the high surface energy of the

(100) facets, and CeO_2 nanocubes often have rounded corners and edges that expose (110) and (111) facets as shown schematically in Figure 1.9e and in TEM images in Figure 1.9h,k (Florea et al., 2013; Lin et al., 2014). The polar (100) surfaces have complex surface structure and can result in a mixture of Ce, O, and Ce-O surface terminations (Lin et al., 2014). In addition, CeO_2 (100) surfaces have been shown to demonstrate dynamic surface reconstructions and a high degree of reduction in the outermost surface layers (Bhatta, Ian M. Ross, et al., 2012; Bhatta, I M Ross, et al., 2012; Möbus et al., 2011; Bhatta et al., 2013; Lin et al., 2014; Bugnet et al., 2017; Sinclair et al., 2017). Rounded corners and edges become more pronounced for CeO_2 nanocubes that have undergone heat treatments, with nanocubes eventually evolving into truncated octahedron geometries after extended thermal aging (Aneggi et al., 2014; Sayle et al., 2004; Aneggi et al., 2005).

CeO_2 nanorods display more heterogeneity than octahedra or cubes, and synthesis reaction conditions strongly influence the crystal growth direction and exposes surface planes. Typically, CeO_2 rods grow along the [110] direction, exposing (100) and (110) planes as shown in Figure 1.9c (Mai et al., 2005; Zhou et al., 2005). However, rods with exposed (111) and (110) surfaces are also prevalent (Figure 1.9f) and have been shown to grow along the [111], [100] and [211] directions with hexagonal, pentagonal, or rectangular cross-sections (Lu et al., 2011; Yang & Gao, 2006; Du et al., 2007; Ji et al., 2012; Lin et al., 2015). Although not fully understood, the synthesis parameters, such as cerium precursors and calcination temperature, directly affects the nanorod morphology. For example, it was observed that rods enclosed with (110) and (100) facets generally occur when $Ce(NO_3)_3$ is used as a cerium precursor (Liu et al., 2009; Mai et al., 2005; Zhou et al., 2005), whereas rods with (111) and (100) facets occur when $CeCl_3$ is used (Liu et al.,

2009; P. X. Huang et al., 2005; Ji et al., 2012). However, a subsequent study on CeO_2 nanorods synthesized using a similar recipe found that the only well-defined and visible facets were (111) surfaces, with other surface facets being irregular or not well defined (Agarwal et al., 2013). Furthermore, Agarwal *et al.* suggested that the limited resolution of TEM in the early studies of Mai and Zhou (Mai et al., 2005; Zhou et al., 2005) prohibited the accurate characterization of nanorod surface structure, leading to the misassumption that nanorods are made up of (100) and (110) facets (Agarwal et al., 2013). This led to the suggestion that the nanorod synthesis calcination temperature was strongly affecting the surface structure. Several groups then investigated this hypothesis by thermally treating nanorods and demonstrated that (110) and (100) facets generally favor reconstruction to (111) facets when heated to elevated temperatures (> ~400°C) (Lin et al., 2015; Tana et al., 2009; Ta et al., 2012; Shengping Wang et al., 2013). Moreover, (110) CeO_2 surfaces are known to reconstruct into a sawtooth-like profile made up of (111) nanofacets (Figure 1.9l), which are energetically favorable and considered an intrinsic property of ceria (110) surfaces that may cause the higher activity generally observed for previously assumed (110)-terminated surfaces (Crozier et al., 2008; Yang et al., 2017; Tinoco et al., 2015; Bhatta et al., 2013). The morphological complexity of CeO_2 octahedra, cubes, and rods surface structure characterization is clearly a challenging task; however, it is this complex heterogeneity that is likely responsible for the increased reducibility of nanostructured ceria.

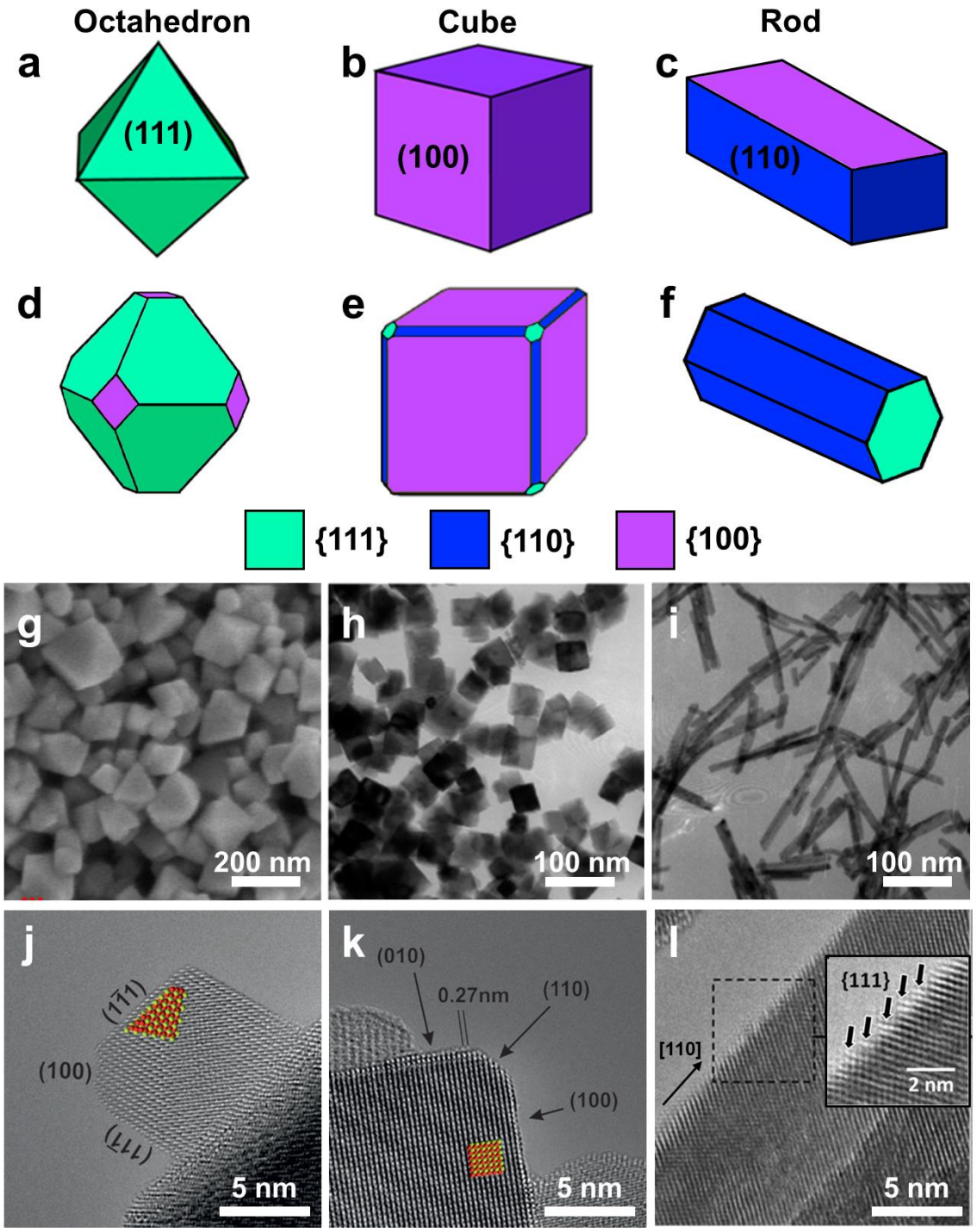

Figure 1.9. Schematic illustrations of an (a) octahedron, (b) idealized cube, (c) rectangular rod, (d) truncated octahedron, (e) cube with rounded edges and corners, and (f) hexagonal rod. Green facets represent (111) surfaces, blue represent (110) surfaces, and purple represent (100) surfaces. Representative low magnification TEM images of CeO_2 (g) octahedra (Wu, Li, & Overbury, 2012), (h) cubes (Mai et al., 2005), and (i) rods (Zhou et

al., 2005). High resolution images of (j) octahedra (Agarwal et al., 2013), (k) rounded cubes (Agarwal et al., 2013), and (l) (111) nanofaceted rods (Yang et al., 2017).

The shape-dependent redox properties of nanostructured ceria have been investigated using OSC measurements and catalytic reactions, such as the CO oxidation reaction. It was first demonstrated that cubes and rods have a higher OSC than octahedra (following the order of cubes > rods, >> octahedra), which was associated with the exposure of more reducible (100) and (110) surfaces on cubes and rods (Mai et al., 2005). A subsequent study found that the OSC followed the order of rods > cubes >> octahedra (Wu, Li, & Overbury, 2012). Regardless, this clearly established that the dynamic OSC of CeO_2 nanorods and nanocubes is significantly higher than CeO_2 octahedra due to the presence of more reactive surface oxygen species (Ishikawa et al., 2016; Zhang et al., 2011). Density function theory (DFT) studies have suggested that highly defective and faceted surfaces, such as those on CeO_2 rods and cubes, are ideal for facile oxygen incorporation/release, which also helps to explain why rods and cubes exhibit higher dynamic OSC than the more well-defined and less-defective octahedra surfaces (Trovarelli & Llorca, 2017).

The surface oxygen exchange behavior of ceria is related to its catalytic properties, and CO oxidation is often used as a model reaction to probe ceria's ability to form oxygen vacancies. The CO oxidation reaction proceeds via a Mars-van Krevelen mechanism where CO reacts with surface oxygen in the ceria lattice to form CO_2, which then desorbs and leaves behind an oxygen vacancy that is subsequently filled by gas phase oxygen. The removal of lattice oxygen from ceria is the rate limiting step (Huang & Fabris, 2008), and therefore the reducibility of the ceria surface is directly related to the reactivity for CO

oxidation. Initially, theoretical calculations predicted that the facile formation of oxygen vacancies on the CeO_2 (110) and (100) surfaces would significantly promote CO oxidation (Sayle et al., 1994; Conesa, 1995). Following the introduction of shape-selective synthesis and using CO oxidation as a model reaction, Zhou *et al.* confirmed that CeO_2 nanorods with (100) and (110) facets displayed higher CO oxidation activity than irregularly shaped nanoparticles (Zhou et al., 2005). Many additional studies have followed and clearly established the correlation between ceria surface/shape reducibility and CO oxidation reactivity (Yan et al., 2008; Lawrence et al., 2011; Tana et al., 2009; Wu, Li, & Overbury, 2012; Xue Wang et al., 2012; Lykaki et al., 2017; Renuka et al., 2013). Wu *et al.* investigated the structural dependence of CO oxidation over CeO_2 rods, cubes, and octahedra and found that the light-off curves followed the order of rods > cubes > octahedra (Wu, Li, & Overbury, 2012). Additionally, they determined the turnover frequency (TOF) for the CeO_2 nanoshapes as shown in Figure 1.10, which shows that the TOF of CO oxidation follows the order of (110) > (100) >> (111) and agrees with the trend of oxygen vacancy formation energies for ceria surfaces (Nolan, Parker, et al., 2005). Given the recent studies that demonstrate rods are generally made up of sawtooth-like (111) nanofacets (Figure 1.9l), it has been suggested that the origin of enhanced CO oxidation reactivity may be caused by defects in the rods, in particular oxygen vacancy clusters (Liu et al., 2009, 2011). The low vacancy formation energy, low coordination number of surface oxygen, and high concentration of surface defects present on (100) and (110) surfaces of rods and cubes is considered responsible for the enhanced catalytic activity of nanostructured ceria.

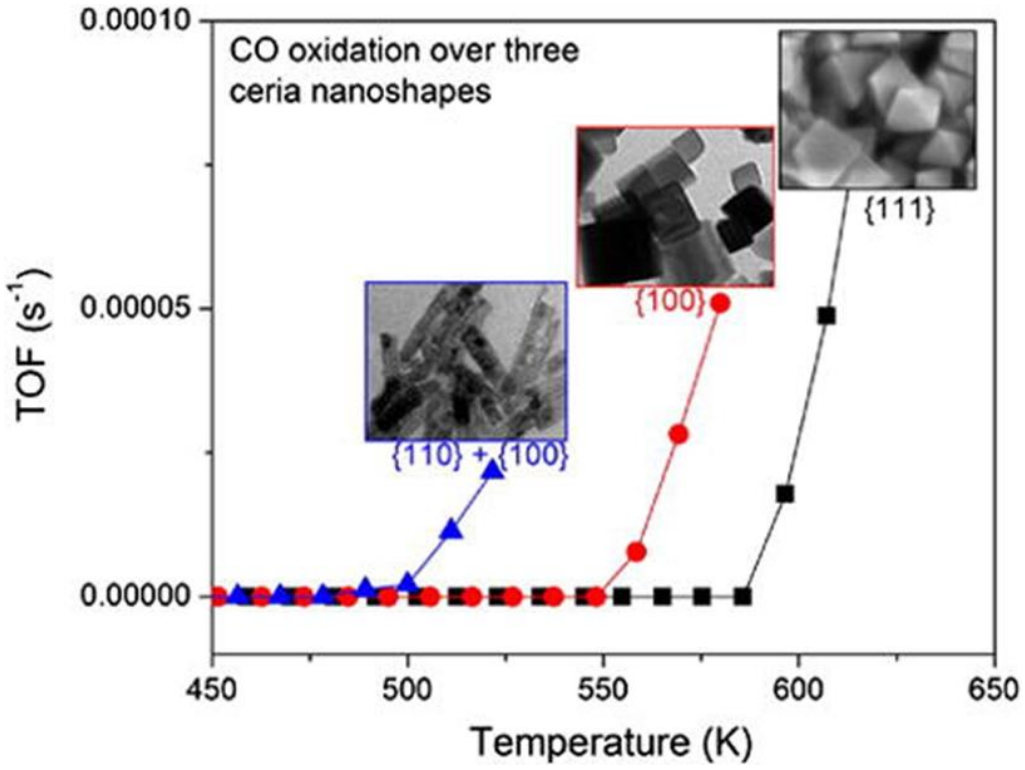

Figure 1.10. Turnover frequency (TOF) of CO oxidation activity on CeO_2 rods, cubes, and octahedra. Insets in plot are TEM images of ceria rods, cubes and scanning electron microscopy (SEM) image of octahedra. The indicated facets are those suggested to be dominant by (Wu, Li, & Overbury, 2012); however, rods have been shown to be dominated by (111) nanofacets and (100) surfaces (Agarwal et al., 2013). Figure from (Wu, Li, & Overbury, 2012).

1.3.6 Influence of Metal-Ceria Interfaces

Supported metal nanoparticles are widely used in heterogeneous catalysis, with the traditional role of the support being to disperse and stabilize the metal nanoparticles; however, several other effects can also occur at the metal-support interface in which the properties of the support can also influence and enhance the catalytic properties. This direct influence of the support on the chemisorption and catalytic properties of the metal phase is known as the metal-support interaction and includes support-induced changes in metal nanoparticle morphology, stability, electronic structure, and chemical state, as well as

nanoparticle-induced changes in the support (Ahmadi et al., 2016; Foger, 1984; Liu, 2011). Metal-ceria interfaces have unique characteristics due to the availability of surface oxygen species that ceria can supply to the metal nanoparticle during a reaction and are often exploited for a variety of catalytic applications. In addition to being preferential sites for oxygen exchange, the metal-ceria interface is known to facilitate the formation of oxygen vacancies and reduced ceria sites in the vicinity of the metal nanoparticles. Moreover, a synergistic effect can occur between the metal nanoparticles and the CeO_2 support, with catalytic reaction rates often being greater than the sum of the rates over ceria and the metal individually (Bunluesin et al., 1998). Regardless of the type of metal, a considerable number of studies have shown that the ceria-metal interface is the preferential location for complex processes to occur, and this typically involves the formation of lattice defects (i.e. oxygen vacancies and Ce^{3+} ions) and electronic state modifications of the metal nanoparticles, both of which contribute to the facile activation of reactant molecules (Aneggi et al., 2016).

A variety of different metals (Ni, Pt, Cu, Au, Ag, Pd, Rh) exhibit a strong metal-support interaction (SMSI) with CeO_2, and the structural and electronic effects of the metal-ceria interaction have been extensively investigated under both reducing and oxidizing conditions for a range of catalytic reactions (Wu & Overbury, 2015; Aneggi et al., 2016; Trovarelli, 1996). For example, the formation of active Ce^{3+} ionic centers and reactivity of ceria surface lattice oxygen has been shown to be responsible for tuning the metal oxidation states during redox reactions for both Cu (Tang et al., 2005; Nagai et al., 2013) and Pd (Iglesias-Juez, 2004; Cargnello et al., 2012). The metal and ceria components at the interface can also have a cooperative effect, which can be exemplified with the water-

gas shift (WGS) reaction: CO is adsorbed onto the metal nanoparticle and then oxidized by oxygen transfer from the ceria, which leaves behind an oxygen vacancy on the ceria surface that is subsequently reoxidized by water (Bunluesin et al., 1998; Li et al., 2000; Fu et al., 2003, 2001; Andreeva et al., 2002; Jacobs et al., 2003). Other studies have provided evidence that the metal-ceria interface itself is the location for molecular activation as a result of facile oxygen transfer and formation of active ionic centers (Shimizu et al., 2010; Grzybek et al., 2016; R Wang et al., 2006; Graciani et al., 2014). The reaction species at the interface can migrate either onto the metal or the support, resulting in a spillover phenomenon that can strongly influence catalytic reaction rates or inhibit deactivation from occurring (Sharma et al., 2012; Pan et al., 2017; Ouyang et al., 2019; Kubacka et al., 2015). For instance, oxygen transfer from ceria-based supports to metal nanoparticles has been shown to reduce undesirable carbon deposition and improve catalyst stability (Ouyang et al., 2019; Kubota et al., 2017; Veranitisagul et al., 2012; Park et al., 2000; Ramírez-Cabrera et al., 2000; Wachsman & Clites, 2002; Murray et al., 1999; Zhou et al., 2012; McIntosh & Gorte, 2004; Lee et al., 2014). The direct role of the metal-ceria interface has been investigated using CO oxidation as a model reaction for a variety of different metals, and it has been shown that the metal atoms at the perimeter and corners of supported nanoparticles on CeO_2 are the active sites, i.e. the interfacial atoms are responsible for catalytic activity (Cargnello et al., 2013; Stacchiola, 2015). Another effect of the SMSI is the decoration or encapsulation of the dispersed metal nanoparticles by the ceria support material (Bernal et al., 1999; Pan et al., 2017; Caballero et al., 2010). HRTEM has provided evidence that ceria can become mobile when partially reduced at elevated temperatures, and several examples of ceria-decorated metal nanoparticles are shown in Figure 1.11

(Bernal et al., 2003; Ta et al., 2012; Ay & Üner, 2015; Bernal et al., 2001, 1995, 1994). In each of the studies from Figure 1.11, the decorating ceria can be identified as a reduced ceria phase, which likely bonds the metal particles more tightly and may change the electronic state of the metal, especially at the interfacial region.

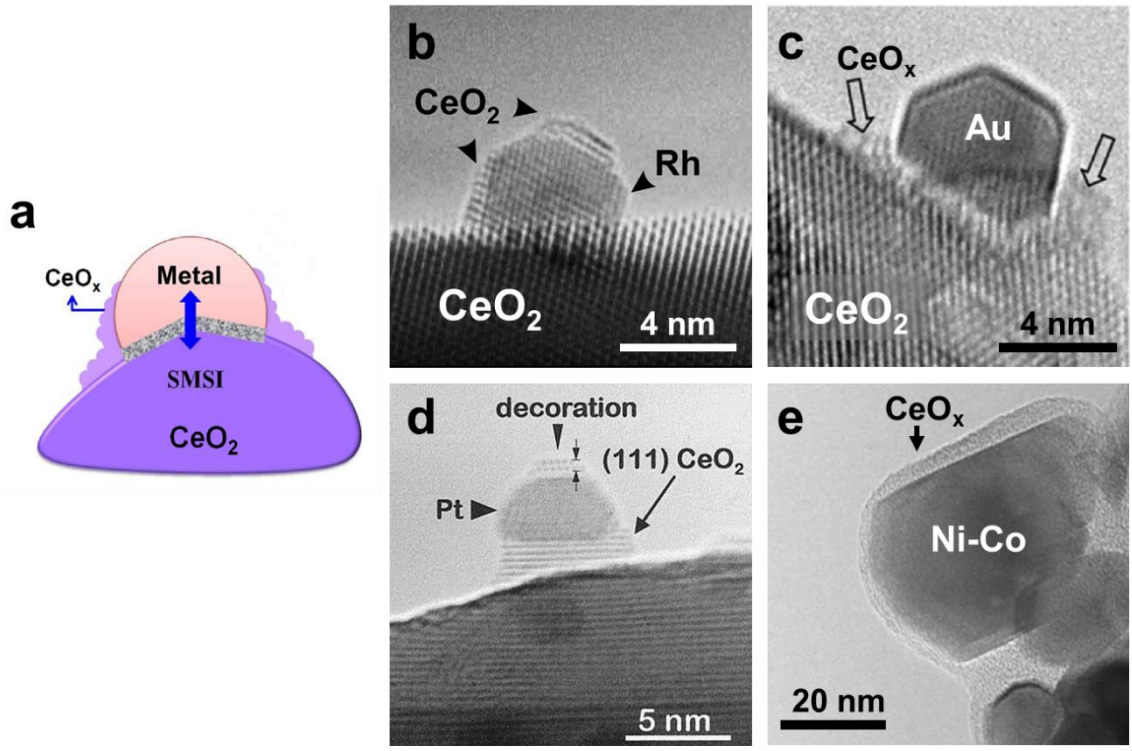

Figure 1.11. Decoration and encapsulation of metal nanoparticles from ceria support (a) Schematic illustration of reduced ceria support material decorating a metal nanoparticle as a result of SMSI. HRTEM images of (b) Rh/CeO_2 (c) Au/CeO_2 (d) Pt/CeO_2 (e) $Ni\text{-}Co/CeO_2$ catalysts decorated with reduced ceria support material. Figure (a) adapted from (Pan et al., 2017), image (b) from (Bernal et al., 2003), image (c) from (Ta et al., 2012), image (d) from (Bernal et al., 1999), and image (e) from (Ay & Üner, 2015).

A crucial aspect of the metal-ceria interface that has been investigated recently is the influence of ceria morphology on the interfacial properties and, consequently, on optimization of the catalytic activity. The surface structure of different ceria facets can promote or inhibit the lattice oxygen mobility, and this can play a significant role in the

stabilization of metal nanoparticles to reduce sintering in reactive environments, such as during CO oxidation or the WGS reaction (Farmer & Campbell, 2010; Campbell, 2013). In addition, the exposed surfaces of different CeO_2 nanostructures can strongly influence the size, morphology, and interface of the metal nanoparticles. For example, Lin *et al.* investigated the WGS reaction for Au nanoparticles supported over CeO_2 cubes and rods by using aberration-corrected scanning TEM (STEM) (Lin et al., 2015). It was determined that Au nanoparticles supported by CeO_2 cubes coarsened and underwent morphological changes after the WGS reaction whereas the Au nanoparticles on CeO_2 rods were almost unchanged after the reaction. The difference in behavior was attributed to the presence of additional oxygen vacancies and Ce^{3+} ions on the polar (100) surfaces of the CeO_2 cubes, which ultimately weakened the Au/CeO_2 interaction and allowed coarsening to occur. In contrast, the oxygen-terminated (111) surfaces present on the CeO_2 rods preserved the SMSI and strongly anchored the Au nanoparticles. This shape-dependent SMSI behavior has also been observed for Ni nanoparticles supported by CeO_2 rods and polyhedra for CO_2 reforming of methane (Du et al., 2012), Pt and Pd nanoparticles supported by CeO_2 rods, cubes, and nanoparticles for the WGS reaction (Torrente-Murciano & Garcia-Garcia, 2015; Han et al., 2009), and Ru nanoparticles supported by CeO_2 rods, cubes, and octahedra for the catalytic combustion of chlorobenzene (Huang et al., 2014). In each of these examples, the high catalytic activity of metal nanoparticles on ceria rods or cubes compared to polyhedra can be attributed to the favorable surface-dependent reduction characteristics of the rod and cube surfaces that ultimately results in a stronger metal-support interaction.

1.4 Goals and Objectives

A long-standing goal in heterogeneous catalysis is to elucidate and optimize the active structures, and the engineering of catalyst nanoparticles at the atomic-level is of great significance for controlling catalytic performance. Ceria-based catalysts have been extensively researched over the past several decades (Trovarelli, 1996, 2002; Aneggi et al., 2016; Montini et al., 2016; Gorte, 2010), and as discussed in previous sections, the manipulation of the shape, size, exposed facets, and interfacial properties of CeO_2 can dramatically alter the material's functionality. Although significant progress has been made in recent years on understanding how nanostructured ceria can be used to tailor the catalytic properties, the complexity and dynamic behavior of surface structures under reactive conditions makes characterization a challenging task (Trovarelli & Llorca, 2017). Consequently, there is a necessity for the accurate characterization, especially at the atomic level, to elucidate how the surface structures of ceria dynamically behave during oxygen exchange processes under various conditions.

In this study, CeO_2 surfaces were characterized with advanced *in situ* aberration-corrected TEM techniques to correlate dynamic behaviors of surface structures with oxygen exchange processes. Time-resolved TEM techniques were developed to extract structural information from image sequences of dynamic surfaces, which enabled unique insights into the behavior of CeO_2 surfaces and their related functionality. The techniques developed herein may also be applied to other materials systems to accelerate understanding of structure-property relationships. The superior spatial resolution of aberration-corrected TEM techniques enabled local, atomic information to be obtained while probing ceria's response to reactive conditions (i.e. temperature, reactive gases,

intense electron irradiation, vacuum). CeO_2 nanocubes and a Ni/CeO_2 catalyst were used as model systems to investigate surface structure and metal-support interactions. Key scientific questions that motivated the research include:

- What is the spatial extent of the strong metal-support interaction on CeO_2 in various gases? How do different gaseous environments affect deactivation mechanisms?

- Is it possible to identify the most active sites for oxygen exchange? How do surface defects (i.e. vacancies, steps, edges, strain) affect the oxygen exchange properties?

- How do dynamic surface structures propagate during oxygen vacancy creation and annihilation and how can these dynamic events be accurately quantified?

- How does surface-dependent strain modulate oxygen exchange? Can local strain promote facile oxygen vacancy creation/annihilation?

To answer the first set of questions, a model Ni/CeO_2 catalyst was exposed to various reactive gases, and the oxygen exchange properties of the metal-support interaction were correlated to catalyst deactivation, as discussed in Chapter 3. Chapter 4 aims to answer the second set of questions in which the surface structures of CeO_2 nanoparticles were analyzed with picometer precision to connect dynamic atomic displacements to oxygen vacancy creation and annihilation. High spatial and temporal resolution were exploited to capture dynamic surface reconstructions related to oxygen vacancy creation

and annihilation on a CeO_2 nanoparticle, and the challenges associated with accurate quantification of low signal to noise and big data sets are discussed in Chapter 5. Strain heterogeneity on CeO_2 surfaces was correlated to oxygen vacancy creation and annihilation, and the details of this are presented in Chapter 6. The results herein demonstrate the importance and capability of atomic-level *in situ* TEM techniques for more completely elucidating the role of CeO_2 surfaces and interfaces and how they influence and control oxygen exchange processes, a key component for the rational design and development of nanostructured catalysts.

2 Methods

As illustrated in Chapter 1, the oxygen exchange properties of ceria-based catalysts are influenced by atomic surfaces and interfaces. Consequently, it is necessary to accurately characterize these structures to develop a deeper understanding of the material's properties and functionalities. In this Chapter, ceria-based catalysts were synthesized and characterized using both *ex situ* and *in situ* techniques. High resolution imaging and spectroscopy were performed using aberration-corrected transmission electron microscopy (TEM) and scanning TEM (STEM). Basic principles of TEM/STEM imaging and aberration-corrected are discussed in detail, and energy-dispersive X-ray and electron energy-loss spectroscopies are also briefly reviewed. In addition, environmental TEM is described in detail to highlight the principles of atomic-level *in situ* TEM.

2.1 Material Preparation

Many different techniques have been used to synthesize ceria-based materials, including but not limited to: spray pyrolysis (Rupp et al., 2007; Angoua & Slamovich, 2012; Elidrissi et al., 2000; Kang et al., 2005), co-precipitation (Hari Prasad et al., 2010; Qi et al., 2004; Higashi et al., 1999), solid-state reactions (Leng et al., 2004), hydrolysis (Hirano & Inagaki, 2000), sol-gel processing (Laberty-Robert et al., 2006; Özer, 2001), electrochemical synthesis (Zhou et al., 1995), sonochemical synthesis (Yin et al., 2002), spray drying (Bowman et al., 2015; Blennow et al., 2009; Lundberg et al., 2011; Sharma et al., 2010), and hydrothermal synthesis (Hirano & Kato, 2004; Yang et al., 2009; Yan et al., 2008). Due to the single-step, simple approach and ability to produce nanoscale powders of tunable composition, spray drying was used to produce NiO/Gd-doped ceria

powders. To control the shape of ceria nanoparticles and produce well-defined nanocubes, a hydrothermal synthesis technique was used.

2.1.1 Spray Dry Synthesis

A spray drying technique was used to synthesize ceria-based powders (Sharma et al., 2010). Figure 2.1 shows a schematic diagram of the spray drying system. Precursors of $Ni(NO_3)_2 \cdot 6H_2O$, $Ce(NO_3)_3 \cdot 6H_2O$, and $Gd(NO_3)_3 \cdot 6H_2O$ (Alpha Aesar, Ward Hill, MA), all of at least 99.99% purity, were combined in appropriate amounts to form a 0.1 M aqueous solution. The solution was sprayed as a fine mist into a stream of hot air (~300°C) to produce a powder of nanoparticles, which was collected from the collection areas shown in Figure 2.1. The as-sprayed powder was a combination of oxide nanoparticles and a disordered phase containing residual nitrate from the precursor solution. The as-sprayed powder was then calcined at 700°C for two hours to facilitate nitrate decomposition and coarsen the oxide crystallites, crushed with a mortar and pestle, and collected as the desired NiO/Gd-doped ceria powder.

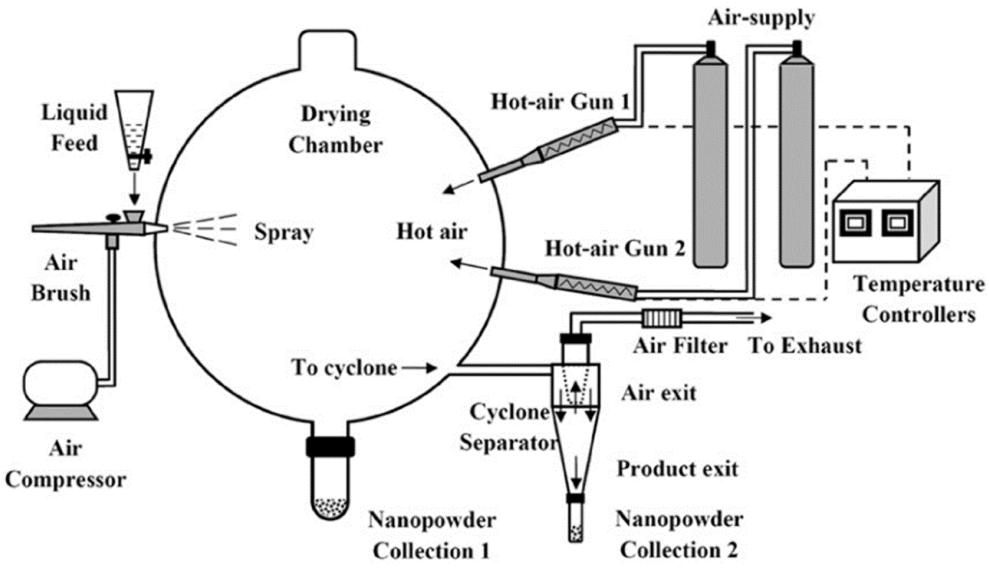

Figure 2.1. Schematic illustration of the spray drying system. Figure from (Sharma et al., 2010).

2.1.2 Hydrothermal Synthesis

CeO_2 cubes were synthesized by the method developed by Yang *et al.* (Yang et al., 2007, 2009). In a typical synthesis, $Ce(NO_3)_3 \cdot 6H_2O$ was dissolved into distilled water and mixed with a 12 M NaOH solution for 30 minutes with stirring. The resulting slurry was placed into a 50 mL autoclave, filled with deionized water up to ~80% of the total autoclave volume, heated to 200°C for 24 hours, and cooled to room temperature. The precipitate was isolated by centrifugation, washed multiple times with deionized water, and dried at 60°C overnight in air.

2.1.3 Metal Impregnation

An incipient wetness technique was used to deposit Ni onto CeO_2 cubes following a method outlined by Banerjee et al. (Banerjee et al., 2009). A nickel nitrate solution was

prepared by dissolving a known amount of 99.999% $Ni(NO_3)_2 \cdot 6H_2O$ into ethanol as a solvent. Impregnation was carried out in a mortar by dropwise addition of the nickel nitrate solution equivalent to the pore volume of the CeO_2 in a saturated ethanol atmosphere inside a glove box. After continuously mixing for 30 minutes in the ethanol environment, the resulting slurry was dried at 60°C in air for two hours to yield a powder, which was calcined at 350°C for 2 hours to facilitate nitrate decomposition.

2.2 Catalyst Characterization

Ex situ catalytic reactions were performed in a microreactor called the RIG-150 from In-Situ Research Instruments (ISRI) to determine the activity of the Ni/SiO_2, Ni/CeO_2, and Ni/GDC catalysts. The RIG-150 microreactor consists of a 10 mm internal diameter quartz tubular fixed-bed flow furnace capable of temperatures up to 900°C. Near the middle of the quartz tube is a quartz frit which keeps the catalyst in position but allows gas flow to pass through it. Gas flow is precisely controlled using mass flow controllers (MFCs); up to three reactant gases can be mixed with a carrier gas and flowed over the catalyst. A thermocouple inserted into the quartz tube and positioned near the catalyst, but separated from the gases by a quartz sheath, monitors and controls the temperature of the catalyst bed. A temperature gradient exists inside the tube furnace, especially near the exit points, so the thermocouple was positioned as close as possible to the catalyst to ensure accurate temperature control.

Exit gases flowing out of the RIG-150 microreactor were analyzed using gas chromatography (GC). Detailed operating principles of gas chromatography can be found in these references (Grob & Barry, 2004; Poole, 2012; McNair & Miller, 2011; Sparkman

et al., 2011). To summarize, a small sample of gas is injected into a long, thin tube called the column where a carrier gas is used to push the mixture through the column. The inside of the column is coated with an adsorbent layer, and different gas species will interact with the adsorbent differently. Distinct gases require different, characteristic amounts of time to pass through the column, and the time for a given gas to reach the end of the column, the elution time, is used to characterize the gas species present in the sample. Gases are thus separated when they exit the column and enter a detector which analyzes the gas species. Once the last gas species exits the column (usually 5-20 minutes depending on the species and column type), another sample is injected into the column to repeat the process.

The GC system used for this work was a Varian 3900 GC equipped with a set of two parallel capillary PLOT (Porous Layer Open Tubular) columns – a 10 m long, 0.32 mm diameter MolSieve5Å column designed to separate permanent gases (H_2, CO, O_2, N_2) and a 50 m long, 0.53 mm diameter PoraBOND Q column designed for CO_2 analysis. A thermal conductivity detector (TCD) installed in the Varian 3900 GC was used for analyzing gaseous products. The TCD functions by measuring the difference in thermal conductivities between the sample gas flow exiting from the RIG-150 microreactor and a reference gas flow. Pure carrier gas (He for experiments in this document) is used as the reference gas while a carrier/sample mixture makes up the sample gas. The reference and sample gases both flow over heated filaments, and when a sample gas species passes over the filament, the resistance of the filament changes due to the difference in thermal conductivity between the carrier and sample gases. This resistance change is monitored by a Wheatstone bridge type circuit, as shown in Figure 2.2, and produces a measurable voltage change proportional to the concentration of sample gases passing through the

column. The resulting spectra, called chromatograms, from the TCD are a function of this voltage change over time, allowing peaks to be identified as individual gas species. An example chromatogram is shown in Figure 2.3 where characteristic peaks are set on a flat baseline. Individual peaks are integrated to determine the concentration of gas species in the product gas, and chromatograms are acquired continuously throughout an experiment to monitor the changes in gas composition.

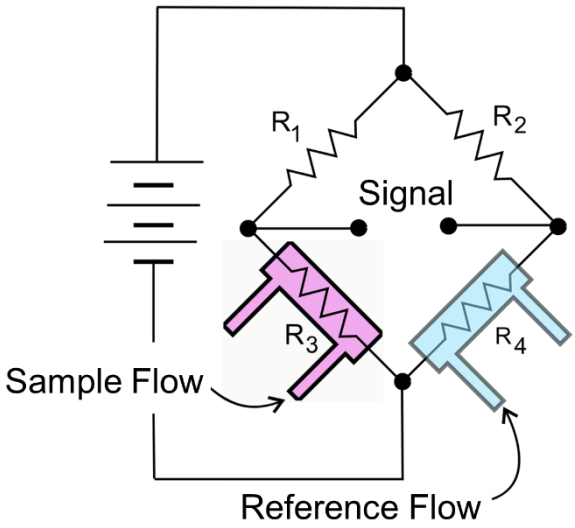

Figure 2.2. Schematic diagram of Wheatstone bridge type circuit used in the Thermal Conductivity Detector (TCD) of the Varian 3900 GC. Figure adapted from Wikimedia Commons.

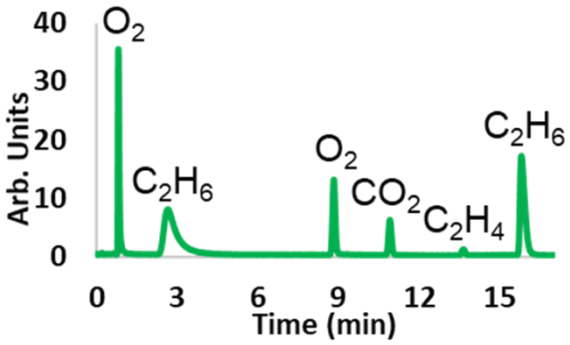

Figure 2.3. Example gas chromatogram acquired from Varian 3900 GC.

2.3 Physical Characterization

2.3.1 Transmission Electron Microscopy (TEM)

TEM is a powerful technique that is widely used throughout physical and biological sciences due to the superior resolving power compared to other forms of microscopy. An electron microscope can produce atomic resolution images and perform nanocharacterization of solids, liquids, and gases, providing information that would otherwise be unobtainable using other techniques. TEM and its related techniques are the primary characterization techniques used to study the materials of this document. Imaging was used to examine structural properties of Ni and CeO_2 nanoparticles using both *ex situ* and *in situ* methodologies while spectroscopy provided electronic structure information of ceria under various stimuli. Extensive details on the development, fundamentals, instrumentation, and capabilities of TEM and related techniques are readily available in these references (Williams & Carter, 2009; Pennycook & Nellist, 2011; Egerton, 2016; Hirsch, 1977; De Graef, 2003; Zuo & Spence, 2017). The following section briefly summarizes the fundamentals of TEM and discusses the techniques most relevant to this dissertation.

With its invention in 1932 by Max Knoll and Ernst Ruska, TEM facilitated a significant improvement in resolution and cemented itself as a critical tool for the research and development of advanced technologies (Knoll & Ruska, 1932; Ruska, 1987). The key feature of the electron microscope that enabled superior resolving power can be revealed by considering the classic Rayleigh criterion for visible-light microscopy, which states that the smallest distance that can be resolved, δ, is approximately equal to half of the

wavelength (λ), which is hundreds of nanometers for visible light. A better approximation for TEM is given by $\delta \sim 1.22\lambda/\beta$ where β is the collection semi-angle of the magnifying lens (Williams & Carter, 2009) and represents the diffraction-limited (theoretical) resolution of the microscope. This clearly demonstrates that a significant improvement in resolving power is achieved through the use of electron radiation ($\lambda \sim$ picometers) compared to visible light ($\lambda \sim$ 380-750 nm).

Electron scattering is at the core of TEM, and occurs when an incident, or 'fast', electron passes through a specimen and interacts with nuclei and electrons via Coulomb interactions. This electron-specimen interaction can be broadly classified into either elastic scattering, where negligible energy transfer occurs, or inelastic scattering, where considerable energy transfer occurs. Elastic scattering results from interactions between incident electrons and atomic nuclei or the crystal lattice, causing the electrons to be deflected through relatively large angles (>1°). Diffraction is an invaluable type of elastic scattering which considers the fast electron's wave nature and the collective scattering by the crystal lattice, resulting in scattered wave interference that is characteristic of the interatomic distances within the crystal. In contrast to elastic interactions, inelastic scattering events are a result of interactions between incident electrons and the atomic electrons in the specimen, typically resulting in very low angle scattering (<1°). A variety of signals are generated through inelastic scattering, including energy-loss electrons, characteristic X-ray emission, and secondary electrons, which can provide a wealth of chemical and electronic information about the specimen. These electron-specimen interactions form the basis of every TEM technique and are expanded upon in the following discussions.

The basic operating principles of conventional TEM image formation are shown schematically in Figure 2.4, which can be divided into three stages for simplicity. The illumination system is shown in Stage A and consists of an electron source and condenser lenses, which takes electrons from the source and transfers them to the specimen. In Stage B, the incident electron beam is scattered by a specimen, and then the scattered electrons pass through the objective lens, forming the primary image. It should be noted that the objective lens is the most important lens in the TEM; however, it is also a resolution-limiting factor in conventional or uncorrected TEM due to the aberrations or imperfections of the lens itself. In Stage C of image formation in Figure 2.4, the primary image formed by the objective lens is highly magnified using intermediate and projector lenses and then focused onto the viewing screen or detector.

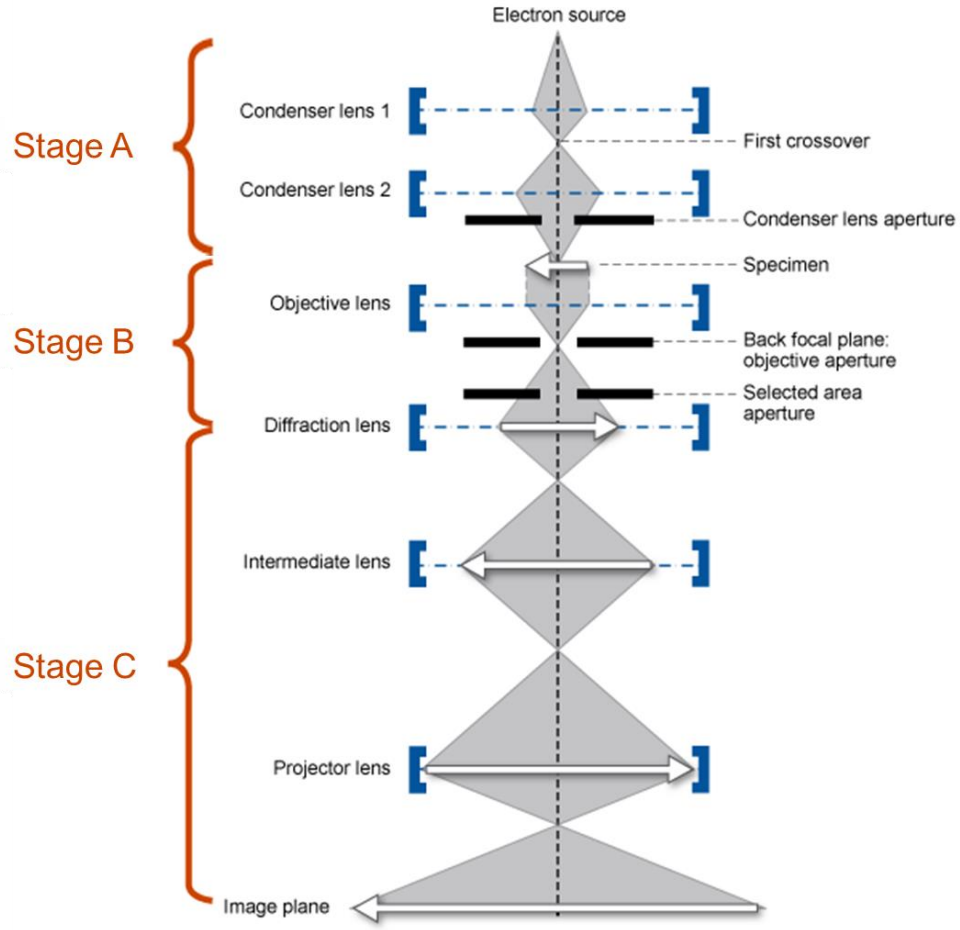

Figure 2.4. Schematic representation of conventional TEM operating principles. Figure adapted from MyScope, an online learning environment developed by Microscopy Australia.

TEM image contrast arises from changes in the amplitude and/or phase of the electron wave as it passes through the specimen. In general, both amplitude and phase contrast are present in an image; however, imaging conditions are often chosen to enable one contrast type to dominate over the other. Amplitude contrast can result from two principle sources, i.e., mass-thickness contrast or diffraction contrast. Rutherford scattering (incoherent elastic scattering), which depends strongly on the atomic number of the atom and the spatial variation in sample thickness, induces mass-thickness contrast. In

comparison, Bragg scattering (coherent elastic scattering) gives rise to diffraction contrast, which is controlled by the crystal structure and orientation of the specimen. By tilting the specimen to a condition where only one Bragg beam is strongly excited along with the direct beam, a two-beam imaging condition can be used to form a strong diffraction contrast image. This diffraction contrast two-beam imaging mode is particularly useful for studying crystal defects because the diffracting planes near the defect are altered by the strain field of the defect.

In comparison, phase contrast occurs due to interference between scattered beams that are out of phase with each other, generating an interference pattern (i.e. lattice fringes). Phase contrast requires multiple beams and is extremely sensitive to instrument and specimen parameters including objective lens defocus and astigmatism, as well as specimen thickness, orientation, and scattering factor. Thus, experimental image interpretation is particularly complex for phase contrast images, and theoretical image simulations are often required to extract and verify detailed atomic structural information of the specimen. However, proper control over instrument parameters generally enables experimental image interference fringes to be correlated to the lattice spacing and orientation of the specimen. As will be shown in subsequent chapters, phase contrast imaging can be used to directly interpret experimental images in terms of atomic structure.

Aberration Correction

The aberrations of the electromagnetic lenses used in a TEM can be a resolution-limiting factor and complicate image interpretation. Ideally, a perfect lens, which focuses a point source to a single image point (Figure 2.5a), would be used; however, all lenses are

inherently imperfect and contain aberrations, so this isn't possible in practice. Aberrations can be classified into two groups: geometrical aberrations and chromatic aberrations. Spherical aberration (C_s), the main resolution-limiting aberration in conventional TEM, is a geometrical aberration that occurs when the lens field behaves differently for off-axis rays. This is demonstrated in Figure 2.5b, which shows that the further off axis the electron is, the more strongly it is bent back toward the axis. A point source is therefore imaged as a disk rather than a single image point, degrading the ability to magnify details and limiting the resolution. Chromatic aberrations are caused by the energy-dependent refraction strengths of the electromagnetic lenses, causing rays with different energies to be focused differently, as shown in Figure 2.5c. Recent technical developments have enabled the successful correction of the dominant electron lens aberrations, resulting in another drastic improvement in resolution.

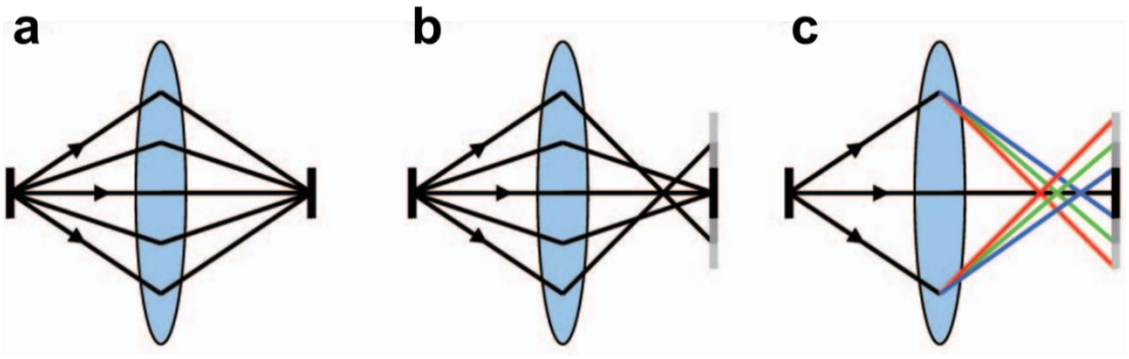

Figure 2.5. Schematics of lens aberrations (a) Perfect lens – focuses a point source to a single image point. (b) Spherical aberration – rays at higher angles are over focused, causing a point source to be imaged as a disk. (c) Chromatic aberration – rays at different energies are focused differently. Image from (Pennycook et al., 2006).

The point resolution of a conventional TEM is defined as $\sim 0.66 \cdot C_s^{1/4} \cdot \lambda^{3/4}$, and is achieved by using a distinct negative defocus condition, called Scherzer defocus, to

partially balance the effect of spherical aberration and optimize information transfer from the specimen (Scherzer, 1949). This condition represents the directly interpretable resolution limit of the microscope and image details smaller than this resolution undergo complicated contrast oscillations and require complex processing schemes to extract useful information. Clearly, reducing the electron wavelength or reducing spherical aberration improves the microscope point resolution, and higher energy electron beams (smaller wavelength) and better pole pieces (reduced C_s) have been developed to steadily improve resolution until ~1Å, as shown in Figure 2.6 (Pennycook et al., 2006; O'Keefe, 2008).

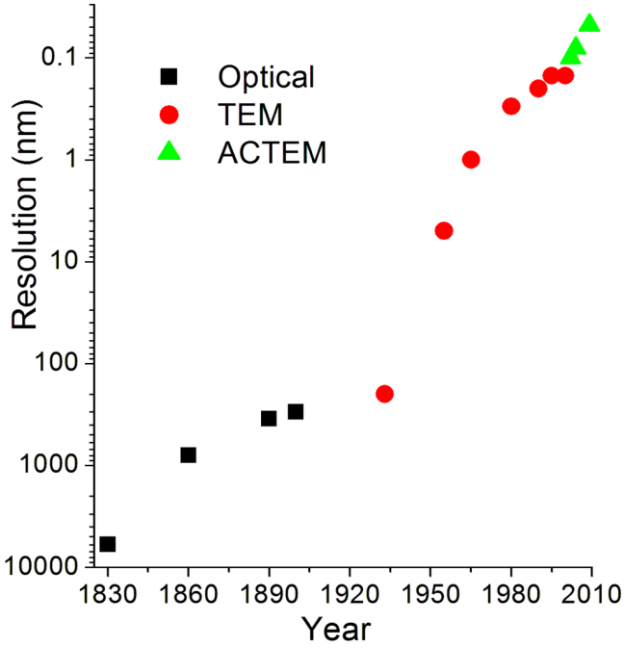

Figure 2.6. The evolution of resolution from optical to electron microscopy. Figure from (Pennycook et al., 2006).

A significant advance has occurred in recent decades as software and hardware aberration correction methods have been invented and enabled aberration-corrected TEM (AC-TEM) to improve the resolution limits even further, as shown in Figure 2.6. The key aspect of this advancement is to use a set of multipole lenses to correct aberrations by

breaking the rotationally symmetric magnetic fields of the lenses. This set of multipole lenses acts as a divergent lens to compensate for the aberrations of the converging lens as shown in Figure 2.7. With the lens aberrations corrected, the complex contrast oscillations occurring at high spatial frequencies in uncorrected TEM are absent. This allows interpretable contrast to be obtained up to the information limit of the microscope, which is determined from partial temporal coherence effects such as the energy spread of the electron source and fluctuations of the accelerating voltage and objective lens current (Barthel & Thust, 2008). It is necessary to rapidly and precisely measure aberrations and iteratively adjust necessary lens' currents, making sophisticated computer control indispensable to aberration correction. Hundreds of aberration-corrected TEMs have been manufactured following the successful demonstration of a hexapole C_s corrector system by Haider *et al*. in 1998 (Max Haider et al., 1998; Maximilian Haider et al., 1998; Uhlemann & Haider, 1998; Haider et al., 2009), enabling the long-standing goal of sub-Å resolution to be routinely achieved. In parallel with Haider's TEM C_s corrector, Krivanek *et al.* successfully demonstrated C_s correction for STEM instruments using a combination of quadrupoles and octupoles (Krivanek et al., 1997, 1998, 1999). Furthermore, chromatic aberrations (C_c) have also been successfully corrected (Haider et al., 2010); however, a C_c-corrected microscope was not used for the work in this dissertation and will not be discussed further.

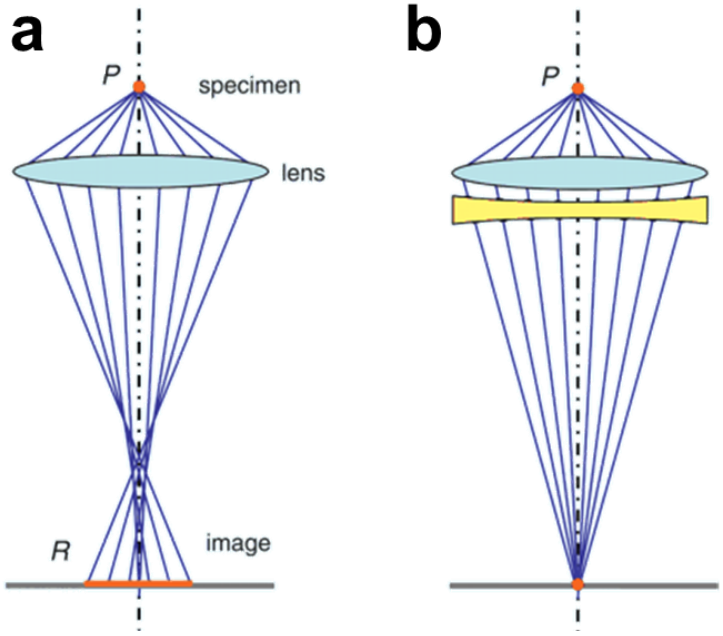

Figure 2.7. Schematic illustration of spherical aberration correction. (a) The scattering power of a convergent lens increases with increasing angle, causing a point to be imaged to a disc. (b) Spherical aberration is corrected by adding a divergent lens, accomplished through a combination of multipole lenses, to image a point to a point – improving the microscope resolution. Figure from (Urban, 2008).

With the wide-spread use of aberration-corrector systems, C_s is no longer viewed as an unchangeable, resolution-limiting property of the microscope but rather as an experimental variable that can be tuned to certain values. For example, it was shown that by tuning C_s to a small negative value (compared to unavoidable positive C_s in conventional TEM) and using an optimum positive overfocus yielded images with dramatically increased contrast of weakly scattering light elements, even in the direct neighborhood of strongly scattering heavy elements (Jia et al., 2004). The contrast enhancement under this so-called negative C_s imaging condition (NCSI) occurs as a result of an additive contribution of phase contrast and amplitude contrast due to electron diffraction channeling (Urban et al., 2009; Jia et al., 2010). NCSI is particularly useful for

direct imaging of light elements such as oxygen, even at partially occupied atomic columns in near surface regions (Lin et al., 2014; Jia et al., 2014). Image delocalization is suppressed under aberration-corrected conditions compared to conventional TEM imaging (Spiecker et al., 2010). To illustrate the suppression of image delocalization using NCSI, Figure 2.8 shows two experimental images of CeO_2 taken under conventional TEM conditions and NCSI conditions. In Figure 2.8a, a CeO_2 nanoparticle is imaged using a non-corrected Tecnai F20 TEM, revealing extended delocalization of contrast into the vacuum region as well as only contrast of Ce atomic columns (Wang et al., 2009). In comparison, Figure 2.8b shows an image acquired using a C_s-corrected Titan TEM of a CeO_2 nanoparticle surface, revealing no delocalization of contrast into the vacuum and both Ce and O atomic columns clearly resolved, even at the surface. The strong contrast of NCSI provides significantly more precise results of atomic column positions and occupancies compared to conventional TEM (Jia et al., 2010), enabling quantitative AC-TEM to be an ideal tool for atomic-level analysis of ceria surfaces. The advantages of NCSI imaging are exploited in Chapters 4-6 to allow precise measurements of atomic columns on ceria surfaces to relate dynamic effects to oxygen exchange processes.

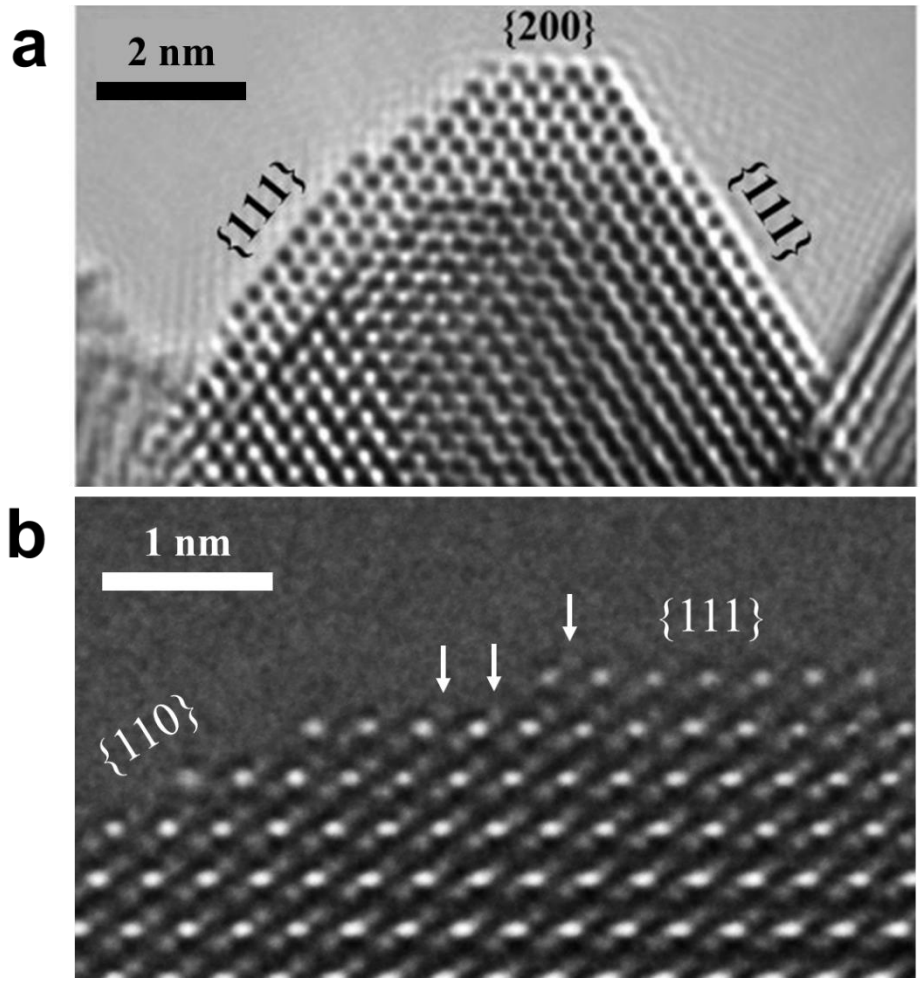

Figure 2.8. Illustration of the benefit of aberration-corrected TEM for imaging of CeO_2 nanoparticle surfaces. (a) Conventional TEM image of CeO_2 nanoparticle in [110] projection. Image delocalization causes contrast oscillations into the vacuum region. Dark contrast arises due to Ce atomic columns. Image adapted from (Wang et al., 2009). (b) C_s-corrected TEM image of a stepped (111) CeO_2 surface in [110] projection. No delocalization of contrast into the vacuum is seen. Bright contrast is Ce columns and faint bright contrast is O atomic columns. White arrows indicate O atomic column contrast visible on the surface. Image is own unpublished data.

2.3.2 Scanning Transmission Electron Microscopy (STEM)

The operating principles of STEM differ from TEM imaging in several ways. In the STEM, incident electrons are converged into a fine probe using the objective prefield, which is then scanned laterally across the specimen using scanning (deflector) coils without

tilting the probe relative to the optic axis. Contrary to TEM image formation, the imaging (objective) lens of the STEM is positioned ahead of the specimen. Therefore, the aberrations in the probe-forming lenses are critical in STEM and control the size, shape, and amount of beam current in the fine probe. Aberration correctors have been coupled to STEM systems and sub-Å probes with high current can routinely be achieved, enabling high spatial resolution and image contrast (Krivanek et al., 1999, 2013; Batson et al., 2002; Erni et al., 2009; Sawada et al., 2009).

As the fine probe is scanned across the specimen, the transmitted electrons can be detected using one or multiple detectors, as shown in Figure 2.9 and Figure 2.10a. Similar to TEM imaging mode, the fast electron can undergo coherent and incoherent elastic scattering when it transmits through the specimen, causing different types of STEM image contrast. A STEM bright field (BF) axial detector collects the transmitted electrons on axis (i.e. the direct beam) and produces a phase contrast image similar to BF TEM as a result of the interference of the direct beam with the diffracted beams. Recently, annular bright field (ABF) detectors, which have an annular shape and are located within the direct beam region (θ <10 mrads), have become increasingly popular due to their ability to directly image light elements, such as oxygen or hydrogen, along with heavy elements (Okunishi et al., 2009, 2012; Ishikawa et al., 2011; Hojo et al., 2010; Findlay et al., 2011). An annular dark field (ADF) detector collects the electrons that are scattered between ~10-50 mrads (sometimes larger) and avoids the direct beam, producing a dark field image. An ADF detector that only collects large angle scattered electrons (θ >100 mrads) and may have an outer collection angle up to several hundreds of mrads is referred to as a high-angle annular dark field (HAADF) detector. It should be noted that the angles mentioned here correspond

to a medium voltage incident electron energy (200-300 keV) and that these angles would increase for lower voltage TEMs (60 keV). Incoherent elastic scattering, or Rutherford scattering, is atomic number (Z) dependent and is the dominant image contrast mechanism for HAADF imaging. Thus, HAADF images are also referred to as Z-contrast images, making image interpretation relatively straightforward as the intensity is proportional to the atomic number of the scattering element. An example of the complimentary ADF and BF signals in STEM imaging is shown in Figure 2.10b-c.

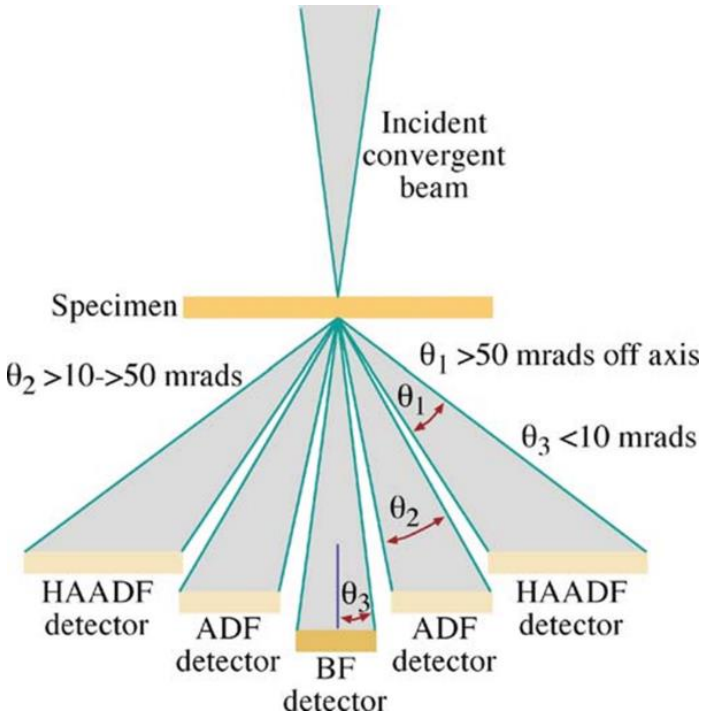

Figure 2.9. Schematic of BF, ADF, and HAADF detector setup and the range of electron scattering angles gathered by each in a STEM operated at medium voltage (200-300 keV). Figure from (Williams & Carter, 2009).

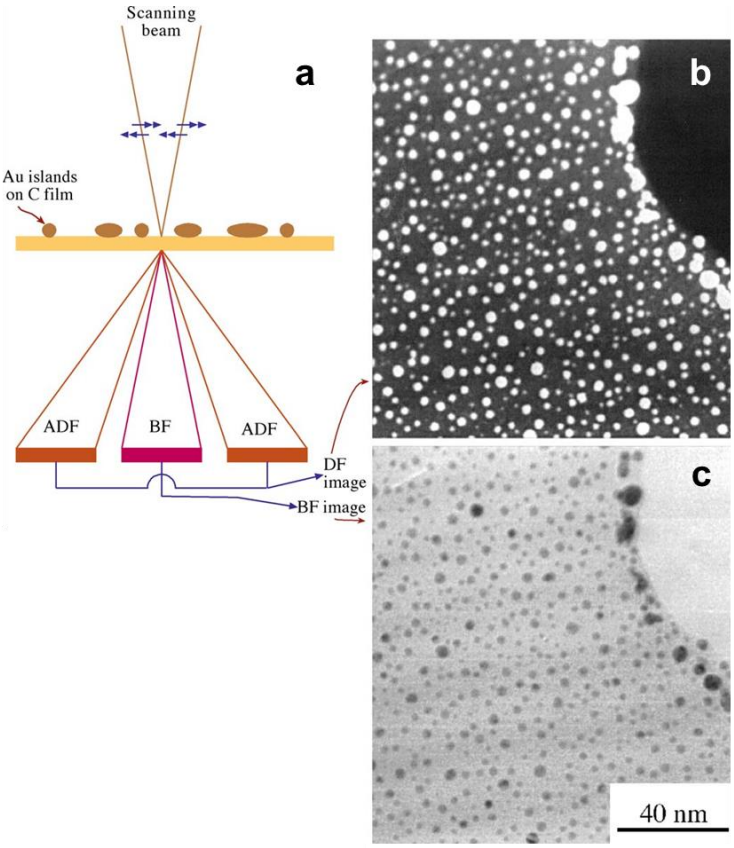

Figure 2.10. STEM image formation using bright field (BF) and annular dark field (ADF) detectors. (a) Schematic of STEM imaging with a BF detector collecting direct beam and electrons scattered <10 mrads whereas an ADF detector collects the higher angle scattered electrons. (b,c) Complimentary ADF and BF (respectively) STEM images of Au nanoparticles on C film. Figure from (Williams & Carter, 2009).

2.3.3 Energy-Dispersive X-Ray Spectroscopy (EDX)

As mentioned previously and shown in Figure 2.11, when a fast electron is inelastically scattered as it transmits through the specimen, an atomic electron can be ejected, and an X-ray characteristic of the atom is emitted when the hole is filled by an outer shell electron. An X-ray spectrometer is located near the specimen location in the TEM to collect the X-rays and determine the elements within the specimen. In TEM mode, the electron beam can be condensed to generate X-rays from an area of interest, whereas

the fine probe can be positioned with more precise control in STEM mode. Limitations of EDX include poor energy resolution (~140 eV), absorption of emitted X-rays before leaving the specimen, spurious X-rays from microscope pole pieces, sample holders or other non-specimen components, low collection efficiency of all isotropically emitted X-rays, and limited spatial resolution. The spatial resolution of EDX is governed by the beam-specimen interaction volume and can be improved by using thinner samples; however, the number of emitted X-rays decreases with smaller interaction volumes. Thus, to improve the signal-to-noise ratio for spatially-resolved EDX, highly-sensitive, large area or multiple X-ray detectors have been integrated into TEMs. In this dissertation, EDX was used in TEM and STEM modes to distinguish and verify the general chemical composition of individual nanoparticles (i.e. NiO, Ni, CeO_2, Gd-doped ceria, SiO_2).

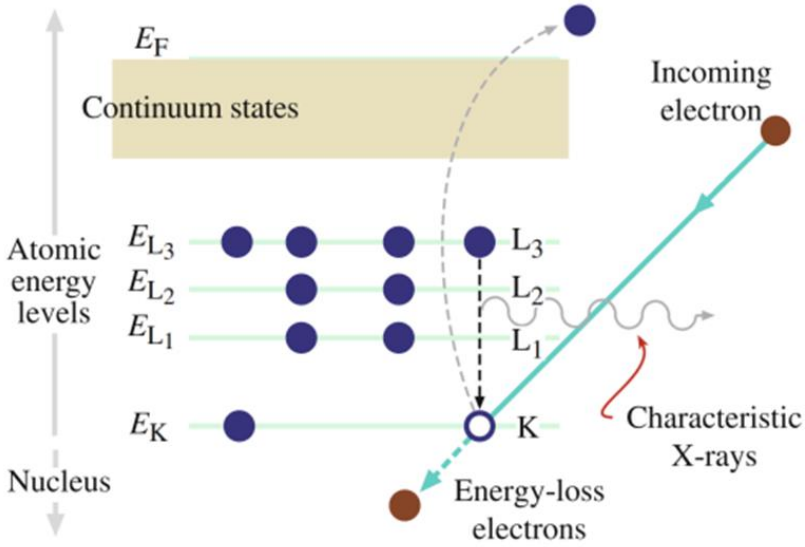

Figure 2.11. Ionization and X-ray emission process. An inner shell electron is ejected by the fast electron beam. A characteristic X-ray is emitted when the hole is filled by an outer shell electron. Figure from (Williams & Carter, 2009).

2.3.4 Electron Energy-Loss Spectroscopy (EELS)

EELS was the primary spectroscopic analysis technique used in this work because it enabled atomic-level characterization of local oxidation state of Ce cations in nanoparticles under various stimuli. EELS relies on the quantification of energy-loss events to probe bonding, oxidation state, local coordination, dielectric properties, bandgap, and thickness of a specimen. There are a variety of different EELS techniques available for use, including TEM EELS, STEM EELS, aloof-beam EELS, monochromated EELS, and energy-filtered imaging (EFTEM) (Egerton, 2009). Operating the microscope in STEM mode offers a key advantage of being able to position the fine probe with sub-nanometer precision at various locations on a specimen, thus allowing EELS to provide structural and chemical information down to the atomic level.

Electron energy-loss spectroscopy quantifies the inelastic scattering events that occur as a result of the Coulombic interactions between incident electrons and the atomic electrons in the specimen. Such events typically result in very low angle scattering; thus, the entrance aperture of an energy-loss spectrometer is placed on the optic axis of the TEM to collect the forward-scattered electrons. The entrance aperture determines the range of scattering angles that contribute to the spectrum (typically between 5-100 mrads) and can also affect the energy resolution and signal-to-noise ratio of the spectrum. The inelastically scattered electrons are collected and dispersed with respect to energy by using a magnetic prism spectrometer as shown in Figure 2.12. Electrons that have undergone more energy loss will have lower velocity and their trajectory through the magnetic prism will be bent more so than electrons that have undergone no energy loss, leading to a dispersion of

energies at the exit of the prism. A series of lenses inside the spectrometer are then used to focus and magnify the energy-loss spectrum onto a charge-coupled device (CCD) camera (Krivanek et al., 1987).

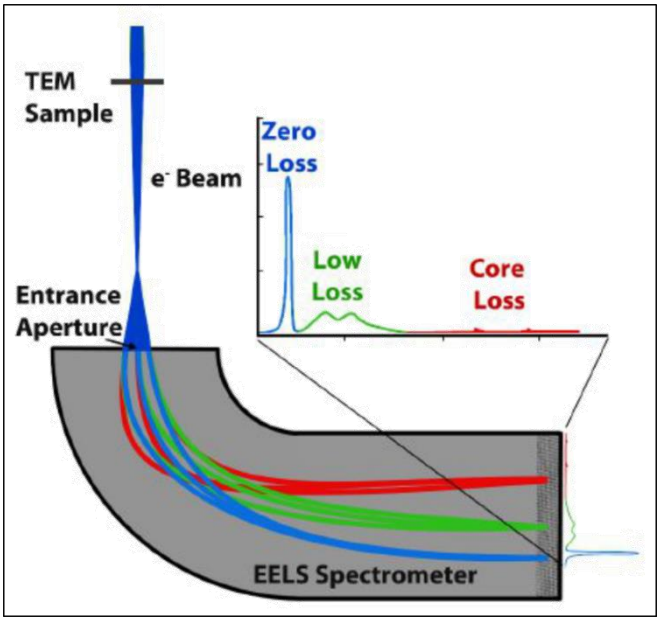

Figure 2.12. Schematic of EELS with a magnetic prism spectrometer. Colors represent the relative final energies of electrons after interacting with the specimen. An example spectrum highlights the three main regions: the zero-loss peak, low-loss, and core-loss or high-loss. Figure from (Crozier & Miller, 2016).

The shape of the energy-loss spectrum and energy of each loss event can provide detailed structural and chemical information about the specimen and a typical energy-loss spectrum consisting of three parts is shown in Figure 2.12. The zero-loss peak (ZLP) consists of electrons that have transmitted through the specimen without undergoing significant energy loss, or inelastic scattering. The ZLP doesn't contain spectroscopic information about the specimen and contains intensity tails that extend into the low-loss region, degrading the ability to quantitatively measure low-loss features of the spectrum. Furthermore, the full width at half maximum (FWHM) of the ZLP represents the energy

resolution of the system. The energy resolution of EELS is fundamentally limited by the energy spread of the incident electrons emitted from the electron source and is typically ~0.25 eV when a cold field emission gun (FEG) is used. Monochromators have recently been used to reduce the energy spread of electrons incident on the specimen, resulting in an order of magnitude improvement in energy resolution (<10 meV) (Krivanek et al., 2014).

The low-loss region of an energy-loss spectrum (typically <50 eV) mainly arises from plasmons, where longitudinal oscillations of the weakly bound, outer-shell electrons (conduction or valance bands) are excited when the incident electron interacts with the specimen. Specimen thickness influences the low-loss region as more energy-loss events occur in thicker samples relative to very thin samples, where only single scattering may occur. The low-loss region can be used to estimate specimen thickness, *t*, by assuming $t = \lambda \cdot \ln[I_T/I_0]$ where λ is a plasmon or total-inelastic mean free path, I_0 is the integrated intensity of the ZLP, and I_T is the total integrated intensity in the spectrum (typically integrated up to ~200 eV to capture most of the intensity) (Egerton, 2009). When a monochromator is used for EELS, low-loss spectral features such as inter-bandgap states and vibration excitations can be more readily observed (Venkatraman et al., 2018; Bowman et al., 2016; Qianlang Liu et al., 2017; Krivanek et al., 2014).

The core-loss region of an energy loss spectrum (>50 eV) contains direct elemental information, such as bonding and atomic position, and arises as an effect of inelastic interactions of the incident electrons with inner-shell electrons. The characteristic ionization threshold determines the onset energy of the so-called ionization ‘edge’. The

features located within ~50 eV after the edge onset, referred to as energy-loss near-edge structure (ELNES), contains information about local bonding and electronic structure such as valence and type of coordination and can be approximated by the local density of unoccupied states above the Fermi level. Ionizations that cause ejected electrons to be excited above the conduction band give rise to intensity features located 50 eV and beyond from the edge onset, referred to as extended energy-loss fine structure (EXELFS), and contain information about interatomic distances and local coordination number. Thus, the detailed shape of an energy-loss spectrum contains a wealth of structural and chemical information related to electronic structure and bonding.

A typical energy-loss spectrum of the core-loss region of CeO_2 is shown in Figure 2.13 and shows the characteristic O K and Ce M_{45} ionization edges. Quantization of ionization edges requires background subtraction to be performed, and detailed explanations for quantification procedures can be found in various texts (Egerton, 2011; Ahn, 2004; Egerton, 1991; Williams & Carter, 2009). The most commonly used background subtraction method, and the one used in this work, is to fit a power law function over a pre-ionization edge energy window. The background fitting function is then extrapolated to higher energy loss and subtracted from the raw spectra, producing a background-subtracted spectrum. In general, the width and the position of the background fitting window should be carefully chosen to reduce errors of the fitting function and improve the accuracy of the signal integration.

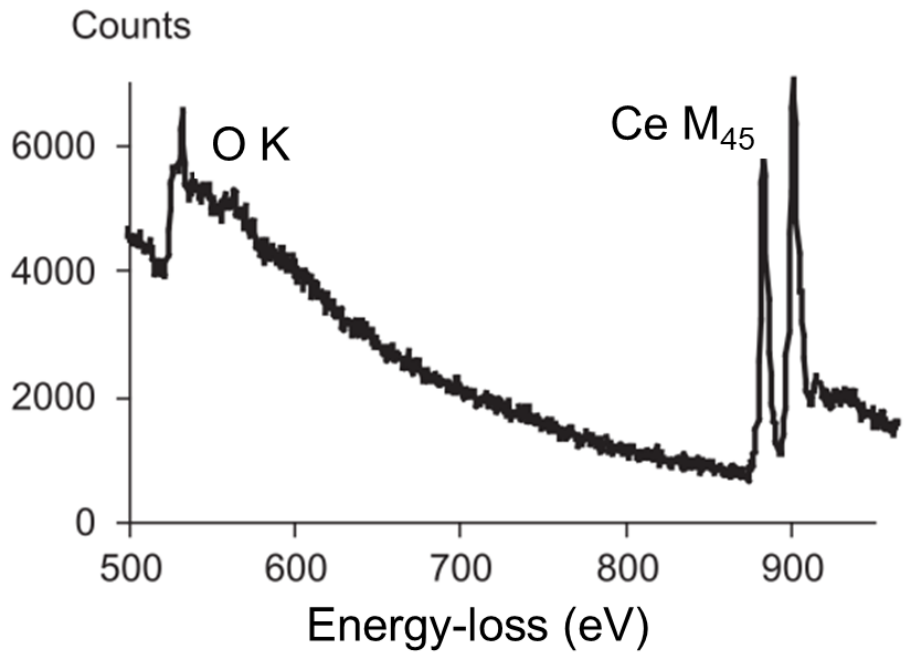

Figure 2.13. Electron energy-loss spectrum of CeO_2 showing core-loss region. Figure from (Sharma et al., 2004).

Following background subtraction, integration of ionization edges can be performed for quantitative analysis. Quantification of the Ce M_{45} edges, or so-called 'white lines', was used to determine the Ce oxidation state in this work and a simple quantification method has been established by Sharma *et al.* (Sharma et al., 2004). In this method, the background is subtracted from the M_{45} edge, the M_4 and M_5 peak intensities are integrated, and a M_5-to-M_4 intensity ratio is calculated. The intensity ratio is dependent on the Ce oxidation state, and the ratios for the limiting cases of Ce^{4+} and Ce^{3+} are determined through calibration. Spectra are acquired at room temperature, where Ce is in Ce^{4+} oxidation state, and under reducing conditions up to 700°C in 2 Torr of H_2, where Ce has transitioned to Ce^{3+}, as shown in Figure 2.14. A linear relationship is assumed between the M_5/M_4 intensity ratio and the Ce oxidation state, with values between the limiting values

representing a mixture of $Ce^{4+/3+}$. This method was used to determine local Ce oxidation states under various stimuli as described in Chapter 3.

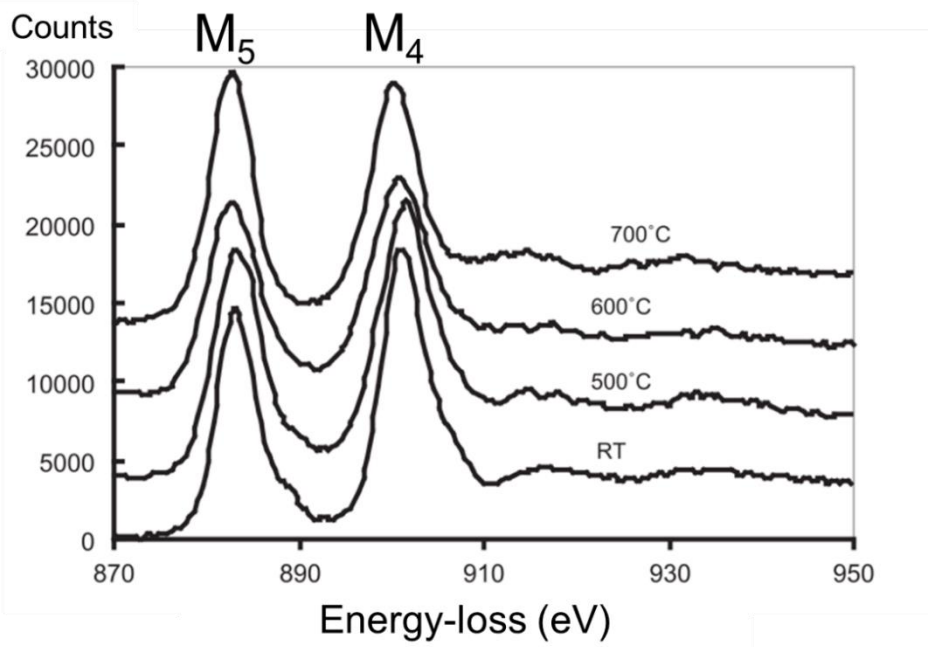

Figure 2.14. Background-subtracted Ce M_5 and M_4 peaks showing relative M_5/M_4 intensity changes with temperature. Ce oxidation state is determined by M_5/M_4 intensity ratio. Figure from (Sharma et al., 2004).

2.3.5 *In situ* Electron Microscopy

Electron microscopy is an ideal tool for obtaining atomic-level structural and chemical information about a specimen; however, for many applications, observing samples in the vacuum environment of a TEM is far from a realistic condition. Therefore, the development of *in situ* (S)TEM characterization techniques has continuously evolved since the electron microscope was invented through various modifications to either the sample holder or the microscope. *In situ* techniques have enabled TEM specimens to be characterized while under thermal, gas, liquid, mechanical, electrical, and optical stimuli

(Taheri et al., 2016; Tao & Crozier, 2016). In the field of catalysis, the functionally-relevant active catalyst structures may only be present during a chemical reaction and may also change *during* the reaction, making *in situ* studies vital for understanding catalytic properties. Additionally, coupling *in situ* characterization of a catalyst with the simultaneous measurement of the catalytic performance, known as *operando* TEM, has greatly enhanced knowledge of structure-property relationships (Crozier & Hansen, 2015; Miller & Crozier, 2014). Accordingly, fundamental, atomic-level insights into catalytic reaction and deactivation mechanisms are greatly enhanced through the direct observation of dynamic nanomaterial responses to controlled stimuli made possible through *in situ* TEM techniques.

Early *in situ* TEM approaches were initially pursued as a possible means to reduce beam damage and specimen contamination (Butler & Hale, 1981; Koh et al., 2016), and it wasn't until the 1970s that the study of chemical reactions at elevated temperatures became a strong driving force for *in situ* environmental TEM (ETEM) development (Hashimoto et al., 1968; Baker & Harris, 1972; Baker, 1979). Since then, the number of publications using *in situ* TEM has steadily increased, as shown in Figure 2.15. This trend has been made possible through two successful modification strategies that have evolved separately, and successfully, alongside TEM, and they are the 'windowed' cell approach, and the differential pumping 'aperture' approach. Recent years have seen a significant increase in publications involving *in situ* TEM, which is likely attributed to the continued development of specimen holders for windowed and aperture systems enabling an even larger breadth of experimental possibilities available to more researchers. A comprehensive review on the development of *in situ* and environmental TEM can be found in these references (Taheri et

al., 2016; Crozier & Hansen, 2015; Wagner et al., 2012; Hansen & Wagner, 2016; Hansen et al., 2010; Jinschek, 2014; Takeda & Yoshida, 2013; Takeda et al., 2015; Jinschek & Helveg, 2012; Gai & Boyes, 2009; Sharma & Crozier, 2005), and a brief introduction on the techniques used in this work are described below.

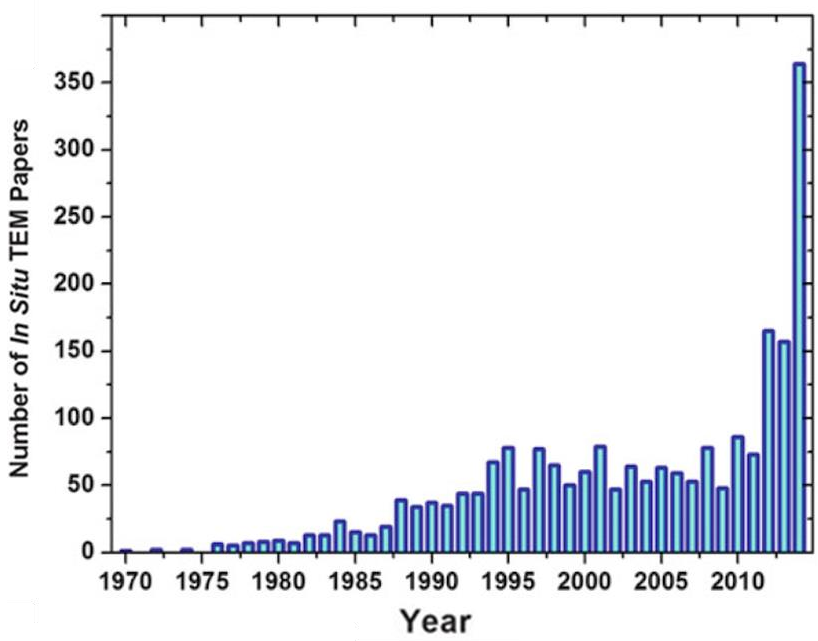

Figure 2.15. Number of publications identified using the keywords "*in situ*", "transmission electron microscopy", and "TEM", showing a steady increase over the last 30 years. Figure adapted from (Koh et al., 2016; Sinclair, 2013).

Traditionally, a high vacuum environment (typically 10^{-7}-10^{-10} Torr) is required for standard operation of a TEM to prevent electron scattering by gas molecules and contamination of the electron gun. Higher pressures or long gas paths result in a higher probability of scattering to occur between fast electrons and the gas species, potentially degrading imaging conditions. Therefore, any gas or liquid must be confined to a small region near the sample to minimize fast electron-gas interactions. The windowed cell method accomplishes this by encapsulating the sample and reaction gases or liquids

between two non-porous, amorphous electron-transparent windows such as SiN or carbon membranes. The windows effectively seal off the specimen and surrounding environment from the high vacuum of the microscope. This approach has the distinct advantages of being able to achieve ambient or higher-pressure conditions, compatibility with different TEMs with no need for modifications to the microscope column, and ability to introduce liquids around the sample for wet chemistry studies. Holders based on microelectromechanical systems (MEMS) have recently enabled miniaturization of the enclosed gas/liquid volume and the integration of a heater, allowing atomic resolution to be achieved at ambient pressures and elevated temperatures (de Jonge et al., 2010; Dai et al., 2017). The main drawbacks to the windowed cell approach include: scattering information from the 'electron-transparent' windows is superimposed on the image of the specimen and compromises the image resolution, hindered EDX acquisition due to adsorption of X-rays by the windows, and limited field of view due to geometry constraints.

In comparison, the aperture approach makes use of several small apertures placed above and below the specimen to restrict gas flow into the microscope column and uses differential pumping to maintain a large pressure difference between the specimen region and the electron gun area. A schematic of a differentially pumped TEM column is shown in Figure 2.16 and illustrates the use of turbo molecular and ion getter pumps placed at each stage of the column to restrict the leakage of gases into the microscope column. This approach requires modification of the microscope column, and various designs were experimented with on individual microscopes until the pioneering Boyes and Gai design was adopted for commercialization in the early 2000s (Boyes et al., 1995; Boyes & Gai, 1997; Gai & Boyes, 1997). In the Boyes and Gai design, radial holes are incorporated into

the objective lens pole pieces for the first stage of differential pumping and the controlled environmental cell is the regular sample chamber of the ETEM, making it an integral part of the microscope column. The key advantage to the differentially pumped aperture ETEM approach is that the basic instrument resolution is preserved as the imaging conditions are not degraded by the presence of membranes. Additional benefits of this approach are that specimen holders used in regular, high-vacuum TEMs are compatible and *in situ* spectroscopy (EDX & EELS) is advantageous, as there is no contribution from window membranes. For example, EELS has been used to quantify the gas composition in the ETEM cell near the sample to probe catalytic gas products (Crozier & Chenna, 2011; Miller & Crozier, 2014; Crozier & Miller, 2016). The pressure in a differentially pumped ETEM is typically limited to ~20 Torr, thus making ambient pressure studies confined to using the windowed-cell approach.

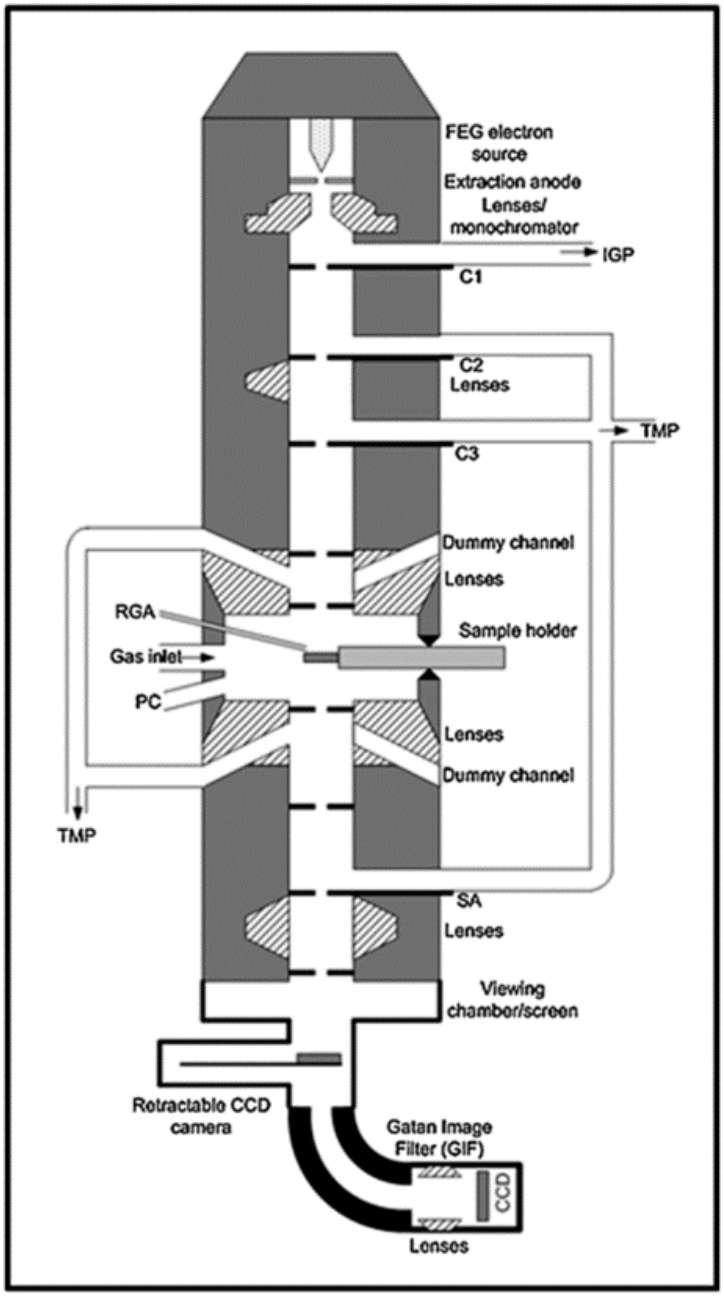

Figure 2.16. Schematic diagram of a differentially pumped TEM column. TMP: turbo molecular pump; IGP: ion getter pump; RGA: residual gas analyzer; PC: plasma cleaner. Image from (Wagner et al., 2012).

The ability to observe materials in gaseous environments and elevated temperatures can result in significant scientific knowledge; however, it comes at the expense of

instrument performance and increased experimental complexity. Elastic and inelastic scattering of the fast electron beam by the gas molecules confined in the windowed cell or environmental cell of the differentially pumped column induces an overall decrease in intensity and a loss of resolution. For the ETEM approach, the electron-gas interactions take place throughout the full volume between the pressure limiting apertures, resulting in a lengthy gas pathway of around 7 mm (Hansen et al., 2010). Electrons that are scattered by gas molecules may be intercepted by apertures and other parts of the microscope. The loss of intensity that reaches the CCD detector has been quantified as a function of gas species and pressure (Hansen & Wagner, 2012, 2016; Zhu & Browning, 2017), and results are shown in Figure 2.17. Unsurprisingly, the measured intensity on the CCD decreases with increasing gas pressure. An increase in pressure increases the density of gas molecules in the path of the electron beam, which therefore increases the probability of an electron-gas scattering event. For heavier molecules such as O_2 and N_2, a higher pressure causes a substantial decrease in the overall intensity that reaches the CCD detector.

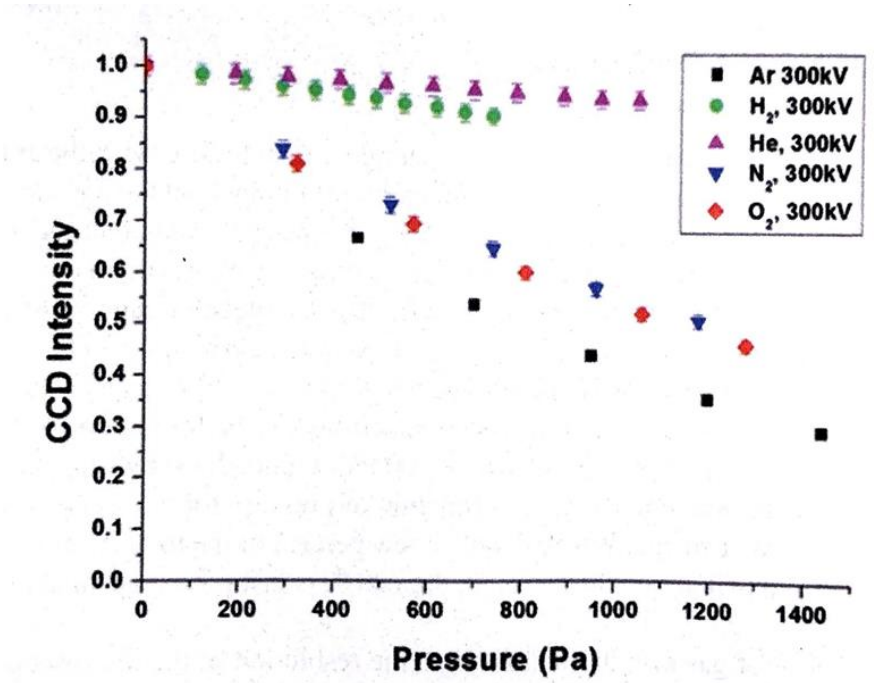

Figure 2.17. Intensity recorded on the CCD camera as a function of gas species and pressure for a 300 keV electron beam. Heavier molecules cause more electron-gas scattering events to occur which are intercepted by apertures and other parts of the microscope. Image from (Hansen & Wagner, 2012, 2016).

The spatial resolution of the microscope is also decreased with increased gas pressure. As shown in Figure 2.18, a damping of the contrast transfer function can be seen in the FFTs in images of amorphous carbon imaged out of focus in the presence of gas. The loss of information from higher spatial frequencies in increased gas pressure occurs due to elastic and inelastic scattering above and below the sample (Yaguchi et al., 2011; Suzuki et al., 2013). Furthermore, a high beam current density or total current causes significant ionization of gas molecules, resulting in structural degradations such as etching and loss of resolution (Jinschek & Helveg, 2012; Bright et al., 2013). To minimize the negative effects of complex electron-gas interactions inside the microscope, it is generally desirable to use reduced beam currents and lower pressures to ensure adequate resolution while studying specimen dynamics.

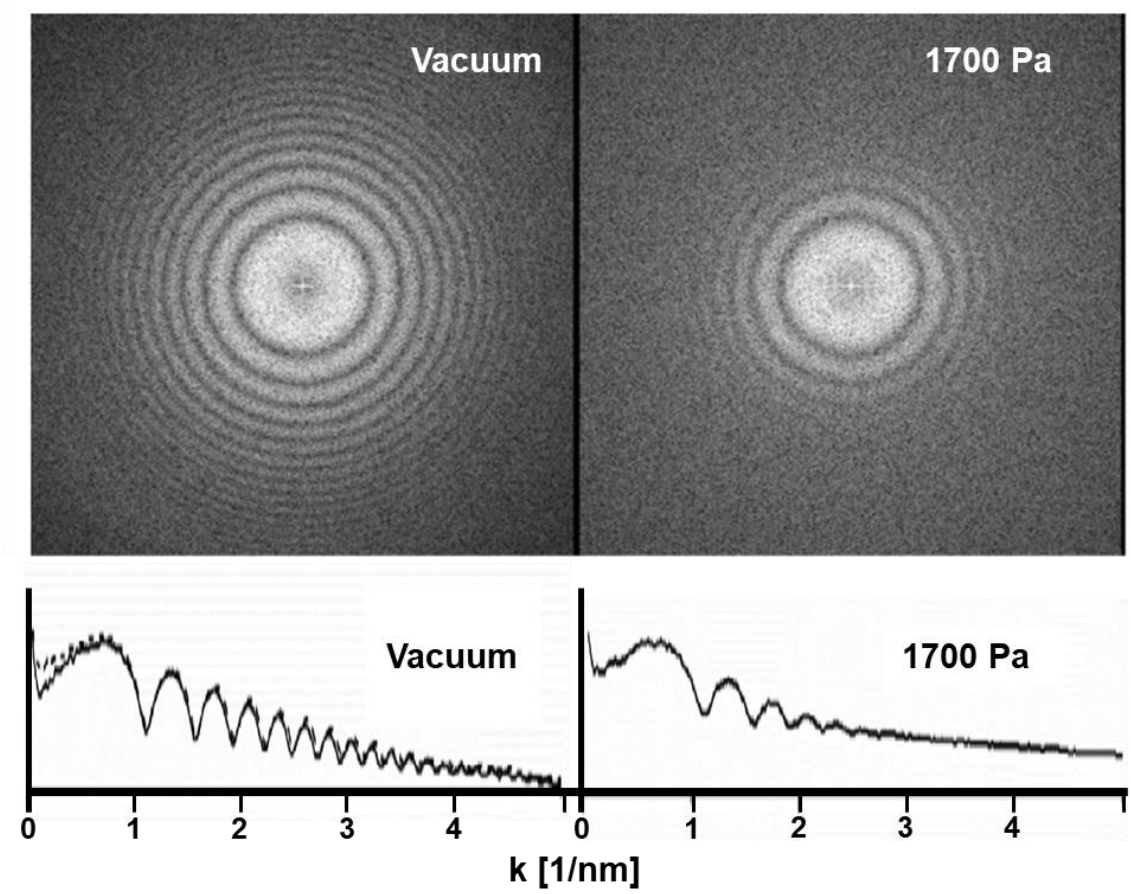

Figure 2.18. Contrast transfer in presence of gas. Top: FFT of amorphous carbon imaged out of focus. Bottom: the radial intensity of the FFT in the top has been extracted. Figure adapted from (Hansen & Wagner, 2012).

Many insights on CeO2-based materials have been enabled through in situ TEM techniques (Zhang et al., 2018). For example, Sharma et al. used in situ ETEM and EELS to investigate the reduction behavior of low-surface area and high-surface area CeO2 catalysts in H2 at elevated temperature (Sharma et al., 2004). It was found that high-surface area CeO2 catalysts underwent reduction at lower temperatures than low-surface area samples, and oxygen vacancy ordering occurred under reduction conditions. In follow-up studies, it was shown that oxygen vacancy ordering led to the formation of C-type Ce2O3 and was easily reversible during re-oxidation, revealing the structural mechanism for the

rapid storage and release of oxygen in CeO2 redox applications (Crozier et al., 2008; Wang et al., 2009). In situ TEM imaging and simultaneous electrical biasing of CeO2 revealed that oxygen vacancy ordering was responsible for the resistance switching effect in ceria and demonstrated that redox processes could be electrically driven at ambient temperature (Gao, Wang, et al., 2010; Gao, Kang, et al., 2010). The important influence of metal-ceria interfaces on redox reactions has been characterized for a variety of different metals and reactions using in situ TEM (Cargnello et al., 2013; Uchiyama et al., 2011; Yoshida et al., 2012; Kuwauchi et al., 2013; Zhang et al., 2015; Lawrence & Crozier, 2018). The ability to observe dynamic processes under reaction conditions has clearly expanded our fundamental understanding of CeO2-based materials.

2.3.6 Specimen Preparation

TEM powder specimens were prepared by sprinkling nanoparticles onto a thin, holey carbon film (~15 nm thick) supported on a 200 mesh Cu grid (Grid Tech). Thin, high quality amorphous carbon films were necessary for aberration measurement and correction when using the FEI Titan microscope. For *in situ* experiments, the microscope was first aligned using the holey carbon films and then a Pt grid was loaded into the heating holder. Carbon films were not used for heating/gas experiments to avoid corrosion/etching of the carbon film and to ensure the experimental observations were due to the desired catalyst-gas interaction and not catalyst-carbon film interactions. The Pt mesh grids were punched out of a 100-mesh woven Pt mesh using a $1/8^{th}$ inch hole punch, similar to a paper hole punch. To increase rigidity and interconnect of mesh fibers, a glass vial was used to ‘crush’

the Pt mesh. Samples were then prepared by immerging Pt mesh grids in a vial of nanoparticle powder to coat the grid bars.

2.3.7 TEM Imaging Cameras

A conventional charge-coupled device (CCD) camera was used for the work in Chapter 3 while an advanced direct detection camera was used for image formation in Chapters 4-6. Conventional CCD detectors used in TEM imaging cameras use an indirect detection method for image formation. As shown in Figure 2.19., CCD cameras convert incident electrons into light using a scintillator, then the light is transferred through an optical fiber to a CCD sensor to convert the light into charge, which is transferred pixel-by-pixel to be read out as an image. The scintillator design of the CCD camera provided protection against radiation damage of the sensor from high-energy electrons and led to the widespread adoption of CCD cameras for electron microscopy in the 1980s (Spence & Zuo, 1988). However, the scintillator is a limiting factor for camera performance, and recent developments in CMOS active pixel sensor (APS) technology has enabled direct detection cameras to become the future norm in electron microscopy. As shown in Figure 2.19., direct detection cameras eliminate the scintillator and directly convert incident electrons to charge. In this design, each pixel contains a photo detector and active amplifier and pixels are read out individually. Direct detection cameras have led to significantly improved performance in read-out speed, image resolution, and sensitivity compared to traditional CCD cameras (Faruqi et al., 2005; McMullan et al., 2014; Faruqi & McMullan, 2018; Ruskin et al., 2013). For scintillator-based cameras, electrons can be scattered in the optical fiber, generating a major source of noise. In contrast, the thin and transmission

sensor of the direct detection method dramatically minimizes the noise, which leads to improved signal-to-noise. Ultimately, this results in an increased detective quantum efficiency (DQE), which is a measure of the ability of an imaging device to generate image contrast above noise (Pan & Czarnik, 2016). By reducing the noise and directly counting incident electrons, direct detection cameras provide improved DQE values across all spatial frequencies, leading to better sensitivity and resolution.

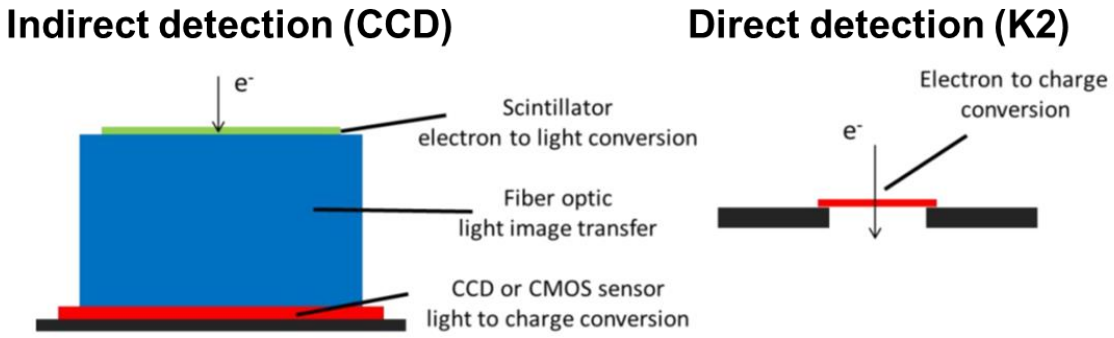

Figure 2.19. Schematic illustration of indirect and direct detection methods for electron microscopy imaging cameras. Figure adapted from Gatan K2-IS User Guide, Gatan, Inc.

3 Oxygen Transfer at Metal-Reducible Oxide Nanocatalyst Interfaces: Contrasting Carbon Growth from Ethane and Ethene

3.1 Motivation

As discussed in Section 1.3.6., metal-ceria interfaces can strongly influence catalytic activity and reduce carbon deposition on metal nanoparticles through facile oxygen transfer from the ceria support. During hydrocarbon reforming reactions, hydrocarbons are often converted to syngas (CO and H_2), and carbon deposition is an undesirable side reaction which can deactivate the catalyst and cause mechanical degradation (Ghoneim et al., 2016). For example, during direct reforming on SOFC anodes, carbon deposition not only deactivates the catalyst but may also fracture or destroy the anode microstructure if not controlled (Zhan & Barnett, 2005; Bierschenk et al., 2010; Pillai et al., 2010). Nickel, in the form of nanoparticles, is often employed as the catalyst for hydrocarbon reforming because of its ability to activate the C-H bond and its low cost (Abatzoglou & Fauteux-Lefebvre, 2016). For processes such as steam reforming, dry reforming, or partial oxidation, the oxidizing reactant is introduced to the reactor in gaseous form (H_2O, CO_2 or O_2) which adsorbs and dissociates on the catalyst surface (Rostrup-Nielsen, 1993; Liu et al., 2010). For reforming on SOFC anodes, the oxidizing reactant is reactive lattice oxygen which diffuses through the fuel cell from the cathode. Any restriction in access or decrease in the supply of oxidizing reactants may result in carbon formation and subsequent degradation.

Metal catalysts supported on ceria-based supports provide a bifunctionality during reforming reactions since the metal surface can activate the hydrocarbon and the ceria is effective for the oxidation of carbon species (Ruiz Puigdollers et al., 2017). The use of

Ni/ceria-based catalysts has provided improved carbon-resistant systems for industrial steam reforming, dry reforming, partial oxidation, and autothermal reforming processes due to the high oxygen mobility introduced by the ceria component (Montini et al., 2016; Ghoneim et al., 2016; Aneggi et al., 2016; Ta-Jen Huang et al., 2005). In particular, Gd-doped ceria (GDC) has displayed improved carbon resistance and is frequently used to minimize carbon deposition during reforming reactions over Ni/ceria-based catalysts (Gür, 2016; Wang et al., 2017; Zha, 2004; Duboviks et al., 2015). In such Ni-ceria composite systems, interfacial interactions are critical in controlling the chemical reactions occurring on the material's surface. Despite Ni/ceria-based catalysts exhibiting improved carbon-resistance, the literature on reforming light hydrocarbon components of important feedstocks, such as natural gas, over Ni/ceria-based catalysts lacks comparative analysis of carbon formation from different hydrocarbons. Most studies have focused on methane (CH_4) reforming to syngas, since CH_4 is the predominant component of natural gas (Wei Wang et al., 2006; Souentie et al., 2013; Niakolas et al., 2013; Zongyuan Liu et al., 2017; Kho et al., 2017; Ay & Üner, 2015; Liu et al., 2016). For example, Liu *et al.* investigated the effects of metal-support interactions on C-H bond breaking for dry reforming of methane over a Ni/CeO_2 catalyst (Liu et al., 2016). However, to obtain a more complete picture of carbon deposition associated with natural gas and metal-oxide interfacial processes, it is important to investigate the behavior of higher hydrocarbons, such as ethane (C_2H_6) and propane (C_3H_8). Recently, a few studies have examined the carbon formation processes associated with ethane and propane reforming over various catalysts (Bierschenk et al., 2010; Schädel et al., 2009; Solsona et al., 2012; Xufeng Lin et al., 2012; Huang & Reimert, 2013). The deposition of carbon from these gases has been shown to occur more

easily than from methane (Eguchi et al., 2002; Kishimoto, 2004; Kishimoto et al., 2005; Bierschenk et al., 2010), making their behavior of paramount importance.

To understand differences in the carbon deposition behavior from various gases, it is important to characterize the interactions that take place at the metal-oxide interface. The rate at which adsorbates are oxidized at the metal-oxide interface depends on the concentration of adsorbate species at the interface and the oxygen vacancy formation energy at the three-phase boundary, i.e. the line of contact between the gas phase, the metal, and the oxide. Ceria has an inherently high oxygen storage capacity and serves as an oxygen source during initial oxidation reactions on the surface. Moreover, it is also a fast oxygen ion conductor, and it may be initially easier to backfill the surface oxygen vacancy by oxygen migration from the lattice rather than the potentially more difficult four electron transfer process required for the dissociation of a molecular O_2 adsorbate (Adler et al., 2007). However, after oxygen is removed from the outer layers of the crystal, the distance that lattice oxygen must diffuse from the crystal interior becomes larger. Thus, the oxygen storage capacity becomes depleted and oxygen may become much harder to donate to the catalytic reaction in highly-reduced ceria (i.e. Ce_2O_3), and the molecular dissociation of reactant species may become more favorable.

In situ studies, which directly probe the metal-oxide interface evolution in the presence of different hydrocarbons, can provide valuable insights on the atomic-level mechanism leading to carbon deposition (Ertl et al., 2008). For example, *in situ* ETEM has been used to investigate atomic-level nucleation and growth mechanisms of carbon nanotubes over Ni catalysts (Hofmann et al., 2007; Lin et al., 2006; Sharma et al., 2005;

Sharma & Iqbal, 2004; Kling et al., 2016). In this chapter, *ex situ* characterization and aberration-corrected, *in situ* ETEM techniques were used to investigate the atomic-level metal-support interactions occurring during initial stages of carbon deposition from light hydrocarbons over model Ni reforming catalysts. To determine species-dependent differences in carbon deposition behaviors, representative natural gas species were reformed separately over a Ni/GDC catalyst, and the amount of carbon deposited by each species was quantified. A Ni/GDC catalyst was selected due to its widespread use as a carbon resistant material (Wei Wang et al., 2006; Ge et al., 2012). However, to isolate and probe the role of the Ni/ceria interface, a model Ni/CeO_2 nanocube catalyst system was chosen to facilitate the interpretation of *in situ* ETEM experiments. To elucidate the role of ceria on regulating carbon deposition from light hydrocarbons, the same *ex situ* and *in situ* experiments were performed on a Ni catalyst supported on SiO_2, a non-reducible oxide. The Ce oxidation state was monitored with EELS (Sharma et al., 2004) and when combined with STEM, provided nanometer level resolution; thus, local structural evolution was correlated with catalytic properties under reactive conditions. *In situ* atomic-resolution TEM images and STEM/EELS linescans of the catalyst particles and interfaces were used to identify the mechanisms that enable Ni/CeO_2-based catalysts to inhibit carbon deposition from light hydrocarbons. The primary focus of this work was to explore the fundamental carbon formation behavior taking place under conditions when gaseous oxygen is not readily available (e.g. a solid oxide fuel cell anode).

3.2 Experimental

3.2.1 Catalyst Synthesis

A 20 wt% Ni/$Gd_{0.15}Ce_{0.85}O_2$ (GDC) powder was synthesized using the one-step spray drying synthesis technique as described in Section 2.1.1. A subsequent reduction in H_2 at 400°C was necessary to convert NiO/GDC into the catalytically active phase of interest, Ni/GDC, which is seen in Figure 3.1a. A 10 wt.% Ni/CeO_2 nanocube catalyst was synthesized using the hydrothermal synthesis and wet impregnation procedures described in Section 2.1. Following a reduction in H_2 at 400°C for two hours, the resulting Ni/CeO_2 catalyst yielded an average Ni particle size of 8.6 nm. A typical Ni/CeO_2 nanocube catalyst is shown in Figure 3.1b following NiO reduction. A 7.3 wt.% Ni/SiO_2 catalyst synthesized by Chenna *et al*. was chosen for this study due to a nearly identical particle size distribution to the 10 wt.% Ni/CeO_2 catalyst (Chenna et al., 2011); the average Ni particle size on the 7.3 wt.% Ni/SiO_2 catalyst was 8.9 nm. For the 7.3 wt.% Ni/SiO_2 catalyst, amorphous SiO_2 spheres were synthesized via the Stöber method (Stöber et al., 1968) and then calcined at 500°C for two hours to remove any precursor residues. The resulting amorphous silica spheres were impregnated with 7.3 wt.% Ni using the same incipient wetness impregnation method as described by Banerjee *et al.* (Banerjee et al., 2009; Chenna et al., 2011) and summarized in Section 2.1.3. The resulting Ni/SiO_2 catalyst is shown in Figure 3.1c after NiO reduction. Although the Ni loading amount was different for each support, this was not a critical concern because the focus of this work was to study the Ni/support interfaces, independent of the metal loading. The resulting catalysts produced particle size

distributions and dispersions that were suitable for TEM observations, and therefore the different metal loading of each catalyst was appropriate for this work.

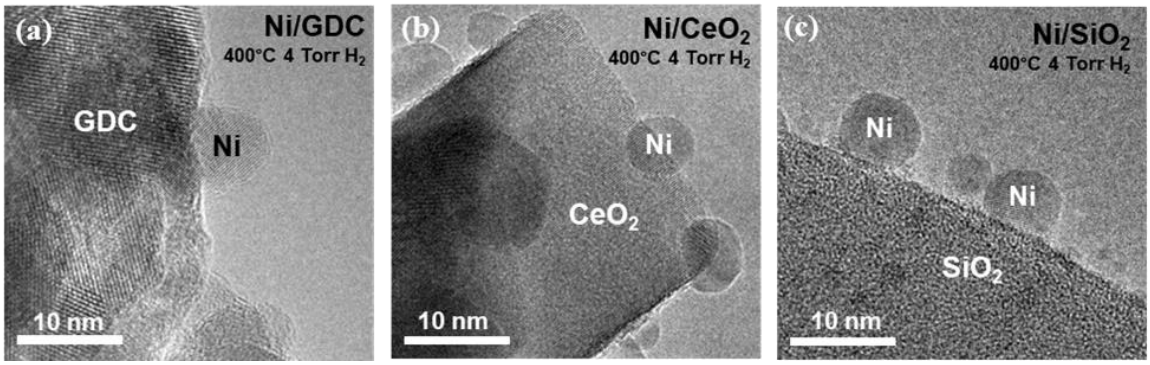

Figure 3.1. Typical images of fresh catalysts in 4 Torr H_2 at 400°C. (a) Ni/GDC, (b) Ni/CeO_2, (c) Ni/SiO_2.

3.2.2 *Ex situ* Catalyst Characterization

The freshly calcined catalysts' activity for the catalytic partial oxidation of methane to syngas ($CH_4 + ½O_2 \rightarrow CO + 2H_2$) was determined using an In Situ Research Instruments (ISRI) RIG-150 microreactor with a 10 mm internal diameter quartz tubular fixed-bed flow furnace. Under similar experimental conditions, the activity for the catalytic partial oxidation of ethane was determined. Product gases were analyzed with a Varian 3900 Gas Chromatograph (GC). This system was used for all *ex situ* reforming and carbon deposition experiments. For *ex situ* reforming experiments, the input reactant gas was a mixture of CH_4/O_2/He or C_2H_6/O_2/He, with typical flow rates of 8 cc/min C_2H_6 or C_2H_4, 4 cc/min O_2, and 50 cc/min He. The catalyst bed temperature was increased from 30°C to 900°C at a rate of ~4°C/min, and the conversion of fuel to products was monitored as a function of temperature.

For *ex situ* carbon deposition experiments, the Ni-supported catalysts were first reduced at 400°C for two hours in 5% H_2/Ar and then heated to 550°C in 5% H_2/Ar at a heating rate of ~4°C/min. Once the catalyst reached 550°C, the temperature was held constant as the gas flow was immediately switched to either C_2H_6, C_2H_4, CH_4, or CO, each of which are either present in natural gas or observed during reforming. The catalyst was exposed to the carbonaceous gas for 10 min. The gas flow was then immediately switched to He carrier gas and the furnace was turned off to allow the catalyst to cool to room temperature. To quantify the amount of carbon deposited during the reaction, temperature programmed oxidation (TPO) was carried out by flowing 50 cc/min He and 3 cc/min O_2 while heating to 750°C at a rate of 2°C/min. The deposited carbon was oxidized to CO_2, and the resulting output gas flow was analyzed using a Varian 3900 GC. A JEOL 2010F TEM was used to image all *ex situ* carbon deposition catalysts.

3.2.3 *In situ* Catalyst Characterization

In situ electron microscopy experiments were undertaken to obtain a deeper understanding of the relationship between the carbon deposition process, the oxide support, and the hydrocarbon source. The experiments were performed on an FEI Titan ETEM equipped with a Gatan Imaging Filter (GIF) which was used for EELS. For all experiments, Ni/SiO_2 and Ni/CeO_2 powders were dispersed onto a Pt mesh TEM sample grid and loaded into a Gatan hot stage. The catalysts were initially reduced at 400°C for 2 hours in 5% H_2/Ar in an ISRI RIG-150 microreactor. The sample was transferred to the FEI Titan ETEM and further reduced *in situ* at 400°C for 2 hours in 4 Torr H_2 to remove any surface oxides that may have formed during transfer to the microscope. Regions of interest were

imaged in H_2 and the sample was cooled to 100°C. Hydrocarbon gas was then introduced to the sample chamber, heated to 550°C, and the same regions were imaged as in H_2. Images were acquired over 1-4 hours of hydrocarbon exposure. Under real internal reforming conditions, H_2O and CO_2 will also be present on the anode. However, it is important to recognize that the reforming conditions will be very different along the anode flow channel (Chenna et al., 2011). Close to the inlet, the concentration of H_2O and CO_2 will be very low, whereas at the outlet, these products will dominate (Paradis et al., 2011). Thus, it was anticipated that the conditions present in the ETEM would be close to those present at the anode inlet.

For *in situ* STEM experiments, a nominal probe size of ~2 Å was used; however, in practice, instabilities in both the hot stage and sample at elevated temperature degraded the spatial resolution of the spectroscopy up to 1 nm although this did not impact the overall conclusions from the analysis. *In situ* EELS was used to monitor the oxidation state of Ce^{3+}, which varies with the oxygen content of the ceria according to $Ce_x^{3+}Ce_{1-x}^{4+}O_{2-x/2}$. Transitions from the occupied $3d^{5/2}$ band and the $3d^{3/2}$ band to unoccupied 4f states above the Fermi level give rise to sharp spectral peaks at 879eV (M_5) and 900 eV (M_4), the so-called Ce M_{45} edge. The occupancy of the 4f band changes from 0 to 1 as the oxidation state of Ce changes from 4+ to 3+. A simple method to determine the occupancy of the 4f states is to use the relative intensity ratio of the M_5 and M_4 peaks as described in Section 2.3.4 (Sharma et al., 2004). It was assumed that the M_5-to-M_4 intensity ratio measured at room temperature in vacuum represented the Ce^{4+} state while the intensity ratio measured at 800°C in H_2 represented a Ce^{3+} oxidation state. Values between these two limiting values

represent a mixture of Ce^{4+} and Ce^{3+} oxidation states. All experimental data was quantified assuming a linear relationship between the M_5-to-M_4 intensity ratio and the Ce oxidation state. The local Ce oxidation state, and thus the local oxygen content of the ceria support was determined. Spectra were acquired over 1-4 hours of hydrocarbon exposure.

3.3 Results and Discussion

3.3.1 Catalytic Activity of Reforming Reactions

The partial oxidation of methane to syngas ($CH_4 + ½ O_2 \rightarrow CO + 2H_2$) over a Ni/GDC catalyst was investigated from 100°C to 900°C. As seen in Figure 3.2a, CH_4 and O_2 conversion began around 350°C and produced CO_2 and H_2O (complete oxidation of methane) until ~700°C. At 700°C, O_2 conversion reached 100% and a significant increase in CH_4 conversion occurred. This large increase in CH_4 conversion has been discussed previously (Chenna et al., 2011) and is attributed to NiO particles converting to Ni metal once a reducing environment has been established by complete O_2 conversion. Once reduced to Ni, the catalyst produced CO and H_2 (partial oxidation of methane), and for the reactor conditions employed here, showed methane conversion that was near thermodynamic limits.

The partial oxidation of ethane was also investigated over a Ni/GDC catalyst from 100°C to 900°C. Conversion results are also shown in Figure 3.2a. C_2H_6 and O_2 began converting at roughly the same temperature (350°C) as CH_4 and O_2 reforming. During C_2H_6 reforming, the O_2 conversion reached 100% at 600°C and a significant increase in C_2H_6 conversion occurred. This significant increase in conversion can again be associated

with the conversion of NiO to Ni. 100% C_2H_6 conversion occurred around ~700°C while CH_4 was not fully converted until ~800°C. Notably, carbon deposits (graphite layers) were observed with TEM on the catalyst following C_2H_6 reforming but not after CH_4 reforming. Thus, reactions occurring with gases present during C_2H_6 reforming caused carbon deposition onto the Ni/GDC catalyst. Figure 3.2b shows the carbon-containing products detected during the partial oxidation of ethane. Ethene (C_2H_4), CH_4, CO, CO_2, and residual un-reformed C_2H_6 were all detected at various temperatures and were the focus for *ex situ* carbon deposition experiments.

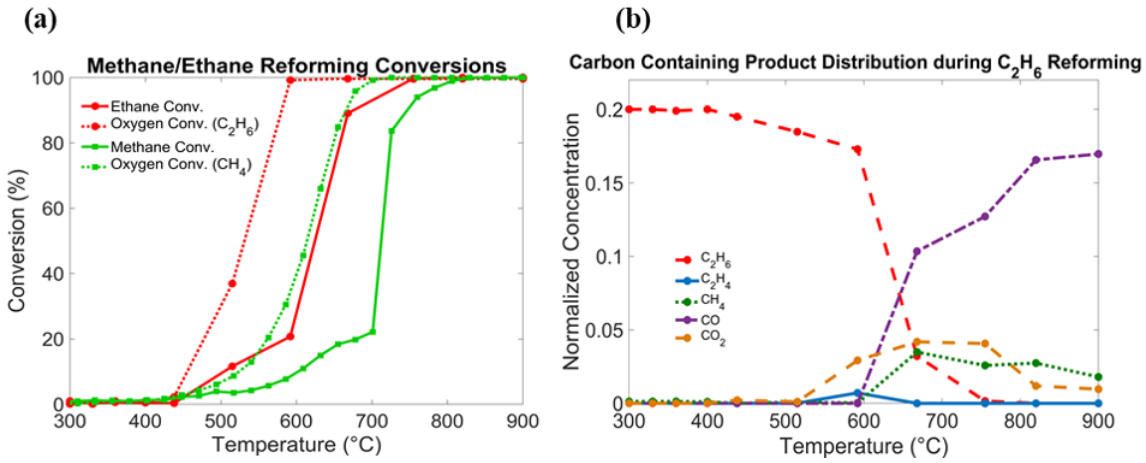

Figure 3.2. (a) Conversion data for partial oxidation of methane and partial oxidation of ethane over Ni/GDC catalyst. The ethane reforming reaction proceeded at lower temperatures than methane reforming. Carbon deposits were observed after ethane reforming but not after methane reforming. (b) Carbon-containing products present during C_2H_6 reforming reaction.

3.3.2 *Ex situ* Carbon Deposition

The carbon deposition observed following C_2H_6 reforming may have been deposited by the reactants, products, and/or intermediate gas species present at the surface of the Ni/GDC catalyst. To determine the carbon species most likely to cause carbon

deposition, a set of experiments was performed to quantify the amount of carbon deposited individually by each of these gases: C_2H_6, C_2H_4, CH_4, and CO. The Ni/GDC catalyst was heated to 550°C, a temperature at which all four carbon-containing gases were observed during the C_2H_6 reforming experiment, in an ISRI RIG-150 microreactor and exposed to each of the four carbon-containing gases separately under conditions specified previously in the experimental section. The TPO results are summarized in Figure 3.3, and it is shown that C_2H_4 is responsible for the largest amount of deposited carbon as evidenced by the largest peak. C_2H_6 was responsible for the second largest amount. CO deposited a minimal amount of carbon under these conditions. CH_4 also showed minimal carbon deposition when compared to C_2H_4 and C_2H_6. These observations are consistent with prior work showing that two-carbon molecules deposit carbon more easily than CH_4 (Eguchi et al., 2002; Kishimoto, 2004; Kishimoto et al., 2005; Bierschenk et al., 2010), further underscoring the need to evaluate the performance of catalysts under representative light hydrocarbon environments. To isolate and probe the role of the Ni/ceria interface, C_2H_4 and C_2H_6 were selected for further investigation of carbon deposition behaviors onto the model Ni/CeO_2 and Ni/SiO_2 systems.

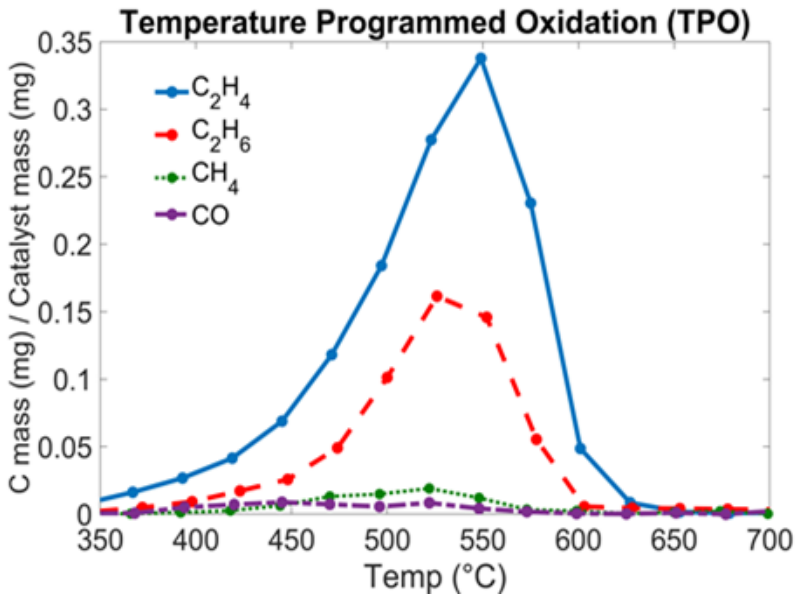

Figure 3.3. Temperature programmed oxidation results from four different carbon-containing gases on a Ni/GDC catalyst. Ethene (C_2H_4) and ethane (C_2H_6) were responsible for large deposits on the catalyst.

To determine the differences in carbon deposition behaviors between C_2H_4 and C_2H_6, ex situ carbon deposition experiments were performed using model Ni/CeO2 and Ni/SiO_2 catalysts. The Ni/CeO_2 and Ni/SiO_2 catalysts were heated to 550°C and exposed to either C_2H_6 or C_2H_4 for 10 minutes. Following cool down, the catalysts were examined with a JEOL 2010F TEM. Ni particles re-oxidized to NiO during transfer to the microscope. Many carbon nanofibers (CNFs) were observed on the Ni/SiO_2 catalyst when exposed to C_2H_4 as is seen in Figure 3.4a. The growth of CNFs is consistent with other studies on Ni/SiO_2 and C_2H_4 exposure (Esconjauregui et al., 2009). Graphite growth was observed on Ni/CeO_2 during C_2H_4 exposure and some Ni particles were encapsulated with graphite, as shown in Figure 3.4b. Ceria surfaces were void of graphite; only Ni particle surfaces showed carbon. TPO was performed to quantify the amount of carbon present on the model Ni/CeO_2 and Ni/SiO_2 catalysts. TPO results in Figure 3.4c show that large

carbon deposits were on Ni/SiO_2 (solid blue line) relative to Ni/CeO_2 (dotted red line), likely due to the large number of CNFs present on Ni/SiO_2. Thus, carbon deposition occurred on both Ni/SiO_2 and Ni/CeO_2, indicating that the CeO_2 support was unable to inhibit carbon deposition during C_2H_4 exposure. During C_2H_6 exposure, all Ni/SiO_2 particles showed a large degree of CNF growth as seen in Figure 3.5a, but no CNFs were observed on any Ni/CeO_2 catalyst (Figure 3.5b). TPO was also used to quantify the deposited carbon from C_2H_6 onto each catalyst; results are shown in Figure 3.5c. Additionally, each bare support was subjected to the same hydrocarbon conditions and the TPO results are included in Figure 3.5c. Bare SiO_2 and CeO_2 had no carbon deposits as evidenced by the lack of peaks in the TPO results. The lack of carbon deposition on the bare supports is consistent with other studies that have examined carbon deposition on these supports, which concluded that Ni is necessary to catalyze hydrocarbon decomposition (Takenaka et al., 2001; Zhang & Amiridis, 1998). As evidenced by the largest peak in Figure 3.5c, Ni/SiO_2 had a large amount of carbon deposition when compared to the very small peak from Ni/CeO_2. The comparison of Ni on these two different supports suggests that the metal-support interaction between Ni and CeO_2 plays a key role in suppressing carbon deposition onto the Ni/CeO_2 catalyst during C_2H_6 exposure.

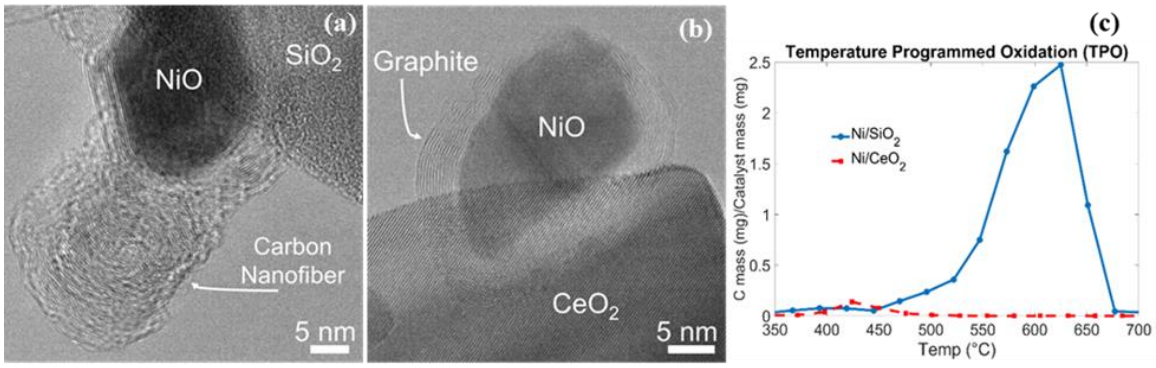

Figure 3.4. *Ex situ* carbon deposition from ethene (C_2H_4) on Ni/SiO_2 and Ni/CeO_2. A large amount of carbon nanofibers grew on Ni/SiO_2 as seen in (a). Carbon deposited in the form of graphite onto Ni/CeO_2, (b) shows a Ni particle that was encapsulated with graphite during C_2H_4 exposure. (c) Temperature programmed oxidation results from C_2H_4 onto model Ni/CeO_2 and Ni/SiO_2 catalysts. Ni/CeO_2 was unable to inhibit carbon deposition as evidenced by the peak at ~425°C in the red dotted line.

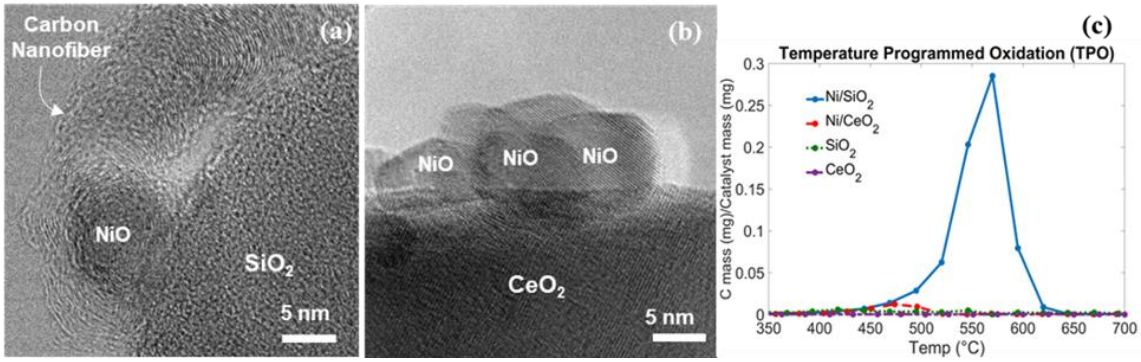

Figure 3.5. *Ex situ* carbon deposition from ethane (C_2H_6) on Ni/SiO_2 and Ni/CeO_2. Carbon nanofibers grew on Ni/SiO_2 as seen in (a) No carbon deposition was observed on Ni/CeO_2. Ni particle surfaces were clean when supported by CeO_2 as seen in (b). (c) Temperature programmed oxidation results from carbon deposited during C_2H_6 exposure on Ni/SiO_2, Ni/CeO_2, SiO_2, and CeO_2. SiO_2 and CeO_2 had no carbon deposits. Ni/CeO_2 had a minimal amount of deposited carbon compared to Ni/SiO_2.

3.3.3 *In situ* Carbon Deposition

In situ ETEM experiments were conducted to investigate the differences in carbon deposition behaviors between C_2H_4 and C_2H_6 exposure during reaction conditions. Initial images were recorded in a H_2 environment to ensure NiO particles had been reduced to Ni

and to have baseline structural information to facilitate the identification of changes induced by hydrocarbon introduction. Figure 3.6a-b shows a Ni/SiO_2 particle at 400°C in 4 Torr H_2 and 550°C in 0.5 Torr C_2H_4, respectively. Graphite layers were seen growing on the Ni surface during C_2H_4 exposure. Likewise, graphite layers formed on Ni/CeO_2 as can be seen in Figure 3.6c-d which were acquired under the same conditions as Figure 3.6a-b. Images in Figure 3.6b,d were acquired after ~2 hours of C_2H_4 exposure. Figure 3.7a-b shows Ni/SiO_2 at 400°C in 4 Torr H_2 and at 550°C in 1 Torr C_2H_6, respectively. Several graphite layers formed on the surface of the Ni particle on SiO_2 after ½ hour. All Ni/SiO_2 catalyst particles showed graphite formation. Figure 3.7c-d shows Ni/CeO_2 at 400°C in 4 Torr H_2 and at 550°C in 1 Torr C_2H_6, respectively. Contrary to what was seen on Ni/SiO_2, Ni/CeO_2 showed no signs of graphite formation even after 4 hours of C_2H_6 exposure. In Figure 3.7d, the crystalline CeO_2 present in Figure 3.7c has become an amorphous CeO_{2-x} phase. The representative structural change is shown in additional Ni/CeO_2 regions in Appendix 8.1. No structural changes were seen in Ni/CeO_2 during C_2H_4 exposure and the ceria support remained crystalline as Ni particles were encapsulated with graphite, as shown in Figure 3.6d and in additional regions in Appendix 8.1. The transformation from crystalline to amorphous ceria is thus facilitated by C_2H_6 exposure. It was hypothesized that this structural transformation was the result of oxygen being removed from the CeO_2 lattice to inhibit graphite formation. To further test this hypothesis, *in situ* spectroscopy experiments were performed.

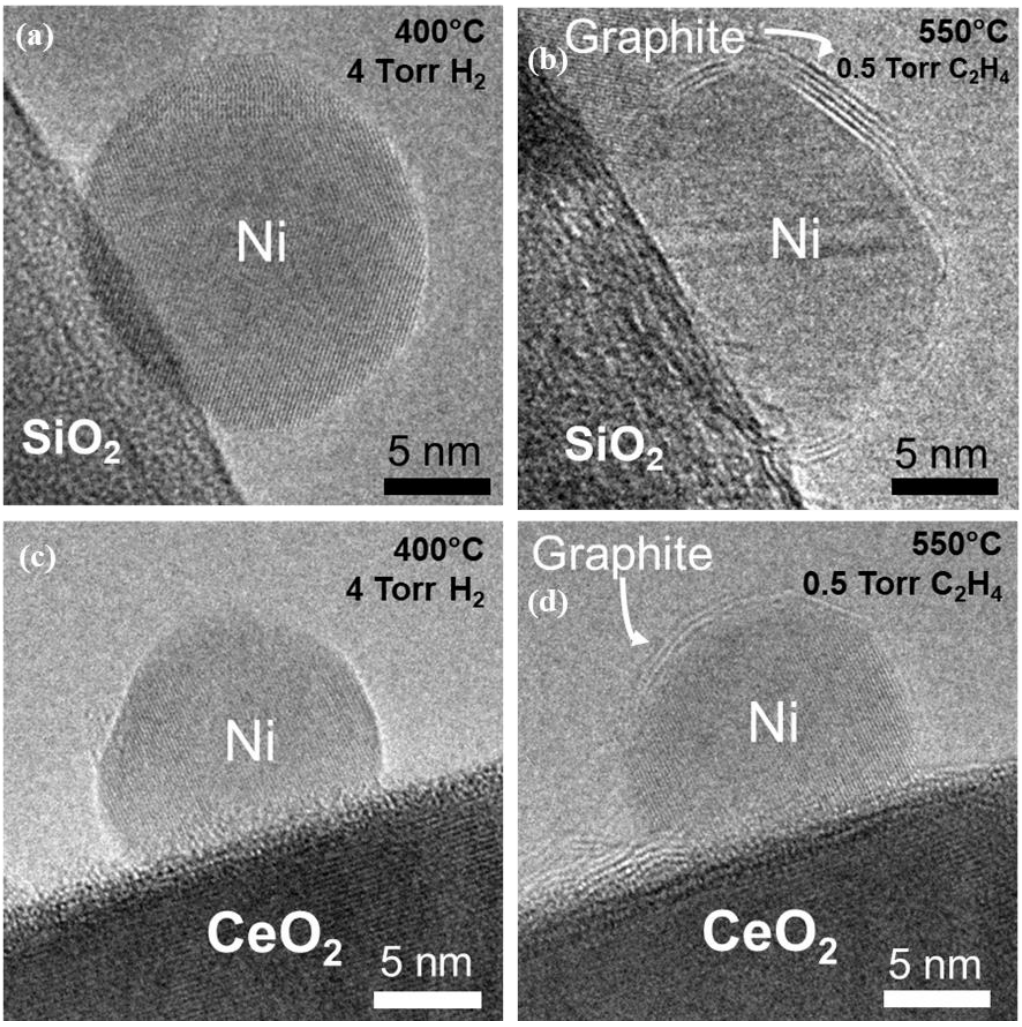

Figure 3.6. *In situ* C_2H_4 carbon deposition on Ni/SiO_2 and Ni/CeO_2. Images were acquired in H_2 (a) & (c) to ensure that the catalyst was in the active Ni metal phase. Graphite was observed on the surface of Ni particles on both Ni/SiO_2 (b) and Ni/CeO_2 (d) when exposed to C_2H_4. Both images in (b) and (d) were acquired after ~2 hours of C_2H_4 exposure.

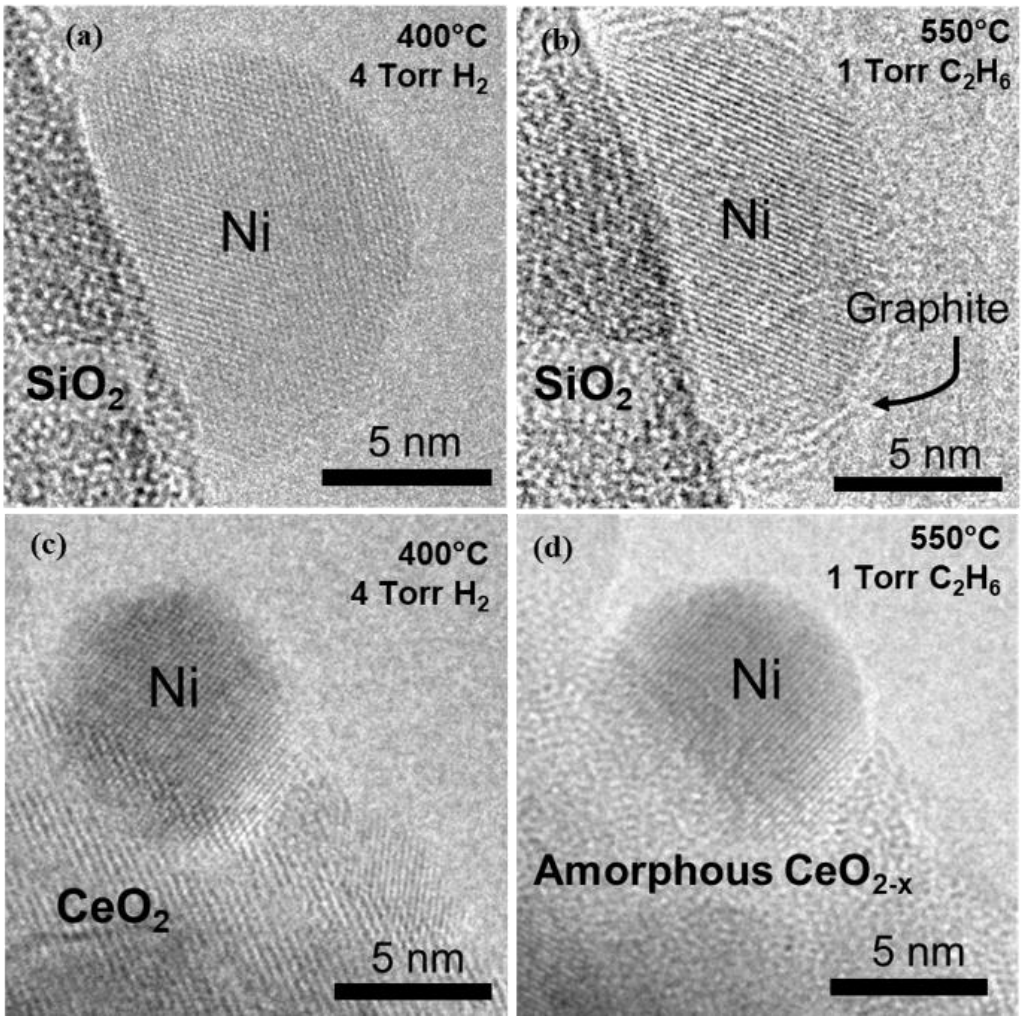

Figure 3.7. *In situ* C_2H_6 carbon deposition on Ni/SiO_2 and Ni/CeO_2. Images were acquired in H_2 (a) & (c) to ensure that the catalyst was in the active Ni metal phase. Graphite was observed on surfaces of Ni particles on Ni/SiO_2 after ½ hour exposure (b) but not on Ni/CeO_2 (d) when exposed to C_2H_6 for four hours. The ceria support has become amorphous after four hours of C_2H_6 exposure (d).

In situ STEM experiments were conducted to probe local Ce oxidation states during C_2H_6 and C_2H_4 exposure at locations in the CeO_2 cubes near Ni/CeO_2 interfaces and at regions without any Ni particles nearby. Figure 3.8a shows a typical high-angle annular dark-field (HAADF)-STEM image of the Ni/CeO_2 catalyst. EELS linescans were acquired initially at 400°C in 4 Torr H_2 to use as a reference before hydrocarbon exposure. The linescans allowed the Ce oxidation state to be determined at each point along the line, thus

providing spatially resolved information on oxidation state as a function of distance from the Ni/CeO_2 interface. The dotted line in Figure 3.8a indicates the EELS linescan direction. Figure 3.8b is a typical spectrum from the EELS linescan near the Ni/CeO_2 interface (indicated by the red star on the linescan) in C_2H_4. Little change was observed in the Ce M_{45} relative peak intensity ratio when C_2H_4 was introduced and the sample heated to 550°C compared to spectra acquired in 4 Torr H_2 at 400°C, showing that the Ce near the metal-oxide interface was predominantly 4+. Figure 3.9a shows a representative HAADF-STEM image of another Ni/CeO_2 catalyst region. Figure 3.9b provides an energy-loss spectrum near the Ni/CeO_2 interface where the catalyst is in 4 Torr H_2 at 400°C. A change in the Ce M_{45} relative peak intensity ratio is observed when 1 Torr C_2H_6 is introduced and the sample is heated to 550°C as seen in Figure 3.9c. This Ce M_{45} peak intensity ratio change indicates a transition from Ce^{4+} to Ce^{3+} near the Ni/CeO_2 interface. In each *in situ* STEM EELS experiment, EELS linescans were acquired from 5-7 regions of interest in H_2. Following hydrocarbon introduction, EELS linescans were acquired from the same regions that were observed in H_2 exposure. An average Ce oxidation state as a function of distance from the Ni/CeO_2 interface in H_2, C_2H_4, and C_2H_6 was determined and is plotted in Figure 3.10. The Ce oxidation state remained near 4+ when the catalyst was in 4 Torr H_2 at 400°C as shown by the solid orange line. A slight reduction was observed near the Ni/CeO_2 interface when in 1 Torr C_2H_4 at 550°C as shown by the dashed blue line. A large change in Ce oxidation state (and thus oxygen removal) was seen at the Ni/CeO_2 interface when exposed to 1 Torr C_2H_6 at 550°C as evidenced by the dotted red line. Energy-loss spectra were also acquired at the surfaces and corners of bare CeO_2 cubes (without Ni particles) in H_2, C_2H_4, and C_2H_6, and the average Ce oxidation state in each gas was 4+. It was concluded that the localized

reduction zones near Ni/CeO_2 interfaces are caused by a removal of oxygen during hydrocarbon exposure facilitated by the Ni particles. Furthermore, this evidence also suggests that the structural transformation observed in Figure 3.7d and Appendix 8.1 is related to oxygen deficiency in the ceria support.

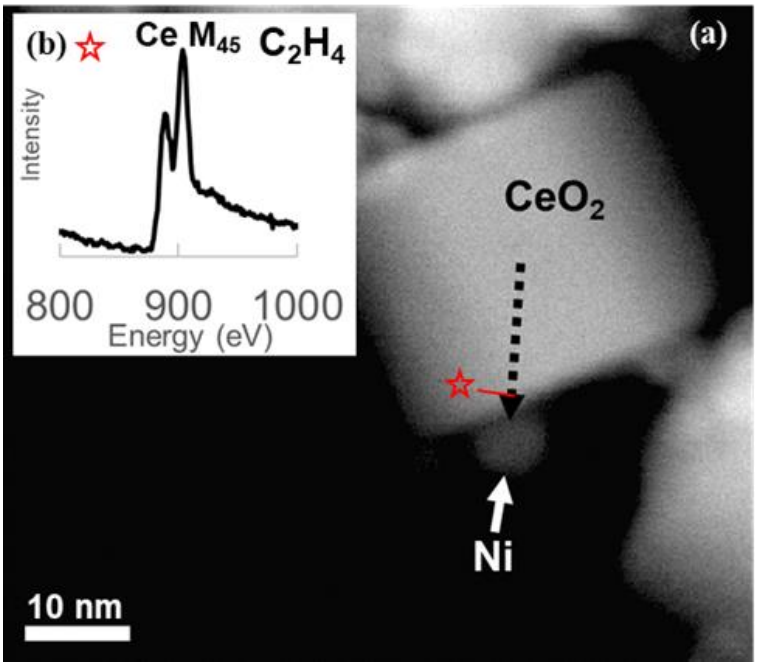

Figure 3.8. (a) HAADF-STEM image of Ni/CeO_2 catalyst. Dotted line indicates EELS linescan. Red star indicates the position on the linescan where (b) was acquired. (b) Energy-loss spectrum near Ni/CeO_2 interface (red star position) in 0.5 Torr C_2H_4 at 550°C. Little to no change of the Ce M_{45} edge intensity ratio from the spectrum (not shown) acquired in 4 Torr H_2 at 400°C was observed.

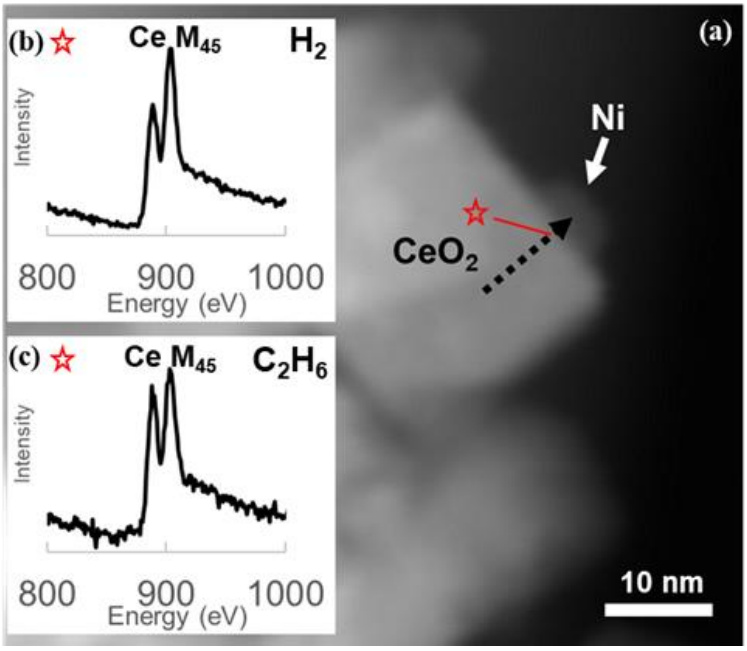

Figure 3.9. (a) HAADF-STEM image of Ni/CeO_2 catalyst. Dotted line indicates EELS linescan. Red star indicates the position on the linescan where the inserts were taken. (b) Energy-loss spectrum near Ni/CeO_2 interface (red star position) in 4 Torr H_2 at 400°C. (c) Energy-loss spectrum near Ni/CeO_2 interface (red star position) in 1 Torr C_2H_6 at 550°C. Ce M_{45} edge intensity ratio changes during C_2H_6 exposure indicating a transition from Ce^{4+} to Ce^{3+}.

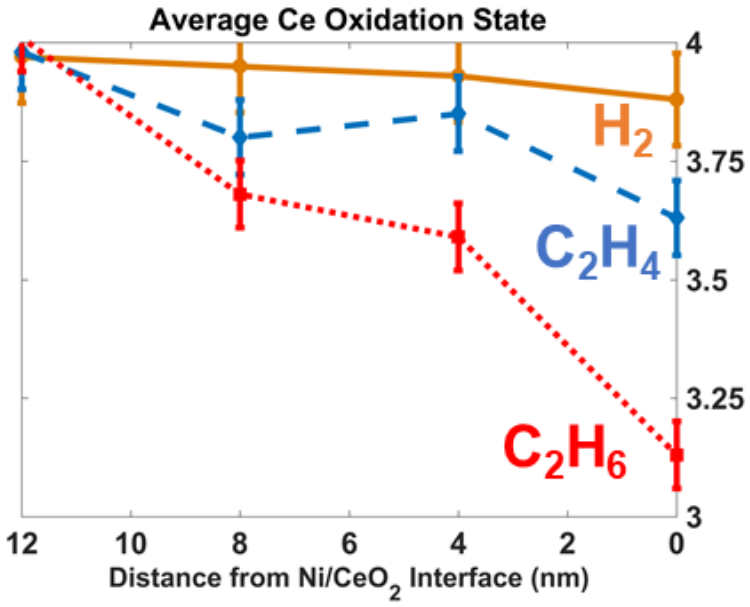

Figure 3.10. Plot of average Ce oxidation state as a function of distance from Ni/CeO_2 interfaces in C_2H_6 and C_2H_4. EELS linescans were acquired from several regions of interest

in each gas. The plot shows a slight reduction near the Ni/CeO_2 interface during C_2H_4 exposure and a large reduction near the Ni/CeO_2 interface during C_2H_6 exposure.

3.4 Discussion

Differences in the C_2H_6 and C_2H_4 molecules, as well as their molecular interactions with Ni/CeO_2, contribute to the different carbon deposition behaviors observed in these experiments. C_2H_4 (ΔH_f = +52 kJ/mol) is more thermodynamically unstable than C_2H_6 (ΔH_f = -84 kJ/mol) and is more likely to readily decompose. The thermal dehydrogenation of ethene to acetylene ($C_2H_4 \rightarrow C_2H_2 + H_2$) is an endothermic reaction (ΔH = 174 kJ/mol). However, once C_2H_2 is formed, subsequent decomposition reactions will occur rapidly to form carbon and hydrogen (Baker et al., 1972; Sharma & Iqbal, 2004; Feng et al., 2011; Otsuka et al., 2001). Ethane's thermal dehydrogenation to ethene ($C_2H_6 \rightarrow C_2H_4 + H_2$) is also an endothermic reaction (ΔH = 136 kJ/mol) (Qiao et al., 2016; Gerzeliev et al., 2015). However, an alternative way to dehydrogenate C_2H_6 is through partial oxidation, otherwise known as oxidative dehydrogenation (ODH) ($C_2H_6 + ½\ O_2 \rightarrow C_2H_4 + H_2O$), which is exothermic ($\Delta H$ = -106 kJ/mol) (Gärtner et al., 2013). Consequently, the dehydrogenation of C_2H_6 is thermodynamically favored in the presence of an oxidizing agent. During catalysis, the C-H bond is activated by a metal surface, in this case Ni (Santen & Niemantsverdriet, 1995; Vang et al., 2006). The rate limiting step of C_2H_6 decomposition on a Ni(111) surface is the initial C-H bond activation (E_a = 257.9 kJ/mol), whereas the initial C-H activation is more facile on Ni(111) for C_2H_4 decomposition (E_a = 47 kJ/mol) (Zhang et al., 2009; Basaran et al., 2011; Lehwald & Ibach, 1979; Vang et al., 2006). Compared to a C_2H_6 molecule, the C_2H_4 molecule's relative instability and low C-H bond

activation energy suggests that more rapid decomposition will take place directly on the Ni surface.

If the rate at which carbon atoms accumulate on the Ni particle surface exceeds the rate at which carbon is removed from the surface, then the surplus carbon can arrange into graphene sheets and form graphite layers. Recent density functional theory (DFT) studies have examined C_2H_6 and C_2H_4 dehydrogenation reactions on Ni surfaces and examined each intermediate product; they concluded that binding energies (BE) exhibit the following trend: $C_2H_6 < C_2H_4 < C_2H_2 < C_2H < C_2 < C$ (Zhang et al., 2009; Mueller et al., 2010; Basaran et al., 2011). For example, the BE of C_2H_4 on Ni is 63 kJ/mol, whereas C_2H_2 is bound to the Ni surface with a BE of 251 kJ/mol. Carbon dimers (C_2) are strongly bound to Ni with a BE of 708 kJ/mol and can be considered graphite-forming precursors. The formation of a carbon dimer (C_2) from individual C atoms ($C + C \rightarrow C_2$) is an exothermic reaction (ΔH = -71 kJ/mol) on Ni, thus facilitating facile C-C bond formation and subsequent graphite formation (Mueller et al., 2010; Basaran et al., 2011). Therefore, C_2H_4 not only dissociates more rapidly than C_2H_6 but also leads to an increase in graphite-forming precursors that are strongly bound to Ni surfaces resulting in the graphite layers seen on Ni surfaces in Figure 3.6d.

In contrast to the behavior of C_2H_4, the thermodynamically favorable location where decomposition of the C_2H_6 molecule will occur is near an oxidant – in this case at Ni/CeO_2 interface sites. At Ni/CeO_2 interface sites, or Ni particle "perimeter" sites, Ni can catalyze the ODH reaction ($C_2H_6 + ½\ O_2 \rightarrow C_2H_4 + H_2O$) through the consumption of surface oxygen atoms in the CeO_2 support due to its exothermic nature. The endothermic

dehydrogenation reaction ($C_2H_6 \rightarrow C_2H_4 + H_2$) may still occur on Ni surfaces, albeit at a much slower rate than the ODH reaction route preferred at Ni perimeter sites. While the decomposition of C_2H_6 and C_2H_4 may both lead to graphite-forming precursors, facile C_2H_6 decomposition is restricted to Ni/CeO_2 interface sites. Furthermore, graphite-forming precursors, such as C or C_2, generated near the Ni/CeO_2 interface sites can then be oxidized with surface oxygen atoms from the ceria support to form CO or CO_2, leaving behind oxygen vacancies. This mechanism is likely to inhibit carbon deposition on Ni/CeO_2 during C_2H_6 exposure.

For catalytic reforming processes where O_2 is present (e.g. partial oxidation or autothermal reforming), surface vacancies can be filled by molecular oxygen and a Mars-van Krevelen-like carbon oxidation mechanism occurs, whereas surface vacancies on a SOFC anode are backfilled from bulk oxygen ion diffusion. In these *in situ* experiments, the O_2 partial pressure is very low and the primary source of oxygen was the CeO_2 support (at least initially). Due to ceria's high oxygen ion conductivity, oxygen atoms in the bulk can quickly migrate to backfill the vacancies left behind at the surface. As oxygen is continuously removed at the Ni/CeO_2 interface, an oxygen-depleted region is formed surrounding the Ni particle. The suggested carbon oxidation mechanism is supported by Figure 3.10, where it is shown that reduction of the CeO_2 support occurs near Ni particles when exposed to C_2H_6. Furthermore, the structural changes seen in Figure 3.7d and Appendix 8.1 are also consistent with a loss of oxygen surrounding the Ni particle. The transition from crystalline CeO_2 to an amorphous CeO_{2-x} phase has also been observed in Ni/Pr-doped ceria due to a hydrogen spillover effect (Sharma et al., 2012). Thus, it was concluded that the lack of carbon on Ni/CeO_2 during C_2H_6 exposure is due to the rapid

removal of adsorbed decomposed hydrocarbon products, facilitated by a removal of oxygen from the CeO_2 support. A schematic illustration highlighting the processes that occur during the carbon oxidation mechanism has been provided in Figure 3.11.

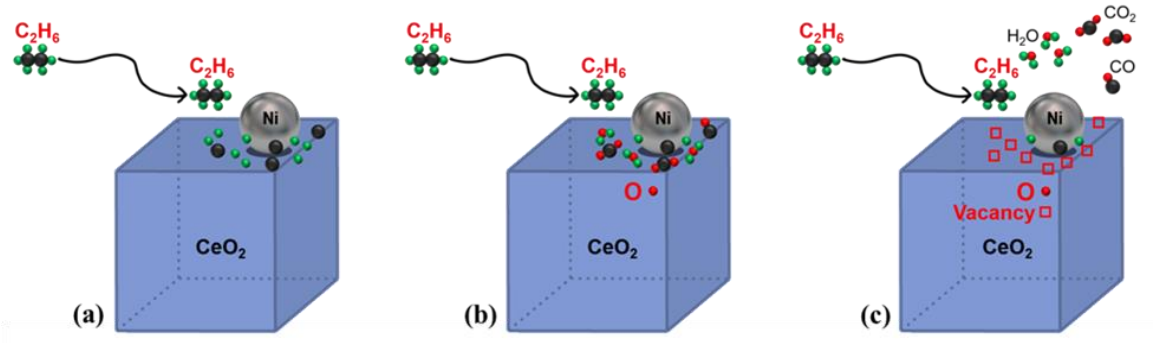

Figure 3.11. Schematic of carbon oxidation mechanism during C_2H_6 decomposition. (a) C_2H_6 is preferentially decomposed at the Ni/CeO_2 interface and atomic C and H are generated. (b) Oxygen from the CeO_2 lattice oxidizes C and H. (c) H_2O, CO_2, and CO desorb from CeO_2 surface and leave behind oxygen vacancies.

The carbon oxidation mechanism allows CeO_2 to initially remove C_2H_4 decomposition products at the Ni/CeO_2 interface. As adsorbed cracked hydrocarbon products from C_2H_4 decomposition become oxidized at the Ni/CeO_2 interface, the removal of oxygen causes the less pronounced reduction zone at the Ni/CeO_2 interface seen in Figure 3.10. However, due to rapid C_2H_4 decomposition over the entire Ni surface and strongly bound carbon-containing decomposition products, graphite layer formation dominates and quickly covers the Ni particles. Once graphite layers have formed on the Ni particles, the ceria is unable to easily remove the carbon atoms (graphite is the low energy state of carbon), and the loss of oxygen from the ceria support is stopped, thus halting Ce oxidation state change and preserving the crystalline structure. The resulting Ni particles are encapsulated in graphite layers and have a crystalline CeO_2 support that exhibits slight reduction zones near Ni/CeO_2 interfaces. Both Figure 3.6d and Figure 3.10 support these

conclusions by showing graphite layers on Ni/CeO_2 and a slight reduction in Ce oxidation state near Ni/CeO_2 interfaces during C_2H_4 exposure.

To summarize, chemisorbed C_2H_4 will be present in both gases, but it is located at different places on the catalysts. For the reactions in C_2H_4 gas, the chemisorbed C_2H_4 will be on the Ni metal surface where rapid dehydrogenation will lead to carbon formation. For reactions in C_2H_6 gas, most of the chemisorbed C_2H_4 will be located at the metal-oxide interface since this is where oxidative dehydrogenation occurs. In this case, the oxide provides a supply of oxygen which can then be used to oxidize the subsequent C_2H_4 dehydrogenation products. These contrasting behaviors of the Ni/CeO_2 catalyst in C_2H_4 and C_2H_6 are shown schematically in Figure 3.12.

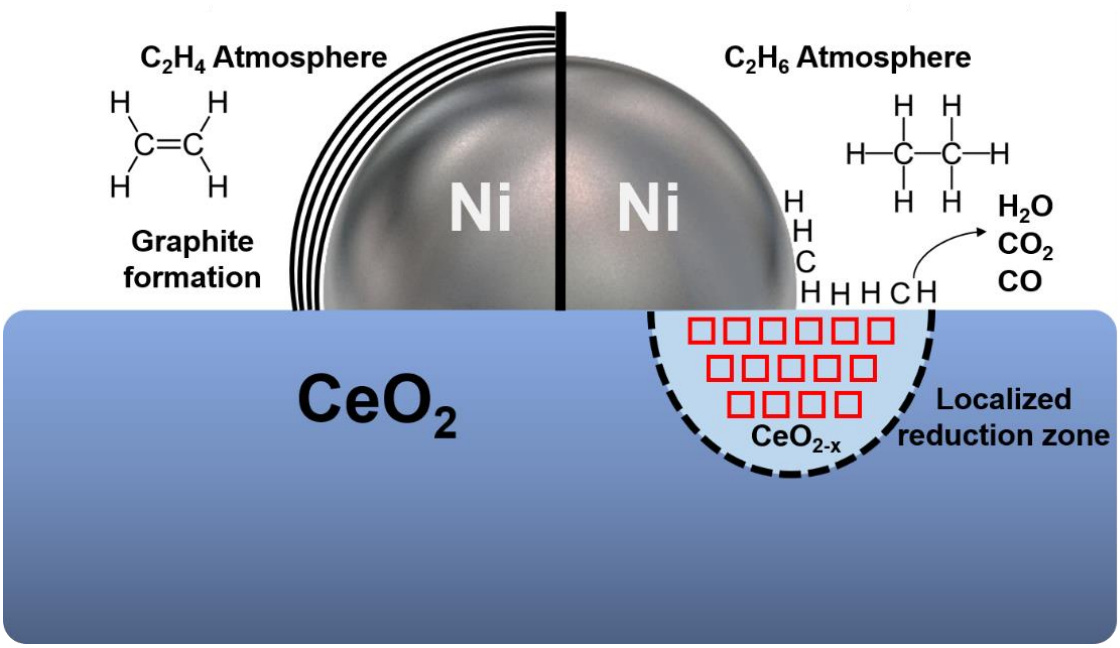

Figure 3.12. Schematic diagram of contrasting behavior of Ni/CeO_2 catalyst in C_2H_4 and C_2H_6 environments.

3.5 Summary

In situ ETEM techniques revealed the atomic-level three-phase interactions occurring at the metal-support interface during carbon deposition from light hydrocarbons over model Ni/CeO_2 and Ni/SiO_2 catalysts. Structural and chemical interfacial changes occurring during species-dependent carbon deposition were determined using atomic-level imaging and electron energy-loss spectroscopy. No carbon deposition occurred during C_2H_6 exposure, and localized reduction zones formed at the Ni/CeO_2 interface through a carbon oxidation mechanism. In contrast, less pronounced reduction zones occurred during C_2H_4 exposure, and carbon deposition occurred on Ni surfaces. Rapid dehydrogenation and subsequent graphite formation occurred on Ni surfaces during C_2H_4 exposure, whereas the metal-support interface catalyzed the oxidative dehydrogenation of C_2H_6 and oxidized the resulting carbonaceous species during C_2H_6 exposure. These experiments demonstrate that the ability of the interfacial sites on Ni/CeO_2 to inhibit carbon deposition during reforming is strongly influenced by thermodynamic and kinetic considerations which may show significant variation among different hydrocarbon species.

4 Locating Active Sites for Oxygen Vacancy Creation and Annihilation on CeO_2 Nanoparticle Surfaces

4.1 Motivation

As discussed in Section 1.2, oxygen exchange is often rate-limiting in technological applications and consists of complex, multistep processes such as O_2 adsorption/desorption, molecular dissociation/association, electron transfer, and incorporation/removal oxygen into or from surface vacancies. The overall surface exchange kinetics therefore results from a complex interplay between the many possible reaction steps and many possible intermediate species that may be associated with these processes (Adler et al., 2007; De Souza, 2017; Kilner et al., 1996; De Souza, 2006), and detailed surface oxygen exchange mechanisms are not always fully understood. Regardless of the detailed surface exchange mechanism, facile oxygen vacancy creation and annihilation is a fundamental surface functionality required for the rational design of materials for oxygen exchange applications, and it is therefore desirable to investigate the role that atomic structures have on modulating surface oxygen vacancy reaction rates.

Nanoscale engineering of CeO_2 to preferentially expose highly-reactive facets has been shown to enhance the surface oxygen reactivity as was discussed in Section 1.3.5, and theoretical calculations have predicted significant variations in activation energies for lattice oxygen removal at different surface sites (Migani et al., 2010a), which is likely to be associated with orders of magnitude differences in local oxygen incorporation and removal rates. Quantitative characterization methods are necessary to describe the structural heterogeneities present on individual nanoparticle surfaces; however, to date there has been no reported experimental method to probe and correlate the local lattice

oxygen vacancy creation and annihilation rates with atomic surface structure. To address this problem, the work presented in this chapter demonstrates that time-resolved *in situ* aberration-corrected TEM can observe atomic-level variations in the oxygen vacancy creation/annihilation rates on CeO_2 nanoparticle surfaces via the observation of the associated relaxation of the adjacent cations. The methodology described herein provides a local indicator of oxygen vacancy activity by monitoring the frequency of cation displacements associated with the creation and annihilation of surface oxygen vacancies. Atomic column positions were tracked in image sequences with picometer precision to investigate the role of crystal facet, strain, and surface defect structures, which were found to strongly influence the oxygen vacancy creation rates. This approach has the potential to be applied to a much wider class of materials and catalysis problems involving surface and interfacial transport and exchange functionalities.

4.2 Experimental

4.2.1 Microscope and Imaging Parameters

CeO_2 nanoparticles synthesized via the method described in Section 2.1.2 were imaged at 40 frames/second (fps) using an FEI Titan ETEM 80-300, aberration-corrected, environmental transmission electron microscope (AC-TEM), operated at 300 kV at room temperature. The microscope is equipped with a post sample C_s-corrector for atomic resolution TEM imaging. The microscope was used in ETEM mode with a pressure of $<10^{-6}$ Torr at the sample. A negative spherical aberration imaging (NCSI) technique was used to enhance contrast from weakly scattering oxygen atomic columns (Jia et al., 2004). C_s = ~ -20 μm was used for all experiments. (111) and (110) CeO_2 nanoparticle surfaces were

imaged in a [110] projection at 5000 $e^{-}Å^{-2}s^{-1}$ with Ce and O atomic columns visible at the surface. Images were acquired using a Gatan K2 IS direct electron detector operated at 40 fps with 8k x 8k pixels, which gave a pixel size of ~2.5 pm/pixel. Image series were acquired with a 1 second total exposure time.

4.2.2 Time-Resolved Atomic Column Tracking (TRACT)

The displacements of Ce cation columns in time series image stacks were tracked using custom MATLAB scripts that were written by Dr. Barnaby D.A. Levin, and a brief description of the code is presented here. Time series image stacks were first aligned by cross-correlation in Digital Micrograph (Gatan, Inc.) to correct for drift and then exported for analysis in MATLAB. Images were re-binned to ~5 pm/pixel resolution, and then a Gaussian smoothing filter with a 2-pixel radius was applied in ImageJ to reduce noise in the images. A Gaussian filter convolves an image with a 2D Gaussian function and is effectively a low-pass filter that attenuates high frequency signals, which makes it a useful denoising filter for AC-TEM images (Krivanek et al., 2010, 2012). This image processing procedure is written algebraically in Appendix 8.2. After loading image stacks into MATLAB, a 2D lattice was generated over an image of the CeO_2 nanoparticle, where each lattice point roughly corresponded to the position of a Ce cation column. Once the lattice was generated, the MATLAB script took a summed image of the time series (a Z-projected image), and precisely located the cation column positions by finding the local maximum within a user-specified radius from each lattice point, fitting a centroid around each local maximum, and then fitting a 2D elliptical Gaussian around each centroid position. The coordinates of the maxima of each of the 2D Gaussians in the Z-projected image defined

the positions of each cation column. The centroid fitting stage of coding made use of the particle tracking scripts originally written for the programming language IDL by Crocker, Grier, and Weeks (Crocker & Grier, 1996), and implemented in MATLAB by Blair & Dufresne (Blair & Dufresne, 2011). The Gaussian fitting stage of coding made use of the 2D Gaussian MATLAB function written by Gero Nootz (Nootz, 2012). After cation column positions were found in the Z-projected image, the script then ran through each frame of the time series to track cation column displacements from the Z-projected position. In each frame, a 2D elliptical Gaussian was fitted within a user specified window around each of the Z-projected positions as determined in the previous step. For each cation column in each frame, the displacement of the column away from its position in the Z-projected image was calculated. From these values, the script calculated the standard deviation of each cation column position.

4.2.3 Molecular Statics (MS) Simulations

To investigate how cation displacements and local crystal structure were influenced by the presence of various oxygen vacancy motifs on the CeO_2 (111) terrace and step-edge surface sites, molecular statics (MS) simulations were performed by Tara Boland, and a brief description of the simulation parameters are presented here. Simulations were carried out with 0, 1, and 2 oxygen vacancies in a single oxygen atomic column on steps and terraces for both 4 atom and 8 atom thick CeO_2 half-slabs. The calculations were performed using the LAMMPS code (Plimpton, 1995). The interatomic forces were represented by parameterized pair potentials using classical interatomic potentials (Minervini, 1999). The short-range interactions used to model CeO_2 were represented using rigid-ion Buckingham

pair potentials while the long-range Coulombic (electrostatic) forces were summed using Ewald's method (Plimpton et al., 1997). Both the short and long-range forces were truncated at a cut-off radius of 10 Å. The CeO_2 slab geometries were created using an orthogonal supercell approach. The oriented cells x-, y-, and z-axis correspond to the $[2\overline{11}], [\overline{111}], [01\overline{1}]$ crystallographic directions, respectively. The periodic repeat unit along each axis of the oriented cell are $\sqrt{6}a_{o,}$ $\sqrt{3}a_o, \sqrt{2}a_o$, where a_o is the equilibrium bulk lattice constant of 5.413 Å. A constant vacuum distance of $4\sqrt{3}a_o$ was introduced along the y-axis of the supercell, perpendicular to the (111) surface, to simulate a free surface and eliminate any surface-surface interaction across the periodic boundaries. For all calculations, the length of the x-axis was fixed at $2\sqrt{6}a_o$ while the length of the z-axis was scaled from $2\sqrt{2}a_o$ to $4\sqrt{2}a_o$ for the 4 and 8 atomic layer cases, respectively. To create a (111)-(110) step-edge, the top 3 atomic layers were removed from the model starting at $x = 2\sqrt{3}a_o - 4\sqrt{3}a_o$. The (111) surface is known as a type 2 surface (Tasker, 1979), meaning that some atoms must be removed to create a charge neutral step-edge. The removal of the symmetrically equivalent atomic layers from the bottom surface ensures no net dipole moment exists at either surface. The inclusion of vacancy motifs was performed under the assumption that oxygen atoms were removed along a single atomic column when viewing the structure model along the $[01\overline{1}]$ direction. When creating oxygen vacancies, the stoichiometry of each atomic column was constrained between CeO_2–Ce_2O_3. Furthermore, the creation of oxygen vacancies located within the first nearest neighbor shell of existing oxygen vacancies was restricted. For every oxygen vacancy induced on the surface, the interatomic potential parameters of two nearest neighbor Ce^{4+} ions were

switched to the parameters which more correctly describe the bonding for a Ce^{3+} ion. The $Ce'_{Ce} - V_{\ddot{o}} - Ce'_{Ce}$ motif, which best reproduces the observed displacements seen in the experimental TEM micrographs, was used for further analysis. Once relaxed, the MS structure models were exported as supercells. The bond changes predicted by MS were in reasonable agreement with DFT simulations on a (111) surface (Nolan, Parker, et al., 2005).

4.2.4 TEM Image Simulations

Image simulations were performed using a multislice approach in the JEMS software developed by Pierre Stadelmann (Stadelmann, 2018). Supercells from molecular statics simulations were imported into JEMS and sliced such that each slice contained a single layer of atoms. Image simulation parameters are shown in Table 4.1. Microscope accelerating voltage, spherical and chromatic aberration coefficients, beam half convergence angle, and defocus conditions were matched to experimental conditions. Additional lens aberrations and noise were set to zero for simplicity. A partially coherent (envelope) illumination model was used. Results of the MS calculations for 4 and 8 atom thick half-slabs with 0, 1, and 2 oxygen vacancies were used as input for image simulations.

Table 4.1. Image Simulation Parameters.

Image Simulation Parameters	
Accelerating Voltage	300 kV
3rd order Spherical Aberration (C_3)	-0.03 mm

Chromatic Aberration (C_c)	1 mm
Beam half convergence angle (α)	0.15 mrad
Defocus (C_1)	7.8 nm
Defocus spread (*f*)	1 nm
2-fold (A_1) /3-fold (A_2) astigmatism	0 nm
2^{nd} order Coma (B_2)	0 nm
5^{th} order Spherical Aberration (C_5)	3 mm

Simulated images were compared to experimental images through an integrated intensity look-up table. This was calculated from image simulations of a (111) surface with no oxygen vacancies that was carried out over a range of thicknesses from 1 Ce atom per column to 12 Ce atoms per column. A value for the intensity of Ce columns at each thickness was calculated by fitting a 2D elliptical Gaussian to columns at different sites (this was performed using the same code that was used to analyze experimental data). Four different sites were chosen for intensity calculations: two sites at the (111) surface of the simulated half-slab, and two "bulk" sites several layers away from the (111) surface. 'A' sites are those where the Ce atoms in the column appear in the odd-numbered slices in the simulations. 'B' sites are those where the Ce atoms in the column appear in the even-numbered slices in the simulations. The results of these calculations are given in the look-up table in Figure 4.1. Intensity is observed to increase roughly linearly between 1 and 4 atoms in thickness, before peaking at 6 atoms in thickness and decreasing thereafter. Relatively little difference in intensity is observed between different sites (A and B, surface and bulk) until 10 atoms in thickness is reached.

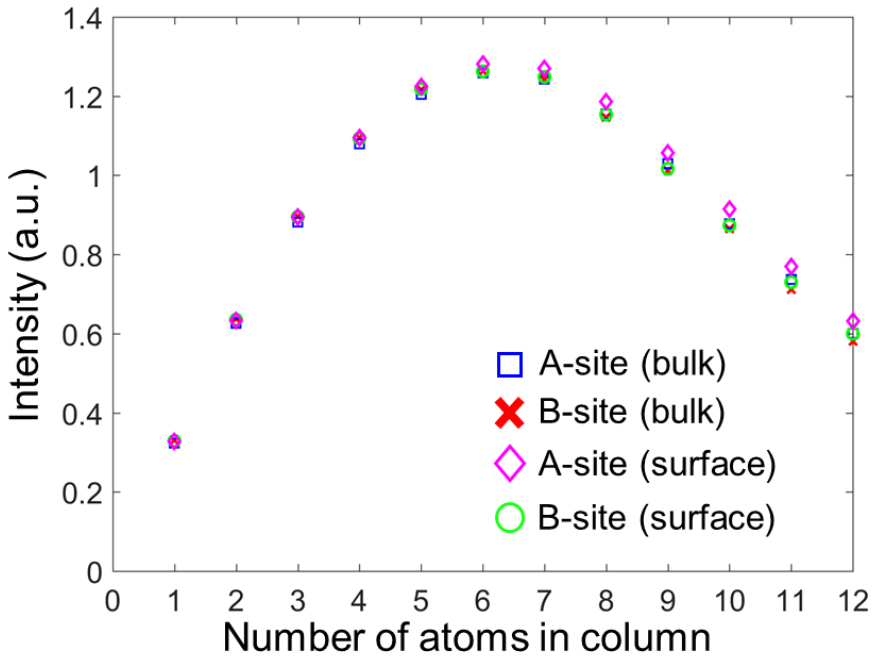

Figure 4.1. Look-up table: Calculated intensities of Ce columns for different thicknesses at different atomic sites produced using a 2D Gaussian fitting procedure on simulated images. Intensity is given in arbitrary units and has been normalized to the average intensity per square Angstrom in vacuum away from the particle (which was in turn calculated by measuring the total intensity in 1 nm^2 of vacuum and dividing by 100).

4.3 Results and Discussion

4.3.1 Imaging Cation Motion

Figure 4.2a shows an AC-TEM image of a CeO_2 (111) surface in the [110] projection with a 1 s total exposure time. The observations were performed at room temperature in an O_2 partial pressure of 10^{-6} Torr using negative spherical aberration (C_s) imaging where atomic columns appear with bright contrast (Jia et al., 2004; Lin et al., 2014; Zhang et al., 2018). Inspection of the step edge sites on the surface reveals that Ce atomic columns are diffuse relative to the columns at terrace sites. Figure 4.2b-d shows a time sequence of the step edge region with a 25 ms exposure time. As highlighted by the arrows, the Ce column on the step edge site (Figure 4.2b) initially shifts by ~20 pm in the 25 ms

frame (Figure 4.2c), returns to its equilibrium position for frames at 50 and 75 ms (not shown) and undergoes a subsequent shift of 35 pm in the 100 ms frame (Figure 4.2d). The variation in the position of the column in the individual frames results in the diffuse appearance of the Ce column when the frames are integrated to give a 1 s total exposure. The image sequence is also shown in Figure 4.3 with the raw unfiltered data compared to Gaussian-filtered images.

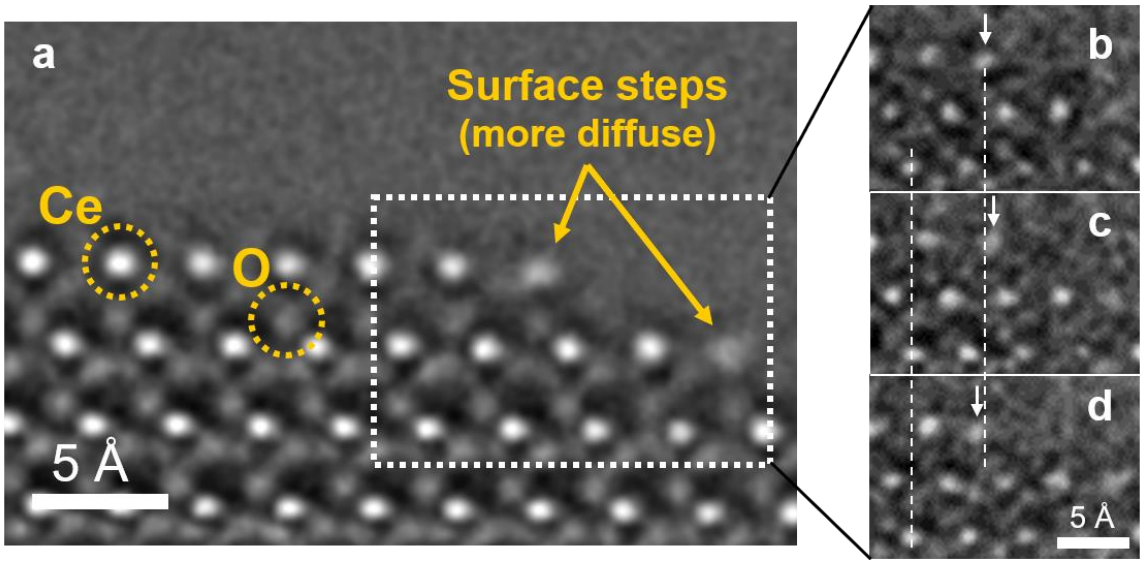

Figure 4.2. (a) Integrated (1 s) AC-TEM image of a (111) step edge of a ceria (CeO_2) nanoparticle imaged in [110] projection at room temperature in an oxygen partial pressure of 10^{-6} Torr. Ce and O columns are labeled. Ce atomic columns at step edge sites are more diffuse than terrace sites. (b,c,d) Image sequence of the CeO_2 (111) stepped surface from white box in (a) with 25 ms frames. The Ce column at the step edge site is centered on the white line at 0 s in (b). As highlighted by the white arrows, the Ce column has shifted ~20 pm in the 25 ms frame in (c), returns to equilibrium in the 50 and 75 ms frames (not shown), then shifts ~35 pm in the 100 ms frame in (d). The dotted white line centered on the subsurface Ce column shows no corresponding shift in position.

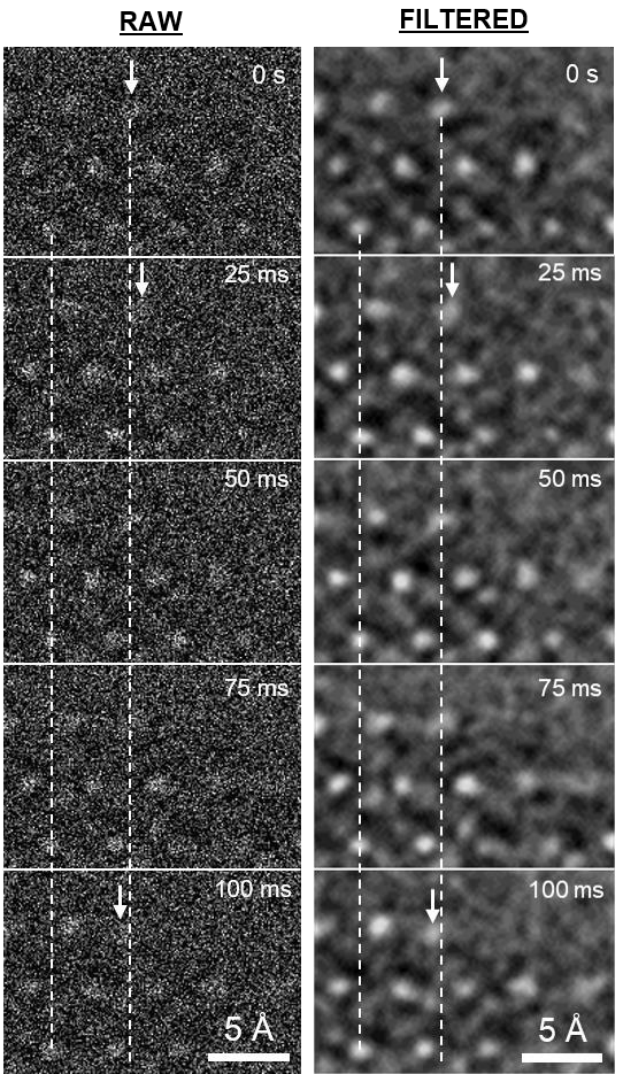

Figure 4.3. Image sequence of unfiltered vs. filtered CeO_2 (111) stepped surface with 25 ms frames. Images are displayed at 10 pm/pixel. A Gaussian smoothing filter was applied produce the "filtered" images to aid in atomic column visualization. As highlighted by the arrows, we observe that the Ce column on the step edge site centered on the dotted line at 0 s, shifts by ~20 pm in the 25 ms frame, returns to its equilibrium position for frames at 50 and 75 ms and shifts by ~35 pm in the 100 ms frame. Although the data is very noisy in the raw frames, the column displacement can still be readily identified in the raw data.

The standard deviation of the position of each Ce column was measured to quantify the average displacement from their mean position during the observation time as outlined in Section 4.2.2. Figure 4.4a is an integrated set of 40 frames (25 ms frames aligned and summed together) of an extended (111) surface which shows a series of steps. Figure 4.4b

shows the standard deviation of each Ce atomic column position. The lower left part of the image was not analyzed as the crystal was too thick and did not provide directly interpretable Ce atomic columns. The minimum standard deviation for the columns at non-surface profile sites, which appear stationary, is 5 pm and represents the precision of the measurement. These non-surface profile columns are composed mainly of atoms at subsurface sites and include a small number of top and bottom surface sites (i.e. 2D projection of the 3D structure); however, they are referred to as bulk columns here for simplicity. The surface atomic columns, especially at the step edges, show much larger standard deviations (~12–16 pm) than bulk columns. Many of the terrace cations show a significantly smaller standard deviation than the step edges. The terrace columns contain edge and terrace face sites in projection but are still referred to as terrace columns here for simplicity. In Figure 4.4b, inspection of terrace column positions within 1-4 nearest neighbor distances from step edge sites shows that some columns are compressed inward to the bulk, while others are bowed outward, indicating local strain. These strained (111) terrace sites display larger standard deviations than non-strained terrace sites. Figure 4.4c is a (110) nanofacet which shows many diffuse surface cation columns at both terrace and edge sites. The standard deviation analysis shows much larger average displacement values across the (110) nanofacet in Figure 4.4d compared to the more stable (111) terraces of Figure 4.4b.

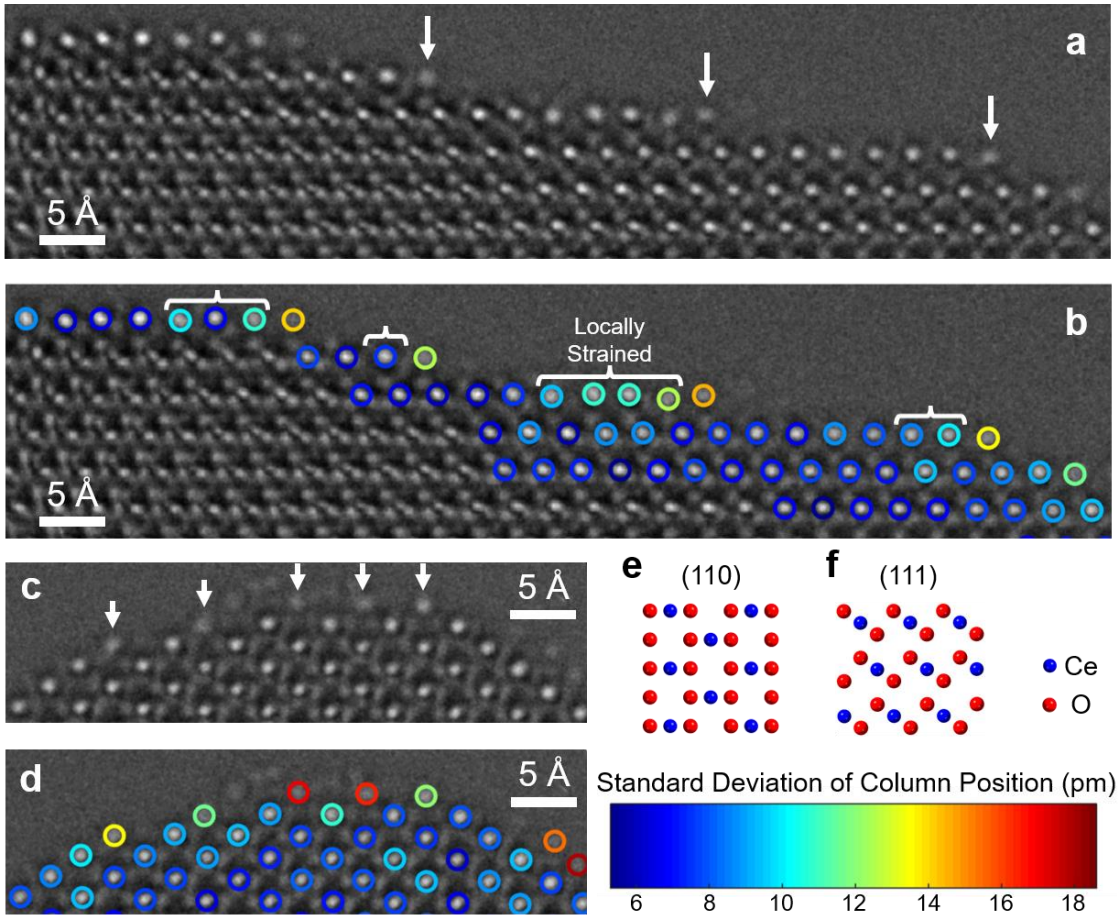

Figure 4.4. (a) Extended AC-TEM image of the stepped (111) surface of CeO_2 from Figure 4.2. White arrows indicate Ce atomic columns that appear diffuse due to dynamic displacement of cation columns between individual frames. (b) Standard deviation in column position over 40 frames indicated by colored markers overlaid on atomic columns in the image. A higher standard deviation in position is correlated with more frequent displacements. Locally-strained terrace edge sites are indicated by white brackets. (c) and (d) show data similar to (a) and (b) but for a (110) nanofacet of CeO_2 imaged in [110] projection. Schematic models of both surfaces are shown in (e) and (f).

4.3.2 Modeling Cation Motion Induced by Oxygen Vacancies

The observed cation oscillations are not atomic vibrations, which can be induced thermally or by collisions with the fast electron beam, because atomic vibrations occur with frequencies on the order of 10^{13} Hz and are much faster than the time resolution used here. Instead, the observed cation displacements can be explained in terms of the creation and

annihilation of oxygen vacancies on the CeO_2 surfaces. As described in Section 1.3.1, it is well known from X-ray crystallography that lattice relaxation and expansion occurs as CeO_2 undergoes reduction, resulting in cation displacements of ~20–30 pm from the fluorite positions (Villars & Calvert, 1989; Chiang et al., 1993: 1; Mogensen, 2000). Structural changes have also been validated with TEM imaging and theoretical simulations (Graciani et al., 2011; Da Silva et al., 2007; Paier et al., 2013; Ou et al., 2008; Wang et al., 2009; Chen et al., 2010). Moreover, local strain can be induced as nanoparticles undergo structural transformations (Gilbert, 2004; Sen Zhang et al., 2014; Wang et al., 2014).

To examine specific oxygen vacancy induced displacements at surface defects, molecular statics (MS) simulations of a stepped (111) CeO_2 surface were performed by Tara Boland on models with different thicknesses and oxygen vacancy concentrations for various surface sites. TEM image simulations were performed to assess the sensitivity of the image to 3D cation displacements. Comparing the experimental data of Figure 4.4 with the intensity look up table of Figure 4.1, it was estimated that a majority of Ce columns analyzed were between 3 and 6 atoms in thickness. Simulations involving 4 atoms per column therefore represent a typical experimental thickness, and simulations involving 8 atoms per column explore the sensitivity of the outlined method at thicknesses beyond those in these experiments. A typical sequence of simulations where one and two oxygen vacancies were introduced at a step edge site in a 4-atom thick slab of CeO_2 is shown in Figure 4.5. In Figure 4.5a, MS simulations highlight the effect of oxygen vacancies, and the resulting cation column shifts were determined to be ~14–25 pm from TEM image simulations (Figure 4.5b), which is in good agreement with the experimental observations. If many oxygen vacancies are created and annihilated at different anion sites around a

cation column, it will appear diffuse in an integrated image because of the superposition of multiple displacements as seen in Figures 4.2-4. Red/cyan color overlays are provided in Figure 4.5c, where red is the color of the no-vacancy image and cyan is the color of the single or double oxygen vacancy simulated image. In the overlay, identical red and cyan regions combine to form white. At the step edge atomic column red and cyan features are distinct, indicating a difference between the images due to a cation column shift. Additional vacancy configurations are provided in Appendix 8.2.

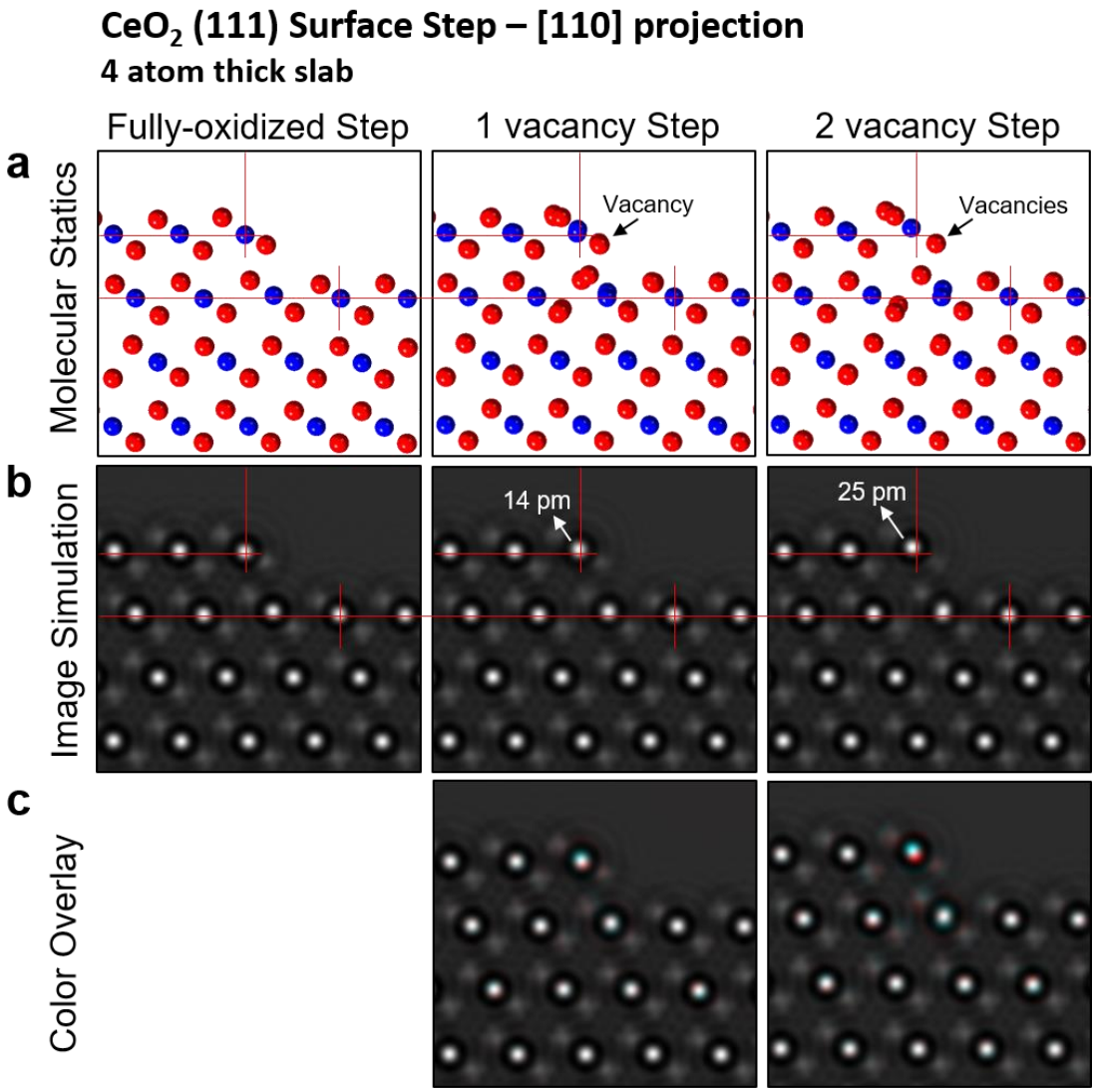

Figure 4.5. (a) Relaxed molecular statics (MS) models of a CeO_2 (111) surface step that is fully oxidized (left), contains 1 O vacancy (middle) and contains 2 O vacancies along the step edge (right) with Ce shown as blue and O as red. The slab is 4 Ce atoms thick (into the plane of the page) and the O vacancies are introduced along the O column indicated in the figures. (b) Simulated AC-TEM images from the three structures with arrows indicating the cation column displacement resulting from the presence of oxygen vacancies. (c) Red/cyan color overlays where red is the color of the no-vacancy image and cyan is the color of the single or double oxygen vacancy simulated image.

4.3.3 Oxygen Vacancy Creation and Annihilation Processes

During the process of vacancy creation, it's assumed that the rate of vacancy creation will depend on an activation energy, E_a, which will be site specific. In the TEM, vacancy creation can be caused by thermal fluctuations or the electron beam. The kinetics of the thermally-activated vacancy creation process can be modeled using an Arrhenius equation. The number of oxygen vacancy creation events, N_{th}, per second per atomic site can be estimated as a function of the activation energy, E_a, as:

$$N_{th} = Ae^{-\frac{E_a}{k_B T}} \tag{4.1}$$

where A is the attempt frequency, T is temperature, and k_B is the Boltzmann constant. The vacancy creation is driven by thermal fluctuations, and the attempt frequency can be approximated by the mean vibrational frequency of the occupied phonon states in CeO_2 at room temperature, $\nu \sim 10^{13}\ s^{-1}$. This was calculated by multiplying the density of phonon states for CeO_2, as published by Jung *et al* (Jung et al., 2018), by the probability of those states being occupied (the Bose-Einstein distribution), and then calculating the mean vibrational frequency. The mean vibrational frequency was calculated to be ~0.0398 eV, which corresponded to a frequency of $9.6 \times 10^{12}\ s^{-1}$, or $\nu \sim 10^{13}\ s^{-1}$. Figure 4.6 shows N_{th} versus E_a for various temperatures. The thermally-activated oxygen vacancy creation rate is a strong function of E_a, with sites of activation energy less than 0.77 eV showing more than one removal per second.

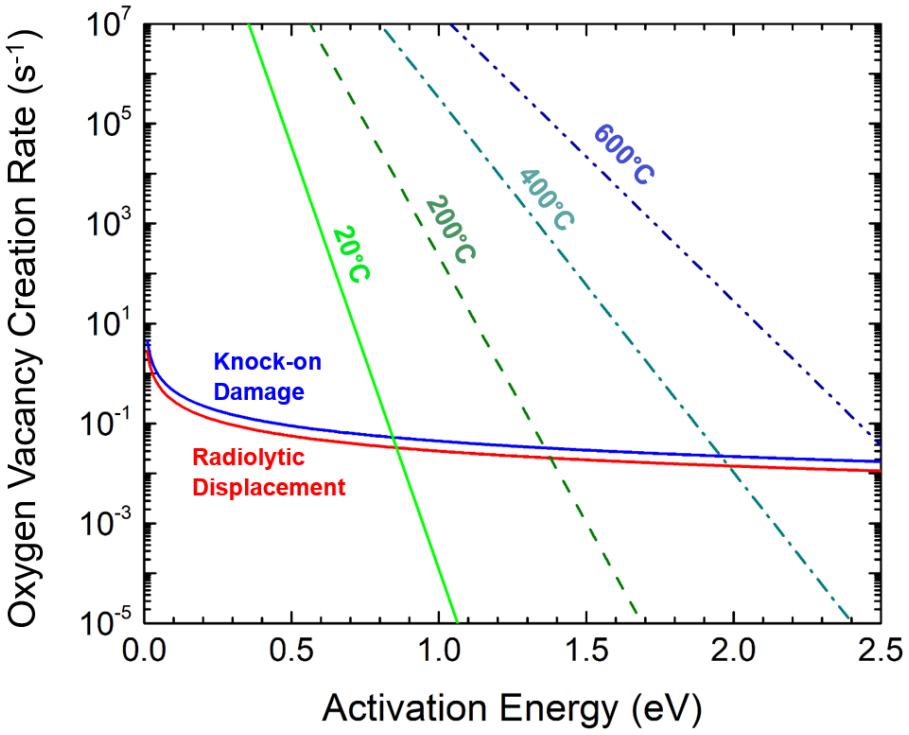

Figure 4.6. Thermally-activated oxygen vacancy creation rates at different temperatures (green and dashed lines), knock-on damage (blue) and radiolytic displacement (red) for an electron flux of 5000 $e^{-}A^{-2}s^{-1}$. Thermally-activated rates are calculated using Equation (4.1). Details of the calculations for the electron beam induced rates are given below and Equations (4.10) and (4.13) are plotted as knock-on damage and radiolytic displacements, respectively.

The electron beam can also create surface oxygen vacancies either via ionization processes (radiolytic displacement) or direct collisions with the nucleus (knock-on damage) (Egerton et al., 2004; Hobbs, 1984, 1979) with the removal rate depending on the electron flux. For an oxygen atom to be ejected from the surface, the energy transfer from the electron beam to the oxygen atom must be greater than or equal to the activation energy for oxygen vacancy creation, E_a. For the experiments in this Chapter, a flux of 5000 $e^{-}Å^{-2}s^{-1}$ was used, which has been shown to minimize radiation damage effects in CeO_2 (Johnston-Peck et al., 2016; Sinclair et al., 2017). The low rate of damage is confirmed

with detailed derivations of the rate of oxygen vacancy creation due to radiolytic displacement and knock-on damage as provided below.

Knock-on Displacement Damage of Oxygen

The following derivation is based on that of Egerton, Wang, and Crozier for electron beam damage from an intense probe (Egerton et al., 2006). Knock-on displacement damage may be considered to be an elastic scattering process. During elastic scattering by an atom, an electron that undergoes an angular deflection θ transfers to the nucleus an amount of energy equal to:

$$E = E_{max} sin^2(\theta/_2) \quad (4.2)$$

where E_{max} is the maximum possible energy transfer, corresponding to θ = π rad. Relativistic kinematics gives:

$$E_{max} = 2E_0(E_0 + 2m_0c^2)/Mc^2 \quad (4.3)$$

where M is the mass of the scattering atom, assumed initially at rest, and E_0 is the kinetic energy of the incident electron (rest mass m_0); c is the speed of light in vacuum and m_0c^2 = 511 keV is the electron rest energy. M = 15.994 /6.022x10^{23} mol^{-1} = 2.65682 x 10^{-23} g = 2.65682 x 10^{-26} kg / 1.6 x 10^{-19} C = 1.66 x 10^{-7}.

For an O atom: $$E_{max} = \frac{2(300kV)[300kV+2*511kV]}{[(1.66\ x\ 10^{-7})(2.998\ x\ 10^8)^2]} = \frac{[7.932\ x\ 10^{11}]}{[1.492\ x\ 10^{10}]} = 53.1\ eV \quad (4.4)$$

The minimum energy that must be transferred to cause displacement of O is the oxygen vacancy activation energy, E_a, which is left as a variable in the derivation to produce an

equation where the displacement rate is a function of activation energy. Neglecting screening of nuclear field, which is a good approximation for large scattering angles, the differential cross section for such Rutherford-type scattering is:

$$\frac{d\sigma}{d\theta} = \left[\frac{e^2 Z}{(8\pi\varepsilon_0 E_0)}\right]^2 \left[\frac{E_0 + m_0 c^2}{E_0 + 2m_0 c^2}\right]^2 * \left[\frac{2\pi sin\theta}{\sin^4\left(\frac{\theta}{2}\right)}\right] \quad (4.5)$$

This expression can be integrated over the scattering angle, from $\theta = \pi$ to a minimum value given by $\sin^2(\theta/2) = E_{min}/E_{max}$, to give a cross section for energy transfer in the range E_{min} to E_{max}:

$$\sigma = (2.45\ x\ 10^{-29} m^2) Z^2 \left[\frac{1-\frac{v^2}{c^2}}{\left(\frac{v^2}{c^2}\right)^2}\right] * \left[\left(\frac{E_{max}}{E_{min}}\right) - 1\right] \quad (4.6)$$

Equations (4.5) and (4.6) ignore electron spin effects, and a solution of the Dirac equation indicates that the Rutherford cross section given by Equations (4.5) and (4.6) should be multiplied by a correction factor as given in (McKinley & Feshbach, 1948). Calculations of the elastic cross section using this correction factor (not shown) indicated that the correction factor was approximately 1 for an oxygen atom. In addition, Mott cross sections take into account electron spin effects, and the ratio between the Mott cross section and the Rutherford cross section was slightly below 1 for an oxygen atom under the experimental conditions of this Chapter (Reimer & Lödding, 1984). Therefore, Equation (4.6) provided a reasonable estimation of the elastic cross section for oxygen.

For an O atom: $\sigma = (2.45\ x\ 10^{-29} m^2)(8)^2 \left[\frac{\left(1-\frac{(2.33\ x\ 10^8)^2}{(2.998\ x\ 10^8)^2}\right)}{\left(\frac{(2.33\ x\ 10^8)^2}{(2.998\ x\ 10^8)^2}\right)^2}\right] * \left[\left(\frac{53.1eV}{E_a}\right) - 1\right]$ (4.7)

The elastic cross section simplifies to: $\sigma = (1.7019\ x\ 10^{-27}) \left[\left(\frac{53.1eV}{E_a}\right) - 1\right]$ (4.8)

For a flux of D electrons per unit area, and damage cross section σ_D, the number of damage events per unit volume (or surface area in the case of sputtering), n_D, is given by $n_D = D\ \sigma_D\ n_{at}$ where n_{at} is the number of target atoms per unit volume (or surface area in the case of sputtering). A more general quantity that can be used for critical flux calculations is the number (or fraction) of displacement events per target atom (Levin, 2017):

$$N = \frac{n_D}{n_{at}} = D\sigma_D \quad (4.9)$$

In the experiments of this Chapter, a flux of 5000 $e^{-}Å^{-2}s^{-1}$ was used, which gives the following formula for knock-on displacement rate of oxygen:

$$\frac{n_D}{n_{at}} = D\sigma_D = \left(5000\ \frac{e^-}{Å^2 s}\right) * (1.7019\ x\ 10^{-27}) \left[\left(\frac{53.1eV}{E_a}\right) - 1\right] \quad (4.10)$$

Equation (4.10) is plotted as a function of activation energy by the blue line in Figure 4.6.

Radiolytic Displacement Damage of Oxygen

The following derivation follows that of Hobbs (Hobbs, 1984). Radiolytic displacement may be considered to be an inelastic scattering process. The inelastic displacement cross section is given by:

$$\sigma = 7x10^6\ \xi\ \left(\frac{Z}{E_a}\right) * \left(10^{-28}\frac{m^2}{barns}\right) \quad (4.11)$$

ξ is an efficiency factor and is typically an empirically derived value. For silica, the value is 10^{-4}. The efficiency factor decreases for more conductive materials. For the derivation presented here, $\xi = 10^{-5}$ is used as a conservative upper bound for the efficiency factor of CeO_2 because the conductivity of CeO_2 is orders of magnitude greater than that of SiO_2. The inelastic cross section for oxygen is given by:

$$\sigma = 7x10^6\ (10^{-5})\left(\frac{8}{E_a}\right) * \left(10^{-28}\frac{m^2}{barns}\right) \quad (4.12)$$

Inserting Equation (4.12) into Equation (4.9) provides the following formula for the radiolytic displacement rate for oxygen:

$$\frac{n_D}{n_{at}} = D\sigma_D = \left(5000\,\frac{e^-}{Å^2 s}\right) * (5.6x10^{-6}Å^2)\left(\frac{1}{E_a}\right) \quad (4.13)$$

Equation (4.13) is plotted as a function of activation energy by the red line in Figure 4.6.

At room temperature, the electron beam removal rates exceed the thermal removal rate only when the activation energy exceeds 0.9 eV. Even then, the removal rates are slow at one vacancy creation event every 10–100 s, which is much slower than the experimental observations that show multiple displacements per second for some surface sites (Figure 4.4).

Knock-on and Radiolytic Displacement Damage for Ce Sub-lattice

Following the same approach derived for the oxygen sub-lattice, additional calculations shown below indicate that the effects of the electron beam on the Ce sub-lattice are negligible. For knock-on displacement damage of Ce atoms, E_{max} is given by:

$$E_{max} = \frac{2(300kV)[300kV+2*511kV]}{[(1.45\ x\ 10^{-6})(2.998\ x\ 10^{8})^2]} = \frac{[7.932\ x\ 10^{11}]}{[1.307\ x\ 10^{11}]} = 6.1\ eV \quad (4.14)$$

The elastic cross section is given by:

$$\sigma = (2.45\ x\ 10^{-29} m^2)(58)^2 \left[\frac{\left(1-\frac{(2.33\ x\ 10^{8})^2}{(2.998\ x\ 10^{8})^2}\right)}{\left(\frac{(2.33\ x\ 10^{8})^2}{(2.998\ x\ 10^{8})^2}\right)^2}\right] * \left[\left(\frac{6.1eV}{E_a}\right) - 1\right] \quad (4.15)$$

which simplifies to: $$\sigma = (8.946\ x\ 10^{-26}) \left[\left(\frac{6.1eV}{E_a}\right) - 1\right] \quad (4.16)$$

Equation (4.16) ignores electron spin effects; however, the correction factor mentioned above is a low atomic number approximation and can underestimate the cross section by a factor of two for a heavy element such as cerium (Bradley, 1988). Therefore, the correction factor was ignored. Furthermore, the ratio of the Mott cross section to the Rutherford cross section ranged from ~1 to ~0.5 for the range of scattering angles given by various values of E_{min} for a cerium atom under the experimental conditions of this Chapter (Reimer & Lödding, 1984). Therefore, the Rutherford elastic cross section given by Equation (4.16) provided a conservative upper bound of the cross section and was used as the elastic cross section in this Chapter. Inserting Equation (4.16) into Equation (4.9) provides the following formula for the knock-on displacement rate for cerium:

$$\frac{n_D}{n_{at}} = D\sigma_D = \left(5000\frac{e^-}{Å^2 s}\right) * (8.946\ x\ 10^{-26}) \left[\left(\frac{6.1eV}{E_a}\right) - 1\right] \quad (4.17)$$

The inelastic displacement cross section for cerium is given by:

$$\sigma = 7x10^{6}\ (10^{-5})\left(\frac{58}{E_a}\right) * \left(10^{-28}\,\frac{m^2}{barns}\right) \tag{4.18}$$

Inserting Equation (4.18) into (4.9) gives the radiolytic displacement rate for cerium:

$$\frac{n_D}{n_{at}} = D\sigma_D = \left(5000\,\frac{e^-}{\text{Å}^2 s}\right) * (4.06x10^{-5}\text{Å}^2)\left(\frac{1}{E_a}\right) \tag{4.19}$$

To choose a sensible range of values for E_a of cerium, it is noted that an experimental study by Routbout *et al.* determined the activation energy of Ce self-diffusion to be 480 kJ/mol ± 100 kJ/mol, which is equivalent to 4.97 eV per atom ± 1.03 eV (Routbort et al., 1997). Additionally, Beschnitt *et al.* computationally investigated the activation energies for Ce vacancy and interstitial formation and calculated a range of ~4–13 eV (Beschnitt et al., 2015). Based on these results, displacement rates for activation energies of Ce displacement were calculated in the range 4–8 eV, which are shown in Figure 4.7 below. With a 300-kV electron beam, E_{max} = 6.1 eV so the displacement rate for knock-on damage is zero for activation energies above 6.1 eV. The thermal displacement rate (Equation (4.1.)) was excluded from this graph because it was below 10^{-50} s^{-1} for the energy range chosen here. Comparing Figure 4.7 to Figure 4.6, it is concluded that the beam-induced Ce displacement rates are extremely low relative to oxygen displacement rates under the experimental conditions used in this Chapter.

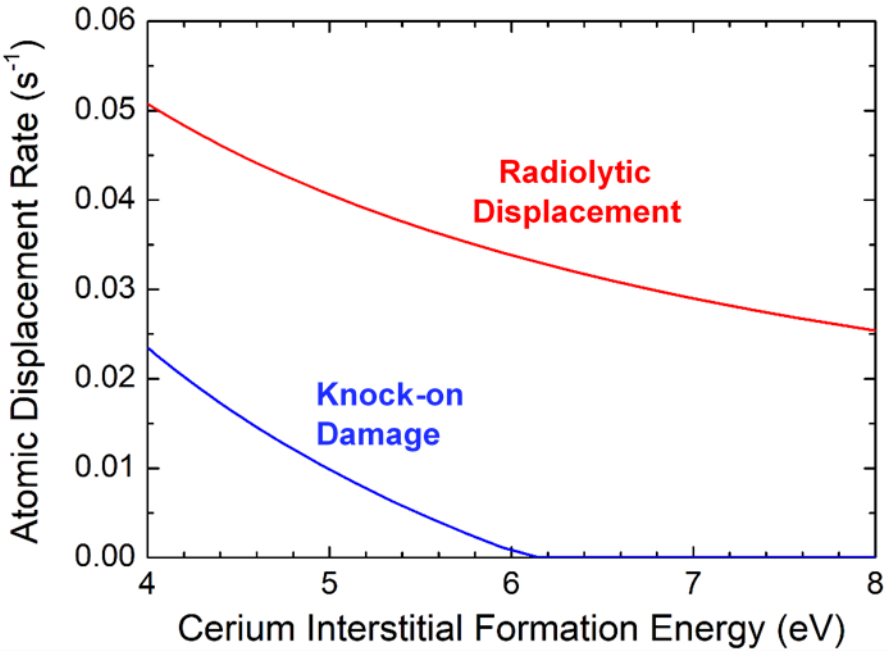

Figure 4.7. Displacement rate of Ce atoms by knock-on damage and radiolytic displacement as a function of Ce interstitial/vacancy formation energy, calculated from the equations in the discussion above. The thermal displacement rate (not shown) is below 10^{-50} s^{-1} for all energies within this range.

As a further check on electron beam effects, experimental images were acquired with a flux of only 50 $e^{-}Å^{-2}s^{-1}$, as shown in Figure 4.8. The integrated width of the atomic columns in a 1 s total exposure image did not change at low flux compared to the higher flux of 5000 $e^{-}Å^{-2}s^{-1}$, providing further evidence that electron beam effects had a minimal impact on the observations. If the displacements were significantly impacted by the electron beam, it's expected that the integrated widths of the atomic columns would be greater with higher flux as a result of the superposition of more displacements. It was therefore concluded that the cation displacements observed are not electron beam-induced, but rather are driven by thermally-activated processes, leading to oxygen vacancies being created or annihilated on the surface.

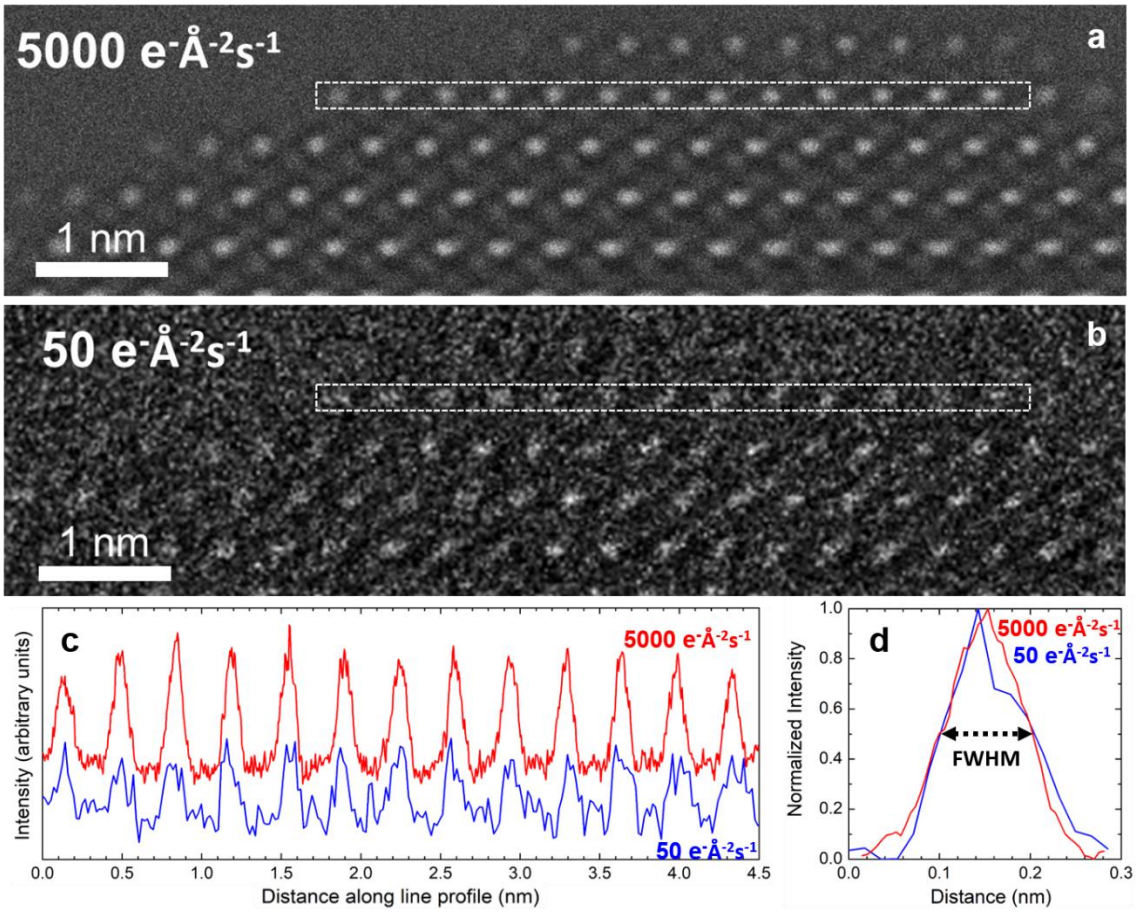

Figure 4.8. (a) Image of CeO_2 (111) facet with electron beam flux of 5000 $e^-Å^{-2}s^{-1}$. (b) Image of the same CeO_2 (111) facet from (a) but with 50 $e^-Å^{-2}s^{-1}$ flux. (c) Integrated intensity plot from the boxed regions in (a) and (b). (d) Normalized average of peaks in (c). The full width at half maximum (FWHM) does not show any difference between 5000 and 50 $e^-Å^{-2}s^{-1}$.

Several processes can cause oxygen vacancies to form at a particular surface site (Figure 4.9), such as migration of lattice oxygen to subsurface bulk sites (bulk diffusion) or migration of oxygen between different lattice sites on the surface (surface diffusion). Oxygen can also transfer out of a lattice site to an adsorbed site (Choi et al., 2006; Pushkarev et al., 2004; Wu et al., 2010), and it may then either re-incorporate back into the vacancy or react with another adsorbate such as oxygen, hydrogen, or carbon monoxide. Bulk diffusion of oxygen can be ruled out as the cause of the observed displacements since

the activation energy has been experimentally measured using isotopic exchange techniques to be between 0.9-2.3 eV, which yields a negligible diffusion rate at room temperature (Kamiya et al., 2000; Perkins et al., 2001). Surface lattice diffusion has been examined on CeO_2 (111) surfaces at room temperature with scanning probe microscopies. Namai *et al.* found that single oxygen vacancies were immobile while a multiple vacancy cluster hopped to its nearest neighbor site after 182 s (Namai, Ken-Ichi Fukui, et al., 2003; Namai, Ken-ichi Fukui, et al., 2003) whereas Esch *et al.* reported that oxygen vacancies were completely immobile at room temperature (Esch et al., 2005). In the experiments in this Chapter, if there was significant migration of lattice oxygen along the (111) surface, diffuse contrast for *all cations on the surface especially those adjacent to the step edge would be observed*. Lattice surface diffusion may occur on the locally strained parts of the terraces but the non-strained (111) terraces show considerably less motion, implying relatively minimal jumping between surface lattice sites in agreement with the scanning probe microscopy measurements. Thus, at room temperature, the most likely mechanism for creation of vacancies on the surface is *transfer of oxygen out of a lattice site* to an adsorbed site.

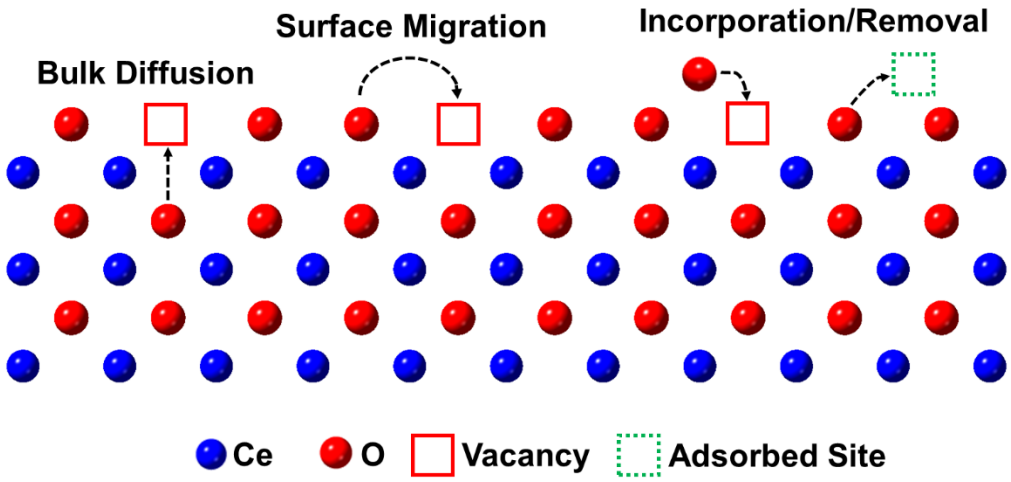

Figure 4.9. Thermally-activated oxygen vacancy creation processes: Bulk diffusion, surface migration, and transfer of oxygen out of a lattice site to an adsorbed site and vice versa.

4.3.4 Quantifying Activation Energies for Vacancy Creation at Individual Atomic Sites

The standard deviation of the cation column displacement gives an indication of the variation in the oxygen vacancy creation and annihilation rates at different sites. Furthermore, by considering the frequency of vacancy creation, it is possible to estimate the relative activation energy for each site. Since the columns oscillate about a mean position, the number of oxygen vacancy annihilation events is approximately equal to the number of oxygen vacancy creation events during the observation period. For simplicity, the rate at which oxygen vacancies are created adjacent to specific cation columns was determined since the vacancy formation energy is a well-defined quantity.

The MATLAB script described in Section 4.2.2 was used to calculate the oxygen vacancy creation frequency, N_{th}, at each atomic site by counting the number of times a

cation column was displaced, subject to a threshold that defined when a cation column displacement may be considered to occur due to oxygen vacancy creation. In a time sequence of n images, the atomic column position measured in frame j was defined to be r_j and the mean and standard deviation (error) across all n frames as $\bar{r}$ and σ, respectively. For sub-surface cations, the minimum observed standard deviation in position is 5 pm (Figure 4.4), which was taken to be the precision of the measurement. Assuming normal statistics, the probability of random noise causing the cation to be displaced beyond 2σ (i.e. 10 pm) from the mean position will be ~5%. Therefore, it was assumed that a displacement of greater than 10 pm from the mean is associated with the presence of oxygen vacancies to 95% confidence. If the atom is displaced by 10 pm in two consecutive frames, then the probability of such an observation being due to random noise will be 0.25%, which is very small. Random noise will cause the atom to fluctuate around its new displaced position. It was further assumed that the cation column remains in its displaced position if the relative displacement between two frames is less than or equal to 2σ. Thus, the number of vacancy creation events in a sequence of n frames is defined to be those frames for which $|r_j - \bar{r}| \geq 2\sigma$ and $|r_j - r_{j-1}| \geq 2\sigma$. In addition, comparisons of experimental images and the look-up table of Figure 4.1 show that each cation column consists of ~1–6 Ce atoms, and MS simulations coupled with TEM image simulations show that the cation column displacement associated with a single oxygen vacancy in a typical column of 4 atoms gives rise to a cation column shift of ~10–15 pm (see Figure 4.5), which further strengthens the argument to use 10 pm (2σ) as a constraint condition. Figure 4.10 shows the number of displacement events as a function of column position for the (111) and (110) surfaces, subject to the constraint $|r_j - \bar{r}| \geq 10$ pm and $|r_j - r_{j-1}| \geq 10$ pm. On the (111) surface in

Figure 4.10a, step edge sites show greater displacement frequencies than terrace sites and locally strained terrace sites show greater displacement frequencies than those on non-strained terrace sites. Furthermore, Ce columns on the surface of the (110) nanofacet show greater displacement frequencies than those on the (111) surface.

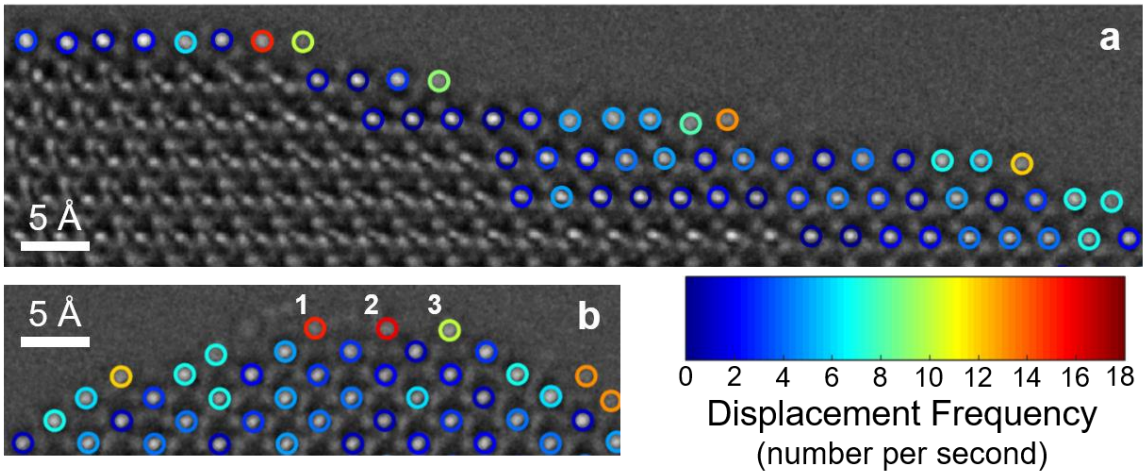

Figure 4.10. (a) The stepped (111) surface and (b) the (110) nanofacet of a CeO_2 nanoparticle as in Figure 4.4. These images are overlaid with colored markers on Ce atomic columns, which indicate the number of displacement events per second associated with oxygen vacancy creation at each atomic site.

With knowledge of the number of oxygen vacancy creation events (N_{th}) taking place per second, the Arrhenius equation (Equation (4.1)) can be used as a simple model to estimate local activation energies for oxygen vacancy creation. By comparing the vacancy creation rates at two different surface sites (*e.g.* N_1 and N_2) and assuming that the attempt frequency is the same at different sites, it can be shown that:

$$E_2 - E_1 = k_B T \ln\left(\frac{N_1}{N_2}\right) \tag{4.20}$$

which shows that the difference in activation energies is related to the natural logarithm of the ratio of the vacancy creation rates. Even if the absolute energies are not correct because

of uncertainty in the attempt frequency pre-exponential factor, the differences in activation energy should be accurate according to Equation (4.20). Image sequences were recorded only over 1 s, but there are multiple measurements of symmetrically similar types of sites at different locations in the images. The number of vacancy creation events at similar sites can therefore be averaged to improve the estimates of activation energy and gives sensitivity to sites where the oxygen vacancy creation rate is slower than once per second. The time resolution of the images is limited to 25 ms, so it is not possible to quantify sites where the activation energy is below ~0.69 eV (N_{th} = 20). Assuming each vacancy creation event is associated with a single oxygen vacancy creation within the column, the local activation energy can be determined. For example, in Figure 4.10a, there are 12 non-strained (111) terrace columns that show a total of 22 vacancy creation events within 1 s. The number of Ce atoms in each column was estimated by comparing experimental column intensities to the look-up table generated from multislice image simulations in Figure 4.1 and showed that there are a total of 54 Ce cations in those 12 columns. Therefore, the probability of a vacancy creation event occurring in 1 s at a non-strained terrace site is 22/54, which gives an activation energy of ~0.790 eV. Table 4.2 shows estimated activation energies for oxygen vacancy creation at different types of surface sites. There is error associated with counting cations in each column, which is estimated to be ±1 atom per column. Additional error arises from setting the threshold criteria to 2 standard deviations for identifying displacement events. Combining both error sources gives typical errors in the activation energy estimates of ~0.005-0.02 eV.

Table 4.2. Estimated activation energy for oxygen vacancy creation at different sites in CeO_2.

Site Type	# of Atoms	Total # of Displacement Events	N_{th} (s^{-1})	Activation Energy (E_a)
Non-strained (111) Terrace Edges	54	22	0.41	0.790 ± 0.005 eV
Locally strained (111) Terrace Edges	40	61	1.53	0.755 ± 0.005 eV
(111) Step Edges	10	70	7	0.72 ± 0.01 eV
(110) Nanofacet - 1	1	15	15	0.70 ± 0.02 eV
(110) Nanofacet - 2	1	16	16	0.70 ± 0.02 eV
(110) Nanofacet - 3	3	10	3.33	0.74 ± 0.01 eV

A possible random error of ±1 Ce atom in each atomic column was assumed for each site type. The probability of an apparent displacement event due to random noise in the image is 5%. Calculating upper and lower bounds of activation energy based on these error sources provided the errors in activation energy, which are included in the table.

On the (111) surface, the low coordination step edge sites show a lower activation energy of ~0.72 eV compared with the more stable, high coordination (111) terrace sites. These experimental trends observed in activation energy are qualitatively consistent with recent theoretical calculations, which predict that step edge sites have significantly lower oxygen vacancy formation energies than terrace sites (Migani et al., 2010a, 2010b; Sk et al., 2014). The correlation between activation energy and formation energy may be an indication of Brønsted-Evans-Polanyi (BEP) type relationships which have been observed on other oxide surfaces (Vojvodic et al., 2011). While density functional calculations show oxygen vacancy formation energy differences on the order of 1 eV between high coordination sites like terraces and low coordination sites like edges and steps, we measure

an activation energy difference of only ~0.09 eV. However, it is important to remember that the columns in the image include contributions from both terrace edge cations at the top and bottom surfaces of the TEM sample and terrace face cations between these surfaces. The total number of displacements will be the sum of the displacements occurring at these symmetrically distinct surface sites. Since the terrace edge sites will be more active due to their lower coordination number, the measurement is most sensitive to the activation energy for the terrace edge sites.

The effect of strain on activation energy can also be determined by comparing the energies of atoms in locally strained terrace sites with those on non-strained terrace sites. A reduction in activation energy of ~0.035 eV was measured at strained sites. It has recently been shown that biaxially straining CeO_2 films causes a decrease in activation energy for oxygen exchange processes (Balaji Gopal et al., 2017), which is consistent with the experimental observation of Figure 4.10 and Table 4.2.

Ce columns on the (110) nanofacet show the highest level of activity, an observation consistent with bulk experiments on the CO oxidation activity of CeO_2 nanorods and nano-octahedra (Zhou et al., 2005), where (110) and (100) facets show higher activity than (111) facets, as discussed in Section 1.3.5. These observations are also consistent with various computational studies, which generally predict that the (111) surface is less prone to releasing lattice oxygen than the (100) or (110) surfaces (Broqvist et al., 2015; Nolan, Parker, et al., 2005; Sayle et al., 1994; Conesa, 1995; Skorodumova et al., 2004; Baudin et al., 2000). The (110) nanofacet in Figure 4.10 shows the presence of low coordination sites on the surface and also local strain. Based on image intensity

analysis, the most active sites labeled “1” and “2” in Figure 4.10 are adatom sites with activation energies of 0.70 eV and are associated with a local tensile strain of 8%. The column labeled “3” occupies an edge site at the intersection of the (110) and (111) facets and has an activation energy of 0.74 eV with an associated compressive strain of 5%. These results indicate that activity may be a complex function of strain as well as surface facet, coordination number, and stability, which will be discussed in Chapter 6.

A considerable degree of diversity and heterogeneity in the type of surface sites that show low activation energy is shown in Figure 4.10 and Table 4.2. It is important to remember that the macroscopic oxygen vacancy creation rate will depend not only on activation energy but also on the number of sites of different types. Equation (4.1) implies that the active sites showing differences of around 0.06 eV in activation energy will have a factor of 10 difference in oxygen vacancy creation rate. Therefore, for example, 10 sites with activation energies of 0.79 eV will collectively give the same oxygen vacancy creation rate as one site with an activation energy of 0.73 eV. This illustrates that atomic-level surface heterogeneity has a strong influence on macroscopic reaction rates, and that to design materials with optimum functionality, both the type and density of surface defects must be considered.

4.4 Summary

Atomic resolution observations of lattice oxygen vacancy creation and annihilation were performed on the surface of CeO_2 nanoparticles. The approach described in this Chapter uses time-resolved *in-situ* AC-TEM to track surface cation displacements associated with oxygen vacancy creation and annihilation to identify the most reactive

surface oxygen sites on a CeO_2 nanoparticle surface. By monitoring the frequency of cation displacements at a surface, a local indicator of activation energy for oxygen vacancy creation was obtained, a fundamental part of the complex oxygen exchange process. A considerable degree of diversity and heterogeneity in the type of surface sites that showed high activity was observed. The highest observed activity occurs at surface defects with low coordination number such as (110) adatoms and (111) step edge sites with measured activation energies in the range 0.70–0.74 eV. Localized strain fields were also observed to enhance the activity for oxygen vacancy creation on both (111) and (110) surfaces. This approach allows atomic defect structure to be experimentally linked with surface oxygen vacancy activity, providing a deeper understanding of the catalytic oxygen exchange cycle. This work will help guide the future engineering of new materials surface structures to optimize oxygen exchange functionalities and is also applicable to other materials where surface atom positions are perturbed by interactions with their environment, such as adsorbate layers.

5 Time-Resolved Transmission Electron Microscopy Approach for Nanoparticle Surface Reconstructions

5.1 Motivation

A nanoparticle's structural parameters determine its physical and chemical properties, and for many nanoparticle systems, particularly in catalysis, dynamic surface reconstructions can occur *during a reaction* (Vendelbo et al., 2014; Kuwauchi et al., 2013; Yoshida et al., 2012). As a result, it is necessary to develop characterization methods that can extract structural information, such as atomic column positions and occupancies, during dynamic structural processes. *In situ* AC-TEM is an ideal tool for the direct observation of dynamic structures, and the recent development of direct electron detectors has led to significantly improved performance in image frame read-out speed over conventional CCD imaging cameras, enabling temporal resolutions on the order of a millisecond (Faruqi et al., 2005; McMullan et al., 2014; Ruskin et al., 2013; Faruqi & McMullan, 2018). The combination of high spatial and temporal resolution imaging results in large data sets that offer a wealth of potential quantitative information about dynamic structures. However, most methods that have been previously developed to extract atomic column positions or occupancies rely on either image averaging procedures or long acquisition times (Yankovich et al., 2014; Nilsson Pingel et al., 2018; Levin et al., 2016; Friedrich et al., 2009; Florea et al., 2013; Bals et al., 2016), both of which are not easily attainable when imaging dynamic surface structures. Therefore, high temporal resolution imaging necessarily means that atomic column positions and occupancies must be determined in individual frames, often which have low signal-to-noise. The apparent solution to increase signal-to-noise and subsequently improve the measurement precision

in individual image frames would be to acquire images with a higher electron flux; however, many materials undergo undesirable beam-induced structural changes.

In this Chapter, the TRACT approach from Chapter 4 is used to explore the practical relationship between measurement precision and temporal resolution by quantitatively characterizing dynamic CeO_2 (ceria) surface reconstructions with high spatial and temporal resolution in large data sets of low signal-to-noise images. The direct observation and quantification of dynamic surface reconstructions is achieved with a spatial precision of 0.25 Å while the 2.5 ms temporal resolution of the original image acquisition is preserved, revealing local lattice expansions and contractions on a ceria (100) surface that have not been previously observed in the literature. The application of this methodology to other materials may also provide new insights into the dynamic behavior of other nanoparticle surfaces that were previously inaccessible using other methods, which can aid significantly in understanding structure-property relationships.

5.2 Experimental

5.2.1 Microscope and Imaging Parameters

CeO_2 nanoparticles synthesized via the method described in Section 2.1.2 were imaged at 400 frames/second (fps) using an FEI Titan ETEM 80-300, aberration-corrected, environmental transmission electron microscope (AC-TEM), operated at 300 kV at room temperature. (111) and (100) CeO_2 nanoparticle surfaces were imaged in a [110] projection at 120,000 $e^{-}Å^{-2}s^{-1}$, equating to 300 $e^{-}Å^{-2}$ per individual 2.5 ms exposure frame. The corresponding displacement rates of oxygen and cerium atoms due to knock-on damage

and radiolytic displacement are provided in Appendix 8.3, which shows that the electron beam can cause multiple displacements of each type of atom per second for the electron flux of this experiment. Images were acquired using a Gatan K2 IS direct electron detector operated at 400 fps with 4k x 4k pixels and a pixel size of ~0.125 Å/pixel. Images were acquired over a ~22 second total exposure time, equating to ~8800 individual image frames.

5.2.2 Image Processing

Visual analysis of the full image sequence showed that reconstructions occurred throughout the observation period. Representative dynamic events of ~500 ms (~200 image frames) were selected for analysis to demonstrate the methodology. For image analysis, individual 2.5 ms exposure images were spatially binned by two (to ~0.25 Å/pixel) and then a 1-pixel radius Gaussian blur filter was applied to reduce noise using ImageJ. The mean and standard deviation (σ_{vac}) of the intensity in vacuum was measured, and these values were used to estimate the error due to noise as discussed below. In practice, all of the images were normalized prior to any further analysis by dividing each individual image by the mean vacuum intensity to set the vacuum level at 1. This facilitated comparison of experimental images with multislice simulations. This image processing procedure is written algebraically in Appendix 8.2.

The Time-Resolved Atomic Column Tracking (TRACT) codes that were described in detail in Section 4.2.2 were used to identify atomic columns and determine their position and integrated intensity. Analysis with the TRACT code was greatly simplified when

applied to images with bright atom contrast, rather than the dark contrast present in the initial images presented in this Chapter. Image contrast was therefore inverted by subtracting each pixel value from the mean intensity in the vacuum. Due to the low signal-to-noise of the 2.5 ms exposure images, two additional criteria were applied to determine if each Gaussian fit in the individual frames was acceptable: the amplitude must be equal to or greater than $2\sigma_{vac}$ of the vacuum intensity value and the goodness of fit (R^2) must be greater than 0.4. Figure 5.1 provides a schematic of the requirement that a Gaussian fit must have an amplitude of greater than $2\sigma_{vac}$. If the amplitude of the Gaussian fit was less than $2\sigma_{vac}$, then the integrated intensity was set to zero. If the amplitude was equal or greater than $2\sigma_{vac}$ but the R^2 value was equal to or less than 0.4, then the fit was rejected and ignored during analysis. The coordinates of the maxima of each of the 2D Gaussians defined the positions of each cation column. A value for column intensity in each frame was calculated using the analytical expression for the integral of a 2D Gaussian function, $I = 2\pi A\sigma_x\sigma_y$, where A is the amplitude of the fit and σ_x and σ_y are the standard deviations (widths of the curves) of the two dimensions of the Gaussian function.

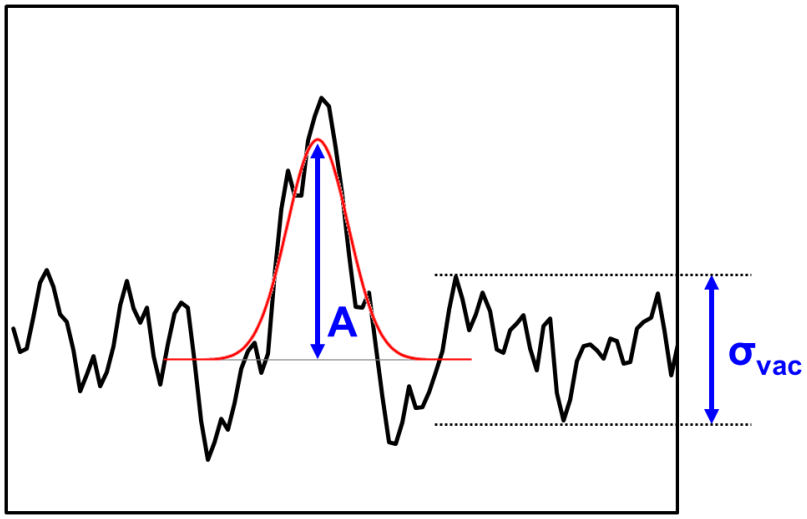

Figure 5.1. Gaussian fitting criteria. The black line is a representative 1D line scan of arbitrary intensity for a single 2.5 ms exposure image frame. For a Gaussian fit to be accepted, the amplitude (A) of the Gaussian fit (red curve) must be greater than $2\sigma_{vac}$ of the vacuum intensity value.

AC-TEM image simulations were performed using a multislice approach in the JEMS software developed by Pierre Stadelmann to produce an image intensity look-up table (Stadelmann, 2018). For image simulations, the microscope accelerating voltage, spherical and chromatic aberration coefficients, beam half convergence angle, and defocus conditions were matched to experimental conditions while additional lens aberrations and noise were set to zero as shown in Table 5.1. A partially coherent (envelope) illumination model was used. To calculate the intensity look-up table, images of a (111) CeO_2 surface were simulated over a range of thicknesses from 1 Ce atom per column to 16 Ce atoms per column. A representative simulated image of 4-atom thickness is presented in Figure 5.2a, and the corresponding inverted image used for intensity calculations is shown in Figure 5.2b. A value for the intensity of Ce columns at each thickness was calculated by fitting a 2D elliptical Gaussian to columns at different sites using the procedure described above.

Four different sites were chosen for intensity calculations: two sites at the (111) surface of the simulated image, and two "bulk" sites several layers away from the (111) surface. 'A' sites are those where the Ce atoms in the column appear in the odd-numbered slices in our simulations. 'B' sites are those where the Ce atoms in the column appear in the even-numbered slices in our simulations. The results of these calculations are given in the look-up table in Figure 5.2c, which shows that the integrated intensity increases roughly linearly between 1 and 7 atoms in thickness, before peaking at 13 atoms in thickness and decreasing thereafter. Relatively little difference in integrated intensity is observed between different sites (A and B, surface and bulk) until 10 atoms in thickness is reached.

Table 5.1. Image Simulation Parameters.

Image Simulation Parameters	
Accelerating Voltage	300 kV
3rd order Spherical Aberration (C_3)	-0.03 mm
Chromatic Aberration (C_c)	1 mm
Beam half convergence angle (α)	0.15 mrad
Defocus (C_1)	-1 nm
Defocus spread (*f*)	1 nm
2-fold (A_1) /3-fold (A_2) astigmatism	0 nm
2nd order Coma (B_2)	0 nm
5th order Spherical Aberration (C_5)	3 mm

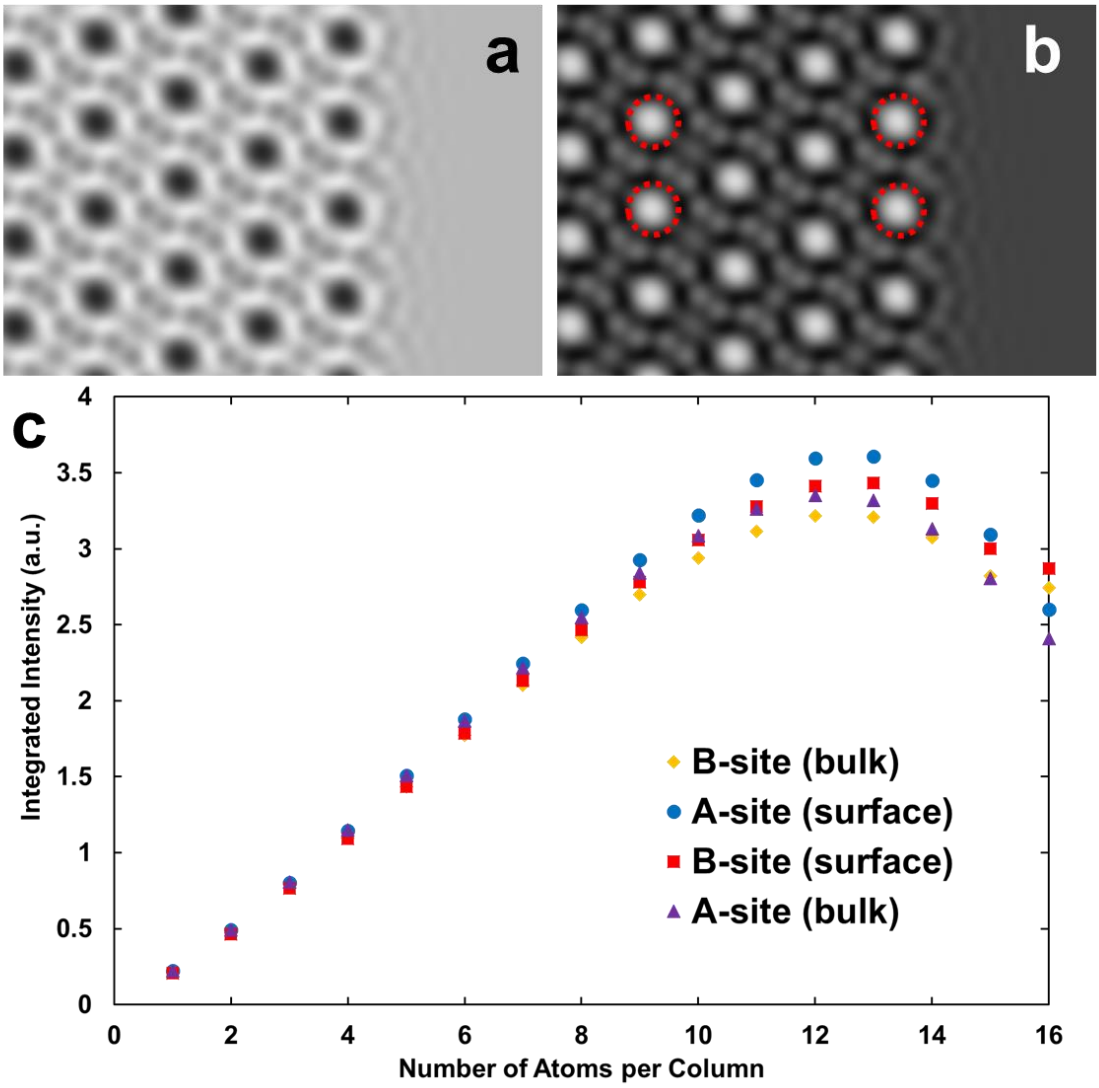

Figure 5.2. (a) Simulated image of (111) CeO_2 surface with 4-atom thickness. (b) Inverted image of the simulated image from (a). Red circles indicate the four different Ce atomic sites that were integrated at each thickness to form the look-up table. (c) Integrated Intensity look-up table: Calculated integrated intensities of Ce columns for different thicknesses at different atomic sites produced using a 2D Gaussian fitting procedure on simulated images. Intensity is observed to increase roughly linearly between 1 and 7 atoms in thickness, before peaking at 13 atoms in thickness and decreasing thereafter. Relatively little difference in intensity is observed between different sites (A and B, surface and bulk) until 10 atoms in thickness is reached. Intensity is given in arbitrary units.

5.3 Results and Discussion

5.3.1 Imaging Surface Structures

Figure 5.3a shows an AC-TEM image of a ~2 nm CeO_2 nanoparticle with a 1 s total exposure time (unprocessed 2.5 ms frames aligned and summed together). Cerium atomic columns have dark contrast in these images; oxygen atomic columns were not visible with the imaging conditions used. Figure 5.3b shows a single, unprocessed 2.5 ms exposure frame from the image sequence used to create the 1 s total exposure image in Figure 5.3a, indicating the low signal-to-noise ratio present in individual images. As evidenced by Figure 5.3a,b, sacrificing signal-to-noise can lead to higher temporal resolution and vice versa. In this orientation, a polar (100) facet is flanked by two non-polar (111) facets. Inspection of the nanoparticle surfaces in Figure 5.3a reveals that the atomic columns on the (100) surface appear slightly diffuse relative to the (111) surfaces and subsurface atomic columns. Variation in the positions and intensities of atomic columns in individual frames causes the more diffuse appearance of columns on the (100) surface, and it is these variations that are characterized in this Chapter.

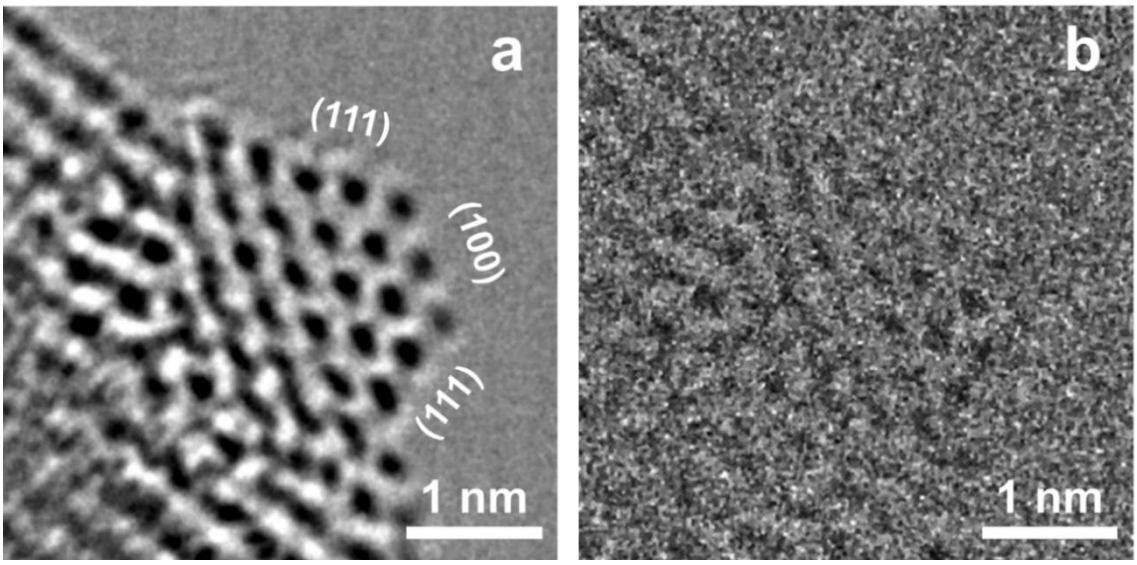

Figure 5.3. Imaging of a CeO_2 nanoparticle. (a) Aberration-corrected TEM image of a ~2 nm CeO_2 nanoparticle with a 1 s total exposure time (unprocessed 2.5 ms frames aligned and summed together). (b) A single, unprocessed 2.5 ms exposure frame from the image sequence used to create the 1 s total exposure image in (a).

5.3.2 Relationship between Measurement Precision and Temporal Resolution

It is important to consider the relationship between the precision of position/intensity measurements and the temporal resolution and understand how it may affect the analysis. Consider an atomic column that is assumed to be stationary and doesn't change occupancy throughout the entire observation period. If Poisson statistics is assumed and M independent measurements of position or intensity are made, then the average of those M measurements provides the best estimate of the "true" value and the standard deviation, σ_M, represents the uncertainty/error associated with each individual measurement. If many additional measurements are made, the measurements will more closely follow a normal distribution; however, the standard deviation of the distribution would remain approximately the same because M was sufficiently large, and the

uncertainty of each measurement would still be σ_M. The uncertainty associated with determining the average value is called the standard error, given by $\sigma_M/\sqrt{M}$.

For atomic column position analysis, subsurface atomic columns in the center of the nanoparticle visually appeared stationary over the representative observation period (200 image frames), and the standard deviation of the position measurements of those columns was measured to be ~0.25 Å. In this case, each measurement corresponded to a single 2.5 ms exposure image frame, which provides a direct link between measurements and temporal resolution. t_0 is defined to be the limit of temporal resolution and t_0 = 2.5 ms for the experiment in this Chapter. For t_0, the precision is defined as σ_0, which is set as 0.25 Å for position measurements in this experiment. Therefore, t_0 and σ_0 are the upper limit of temporal resolution and the lower limit of spatial precision, respectively. If n image frames are averaged together and temporal resolution is sacrificed, then the spatial precision of the average position measurement would be given by $\sigma_n = \sigma_0/\sqrt{n}$. The temporal resolution will be reduced according to $t_n = nt_0$. Solving for n, inserting into σ_n, and simplifying gives $\sigma_n\sqrt{t_n}. = \sigma_0\sqrt{t_0}$. Therefore, this simple expression relates the spatial precision and temporal resolution of a single image frame to any number of averaged images, which is useful for determining the positional error in dynamic structure quantification. This relationship is plotted in Figure 5.4 for the experimental parameters described above. As can be seen from this plot, the spatial precision is 0.25 Å at the limiting case of 2.5 ms temporal resolution but can be improved by averaging images together. For example, if 5 pm spatial precision is desired, then the temporal resolution must be reduced to 62.5 ms, which corresponds to 25 image measurements being averaged together.

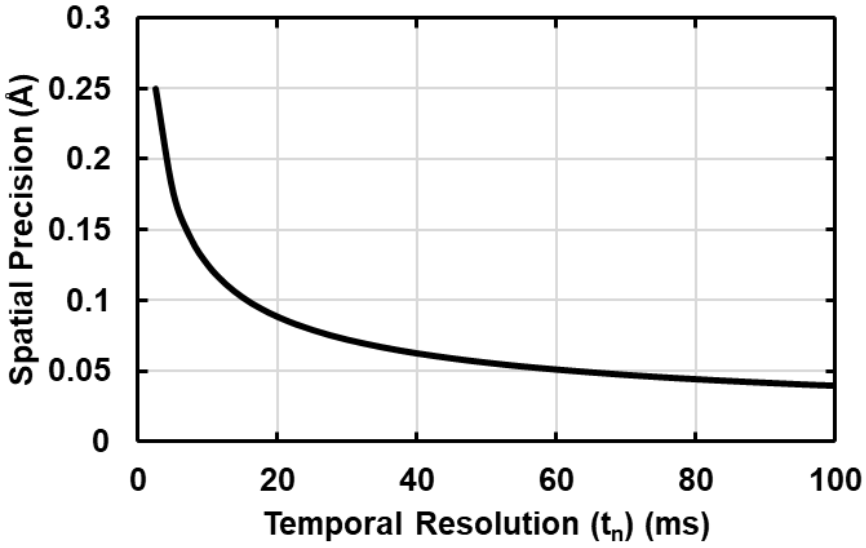

Figure 5.4. Relationship between Spatial Precision and Temporal Resolution. σ0 = 0.25 Å and t0 = 2.5 ms.

For intensity analysis, subsurface atomic columns in the center of the nanoparticle visually appeared to have relatively constant intensity over the representative observation period (200 image frames), and the standard deviation of the integrated intensity measurements of those columns was measured to be ~0.3 arbitrary units. Therefore, the precision of individual measurements of intensity is defined as I_0 = 0.3 arbitrary units at the temporal resolution limit of t_0 = 2.5 ms. Using the same arguments as discussed above for position measurements, if n image frames are averaged together and temporal resolution is sacrificed, then the precision of the average intensity measurement would be given by $I_n = I_0/\sqrt{n}$. This results in a similar expression for relating the intensity precision and temporal resolution of a single image frame to any number of averaged images, $I_n\sqrt{t_n} = I_0\sqrt{t_0}$. Therefore, the relationship between intensity measurement precision and temporal resolution displays identical behavior to that shown for spatial precision in Figure 5.4.

5.3.3 Observing Local Surface Lattice Expansion & Contraction

Local lattice expansions and contractions were observed on the (100) surface over short time periods (~0.2 s), and the position of each Ce atomic column in the nanoparticle in each 2.5 ms image frame was determined using the procedure outlined above and in Section 4.2.2. Figure 5.5 shows a 0.5 s time sequence from the experiment during which a representative lattice expansion and contraction event was observed. As described above in Section 5.3.2, the error in position measurements in 2.5 ms frames was defined to be 0.25 Å. The individual column positional measurement errors were added in quadrature to assign error bars of 0.35 Å to separation distance measurements in 2.5 ms image frames. For visual clarity, each image in Figure 5.5 is a 12.5 ms exposure image (five spatially binned and Gaussian blurred 2.5 ms images summed together), which resulted in the error in separation distance to be reduced to 0.16 Å for these frames ($0.35\ \text{Å}/\sqrt{5}$). Images of Figure 5.5 are shown with dark atom contrast, but the measurement analysis was performed on inverted images. The separation distance between Ce atomic columns on the bulk-terminated (100) surface is 3.825 Å in this projection. As shown in Figure 5.5a, the distance between two (100) surface Ce atomic columns is 3.27±0.16 Å at 0.16 s, expands to 5.03±0.16 Å after 0.21 s (Figure 5.5b), and contracts back to 3.52±0.16 Å after an additional 0.2 s (Figure 5.5c). In Figure 5.5a, there are three (100) surface atomic columns; however, the third surface atomic column is almost invisible in Figure 5.5b when the lattice expansion occurs. It is possible that the large lattice expansion destabilized the third atomic column and caused the atoms in that column to migrate to more stable positions, which is consistent with the experimental observations and may be further verified with future

theoretical simulations. The separation distance between the two (100) surface Ce atomic columns highlighted in Figures 5.5a-c was determined for each 2.5 ms frame in the 0.5 s image sequence and is shown in Figure 5.5d. The blue points indicate measurements from each frame, the solid black line is a 5-frame moving average trendline, and the dashed green line indicates the bulk-terminated (100) separation distance (3.825 Å). The semitransparent blue windows represent the five image frames that were summed together to create Figures 5.5a-c. The local lattice expansion and contraction behavior was cyclical and occurred several times over the full set of experimental image acquisitions (~22 s) (An additional sequence and quantification is shown in Appendix 8.3). This severe local surface lattice expansion and contraction behavior of a CeO_2 nanoparticle (100) surface has not previously been discussed in the literature and has been observed here for the first time due to the high temporal resolution of these measurements. It is hypothesized that this behavior is related to a cyclic oxygen vacancy creation and annihilation process, although additional experiments and theoretical simulations would be needed to confirm this hypothesis.

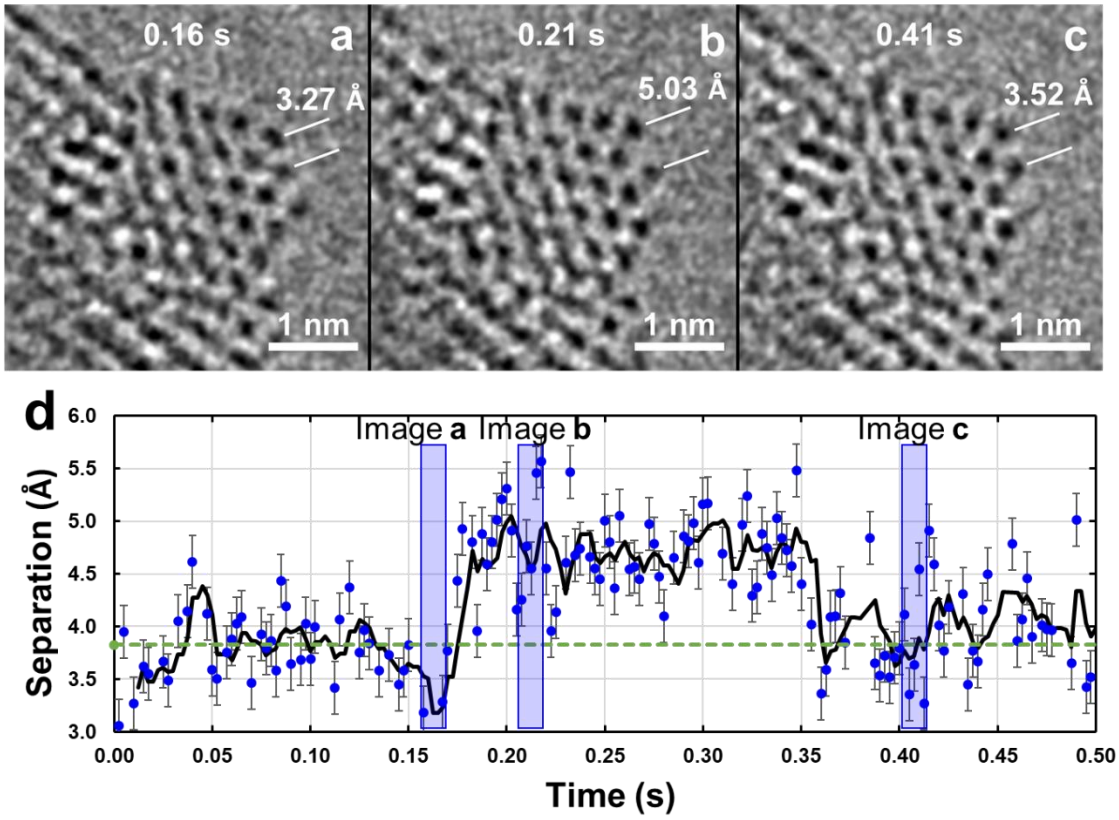

Figure 5.5. Local surface lattice expansion. (a-c) Image sequence of the CeO_2 nanoparticle with 12.5 ms exposure images (five spatially binned and Gaussian blurred 2.5 ms images summed together). Two Ce atomic columns on the (100) surface are separated by 3.27 Å at 0.16 s in (a), expand to 5.03 Å after 0.21 s in (b), and contract to 3.52 Å after 0.41 s in (c). (d) Measurement of the separation of the two marked surface Ce atomic column over 0.5 s image sequence. The blue points indicate measurements from each frame, the solid black line is a 5-frame moving average trendline, and the dashed green line indicates the bulk-terminated (100) separation distance (3.825 Å). Error bars are 0.35 Å. The semitransparent blue windows represent the five image frames that were summed together to create (a-c).

As can be seen in Figure 5.5d, the drastic expansion of the atomic column separation occurs over a short time period. This expansion is shown in Figure 5.6 with 2.5 ms temporal resolution. In Figure 5.6a,e, the distance between the two (100) surface atomic columns is 3.77±0.35 Å. After 2.5 ms, the three surface atomic columns are absent from the image (Figure 5.6b,f). The absence of visible contrast for the three surface atoms in

Figure 5.6b,f may indicate that the atoms are dynamically rearranging, causing diffuse image signal that is indiscernible from the noise. Alternatively, if it's assumed that an atomic column is present and stationary, then based on the criteria described in Section 5.2.2, for the column to be visible it must have an intensity value of $I > I_{vac} + 2\sigma_{vac}$. If the intensity is less than $I_{vac} + 2\sigma_{vac}$, the column will be undetectable. As a result, it can be inferred that the absence of visible signal for the three surface atomic columns in Figure 5.6b,f is either because the atoms are in a 'transition state' where atoms are dynamically rearranging during the exposure time or the atoms are stationary and have signal that is below the detection limit. It seems unlikely that three adjacent, stationary atomic columns would be invisible in the same 2.5 ms frame, so it is much more likely that the three columns are undergoing dynamic rearrangement. In the following frame (Figure 5.6c,g), the signal from the surface atomic columns is visible again, with the separation distance between the two atomic columns increasing to 4.43±0.35 Å. After an additional 2.5 ms, the expansion reaches 4.93±0.35 Å, as shown in Figure 5.6d,h. Although the individual image frames of Figure 5.6 are quite noisy, this approach can clearly extract information about the precise time over which the surface lattice expansion took place.

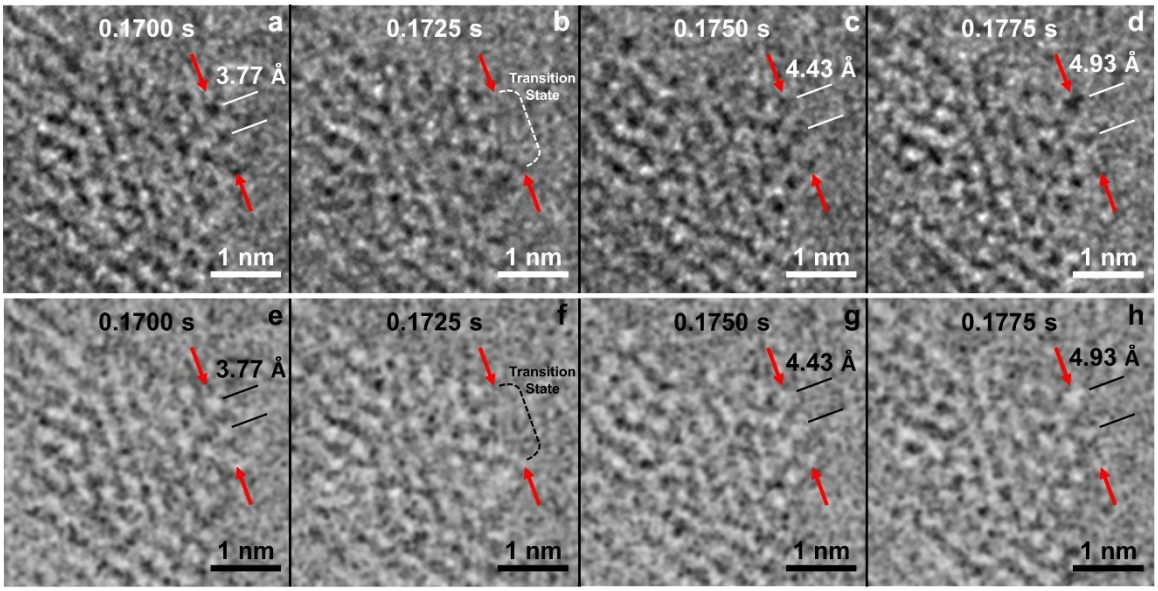

Figure 5.6. Image sequence of local (100) surface lattice expansion of CeO_2 nanoparticle with spatially binned and Gaussian blurred 2.5 ms frames in (a-d) and inverted images in (e-h). Two surface atomic columns are separated by 3.77 Å in (a,e), are absent in (b,f), reappear and expand to 4.43 Å in (c,g), and expand further to 4.93 Å in (d,h). The error in each of these measurements is ±0.35 Å. The absence of the three (100) surface atomic columns in (b,f) suggests that the atoms in these columns are dynamically rearranging in a 'transition state'. The red arrows in each frame provide a guide to the eye for referencing the surface dynamics.

5.3.4 Observing Atom Migration

The integrated intensity of each Ce atomic column in each 2.5 ms image frame was quantified to estimate the number of atoms within each atomic column during surface atom migration. Figure 5.7 shows a representative atom migration sequence of events during 0.5 s of the experiment, and each image is a 12.5 ms exposure image of the inverted images used for MATLAB analysis (five inverted 2.5 ms images summed together). Focusing on the three atomic columns identified by the white arrows and the "1", "2", and "3" labels (referred to as atomic column 1, atomic column 2, and atomic column 3, respectively), it is shown in Figure 5.7a that an atomically sharp tip has formed on the nanoparticle as

indicated by the presence of atomic column 1 and absence of atomic column 2. After 0.21 s (Figure 5.7b), every atom has migrated out of atomic column 1 as evidenced by the lack of intensity, whereas atoms have appeared in atomic column 2. Within an additional 0.11 s, some atoms have migrated back into atomic column 1 (Figure 5.7c). The atom migration events seen in Figure 5.7a-c are highlighted with 0.1 s exposure images in Appendix 8.3.

The number of Ce atoms within atomic columns 1, 2, and 3 were estimated through a comparison of experimental column intensities to the intensity look-up table (Figure 5.2c) and is shown in Figure 5.7d,e,f, respectively. The points indicate atomic column occupancy measurements from each 2.5 ms frame, the solid black line is a 5-frame moving average trendline, and the semitransparent red windows represent the five image frames that were summed together to create Figures 5.7a-c. As discussed in Section 5.3.2, the standard deviation of the integrated intensity measurements of subsurface atomic columns in the center of the nanoparticle was ~0.3 arbitrary units, which is approximately the intensity value for a single atom as shown in Figure 5.2. Therefore, error bars of ±1 atom were assigned to the atomic column occupancy estimates of Figure 5.7. This error is relatively large but would be reduced if a higher electron flux is used or by sacrificing temporal resolution and averaging images together, both of which would increase the signal-to-noise and improve the Gaussian fitting procedure. The integrated intensity was set to 0 when an atomic column was unable to be fitted with a 2D Gaussian according to the criteria described in Section 5.2.2, which could mean that no atoms are in that position, the atoms are dynamically rearranging and causing weak signal, or the signal-to-noise was too low to accurately determine a Gaussian fit. As shown by the black trendline in Figure 5.7d, atomic column 1 has ~2-4 atoms until a sharp drop around 0.17 s, indicating that atoms are

migrating out of the column. Additionally, in Figure 5.7e, it is shown that atomic column 2 is absent until ~0.12 s and jumps up to ~2-3 atoms around 0.17 s, indicating the migration of atoms into the column. In Figure 5.7f, the occupancy of atomic column 3 is consistently ~3-5 atoms throughout the 0.5 s image sequence. Although noise causes some of the fluctuations observed in these three atomic columns, the main source of fluctuation is the change in occupancy, suggesting that atoms are continuously migrating during the observation period. For example, in Figure 5.7d there are two frames (red data points) around ~0.4 s where the estimated number of atoms are much higher than the surrounding data points. This image sequence is provided in Appendix 8.4 and confirms that the large increase in the estimated number of atoms is caused by atoms migrating into and out of atomic column 1 over a short time period.

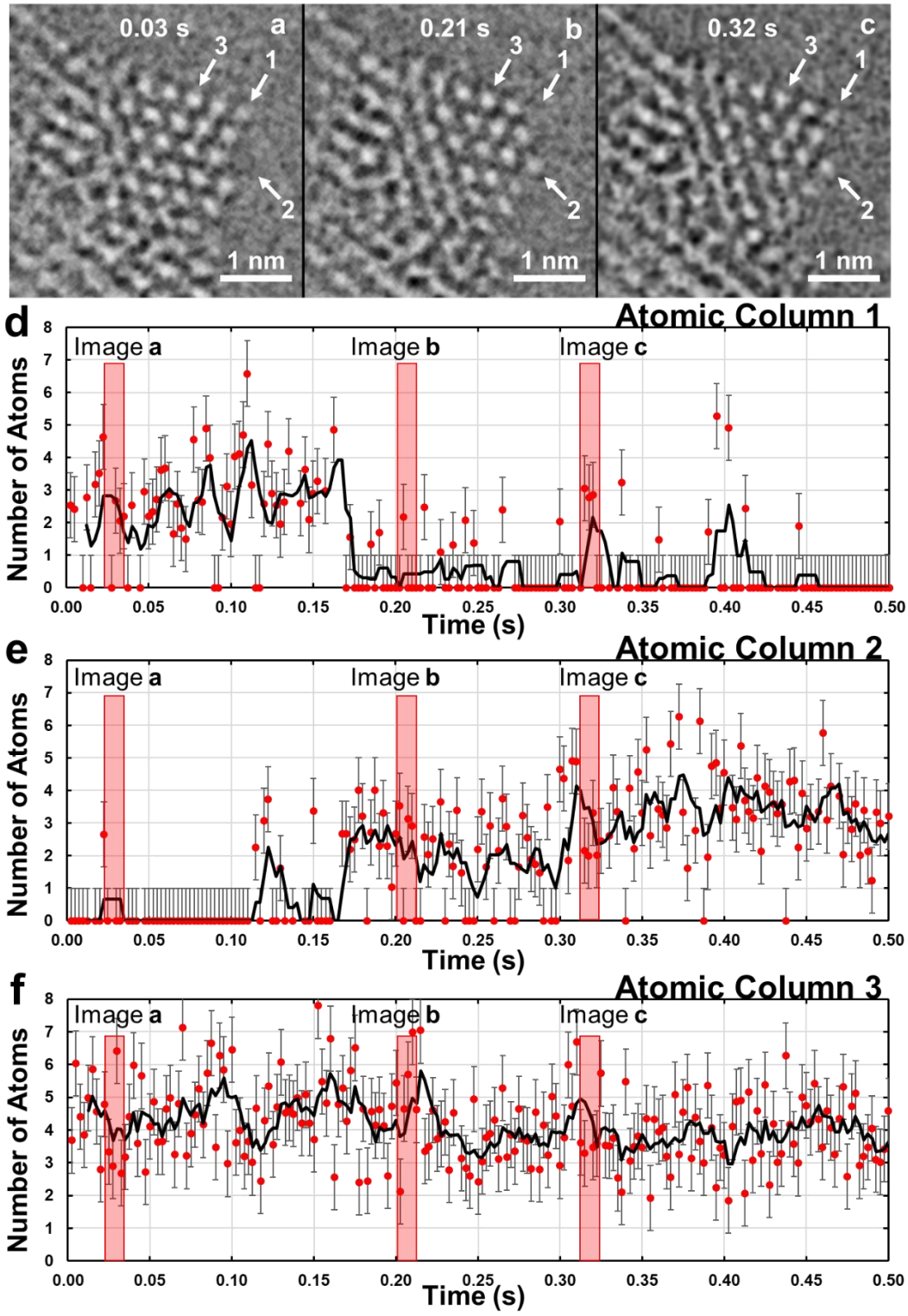

Figure 5.7. Atom migration. (a-c) Image sequence of the CeO_2 nanoparticle with 12.5 ms exposure images of the inverted images used for MATLAB analysis (five inverted 2.5 ms images summed together). As indicated by the "1", "2", and "3" labels, atoms are migrating

into and out of these atomic columns during the observation period. (d,e,f) Estimated atomic column occupancy based on measurements of the integrated intensity from atomic column "1", "2", and "3", respectively, over a 0.5 s image sequence. The points indicate measurements from each frame and the solid black line is a 5-frame moving average trendline. The semitransparent red windows represent the five image frames that were summed together to create (a-c). Error bars are ±1 atom.

To construct a pseudo-3D representation of the nanoparticle, the number of Ce atoms within each atomic column was estimated. A wedge profile model at the (100) surface was assumed based on the truncated octahedral or tetrahedral CeO_2 nanoparticle models observed in other studies (Wang & Feng, 2003; Migani et al., 2012; Tan et al., 2011; Sayle et al., 2004). Approximating the number of atoms in each column in individual frames can therefore observe the evolution of the pseudo-3D structure of the nanoparticle over time. The experimental occupancy estimations of individual frames fluctuate dramatically in Figure 5.7d,e,f, so the 5-frame moving average values were used to estimate the number of Ce atoms in each atomic column, which reduced the error to ~±0.5 atom. For each image in Figure 5.7a-c, a simple 3D model is shown in Figure 5.8 where blue spheres represent Ce atoms and each atomic column has ~0-5 atoms. As was also evidenced in Figure 5.7, Ce atoms migrated out of atomic columns 1 as atoms appeared in atomic column 2. Oxygen atomic columns are omitted as they are not visible in these images and no conclusions can be drawn about their occupancy. Noise fluctuations may influence the atom counting procedure; however, this time-resolved pseudo-3D approach can still provide informative results such as visualization of 3D surface heterogeneity, preferential migration of atoms along a specific direction, or instabilities of a certain surface facet. For more precise quantification of atomic column occupancy, temporal resolution can be sacrificed to sum together more individual image frames for a higher signal-to-noise ratio.

Although beyond the scope of the present manuscript, the pseudo-3D representation of this CeO_2 nanoparticle may be used to guide future theoretical studies as it gives a near real-time look into actual structures that are dynamically reconstructing on polar and non-polar surfaces.

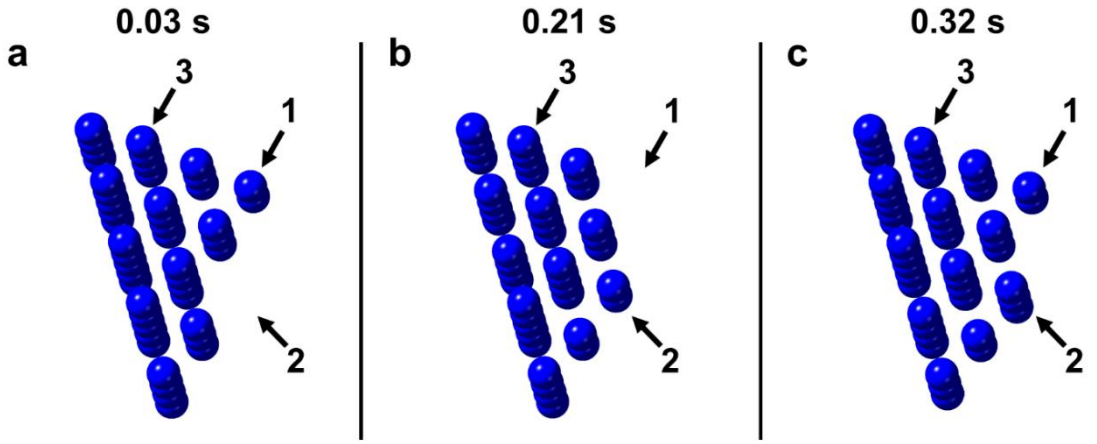

Figure 5.8. Simple 3D model showing number of atoms estimated in each column of the CeO_2 nanoparticle from the images of Figure 4a-c. Blue spheres represent Ce atoms. Oxygen atomic columns are omitted because they are not visible in our images and no conclusions can be drawn about their occupancy. Error is estimated to be ~±0.5 atom/column.

5.4 Summary

A time-resolved AC-TEM approach was used to observe dynamic nanoparticle surface structures with 0.25 Å spatial precision and 2.5 ms temporal resolution, a combination of spatial precision and temporal resolution that has not previously been achieved. The position and occupancy of each atomic column within a CeO_2 nanoparticle was determined using a 2D Gaussian fitting and image simulation procedure. Due to the high spatial precision and temporal resolution, local lattice expansions/contractions and atomic migration were revealed to occur on the (100) surface whereas (111) surfaces were stable throughout the experiment. A pseudo-3D representation was constructed by

estimating each atomic column's occupancy, enabling the visualization of the dynamic evolution of the surface structure. This work provides a time-resolved approach for atomic-level *in situ* imaging of dynamic surface structures and can be applied to other nanomaterials systems that undergo surface reconstructions under intense electron beam exposure to accelerate understanding of structure-property relationships. In future studies, insights into the origin of the dynamic surface structures on the CeO_2 nanoparticle may be gained by considering the role of oxygen vacancies.

6 Preliminary Measurements of Average Local Strain and Correlation to Oxygen Vacancy Creation

6.1 Motivation

As discussed in Section 1.3, the oxygen nonstoichiometry of ceria determines the concentration of mobile oxygen vacancies and electronic defects that mediate oxygen exchange at the oxide/gas interface, oxygen storage at the surface and bulk, and oxygen transport, which can be tuned through doping, nanostructuring, or through the formation of metal-ceria interfaces. However, recent advances in atomic-level control of synthesis techniques and the rapid downsizing of solid-state devices have also made strain engineering an attractive option to tune the properties of nanomaterials (Li et al., 2014; Yildiz, 2014; Sen Zhang et al., 2014; Schweiger et al., 2017). Although it is well established that strain modifies the chemical properties of bulk systems, the effect of strain on nanoparticles is often more complex and has not been fully explored (Nilsson Pingel et al., 2018). Therefore, it is desirable to investigate the role that strain heterogeneities have on local catalytic properties of CeO_2 nanoparticles.

Reductions in oxygen migration energy and vacancy formation energy have been observed for strained CeO_2 and CeO_2-based nanomaterials, resulting in enhanced ionic conductivity and surface reactivity (Balaji Gopal et al., 2017; Kant et al., 2012; Sanna et al., 2010: 201; Rupp et al., 2014; De Souza et al., 2012; Rushton & Chroneos, 2015; Yildiz, 2014; Wen et al., 2015; Tuller & Bishop, 2011). Although the use of nanoscale strain field engineering has been suggested to be useful for improving redox activity through a decrease in oxygen vacancy formation energy (Balaji Gopal et al., 2017), experimental methods that probe and correlate the local lattice oxygen vacancy creation and annihilation

rates with local strain remain limited. In this chapter, atomic resolution strain measurements were extracted from AC-TEM images of CeO_2 nanoparticle surfaces to determine average local strain field maps, which were then compared to the cation displacement frequency results as discussed in Chapter 4. It is found that the sites that exhibit a high degree of local strain in at least one direction were generally associated with a high number of cation displacements, which implies enhanced surface oxygen vacancy activity. Significant average strain heterogeneities were observed across each nanoparticle surface, and further analysis is needed to accurately correlate local oxygen vacancy creation/annihilation rates to local strain. Application of this approach to additional surfaces, dislocations, or metal-ceria interfaces may provide new insights into the behavior of nanoscale strain fields.

6.2 Experimental

6.2.1 Microscope and imaging parameters

CeO_2 nanoparticles synthesized via the method described in Section 2.1.2 were imaged under identical microscope and imaging parameters as described in Section 4.2.1.

6.2.2 Strain Analysis and Visualization

Atomic column positions were determined using the TRACT code that is described in Section 4.2.2. For strain analysis, the atomic column positions were defined by the coordinates of the maxima of each of the 2D Gaussians in a summed image of the time series (a Z-projected image). For each image set, the pixel size was calibrated from the

average nearest-neighbor distances in three crystallographic directions within a region in the bulk of the crystal at least four atomic layers away from a surface. The standard deviation of the atomic column separations within this area was defined to be the image precision (Bals et al., 2006; Kimoto et al., 2010) and was between 3 and 5 pm for the data presented here.

Strain maps were created to visualize the projected nanoparticle lattice deformations. Strain was defined as the deviation of the measured spacing between two adjacent atomic columns from the perfect crystal spacing divided by the perfect crystal spacing, or $\text{Strain}\ (\%) = 100 * \frac{d_{meas} - d_{perf}}{d_{perf}}$, where d_{meas} is the measured spacing and d_{perf} is the perfect lattice spacing. On the strain maps, local average strain is indicated by a colored circular region centered between the two corresponding atomic columns. Separate strain maps were created for different crystallographic directions and highlights the implication that atomic columns can be associated with both compressive and tensile strains in different directions. The color scale was set to ±10% although a small number of strains were measured to be larger. A precision of 3-5 pm in the measurement precision results in a ~1.2-2% error bar for the strain analysis.

6.3 Results and Discussion

6.3.1 Imaging CeO_2 Surfaces

Figure 6.1a shows an AC-TEM image of a CeO_2 nanoparticle stepped surface in the [110] projection with a 1 s total exposure time. The facet on the left side of the image is a (110) surface, the center is a (111) surface, and the right side is a (100) surface. Images

were acquired using negative spherical aberration (C_s) imaging where atomic columns appear with bright contrast (Jia et al., 2004; Lin et al., 2014; Zhang et al., 2018), with both Ce and O atomic columns visible. Inspection of Ce atomic columns on step edges reveals that several columns appear diffuse (highlighted by arrows in Figure 6.1) relative to other columns. The diffuseness is a result of variations in the positions of the atomic columns in the individual frames that were integrated to give a 1 s total exposure.

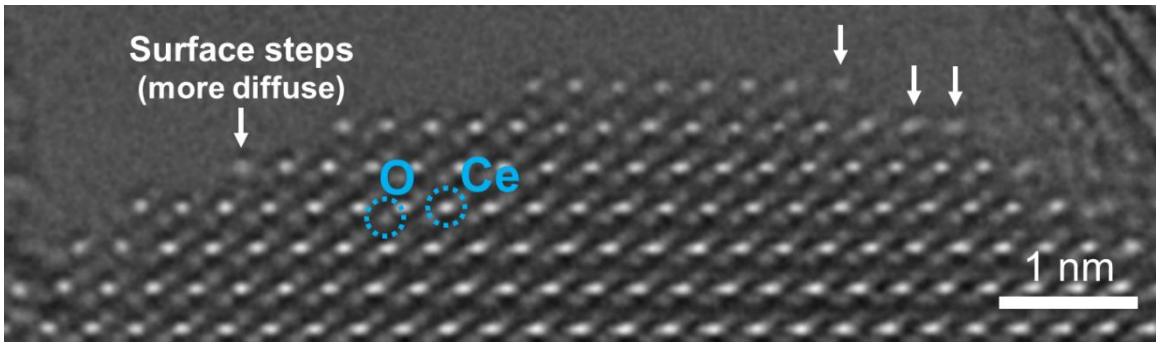

Figure 6.1. Integrated (1 s) AC-TEM image of a stepped surface of CeO_2. White arrows indicate Ce atomic columns that appear diffuse due to dynamic displacement of cation columns between individual frames. Oxygen atomic columns are only visible at several surface sites.

6.3.2 Quantifying Local Strain Variations

Atomic resolution strain measurements were extracted from the summed (1 s) AC-TEM images to have high spatial precision in atomic column position measurements and were then compared to displacement frequency measurements. Figure 6.2 shows the comparison between the displacement frequency measurements and strain maps of the stepped (111) CeO_2 surface that was analyzed in Figure 4.10. As discussed in Section 4.3.4 and shown in Figure 6.2a, the step edge sites display the highest displacement frequency. Atomic resolution strain behavior is shown in Figure 6.2b,c. Black points indicate the

atomic column positions and colored circles represent the local strain measured between each pair of atomic columns. Colored circles are centered between the two corresponding columns that the strain is measured from. Double sided black arrows indicate the direction with which the strain was measured. The outer surface layers in Figure 6.2b,c generally have larger degrees of strain than subsurface layers. The center terrace of the image that shows high displacement frequencies also shows large strain in both Figure 6.2b and c.

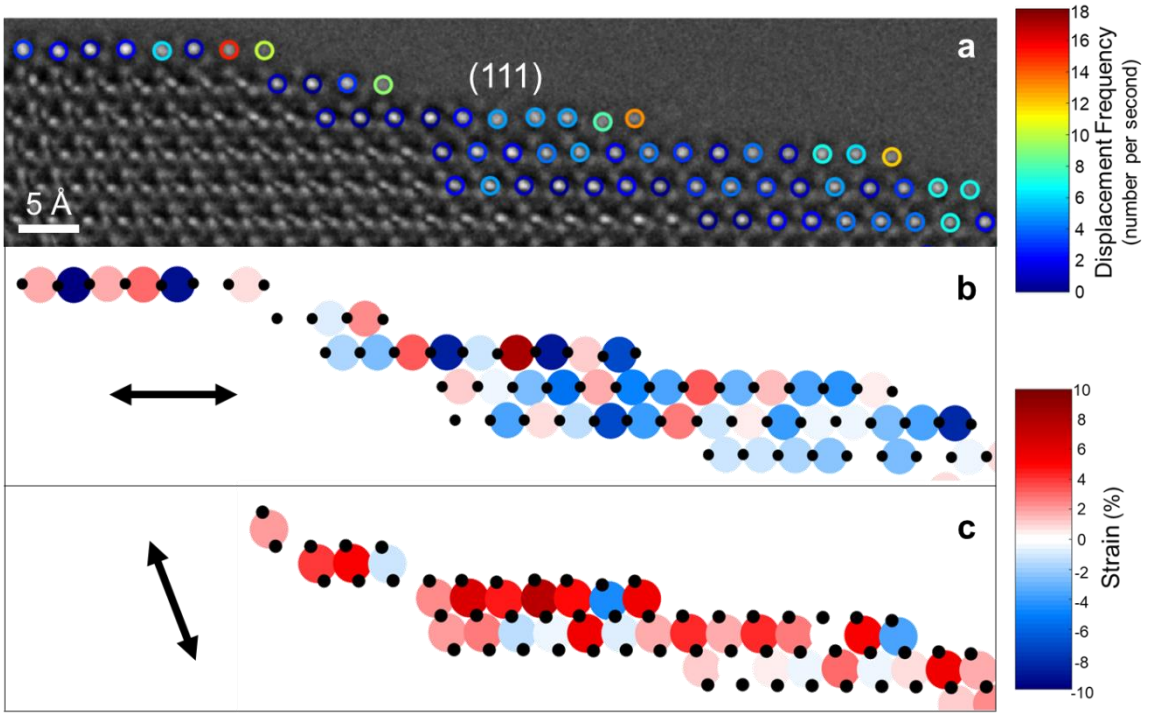

Figure 6.2. (a) Displacement frequency at different atomic sites on CeO_2 stepped (111) surface. (b) and (c) Atomic resolution strain maps of the stepped (111) surface in (a). Black points indicate atomic column positions. Double sided black arrows indicate direction that strain was measured in. Colored circles represent the local lattice strain between two corresponding atomic columns and are centered between the two atomic columns. The error bar for strain measurements was ~1.2%.

Figure 6.3 shows the comparison between the displacement frequency measurements and strain maps of the (110) CeO_2 nanofacet that was analyzed in Figure 4.10. As discussed in Section 4.3.4 and shown in Figure 6.3a, the atomic columns on this

surface show a large displacement frequency, especially the two surface columns that are displaced ~16-18 times that consist of single adatoms. On this (110) nanofacet, each atomic column that shows a high displacement frequency in Figure 6.3a also corresponds to a large value of compressive or tensile strain in Figure 6.3b,c. The two adatom sites that have the highest displacement frequency display the large compressive and tensile strain in both directions.

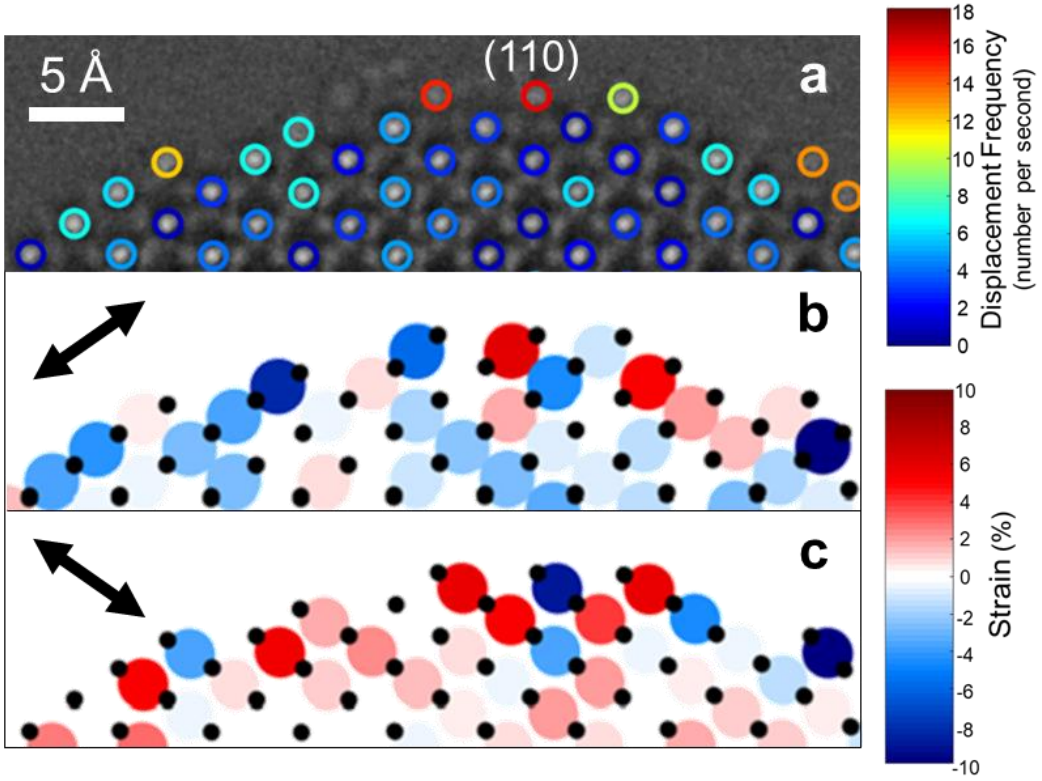

Figure 6.3. (a) Displacement frequency at different atomic sites on CeO_2 (110) nanofacet. (b) and (c) Atomic resolution strain maps of the stepped (111) surface in (a). Black points indicate atomic column positions. Double sided black arrows indicate direction that strain was measured in. Colored circles represent the local lattice strain between two corresponding atomic columns and are centered between the two atomic columns. The error bar for strain measurements was ~1.2%.

Displacement frequencies were determined for the image sequence used to create the summed image in Figure 6.1 using the method described in Chapter 4, and the

displacement frequency results are shown in Figure 6.4a. The strain maps for two different crystallographic directions for this image are shown in Figure 6.4b,c, where the black points indicate the atomic column positions, colored circles centered between two atomic columns indicate the corresponding local strain, and the double sided black arrows indicate the corresponding direction of strain. In general, the strain in Figure 6.4b was relatively tensile whereas Figure 6.4c was relatively compressive. The (111) facet that showed the highest displacement frequency in Figure 6.4a also shows the largest magnitude of strain in Figure 6.4b,c. The step edge sites on the (111) and (100) surfaces display relatively higher strains compared to the bulk strain values; however, the step edge sites on the (110) surface that show high displacement frequencies are relatively unstrained. In Figure 6.4b, the overall strain behavior is relatively tensile whereas the overall strain in Figure 6.4c is relatively compressive. Relative to the (111) surface, the overall in-plane strain of Figure 6.4b is tensile whereas the (111) in-plane strain in Figure 6.2 is generally compressive, with the cross-plane strain showing the same relative contrasting behavior.

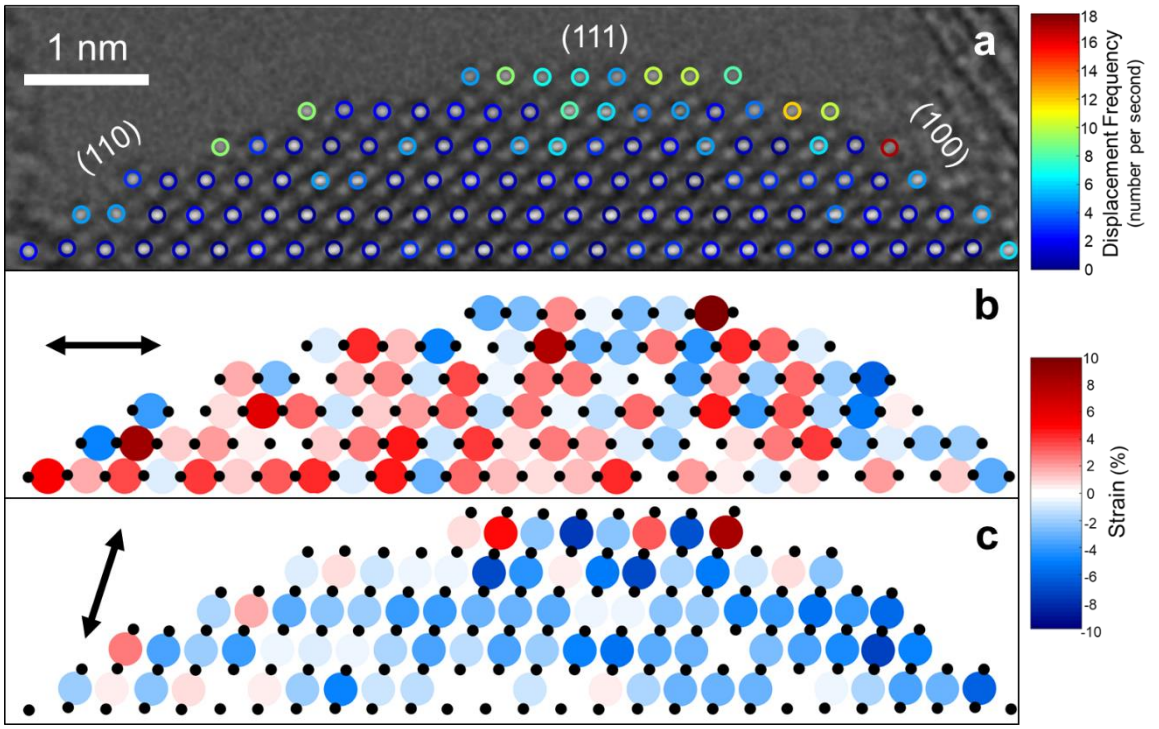

Figure 6.4. (a) Displacement frequency of atomic columns in the image sequence used to create the integrated (1 s) AC-TEM image of Figure 1. (b) and (c) Atomic resolution strain maps of the stepped (111) surface in (a) spanning from -10% (blue) to 10% (red). Black points indicate atomic column positions. Double sided black arrows indicate the direction that strain was measured in. Colored circles represent the local lattice strain between two corresponding atomic columns and are centered between the two atomic columns. The error bar for strain measurements was ~2%.

6.3.3 Relationship between Local Strain and Displacement Frequency

Based on the results of Figure 6.2-4, it can be concluded that there is a large degree of local strain and displacement heterogeneity present at the surfaces of CeO_2 nanoparticles. In addition, the results suggest that atomic sites that are severely strained in at least one direction will generally display higher displacement frequencies; however, high displacement frequencies do not necessarily imply large local strain. Local strain may therefore enhance the surface oxygen vacancy creation rate but isn't necessarily a result of high vacancy creation rates. It is also important to note that displacement frequency is a

time-resolved measurement whereas strain maps were determined from the integrated 1 s image sequences. Measurement of time-resolved strain maps may provide additional insights and enable characterization of possible dynamic strain fields near structural heterogeneities. The preliminary results presented in this chapter ultimately suggest that atomic column displacement frequency and surface oxygen vacancy creation rates are related to local strain; however, the relationship may be a complex function of site type, facet length and stability, thickness, and surface type.

6.4 Summary

Atomic resolution measurements of lattice strain were made on CeO_2 nanoparticle surfaces to produce local strain maps. The strain heterogeneities on different types of surfaces were compared to atomic column displacements, which provides an indicator of oxygen vacancy creation and annihilation. The observations suggest that strain enhances the ability of a surface to create oxygen vacancies, which can result in orders of magnitude differences in catalytic reaction rates. Additional observations would be beneficial to more precisely determine the complex relationship between local strain and oxygen exchange processes. Characterization of strain at the atomic-level may open additional avenues to better understand the catalytic properties of ceria surfaces.

7 Conclusions and Future Work

In this work, various atomic-level characterization techniques were developed and applied to relate the dynamic behavior of CeO_2 surface structures to the oxygen exchange processes. *In situ* aberration-corrected TEM techniques and novel analysis approaches enabled local structural heterogeneities to be correlated to macroscopic deactivation mechanisms and catalytic properties of ceria-based nanocatalysts. The overarching objective was to develop an atomic-level, fundamental understanding of how ceria-based materials influence and control oxygen exchange processes, a critical component for the continued development of energy-related, catalytic technologies.

The contrasting metal-support interactions occurring on Ni/SiO_2 and Ni/CeO_2 catalysts during ethane and ethene exposure were probed with *in situ* ETEM imaging and spectroscopy. It was revealed that the ceria support inhibited carbon formation on Ni metal nanoparticles through the removal of lattice oxygen and subsequent oxidation of adsorbed decomposed hydrocarbon products. Although this mechanism initially occurred during ethene exposure, the rate of decomposition was too fast for the ceria support to oxidize and remove the decomposition products, which resulted in graphite layers forming on Ni nanoparticles. In contrast, the decomposition of ethane was promoted at the Ni-ceria interface, which allowed the decomposition products to be rapidly oxidized by lattice oxygen of the ceria support and carbon formation to be inhibited on the Ni nanoparticles. The use of *in situ* environmental TEM imaging and STEM EELS enabled the observation of localized reduction zones of the ceria support near Ni nanoparticles, which confirmed that lattice oxygen from the support was participating in the carbon oxidation mechanism.

Therefore, oxygen exchange at Ni/ceria interfacial sites actively influenced carbon deposition during reforming and can show significant variation among different hydrocarbon species due to thermodynamic and kinetic considerations.

To investigate the role that surface structures have on the ability to form oxygen vacancies, atomic resolution observations of lattice oxygen vacancy creation and annihilation were performed on the surface of CeO_2 nanoparticles using a novel time-resolved *in situ* AC-TEM approach. Cation displacements were found to be related to oxygen vacancy creation and annihilation, and the most reactive surface oxygen sites were identified by monitoring the frequency of cation displacements. A considerable degree of diversity and heterogeneity in the type of surface sites that showed high activity was observed, with surface defects such as step edges, adatoms, and locally-strained terraces showing the highest displacement frequencies. By monitoring the rates of displacement and estimating occupancies of each atomic column, local activation energies of oxygen vacancy creation were estimated for each type of site. This approach allowed atomic structure to be experimentally linked with surface oxygen vacancy activity, providing a unique analysis tool for evaluating catalytic oxygen exchange processes.

The relationship between position/intensity measurement precision and temporal resolution of AC-TEM was explored by characterizing the dynamic behavior of CeO_2 nanoparticle surfaces with high temporal resolution, resulting in a combination of spatial precision (0.25 Å) and temporal resolution (2.5 ms) that has not previously been achieved before. The position and occupancy of each atomic column within a CeO_2 nanoparticle was determined in every frame of an image sequence, providing a time-resolved observation of

dynamic surface structures. As a result of the high temporal resolution, local lattice expansions and contractions were observed on a CeO_2 (100 surface, which have not previously been observed and are likely related to a cyclic oxygen vacancy creation and annihilation process. This significant improvement in the temporal resolution of atomic-level *in situ* imaging can accelerate understanding of how dynamic CeO_2 surface structures influence and control oxygen exchange processes.

Following the observation that locally-strained terraces exhibited high displacement frequencies and promoted increased oxygen vacancy creation on CeO_2 surfaces, atomic resolution strain measurements were performed to determine the effect of local strain on oxygen vacancy creation and annihilation. Local strain fields were found to vary significantly across CeO_2 nanoparticles. Atomic sites that were severely strained in at least one direction displayed high displacement frequencies; however, high displacement frequency sites did not necessarily exhibit local strain. This analysis suggested that local strain enhances the ability of a surface site to create oxygen vacancies, which may result in large differences of catalytic oxygen exchange reaction rates across a surface. Consequently, the application of local strain measurements to additional surfaces or interfaces may enable identification of highly active oxygen vacancy creation and annihilation sites.

By observing structural changes with advanced AC-TEM techniques, an improvement in the fundamental understanding of how ceria surfaces influence and control oxygen exchange reactions is demonstrated. The ability to accurately and quantitatively characterize structural heterogeneities provides an experimental link between surface

structure and functionality, which demonstrates that the correlation between dynamic surface structure and oxygen vacancies must be considered for the rational design of catalytic oxygen exchange nanomaterials.

Many fundamental questions remain about the atomic-level reaction and deactivation mechanisms on ceria-based catalyst nanomaterials. In Chapter 3, it was shown that local interfacial interactions were responsible for inhibiting carbon deposition; however, the spatial extent of the Ni/CeO_2 interface properties are unknown. For example, if very large Ni nanoparticles are used, it is possible that the ceria support will be unable to inhibit carbon formation on Ni surfaces far away from the interfacial region. CeO_2-based materials are often used at elevated temperatures, in various partial pressures of oxygen, or under electrical bias, and it would therefore be useful to apply the approach described in Chapter 4 to correlate cation displacements to oxygen vacancy creation rates under these conditions. To further explore the relationship between measurement precision and temporal resolution, it would be useful to apply statistical modeling approaches to identify patterns in the large data sets of images presented in Chapter 5 to extract additional structural information. Finally, strain heterogeneities present on nanoparticle surfaces or metal-ceria interfaces can strongly influence the catalytic properties, and it would be beneficial to correlate local strain to oxygen exchange functionalities.

Therefore, future areas of study may include:

- Influence of metal nanoparticle size or metal-support interface length on the ability of a ceria support to inhibit carbon deposition during hydrocarbon reforming reactions.

- A correlated study of cation displacements on ceria surfaces at elevated temperatures or various oxygen partial pressures to probe the Arrhenius behavior of oxygen vacancy creation.

- Big data analysis of dynamic surface structures observed on CeO_2 nanoparticles with high temporal resolution to identify prevalent structural motifs and correlate them to the most likely catalytically active surface structures.

- Extending the local strain and oxygen vacancy creation correlation to metal-ceria interfaces during catalytic reactions to probe the effect of interfacial sites.

- Observation of dynamic ceria surfaces under electrical bias and elevated temperature to enable the preferential migration of oxygen and deliberately deplete or increase the local concentration of oxygen vacancies at a surface.

8 Appendix

8.1 Additional Images of Structural Changes of Ni/CeO_2 during exposure to C_2H_4 and C_2H_6

In Chapter 3, Ni/CeO_2 nanocube catalysts were observed to undergo structural changes during exposure to C_2H_4 and C_2H_6. When exposed to C_2H_4, graphite layers formed on the Ni catalyst nanoparticles while the CeO_2 support remained in a crystalline form. In contrast, the Ni nanoparticles remained free of graphite when exposed to C_2H_6; however, the CeO_2 support transformed into a reduced amorphous ceria phase. These structural changes are shown in Figures 3.6 and 3.7, and additional images of these structural behaviors are shown in Figure 8.1 and Figure 8.2.

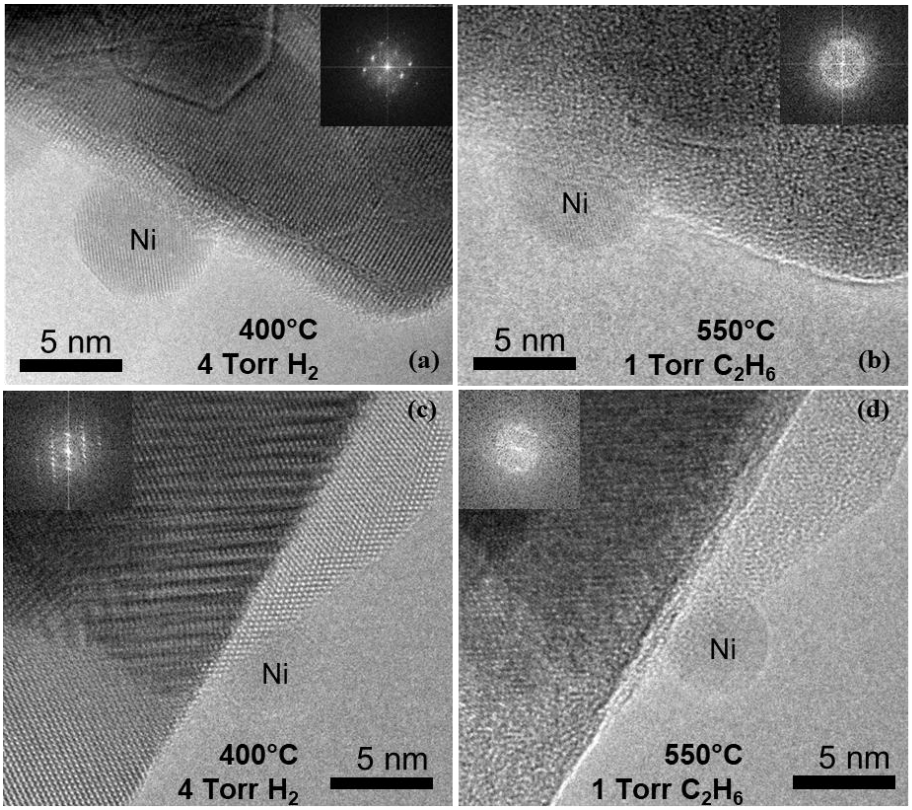

Figure 8.1. Effect of C_2H_6 exposure on CeO_2 structure. (a) & (c) are images recorded in 4 Torr of H_2 at 400°C. (b) & (d) are recorded at 550°C in 1 Torr C_2H_6 (following ½ hour of

exposure) and show the transformation from a crystalline ceria support to a reduced amorphous ceria phase. Insets are FFTs from the ceria support.

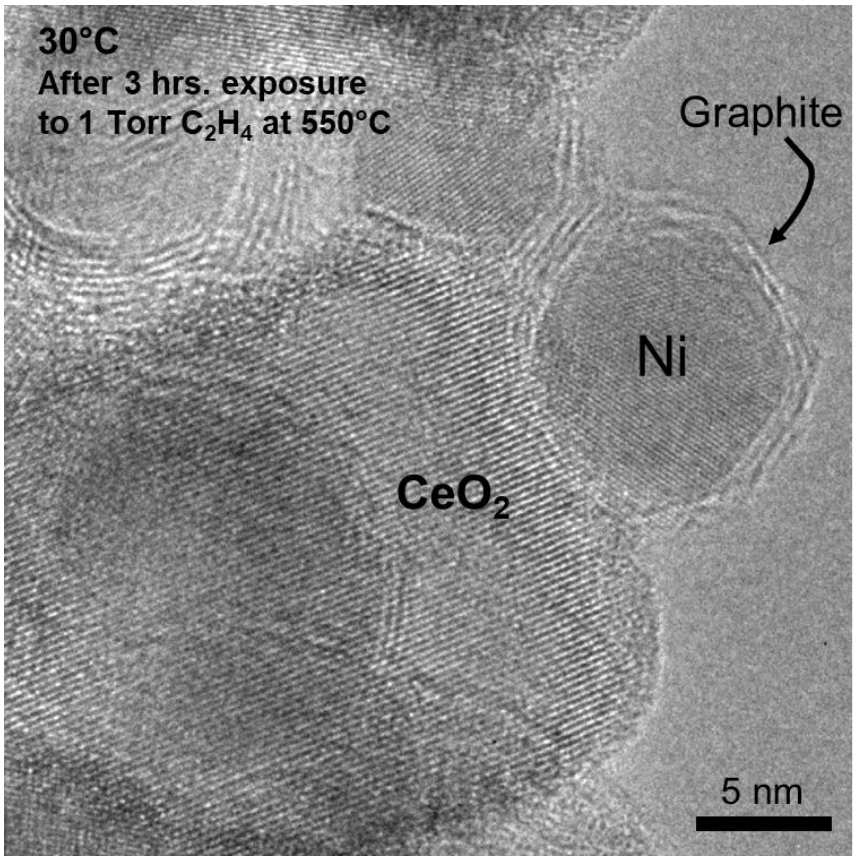

Figure 8.2. Effect of C_2H_4 exposure on Ni/CeO_2 structure. Image is taken at room temperature after 3 hours exposure to C_2H_4 at 550°C. Graphite layers have encapsulated the Ni nanoparticle while the CeO_2 structure remained crystalline.

8.2 Image Processing Procedure

The following provides the image processing procedure that was used in Chapters 4-6.

For each experiment, original 'raw' images of size *n* x *n* pixels were acquired. For each image, the intensity of each individual pixel is defined as $I_{i,j}$ where i,j represents the spatial coordinates of the pixel.

Original images were binned spatially by 2, which makes a new image of size *m* x *m* pixels where *m* = *n*/2. The intensity of each individual pixel in the binned image can then be defined as $I_{e,f}^{Bin} = I_{i,j} + I_{i+1,j} + I_{i,j+1} + I_{i+1,j+1}$ where e,f represent the new spatial coordinates of the pixel.

A Gaussian Blur filter with a 1-pixel radius was then applied to the image in ImageJ. This has the effect of convolving the image with a two-dimensional Gaussian function and acts as a low-pass filter, which attenuates high frequency signals. After the filter is applied, the intensity of each individual pixel is defined as $I_{e,f}^{G} = f\left(I_{e,f}^{Bin}\right)$ where $f(x)$ is the Gaussian function.

A region of the image that has no sample information in it is then defined as the vacuum area with k_{vac} total pixels. The mean vacuum intensity value is then defined as $\bar{I}_{vac} = \frac{\sum_{vac} I_{e,f}^{G}}{k_{vac}}$.

The image is then normalized by dividing each individual pixel by the mean vacuum intensity value. This is given by: $I_{e,f}^{norm} = \frac{I_{e,f}^{G}}{\bar{I}_{vac}}$.

For images with bright atom contrast such as those in Chapter 4 and 6, the images with intensity $I_{e,f}^{norm}$ were then input into MATLAB for analysis.

For images with dark atom contrast such as those in Chapter 5, the images were inverted to transform them into bright atom contrast. This was done through the following operation: $I_{e,f}^{invert} = 1 - I_{e,f}^{norm}$.

8.3 Additional Molecular Statics (MS) and TEM Image Simulations of Various Oxygen Vacancy Motifs

In Chapter 4, MS and TEM image simulations were used to determine the sensitivity of an image to 3D cation displacements induced by oxygen vacancies. Additional vacancy configurations were also investigated and are included here. In Figure 8.3, MS simulations of a fully-oxidized, a single oxygen vacancy, and a two-vacancy structure on an 8-atom thick slab of a CeO_2 (111) surface step are shown in the top row. The upper horizontal line and the left vertical line intersect at the center of the Ce atomic column at the step edge in the fully-oxidized structure. Following the introduction of an oxygen vacancy, Ce atoms within the adjacent atomic column are displaced by up to ~30 pm which causes the projected view of the Ce atomic column to be displaced as shown by the horizontal/vertical line intersection in the vacancy structures. The lower horizontal line shown in the figures intersects the same atomic columns in the oxidized and single/double oxygen vacancy structures, indicating that the oxygen vacancy only causes a displacement in the local structure near the step edge. Image simulations of each structure were performed using microscope parameters identical to those used in experimental images. Noise was excluded from image simulations to provide "ideal" imaging conditions. In the second row, the intersection of the upper horizontal line and the left vertical line on the oxidized simulated image is centered on the atomic column at the step edge. The results show that a single vacancy causes a cation displacement of 10 pm and a double oxygen vacancy causes a displacement of 20 pm. To highlight the effect of oxygen vacancies on the simulated images, the third row in Figure 8.3 provides color overlay images where the oxidized structure image simulation is red, and the one/two oxygen vacancy structures are cyan. Features that are identical in each colored image appear as white, allowing unique

features to appear as red or cyan. In addition to simulations of a single and double oxygen vacancy at a CeO_2 (111) surface step site, the effects of single and double oxygen vacancies on a CeO_2 (111) surface terrace with 4 and 8 atom thick slabs were investigated. The results are shown in Figure 8.4 and Figure 8.5.

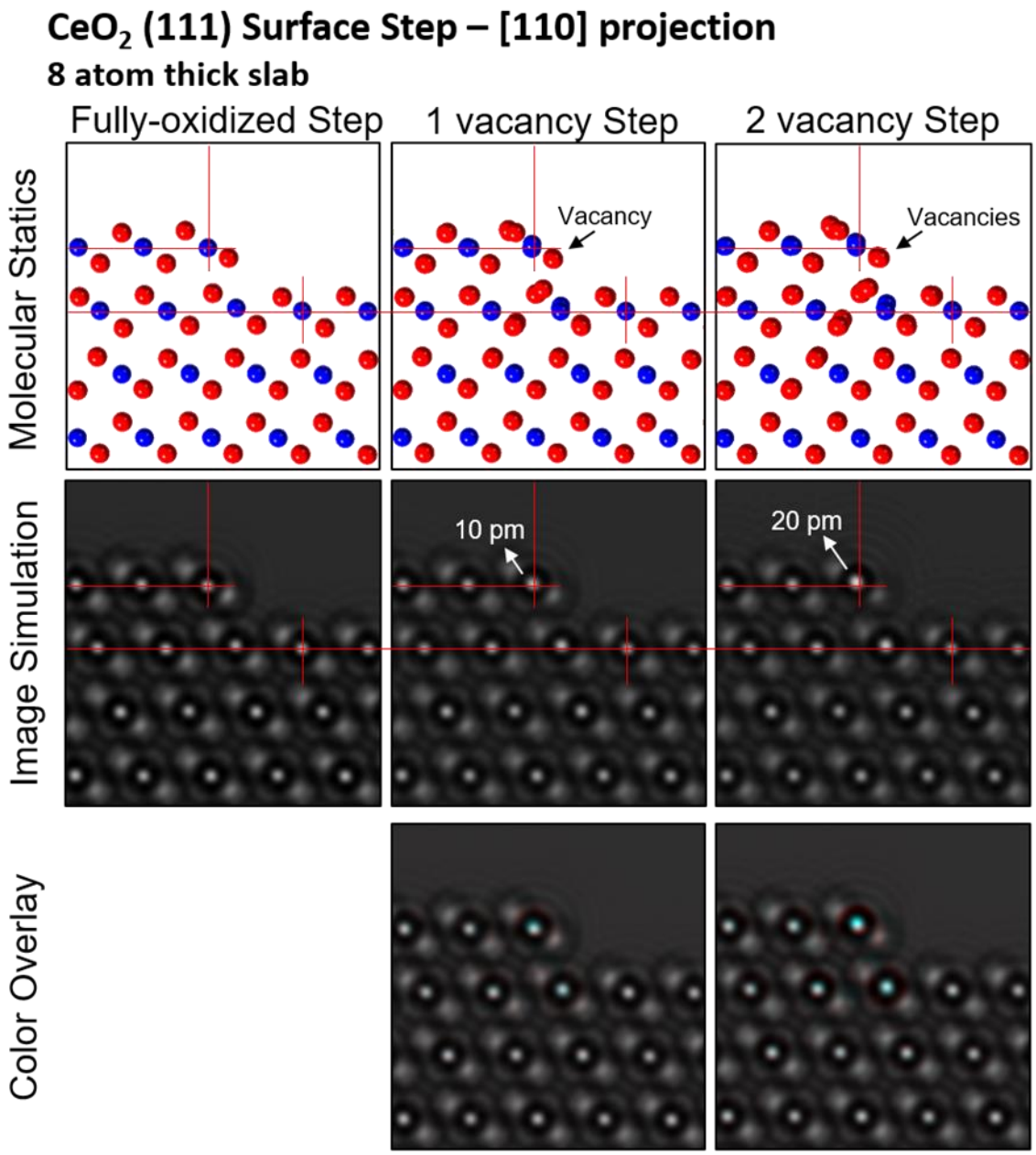

Figure 8.3. Image simulations of a CeO_2 (111) surface step edge that is fully oxidized vs. a single and double oxygen vacancy at the step edge site with an 8-atom thick slab. The step edge atomic column has shifted by 10 pm when a single oxygen vacancy is present at the step edge and 20 pm when a double oxygen vacancy is present. The bottom row provides a color overlay where red is the fully-oxidized image and cyan is either the single or double oxygen vacancy simulated image. Identical features appear white, and distinct red and cyan features illustrate shifts in column positions.

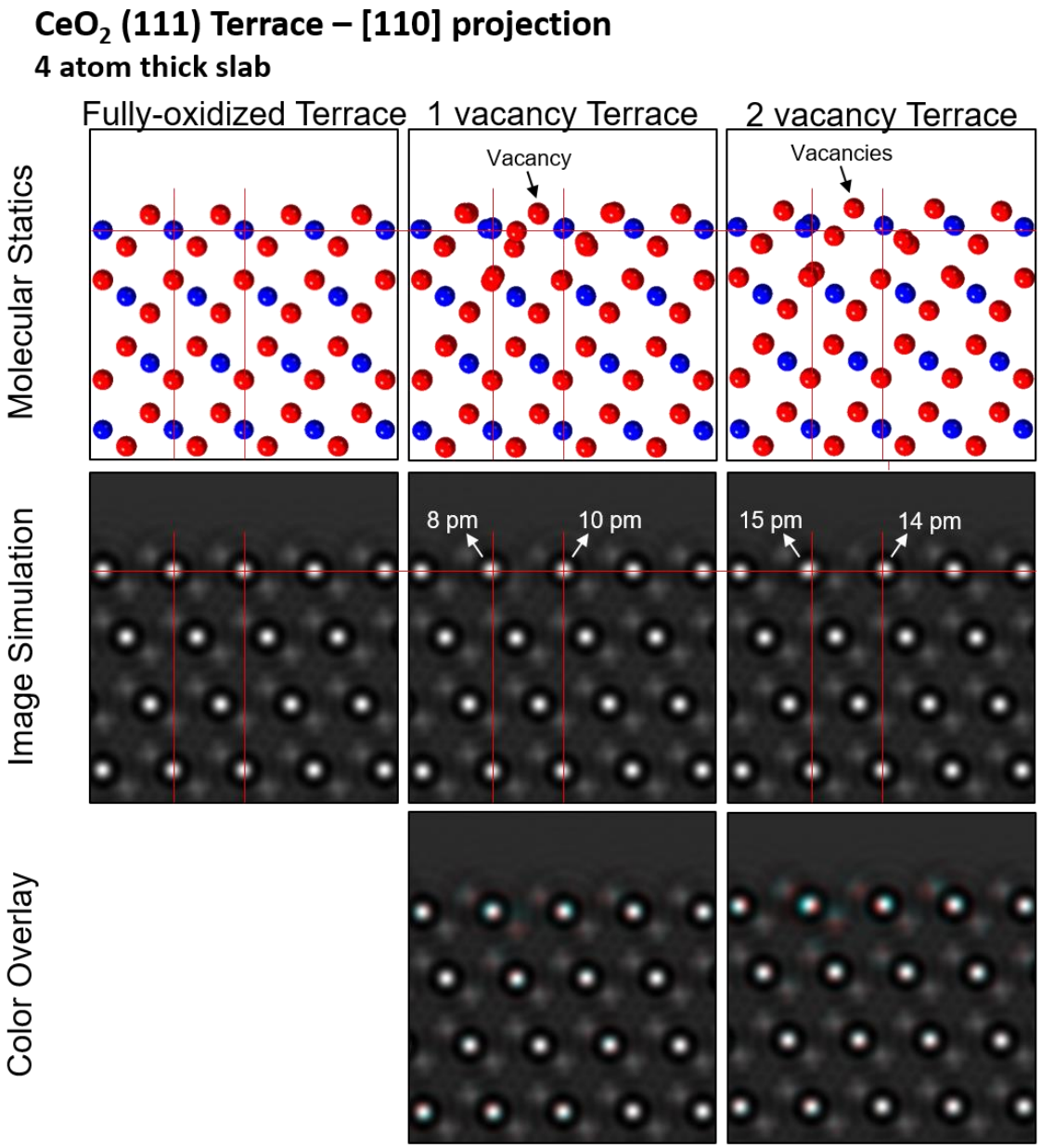

Figure 8.4. Image simulations of a CeO_2 (111) surface terrace that is fully oxidized vs. a single and double oxygen vacancy at the step edge site with a 4-atom thick slab. The two surface atomic columns adjacent to the vacancy have shifted by ~10 pm when a single oxygen vacancy is present and ~15 pm when a double oxygen vacancy is present. The bottom row provides a color overlay where red is the fully-oxidized image and cyan is either the single or double oxygen vacancy simulated image. Identical features appear white, and distinct red and cyan features illustrate shifts in column positions.

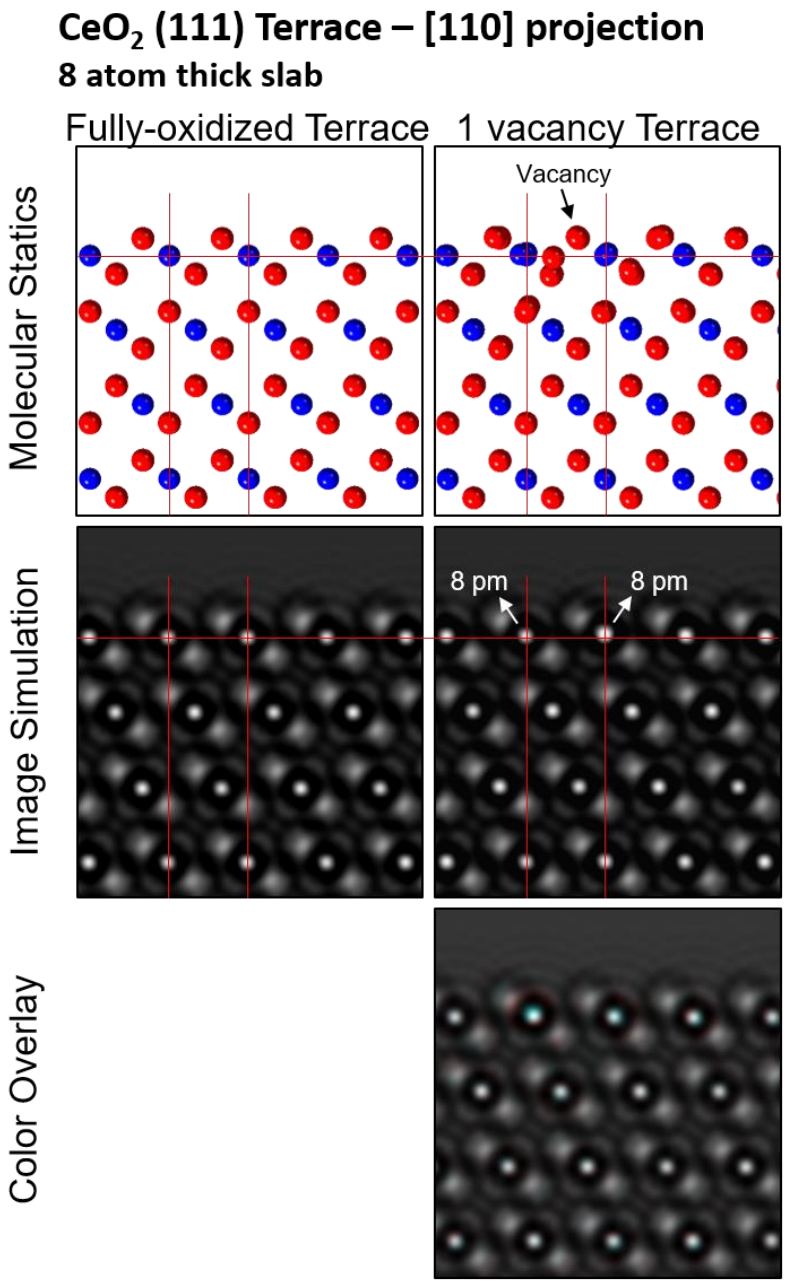

Figure 8.5. Image simulations of a CeO_2 (111) surface terrace that is fully oxidized vs. a single and double oxygen vacancy at the step edge site with an 8-atom thick slab. The two surface atomic columns adjacent to the vacancy have shifted by ~8 pm when a single oxygen vacancy is present. The bottom row provides a color overlay where red is the fully-oxidized image and cyan is the single oxygen vacancy simulated image. Identical features appear white, and distinct red and cyan features illustrate shifts in column positions.

8.4 Additional Quantification of Dynamic CeO_2 Surface Structures

The experiment of Chapter 5 had an electron flux (120,000 $e^-Å^{-2}s^{-1}$) that was much higher than Chapter 4 (5,000 $e^-Å^{-2}s^{-1}$). As a result, the displacement rates of oxygen and cerium atoms by knock-on damage and radiolytic displacement were higher, as shown in Figure 8.6. The plots in Figure 8.6 are based on the derivations in Section 4.3.3 and Equations (4.1, 4.10, 4.13, 4.17, and 4.19).

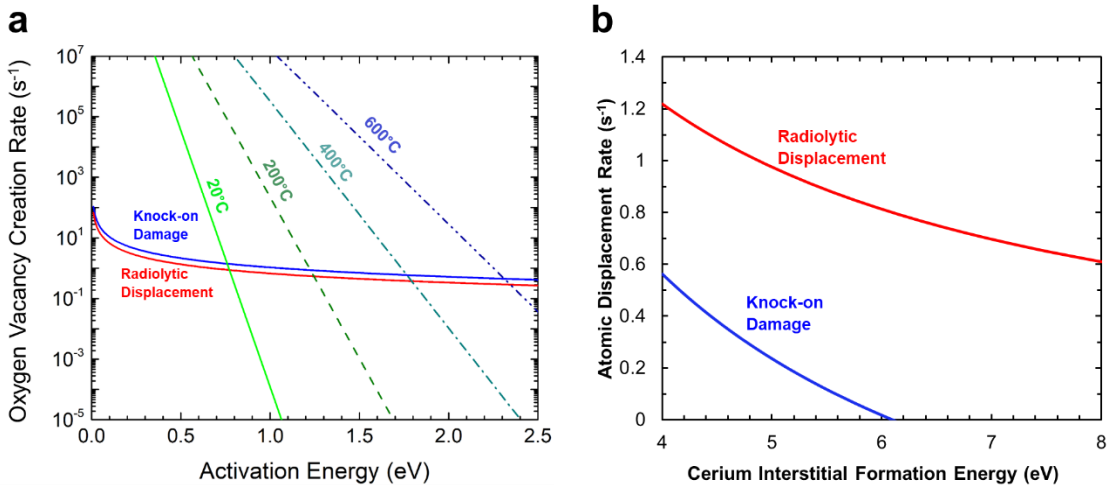

Figure 8.6. (a) Oxygen vacancy creation rates based on derivation in Section 4.3.3 with an electron flux of 120,000 $e^-Å^{-2}s^{-1}$. (b) Displacement rate of Ce atoms by knock-on damage and radiolytic displacement based on derivation in Section 4.3.3 with an electron flux of 120,000 $e^-Å^{-2}s^{-1}$.

A local lattice expansion and contraction was observed on the CeO_2 (100) surface in Chapter 3, and an additional occurrence of this behavior is shown in Figure 8.7. In Figure 8.7, the two surface cation columns have contracted to 3.63 Å and then expand to 4.74 Å in Figure 8.7b. A third atomic column appears when the expansion occurs in Figure 8.7, which is opposite to the behavior of Figure 5.5 where a third surface (100) atomic column disappears when the same two atomic columns expand apart. The two atomic columns contract back to 3.68 Å after ~0.4 s as shown in Figure 8.7c. It is hypothesized that this

local expansion and contract behavior is related to a cyclic oxygen vacancy creation and annihilation process, although additional experiments and theoretical simulations would be needed to confirm this hypothesis.

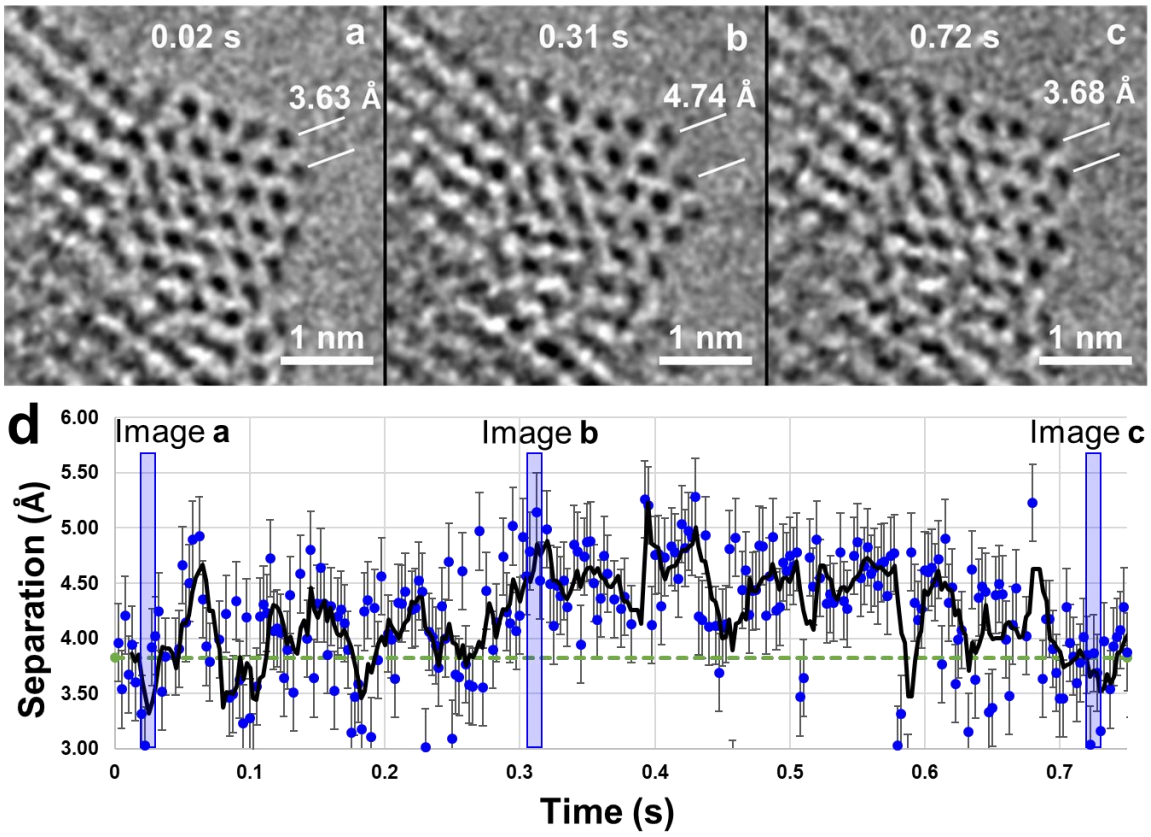

Figure 8.7. Local surface lattice expansion. (a-c) Image sequence of the CeO_2 nanoparticle with 12.5 ms exposure images (five spatially binned and Gaussian blurred 2.5 ms images summed together). Two Ce atomic columns on the (100) surface are separated by 3.63 Å at 0.02 s in (a), expand to 4.74 Å after 0.31 s in (b), and contract to 3.68 Å after 0.72 s in (c). (d) Measurement of the separation of the two marked surface Ce atomic column over 0.5 s image sequence. The blue points indicate measurements from each frame, the solid black line is a 5-frame moving average trendline, and the dashed green line indicates the bulk-terminated (100) separation distance (3.825 Å). Error bars are 0.35 Å. The semitransparent blue windows represent the five image frames that were summed together to create (a-c).

Atomic column occupancy is characterized with 2.5 ms temporal resolution in Figure 5.7, with Figure 5.7a-c showing AC-TEM images of 12.5 ms exposure. Figure 8.8a

provides a summed image of the first 0.1 s of the 0.5 s image sequence from Figure 5.7 and Figure 8.8b provides a summed image of the final 0.1 s of the 0.5 s image sequence from Figure 5.7. Clearly, atoms have migrated out of atomic column 1 and into atomic column 2 in Figure 8.8, which highlights that the 2.5 ms temporal resolution of Figure 5.7 provides dynamic structural information that is unobtainable when using a 0.1 s exposure as in Figure 8.8.

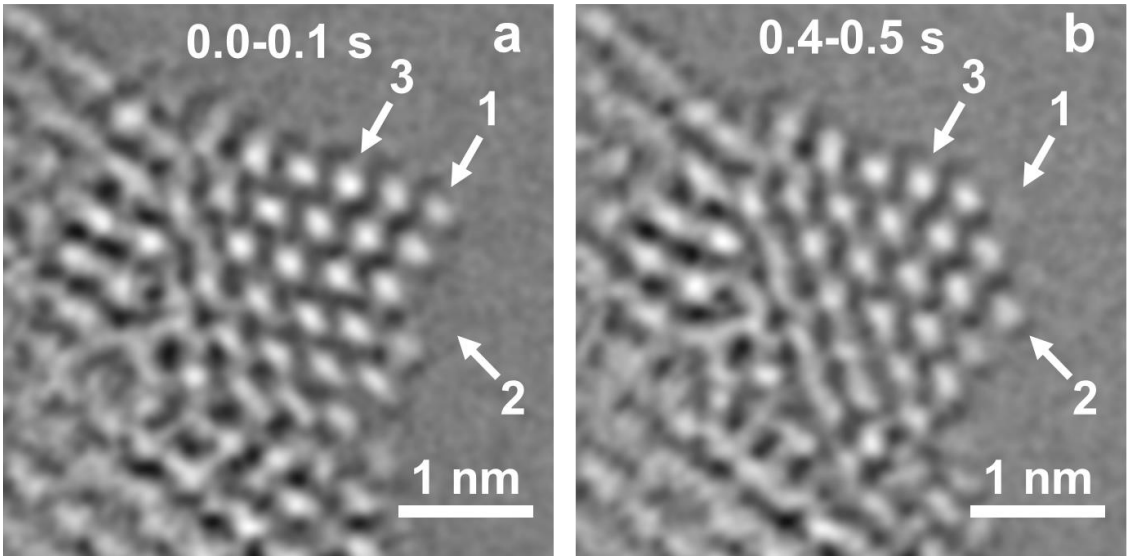

Figure 8.8. Atom migration. (a) 0.1 s exposure image (40 inverted 2.5 ms images summed together). As indicated by the "1", "2", and "3" labels, atoms are present at "1" and "3" but absent at "2". (b) 0.1 s exposure image (40 inverted 2.5 ms images summed together). As indicated by the labels, atoms are present at "2" and "3" but are absent at "1". Atoms have migrated during the 0.3 s between the two images.

In Figure 5.7, atomic column occupancies were estimated for three columns over a 0.5 s image sequence. In some frames, large spikes or drops in the estimated number of atoms were observed which may be caused by noise fluctuations; however, several of these dramatic changes in intensity were indicative of the real data. For example, in Figure 5.7d, there are two data points at ~0.4 s that are much higher than the surrounding data points.

The image frames that correspond to 0.3925 – 0.4075 s are shown in Figure 8.9. In Figure 8.9a, the number of atoms in 'atomic column 1' is shown over the 0.5 s image sequence from Figure 5.7. The transparent red, blue, and green boxes represent the 7.5 ms exposure frames that are shown in Figure 8.9b-d, respectively. The large spike in the estimated number of atoms at ~0.4 s is shown in Figure 8.9b-d to be real and due to atoms migrating into and out of atomic column 1 over a short period of time.

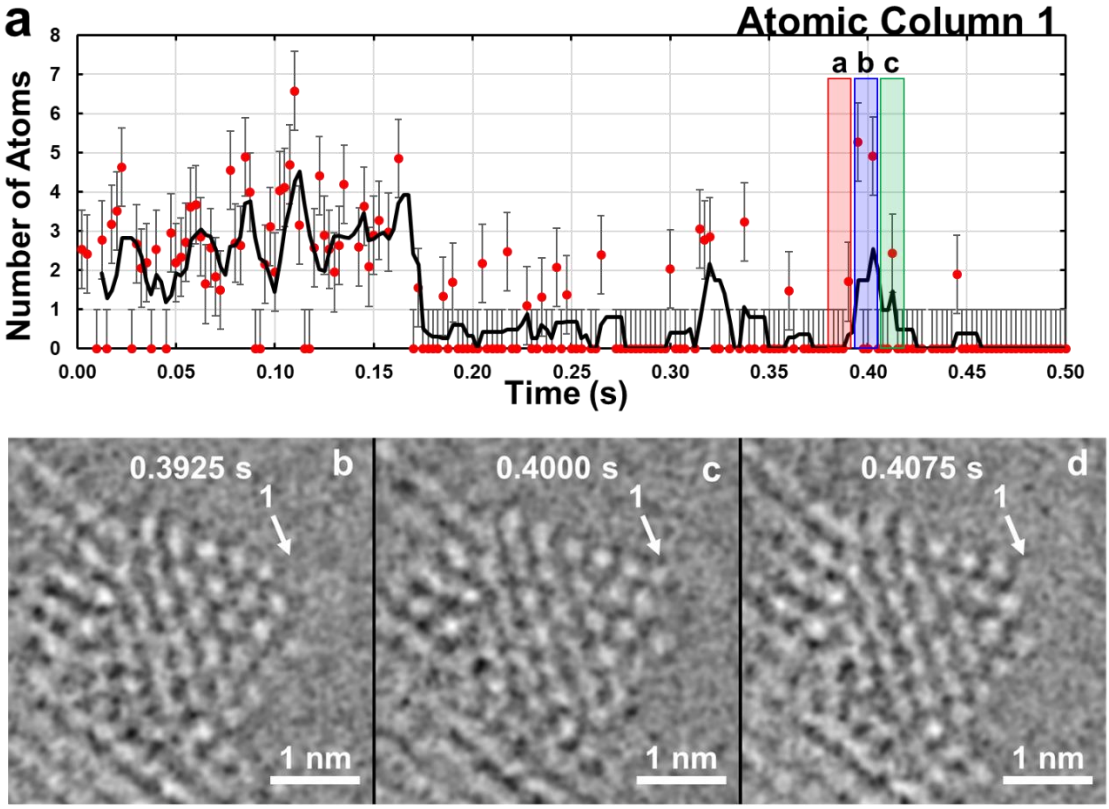

Figure 8.9. Fluctuation in atomic column occupancy. (a) number of atoms in atomic column 1. The points indicate measurements from each frame and the solid black line is a 5-frame moving average trendline. The semitransparent red, blue, and green windows represent the three image frames that were summed together to create (b-d), respectively. Error bars are ±1 atom. (b-d) Image sequence of the CeO_2 nanoparticle with 7.5 ms exposure images of the inverted images used for MATLAB analysis (three inverted 2.5 ms images summed together). Atoms are not present in atomic column 1 in (a), appear in (b), and are absent in (c).

8.5 Design of Heating and Biasing TEM Holder

Many of ceria's applications require the use of high temperature; in particular, when used in fuel cells, ceria is under electrochemical biasing and high temperature conditions. *In situ* TEM has been used to observe resistive switching effects in TiO_2 during electrical bias (Kamaladasa et al., 2015; Yang et al., 2014; Kwon et al., 2010). Oxygen vacancy ordering and resistive switching has also been observed in CeO_2 thin films under electrical bias (Gao, Wang, et al., 2010); however, no such observations have been made under electrical bias *and* high temperature. Additionally, almost complete removal of carbon in the electrochemically active region of ceria at high temperature was observed using *operando* XPS (Chunjuan Zhang et al., 2012). Although there are now commercially available TEM holders which advertise heating and biasing capabilities, there have been no successful publications of simultaneous heating and biasing with atomic resolution. Thus, to study CeO_2 electrolytes and cermets under electrochemical conditions with applications in carbon deposition and oxygen vacancy ordering, we are developing a custom-built heating/biasing TEM sample holder.

Design and Fabrication

A previous student, Dr. William Bowman, initially worked on this project and was responsible for the design and machining of the TEM sample rod. A prototype TEM sample rod was fabricated and initial sample attachment procedures were completed by Dr. Bowman. Figure 8.10 shows the schematics for the main components of the heating/biasing holder. Figure 8.10a highlights the sample area of the TEM holder. A heating/biasing chip (shown in Figure 8.10b) is attached to the sample rod using clamps and four wires contact

the chip, two for heating and two for biasing. A lamella is milled from a bulk sample using a Focused Ion Beam (FIB) lift-out method and is mounted across the 10 μm gap between the two isolated Pt electrodes, as seen in Figure 8.10b. A side view of the heating/biasing chip is shown in Figure 8.10c and highlights the layers that make up the chip. A Si wafer with 100 nm of SiO_2 was chosen as the platform. A thin Ti layer was used as an adhesion layer for the photo-deposited Pt electrodes. A Si-Chrome resist layer was deposited onto the backside of the wafer and acts as a heating element when current is applied. Ti-W contacts were deposited onto the Si-Chrome layer to facilitate a larger contact area when applying a voltage.

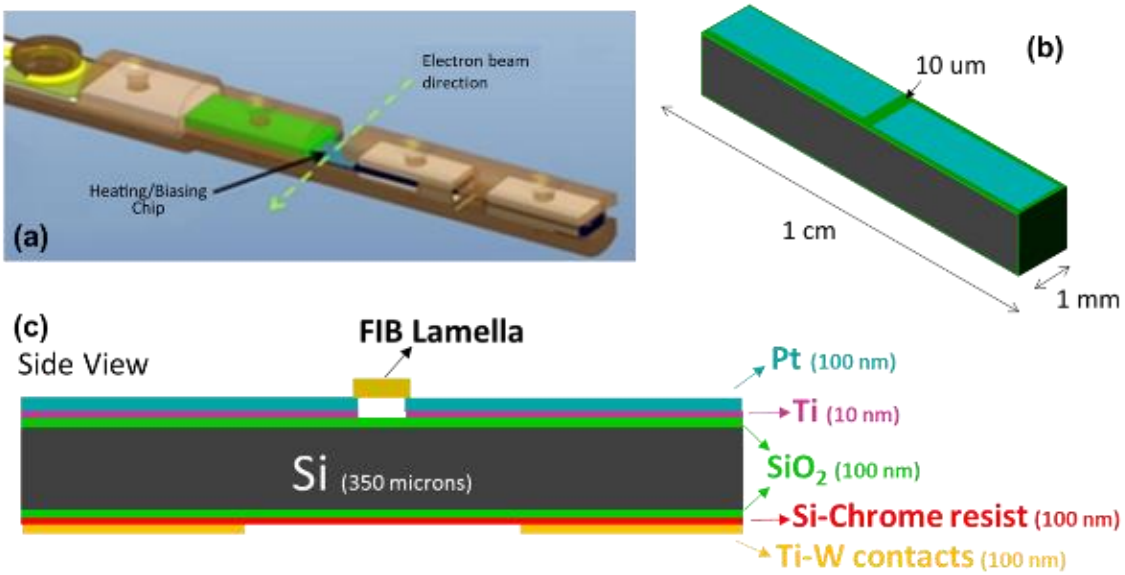

Figure 8.10. (a) Schematic of sample mounting area of TEM holder rod. (b) Top view of the heating/biasing chip. A FIB lamella will be mounted across the 10 μm gap. (c) Side view of heating/biasing chip. The sample side is responsible for electrical bias while the bottom side has Si-Chrome resist layer to provide heating.

Sample Preparation and Initial Results

A Nova 200 SEM-FIB (focused ion beam) system was used to cut out and mount a sample of Gd-doped ceria (GDC) onto the heating/biasing chip. Figure 8.11a shows an SEM image of a blank chip. The light regions are Pt electrodes and the thin black line between them is the 10 μm gap. A lamella was milled out from a GDC electrolyte pellet and mounted across the gap with Pt deposited with the ion beam. The center region was then thinned to produce an electron transparent region suitable for imaging and the resulting lamella is shown in Figure 8.11b. The heating/biasing chip was attached to the TEM sample rod and inserted into an FEI Tecnai TEM for initial observations. A low-magnification image of the lamella is shown in Figure 8.12a. The large black pillars are thick regions of GDC and deposited Pt used to mount the lamella. A higher-magnification image with visible GDC lattice fringes is shown in Figure 8.12b. These images were acquired in vacuum and at room temperature; however, application of heat and bias will be performed in future experiments.

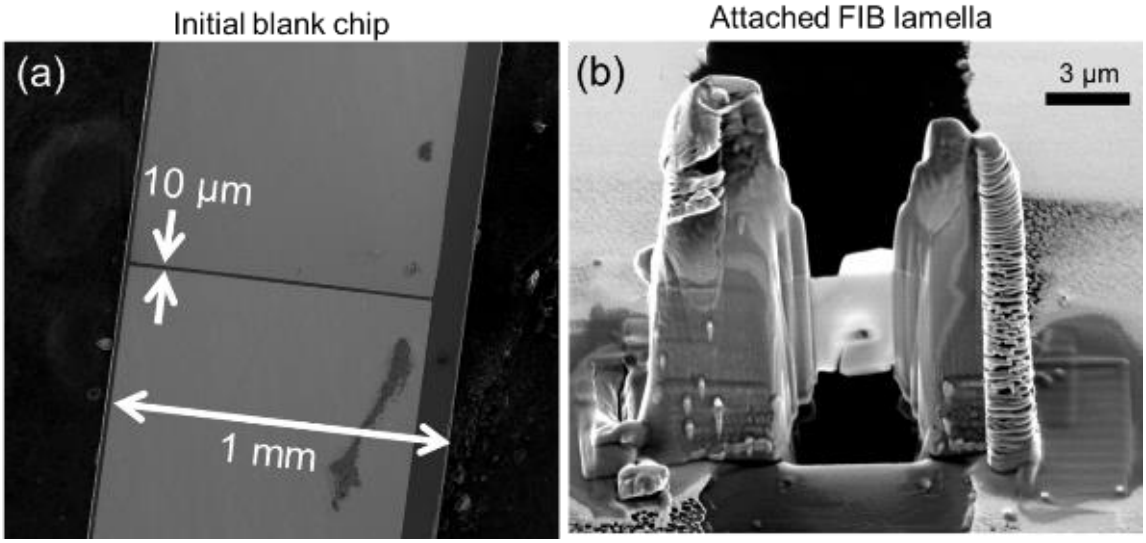

Figure 8.11. (a) SEM image of a blank heating/biasing chip. The thin black line indicated by the small white arrows is the 10 μm gap where the lamella will be mounted. The light-

colored regions are the Pt electrodes. (b) An attached FIB lamella that has been thinned in the center to be electron-transparent.

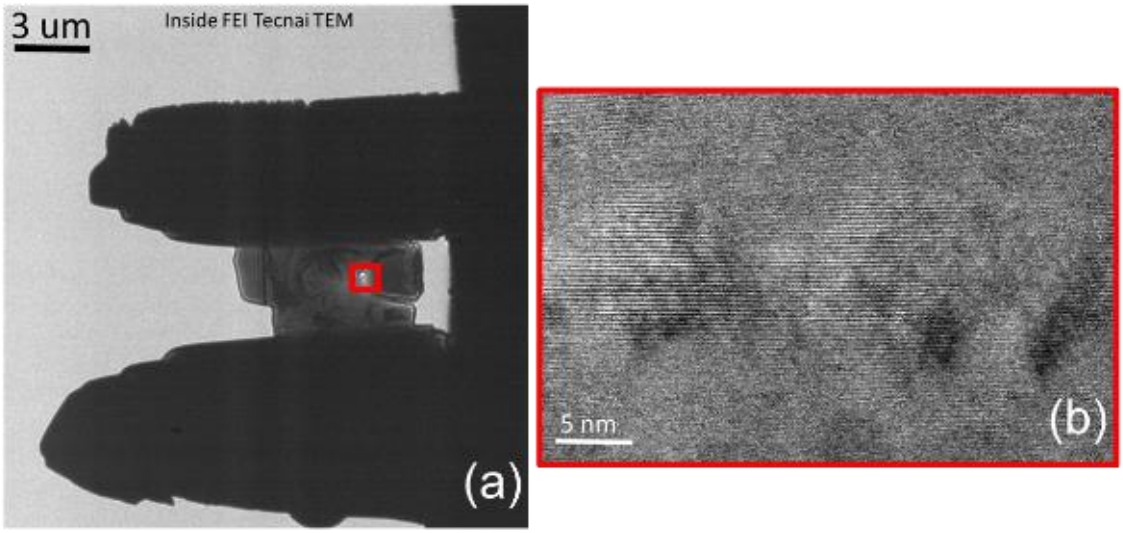

Figure 8.12. (a) Low-mag TEM image of the FIB lamella. The large pillars are Gd-doped ceria and deposited Pt. The small region in the center is the ion-milled thin region. (b) High-mag TEM image with visible GDC lattice fringes from the region highlighted by the red box in (a).

9 References

ABATZOGLOU, N. & FAUTEUX-LEFEBVRE, C. (2016). Review of catalytic syngas production through steam or dry reforming and partial oxidation of studied liquid compounds: Review of catalytic syngas production. *Wiley Interdisciplinary Reviews: Energy and Environment* **5**, 169–187.

ADACHI, G. & IMANAKA, N. (1998). The Binary Rare Earth Oxides. *Chemical Reviews* **98**, 1479–1514.

ADLER, S. B. (2004). Factors Governing Oxygen Reduction in Solid Oxide Fuel Cell Cathodes †. *Chemical Reviews* **104**, 4791–4844.

ADLER, S., CHEN, X. & WILSON, J. (2007). Mechanisms and rate laws for oxygen exchange on mixed-conducting oxide surfaces. *Journal of Catalysis* **245**, 91–109.

AGARWAL, S., LEFFERTS, L., MOJET, B. L., LIGTHART, D. A. J. M., HENSEN, E. J. M., MITCHELL, D. R. G., ERASMUS, W. J., ANDERSON, B. G., OLIVIER, E. J., NEETHLING, J. H. & DATYE, A. K. (2013). Exposed Surfaces on Shape-Controlled Ceria Nanoparticles Revealed through AC-TEM and Water-Gas Shift Reactivity. *ChemSusChem* **6**, 1898–1906.

AGARWAL, V. & METIU, H. (2016). Energy of Oxygen-Vacancy Formation on Oxide Surfaces: Role of the Spatial Distribution. *The Journal of Physical Chemistry C* **120**, 2320–2323.

AHMADI, M., MISTRY, H. & ROLDAN CUENYA, B. (2016). Tailoring the Catalytic Properties of Metal Nanoparticles via Support Interactions. *The Journal of Physical Chemistry Letters* **7**, 3519–3533.

AHN, C. C. (ed.) (2004). *Transmission electron energy loss spectrometry in materials science and the EELS atlas*. 2nd ed. Weinheim, Germany: Wiley.

AKIN, F. T. & LIN, Y. S. (2002). Selective oxidation of ethane to ethylene in a dense tubular membrane reactor. *Journal of Membrane Science* **209**, 457–467.

ALCOCK, C. B. (1993). Thermodynamic and transport properties of electroceramic oxide systems. *Journal of Alloys and Compounds* **197**, 217–227.

ANDERSSON, D. A., SIMAK, S. I., SKORODUMOVA, N. V., ABRIKOSOV, I. A. & JOHANSSON, B. (2006). Optimization of ionic conductivity in doped ceria. *Proceedings of the National Academy of Sciences of the United States of America* **103**, 3518–3521.

ANDREEVA, D., IDAKIEV, V., TABAKOVA, T., ILIEVA, L., FALARAS, P., BOURLINOS, A. & TRAVLOS, A. (2002). Low-temperature water-gas shift reaction over Au/CeO_2 catalysts. *Catalysis Today* **72**, 51–57.

ANEGGI, E., BOARO, M., COLUSSI, S., DE LEITENBURG, C. & TROVARELLI, A. (2016). Chapter 289 - Ceria-Based Materials in Catalysis: Historical Perspective and Future Trends. In *Handbook on the Physics and Chemistry of Rare Earths*vol. 50, Bünzli, J.-C. G. & Pecharsky, V. K. (Eds.), pp. 209–242. Elsevier http://linkinghub.elsevier.com/retrieve/pii/S0168127316300046 (Accessed October 25, 2017).

ANEGGI, E., LLORCA, J., BOARO, M. & TROVARELLI, A. (2005). Surface-structure sensitivity of CO oxidation over polycrystalline ceria powders. *Journal of Catalysis* **234**, 88–95.

ANEGGI, E., WIATER, D., DE LEITENBURG, C., LLORCA, J. & TROVARELLI, A. (2014). Shape-Dependent Activity of Ceria in Soot Combustion. *ACS Catalysis* **4**, 172–181.

ANGELI, S. D., MONTELEONE, G., GIACONIA, A. & LEMONIDOU, A. A. (2014). State-of-the-art catalysts for CH_4 steam reforming at low temperature. *International Journal of Hydrogen Energy* **39**, 1979–1997.

ANGELI, S. D., PILITSIS, F. G. & LEMONIDOU, A. A. (2015). Methane steam reforming at low temperature: Effect of light alkanes' presence on coke formation. *Catalysis Today* **242**, 119–128.

ANGOUA, B. F. & SLAMOVICH, E. B. (2012). Single solution spray pyrolysis of $La_{0.6}Sr_{0.4}Co_{0.2}0.Fe_{0.8}O_{3-\delta}$–$Ce_{0.8}Gd_{0.2}O_{1.9}$ (LSCF–CGO) thin film cathodes. *Solid State Ionics* **212**, 10–17.

ARMSTRONG, E. N., DUNCAN, K. L. & WACHSMAN, E. D. (2013). Effect of A and B-site cations on surface exchange coefficient for ABO_3 perovskite materials. *Physical Chemistry Chemical Physics* **15**, 2298.

ARYANPOUR, M., KHETAN, A. & PITSCH, H. (2013). Activity Descriptor for Catalytic Reactions on Doped Cerium Oxide. *ACS Catalysis* **3**, 1253–1262.

AY, H. & ÜNER, D. (2015). Dry reforming of methane over CeO_2 supported Ni, Co and Ni–Co catalysts. *Applied Catalysis B: Environmental* **179**, 128–138.

BAKER, R. T. K. (1979). In Situ Electron Microscopy Studies of Catalyst Particle Behavior. *Catalysis Reviews* **19**, 161–209.

BAKER, R. T. K., BARBER, M. A., HARRIS, P. S., FEATES, F. S. & WAITE, R. J. (1972). Nucleation and growth of carbon deposits from the nickel catalyzed decomposition of acetylene. *Journal of catalysis* **26**, 51–62.

BAKER, R. T. K. & HARRIS, P. S. (1972). Controlled atmosphere electron microscopy. *Journal of Physics E: Scientific Instruments* **5**, 793–797.

BALAJI GOPAL, C., GARCÍA-MELCHOR, M., LEE, S. C., SHI, Y., SHAVORSKIY, A., MONTI, M., GUAN, Z., SINCLAIR, R., BLUHM, H., VOJVODIC, A. & CHUEH, W. C. (2017). Equilibrium oxygen storage capacity of ultrathin $CeO_{2-\delta}$ depends non-monotonically on large biaxial strain. *Nature Communications* **8**, 15360.

BALS, S., AERT, S. V., TENDELOO, G. V. & ÁVILA-BRANDE, D. (2006). Statistical Estimation of Atomic Positions from Exit Wave Reconstruction with a Precision in the Picometer Range. *Physical Review Letters* **96**, 096106.

BALS, S., GORIS, B., DE BACKER, A., VAN AERT, S. & VAN TENDELOO, G. (2016). Atomic resolution electron tomography. *MRS Bulletin* **41**, 525–530.

BANERJEE, R., CHENNA, S. & CROZIER, P. (2009). Nanocharacterization and Control of Supported Ni Nanocatalysts for Partial Oxidation of Methane. *Microscopy and Microanalysis* **15**, 732–733.

BARTHEL, J. & THUST, A. (2008). Quantification of the Information Limit of Transmission Electron Microscopes. *Physical Review Letters* **101**, 200801.

BASARAN, D., ALEKSANDROV, H. A., CHEN, Z.-X., ZHAO, Z.-J. & RÖSCH, N. (2011). Decomposition of ethylene on transition metal surfaces M(111). A comparative DFT study of model reactions for M=Pd, Pt, Rh, Ni. *Journal of Molecular Catalysis A: Chemical* **344**, 37–46.

BATSON, P. E., DELLBY, N. & KRIVANEK, O. L. (2002). Sub-ångstrom resolution using aberration corrected electron optics. *Nature* **418**, 617–620.

BAUDIN, M., WÓJCIK, M. & HERMANSSON, K. (2000). Dynamics, structure and energetics of the (111), (011) and (001) surfaces of ceria. *Surface science* **468**, 51–61.

BERNAL, S., BLANCO, G., CALVINO, J. J., CIFREDO, G. A., OMIL, J. A. P., PINTADO, J. M. & VARA, A. (1994). HRTEM and TPO Study of the Behaviour under Oxidizing Conditions of some Rh/CeO_2 Catalysts. In *Studies in Surface Science and Catalysis*vol. 82, pp. 507–514. Elsevier https://linkinghub.elsevier.com/retrieve/pii/S0167299108634448 (Accessed March 3, 2019).

BERNAL, S., BLANCO, G., CALVINO, J. J., LÓPEZ-CARTES, C., PÉREZ-OMIL, J. A., GATICA, J. M., STEPHAN, O. & COLLIEX, C. (2001). Electron Microscopy (HREM, EELS) Study of the Reoxidation Conditions for Recovery of NM/CeO_2 (NM: Rh, Pt) Catalysts from Decoration or Alloying Phenomena. *Catalysis Letters* **76**, 7.

BERNAL, S., BOTANA, F. J., CALVINO, J. J., CIFREDO, G. A., PE´REZ-OMIL, J. A. & PINTADO, J. M. (1995). HREM study of the behaviour of a Rh/CeO_2 catalyst under high temperature reducing and oxidizing conditions. *Catalysis Today* **23**, 219–250.

BERNAL, S., CALVINO, J. J., CAUQUI, M. A., GATICA, J. M., LARESE, C., PÉREZ OMIL, J. A. & PINTADO, J. M. (1999). Some recent results on metal/support interaction effects in NM/CeO_2 (NM: noble metal) catalysts. *Catalysis Today* **50**, 175–206.

BERNAL, S., CALVINO, J. J., CAUQUI, M. A., GATICA, J. M., LÓPEZ CARTES, C., PÉREZ OMIL, J. A. & PINTADO, J. M. (2003). Some contributions of electron microscopy to the characterisation of the strong metal–support interaction effect. *Catalysis Today* **77**, 385–406.

BESCHNITT, S., ZACHERLE, T. & DE SOUZA, R. A. (2015). Computational Study of Cation Diffusion in Ceria. *The Journal of Physical Chemistry C* **119**, 27307–27315.

BEVAN, D. J. M. (1955). Ordered intermediate phases in the system CeO_2—Ce_2O_3. *Journal of Inorganic and Nuclear Chemistry* **1**, 49IN157–5659.

BEVAN, D. J. M. & KORDIS, J. (1964). Mixed oxides of the type MO_2 (fluorite)—M_2O_3—I oxygen dissociation pressures and phase relationships in the system CeO_2—Ce_2O_3 at high temperatures. *Journal of Inorganic and Nuclear Chemistry* **26**, 1509–1523.

BHATTA, U. M., REID, D., SAKTHIVEL, T., SAYLE, T. X. T., SAYLE, D., MOLINARI, M., PARKER, S. C., ROSS, I. M., SEAL, S. & MÖBUS, G. (2013). Morphology and Surface Analysis of Pure and Doped Cuboidal Ceria Nanoparticles. *The Journal of Physical Chemistry C* **117**, 24561–24569.

BHATTA, U. M., ROSS, I M, SAGHI, Z., STRINGFELLOW, A., SAYLE, D., SAYLE, T. X. T., KARAKOTI, A., REID, D., SEAL, S. & MÖBUS, G. (2012). Atomic motion on various surfaces of ceria nanoparticles in comparison. *Journal of Physics: Conference Series* **371**, 012007.

BHATTA, U. M., ROSS, IAN M., SAYLE, T. X. T., SAYLE, D. C., PARKER, S. C., REID, D., SEAL, S., KUMAR, A. & MÖBUS, G. (2012). Cationic Surface Reconstructions on Cerium Oxide Nanocrystals: An Aberration-Corrected HRTEM Study. *ACS Nano* **6**, 421–430.

BIERSCHENK, D. M., PILLAI, M. R., LIN, Y. & BARNETT, S. A. (2010). Effect of Ethane and Propane in Simulated Natural Gas on the Operation of Ni-YSZ Anode Supported Solid Oxide Fuel Cells. *Fuel Cells* **10**, 1129–1134.

BISHOP, S. R., STEFANIK, T. S. & TULLER, H. L. (2012). Defects and transport in $Pr_xCe_{1-x}O_{2-\delta}$: Composition trends. *Journal of Materials Research* **27**, 2009–2016.

BLAIR, D. & DUFRESNE, E. (2011). *The Matlab Particle Tracking Code Repository*. http://physics.georgetown.edu/matlab/.

BLENNOW, P., CHEN, W., LUNDBERG, M. & MENON, M. (2009). Characterization of $Ce_{0.9}Gd_{0.1}O_{1.95}$ powders synthesized by spray drying. *Ceramics International* **35**, 2959–2963.

BORCHERT, H., BORCHERT, Y., KAICHEV, V. V., PROSVIRIN, I. P., ALIKINA, G. M., LUKASHEVICH, A. I., ZAIKOVSKII, V. I., MOROZ, E. M., PAUKSHTIS, E. A., BUKHTIYAROV, V. I. & SADYKOV, V. A. (2005). Nanostructured, Gd-Doped Ceria Promoted by Pt or Pd: Investigation of the Electronic and Surface Structures and Relations to Chemical Properties. *The Journal of Physical Chemistry B* **109**, 20077–20086.

BOUWMEESTER, H., KRUIDHOF, H. & BURGGRAAF, A. (1994). Importance of the surface exchange kinetics as rate limiting step in oxygen permeation through mixed-conducting oxides. *Solid State Ionics* **72**, 185–194.

BOWMAN, W. J., KELLY, M., ROHRER, G., HERNANDEZ, C. A. & CROZIER, P. A. (2017). Enhanced Ionic Conductivity in Electroceramics by Nanoscale Enrichment of Grain Boundaries with High Solute Concentration. *Nanoscale*. http://pubs.rsc.org/en/Content/ArticleLanding/2017/NR/C7NR06941C (Accessed October 26, 2017).

BOWMAN, W. J., MARCH, K., HERNANDEZ, C. A. & CROZIER, P. A. (2016). Measuring bandgap states in individual non-stoichiometric oxide nanoparticles using monochromated STEM EELS: The Praseodymium–ceria case. *Ultramicroscopy* **167**, 5–10.

BOWMAN, W. J., ZHU, J., SHARMA, R. & CROZIER, P. A. (2015). Electrical conductivity and grain boundary composition of Gd-doped and Gd/Pr co-doped ceria. *Solid State Ionics* **272**, 9–17.

BOYES, E. D. & GAI, P. L. (1997). Environmental high resolution electron microscopy and applications to chemical science. *Ultramicroscopy* **67**, 219–232.

BOYES, E. D., GAI, P. L. & HANNA, L. G. (1995). Controlled Environment [Ecell] Tem for Dynamic In-Situ Reaction Studies with HREM Lattice Imaging. *MRS Proceedings* **404**. http://journals.cambridge.org/abstract_S1946427400259903 (Accessed January 6, 2019).

BRADLEY, C. (1988). *Calculations of atomic sputtering and displacement cross-sections in solid elements by electrons with energies from threshold to 1. 5 MV*. http://www.osti.gov/servlets/purl/6493690/ (Accessed May 21, 2019).

BRAUER, G., GINGERICH, K. A. & HOLTSCHMIDT, U. (1960). Über die oxyde des cers—IV. *Journal of Inorganic and Nuclear Chemistry* **16**, 77–86.

BRETT, D. J. L., ATKINSON, A., BRANDON, N. P. & SKINNER, S. J. (2008). Intermediate temperature solid oxide fuel cells. *Chemical Society Reviews* **37**, 1568.

BRIGHT, A. N., YOSHIDA, K. & TANAKA, N. (2013). Influence of total beam current on HRTEM image resolution in differentially pumped ETEM with nitrogen gas. *Ultramicroscopy* **124**, 46–51.

BROQVIST, P., KULLGREN, J., WOLF, M. J., VAN DUIN, A. C. T. & HERMANSSON, K. (2015). ReaxFF Force-Field for Ceria Bulk, Surfaces, and Nanoparticles. *The Journal of Physical Chemistry C* **119**, 13598–13609.

BRUIX, A. & NEYMAN, K. M. (2016). Modeling Ceria-Based Nanomaterials for Catalysis and Related Applications. *Catalysis Letters* **146**, 2053–2080.

———— (2019). How to design models for ceria nanoparticles: Challenges and strategies for describing nanostructured reducible oxides. In *Frontiers of Nanoscience*vol. 12, pp. 55–99. Elsevier https://linkinghub.elsevier.com/retrieve/pii/B9780081022320000014 (Accessed October 10, 2018).

BUGNET, M., OVERBURY, S. H., WU, Z. & EPICIER, T. (2017). Direct visualization and control of atomic mobility at {100} surfaces of ceria in the environmental transmission electron microscope. *Nano Letters*. http://pubs.acs.org/doi/10.1021/acs.nanolett.7b03680 (Accessed November 26, 2017).

BUNLUESIN, T., GORTE, R. J. & GRAHAM, G. W. (1998). Studies of the water-gas-shift reaction on ceria-supported Pt, Pd, and Rh: Implications for oxygen-storage properties. *Applied Catalysis B: Environmental* **15**, 107–114.

BUTLER, E. P. & HALE, K. F. (1981). *Dynamic experiments in the electron microscope*. Amsterdam ; New York : New York: North-Holland Pub. Co. ; Sole distributors for the U.S.A. and Canada, Elsevier/North-Holland.

BUTLER, V., CATLOW, C., FENDER, B. & HARDING, J. (1983). Dopant ion radius and ionic conductivity in cerium dioxide. *Solid State Ionics* **8**, 109–113.

CABALLERO, A., HOLGADO, J. P., GONZALEZ-DELACRUZ, V. M., HABAS, S. E., HERRANZ, T. & SALMERON, M. (2010). *In situ* spectroscopic detection of SMSI effect in a Ni/CeO_2 system: hydrogen-induced burial and dig out of metallic nickel. *Chem. Commun.* **46**, 1097–1099.

CAMPBELL, C. T. (2013). The Energetics of Supported Metal Nanoparticles: Relationships to Sintering Rates and Catalytic Activity. *Accounts of Chemical Research* **46**, 1712–1719.

CARGNELLO, M., DOAN-NGUYEN, V. V., GORDON, T. R., DIAZ, R. E., STACH, E. A., GORTE, R. J., FORNASIERO, P. & MURRAY, C. B. (2013). Control of metal nanocrystal size reveals metal-support interface role for ceria catalysts. *Science* **341**, 771–773.

CARGNELLO, M., JAEN, J. J. D., GARRIDO, J. C. H., BAKHMUTSKY, K., MONTINI, T., GAMEZ, J. J. C., GORTE, R. J. & FORNASIERO, P. (2012). Exceptional Activity for Methane Combustion over Modular Pd@CeO_2 Subunits on Functionalized Al_2O_3. *Science* **337**, 713–717.

CAVANI, F., BALLARINI, N. & CERICOLA, A. (2007). Oxidative dehydrogenation of ethane and propane: How far from commercial implementation? *Catalysis Today* **127**, 113–131.

CHEN, G., XU, C., SONG, X., XU, S., DING, Y. & SUN, S. (2008). Template-free Synthesis of Single-Crystalline-like CeO_2 Hollow Nanocubes. *Crystal Growth & Design* **8**, 4449–4453.

CHEN, L., FLEMING, P., MORRIS, V., HOLMES, J. D. & MORRIS, M. A. (2010). Size-Related Lattice Parameter Changes and Surface Defects in Ceria Nanocrystals. *The Journal of Physical Chemistry C* **114**, 12909–12919.

CHENNA, S., BANERJEE, R. & CROZIER, P. A. (2011). Atomic-Scale Observation of the Ni Activation Process for Partial Oxidation of Methane Using *In Situ* Environmental TEM. *ChemCatChem* **3**, 1051–1059.

CHIANG, H., BLUMENTHAL, R. & FOURNELLE, R. (1993). A high temperature lattice parameter and dilatometer study of the defect structure of nonstoichiometric cerium dioxide. *Solid State Ionics* **66**, 85–95.

CHOI, Y. M., ABERNATHY, H., CHEN, H.-T., LIN, M. C. & LIU, M. (2006). Characterization of O_2–CeO_2 Interactions Using *In Situ* Raman Spectroscopy and First-Principle Calculations. *ChemPhysChem* **7**, 1957–1963.

CHUEH, W. C., MCDANIEL, A. H., GRASS, M. E., HAO, Y., JABEEN, N., LIU, Z., HAILE, S. M., MCCARTY, K. F., BLUHM, H. & EL GABALY, F. (2012). Highly Enhanced Concentration and Stability of Reactive Ce^{3+} on Doped CeO_2 Surface Revealed In Operando. *Chemistry of Materials* **24**, 1876–1882.

CONESA, J. (1995). Computer modeling of surfaces and defects on cerium dioxide. *Surface Science* **339**, 337–352.

CORMOS, C.-C., PETRESCU, L. & CORMOS, A.-M. (2014). Assessment of Hydrogen Production Systems based on Natural Gas Conversion with Carbon Capture and Storage. In *Computer Aided Chemical Engineering*vol. 33, pp. 1081–1086. Elsevier http://linkinghub.elsevier.com/retrieve/pii/B9780444634559500155 (Accessed September 8, 2017).

CROCKER, J. C. & GRIER, D. G. (1996). Methods of digital video microscopy for colloidal studies. *Journal of colloid and interface science* **179**, 298–310.

CROZIER, P. A. & CHENNA, S. (2011). *In situ* analysis of gas composition by electron energy-loss spectroscopy for environmental transmission electron microscopy. *Ultramicroscopy* **111**, 177–185.

CROZIER, P. A. & HANSEN, T. W. (2015). *In situ* and *operando* transmission electron microscopy of catalytic materials. *MRS Bulletin* **40**, 38–45.

CROZIER, P. A. & MILLER, B. K. (2016). Spectroscopy of Solids, Gases, and Liquids in the ETEM. In *Controlled Atmosphere Transmission Electron Microscopy*, Hansen, T. W. & Wagner, J. B. (Eds.), pp. 95–141. Cham: Springer International Publishing http://link.springer.com/10.1007/978-3-319-22988-1_4 (Accessed January 3, 2019).

CROZIER, P. A., WANG, R. & SHARMA, R. (2008). *In situ* environmental TEM studies of dynamic changes in cerium-based oxides nanoparticles during redox processes. *Ultramicroscopy* **108**, 1432–1440.

DA SILVA, J. L. F., GANDUGLIA-PIROVANO, M. V., SAUER, J., BAYER, V. & KRESSE, G. (2007). Hybrid functionals applied to rare-earth oxides: The example of ceria. *Physical Review B* **75**. https://link.aps.org/doi/10.1103/PhysRevB.75.045121 (Accessed June 22, 2018).

DAI, S., GAO, W., ZHANG, S., GRAHAM, G. W. & PAN, X. (2017). Transmission electron microscopy with atomic resolution under atmospheric pressures. *MRS Communications* **7**, 798–812.

DALMON, J.-A., CRUZ-LÓPEZ, A., FARRUSSENG, D., GUILHAUME, N., IOJOIU, E., JALIBERT, J.-C., MIACHON, S., MIRODATOS, C., PANTAZIDIS, A., REBEILLEAU-DASSONNEVILLE, M., SCHUURMAN, Y. & VAN VEEN, A. C. (2007). Oxidation in catalytic membrane reactors. *Applied Catalysis A: General* **325**, 198–204.

DANG, F., KATO, K., IMAI, H., WADA, S., HANEDA, H. & KUWABARA, M. (2010). Characteristics of CeO_2 Nanocubes and Related Polyhedra Prepared by Using a Liquid−Liquid Interface. *Crystal Growth & Design* **10**, 4537–4541.

DE GRAEF, M. (2003). *Introduction to conventional transmission electron microscopy*. Cambridge, U.K. ; New York, N.Y: Cambridge University Press.

DE SOUZA, R. A. (2006). A universal empirical expression for the isotope surface exchange coefficients (k*) of acceptor-doped perovskite and fluorite oxides. *Physical Chemistry Chemical Physics* **8**, 890.

DE SOUZA, R. A. (2017). Limits to the rate of oxygen transport in mixed-conducting oxides. *Journal of Materials Chemistry A* **5**, 20334–20350.

DE SOUZA, R. A., RAMADAN, A. & HÖRNER, S. (2012). Modifying the barriers for oxygen-vacancy migration in fluorite-structured CeO_2 electrolytes through strain: a computer simulation study. *Energy Environ. Sci.* **5**, 5445–5453.

DESHPANDE, S., PATIL, S., KUCHIBHATLA, S. V. & SEAL, S. (2005). Size dependency variation in lattice parameter and valency states in nanocrystalline cerium oxide. *Applied Physics Letters* **87**, 133113.

DINCER, I. (2012). Green methods for hydrogen production. *International Journal of Hydrogen Energy* **37**, 1954–1971.

DINCER, I. & ACAR, C. (2015). Review and evaluation of hydrogen production methods for better sustainability. *International Journal of Hydrogen Energy* **40**, 11094–11111.

DU, N., ZHANG, H., CHEN, B., MA, X. & YANG, D. (2007). Ligand-free Self-Assembly of Ceria Nanocrystals into Nanorods by Oriented Attachment at Low Temperature. *The Journal of Physical Chemistry C* **111**, 12677–12680.

DU, X., ZHANG, D., SHI, L., GAO, R. & ZHANG, J. (2012). Morphology Dependence of Catalytic Properties of Ni/CeO_2 Nanostructures for Carbon Dioxide Reforming of Methane. *The Journal of Physical Chemistry C* **116**, 10009–10016.

DUBOVIKS, V., LOMBERG, M., MAHER, R. C., COHEN, L. F., BRANDON, N. P. & OFFER, G. J. (2015). Carbon deposition behaviour in metal-infiltrated gadolinia doped ceria electrodes for simulated biogas upgrading in solid oxide electrolysis cells. *Journal of Power Sources* **293**, 912–921.

DUTTA, P., PAL, S., SEEHRA, M. S., SHI, Y., EYRING, E. M. & ERNST, R. D. (2006). Concentration of Ce^{3+} and Oxygen Vacancies in Cerium Oxide Nanoparticles. *Chemistry of Materials* **18**, 5144–5146.

EGERTON, R. F. (1991). Factors affecting the accuracy of elemental analysis by transmission EELS. *Microscopy Microanalysis Microstructures* **2**, 203–213.

EGERTON, R. F. (2009). Electron energy-loss spectroscopy in the TEM. *Reports on Progress in Physics* **72**, 016502.

EGERTON, R. F. (2011). *Electron energy-loss spectroscopy in the electron microscope*. Third edition. New York: Springer.

EGERTON, R. F. (2016). *Physical principles of electron microscopy: an introduction to TEM, SEM, and AEM*. Second edition. Cham: Springer.

EGERTON, R. F., LI, P. & MALAC, M. (2004). Radiation damage in the TEM and SEM. *Micron* **35**, 399–409.

EGERTON, R. F., WANG, F. & CROZIER, P. A. (2006). Beam-Induced Damage to Thin Specimens in an Intense Electron Probe. *Microscopy and Microanalysis* **12**, 65–71.

EGUCHI, K., KOJO, H., TAKEGUCHI, T., KIKUCHI, R. & SASAKI, K. (2002). Fuel flexibility in power generation by solid oxide fuel cells. *Solid State Ionics* **152**, 411–416.

EGUCHI, K., SETOGUCHI, T., INOUE, T. & ARAI, H. (1992). Electrical properties of ceria-based oxides and their application to solid oxide fuel cells. *Solid State Ionics* **52**, 165–172.

ELIDRISSI, B., ADDOU, M., REGRAGUI, M., MONTY, C., BOUGRINE, A. & KACHOUANE, A. (2000). Structural and optical properties of CeO_2 thin films prepared by spray pyrolysis. *Thin Solid Films* **379**, 23–27.

ERNI, R., ROSSELL, M. D., KISIELOWSKI, C. & DAHMEN, U. (2009). Atomic-Resolution Imaging with a Sub-50-pm Electron Probe. *Physical Review Letters* **102**. https://link.aps.org/doi/10.1103/PhysRevLett.102.096101 (Accessed January 2, 2019).

ERTL, G., KNÖZINGER, H., SCHÜTH, F. & WEITKAMP, J. (eds.) (2008). *Handbook of Heterogeneous Catalysis*. 2nd ed. Weinheim: Wiley-VCH.

ESCH, F., FABRIS, S., ZHOU, L., MONTINI, T., AFRICH, C., FORNASIERO, P., COMELLI, G. & ROSEI, R. (2005). Electron Localization Determines Defect Formation on Ceria Substrates. *Science* **309**, 752–755.

ESCONJAUREGUI, S., WHELAN, C. M. & MAEX, K. (2009). The reasons why metals catalyze the nucleation and growth of carbon nanotubes and other carbon nanomorphologies. *Carbon* **47**, 659–669.

FARMER, J. A. & CAMPBELL, C. T. (2010). Ceria Maintains Smaller Metal Catalyst Particles by Strong Metal-Support Bonding. *Science* **329**, 933–936.

FARUQI, A. R., HENDERSON, R., PRYDDETCH, M., ALLPORT, P. & EVANS, A. (2005). Direct single electron detection with a CMOS detector for electron microscopy. *Nuclear Instruments and Methods in Physics Research Section A: Accelerators, Spectrometers, Detectors and Associated Equipment* **546**, 170–175.

FARUQI, A. R. & MCMULLAN, G. (2018). Direct imaging detectors for electron microscopy. *Nuclear Instruments and Methods in Physics Research Section A: Accelerators, Spectrometers, Detectors and Associated Equipment* **878**, 180–190.

FENG, X., CHEE, S. W., SHARMA, R., LIU, K., XIE, X., LI, Q., FAN, S. & JIANG, K. (2011). *In Situ* TEM observation of the gasification and growth of carbon nanotubes using iron catalysts. *Nano Research* **4**, 767–779.

FINDLAY, S. D., AZUMA, S., SHIBATA, N., OKUNISHI, E. & IKUHARA, Y. (2011). Direct oxygen imaging within a ceramic interface, with some observations upon the dark contrast at the grain boundary. *Ultramicroscopy* **111**, 285–289.

FLOREA, I., FERAL-MARTIN, C., MAJIMEL, J., IHIAWAKRIM, D., HIRLIMANN, C. & ERSEN, O. (2013). Three-Dimensional Tomographic Analyses of CeO_2 Nanoparticles. *Crystal Growth & Design* **13**, 1110–1121.

FOGER, K. (1984). Dispersed Metal Catalysts. In *Catalysis*, Anderson, J. R. & Boudart, M. (Eds.), pp. 227–305. Berlin, Heidelberg: Springer Berlin Heidelberg http://www.springerlink.com/index/10.1007/978-3-642-93250-2_4 (Accessed February 28, 2019).

FRIEDRICH, H., DE JONGH, P. E., VERKLEIJ, A. J. & DE JONG, K. P. (2009). Electron Tomography for Heterogeneous Catalysts and Related Nanostructured Materials. *Chemical Reviews* **109**, 1613–1629.

FU, Q., SALTSBURG, H. & FLYTZANI-STEPHANOPOULOS, M. (2003). Active Nonmetallic Au and Pt Species on Ceria-Based Water-Gas Shift Catalysts. *Science* **301**, 935–938.

FU, Q., WEBER, A. & FLYTZANI-STEPHANOPOULOS, M. (2001). Nanostructured Au–CeO_2 catalysts for low-temperature water–gas shift. *Catalysis Letters* **77**, 87–95.

FUENTES, R. O., ACUÑA, L. M., ZIMICZ, M. G., LAMAS, D. G., SACANELL, J. G., LEYVA, A. G. & BAKER, R. T. (2008). Formation and Structural Properties of Ce−Zr Mixed Oxide Nanotubes. *Chemistry of Materials* **20**, 7356–7363.

GAI, P. L. & BOYES, E. D. (1997). Environmental High Resolution Electron Microscopy in Materials Science. In *In-Situ Microscopy in Materials Research*, Gai, P. L. (Ed.), pp. 123–147. Boston, MA: Springer US http://link.springer.com/10.1007/978-1-4615-6215-3_6 (Accessed January 6, 2019).

———— (2009). Advances in atomic resolution in situ environmental transmission electron microscopy and 1Å aberration corrected in situ electron microscopy. *Microscopy Research and Technique* **72**, 153–164.

GAO, P., KANG, Z., FU, W., WANG, W., BAI, X. & WANG, E. (2010). Electrically Driven Redox Process in Cerium Oxides. *Journal of the American Chemical Society* **132**, 4197–4201.

GAO, P., WANG, Z., FU, W., LIAO, Z., LIU, K., WANG, W., BAI, X. & WANG, E. (2010). *In situ* TEM studies of oxygen vacancy migration for electrically induced resistance change effect in cerium oxides. *Micron* **41**, 301–305.

GAO, Z., MOGNI, L. V., MILLER, E. C., RAILSBACK, J. G. & BARNETT, S. A. (2016). A perspective on low-temperature solid oxide fuel cells. *Energy Environ. Sci.* http://xlink.rsc.org/?DOI=C5EE03858H (Accessed February 24, 2016).

GÄRTNER, C. A., VAN VEEN, A. C. & LERCHER, J. A. (2013). Oxidative Dehydrogenation of Ethane: Common Principles and Mechanistic Aspects. *ChemCatChem* **5**, 3196–3217.

GE, X.-M., CHAN, S.-H., LIU, Q.-L. & SUN, Q. (2012). Solid Oxide Fuel Cell Anode Materials for Direct Hydrocarbon Utilization. *Advanced Energy Materials* **2**, 1156–1181.

GEFFROY, P.-M., BLOND, E., RICHET, N. & CHARTIER, T. (2017). Understanding and identifying the oxygen transport mechanisms through a mixed-conductor membrane. *Chemical Engineering Science* **162**, 245–261.

GERZELIEV, I. M., GYUL'MALIEV, A. M., POPOV, A. YU. & KHADZHIEV, S. N. (2015). Thermodynamic and quantum-chemical study of the oxidative dehydrogenation of ethane to ethylene. *Petroleum Chemistry* **55**, 146–153.

GHONEIM, S. A., EL-SALAMONY, R. A. & EL-TEMTAMY, S. A. (2016). Review on Innovative Catalytic Reforming of Natural Gas to Syngas. *World Journal of Engineering and Technology* **04**, 116–139.

GILBERT, B. (2004). Nanoparticles: Strained and Stiff. *Science* **305**, 651–654.

GORTE, R. J. (2010). Ceria in catalysis: From automotive applications to the water-gas shift reaction. *AIChE Journal* **56**, 1126–1135.

GRACIANI, J., MÁRQUEZ, A. M., PLATA, J. J., ORTEGA, Y., HERNÁNDEZ, N. C., MEYER, A., ZICOVICH-WILSON, C. M. & SANZ, J. FDEZ. (2011). Comparative Study on the Performance of Hybrid DFT Functionals in Highly Correlated Oxides: The Case of CeO_2 and Ce_2O_3. *Journal of Chemical Theory and Computation* **7**, 56–65.

GRACIANI, J., MUDIYANSELAGE, K., XU, F., BABER, A. E., EVANS, J., SENANAYAKE, S. D., STACCHIOLA, D. J., LIU, P., HRBEK, J., SANZ, J. F. & RODRIGUEZ, J. A. (2014). Highly active copper-ceria and copper-ceria-titania catalysts for methanol synthesis from CO_2. *Science* **345**, 546–550.

GROB, R. L. & BARRY, E. F. (2004). *Modern practice of gas chromatography*. http://www.123library.org/book_details/?id=12719 (Accessed December 28, 2018).

GRZYBEK, G., STELMACHOWSKI, P., GUDYKA, S., INDYKA, P., SOJKA, Z., GUILLÉN-HURTADO, N., RICO-PÉREZ, V., BUENO-LÓPEZ, A. & KOTARBA, A. (2016). Strong dispersion effect of cobalt spinel active phase spread over ceria for catalytic N_2O

decomposition: The role of the interface periphery. *Applied Catalysis B: Environmental* **180**, 622–629.

GU, X.-K., SAMIRA, S. & NIKOLLA, E. (2018). Oxygen Sponges for Electrocatalysis: Oxygen Reduction/Evolution on Nonstoichiometric, Mixed Metal Oxides. *Chemistry of Materials* **30**, 2860–2872.

GÜR, T. M. (2016). Comprehensive review of methane conversion in solid oxide fuel cells: Prospects for efficient electricity generation from natural gas. *Progress in Energy and Combustion Science* **54**, 1–64.

HAIDER, M., HARTEL, P., MÜLLER, H., UHLEMANN, S. & ZACH, J. (2009). Current and future aberration correctors for the improvement of resolution in electron microscopy. *Philosophical Transactions of the Royal Society A: Mathematical, Physical and Engineering Sciences* **367**, 3665–3682.

———— (2010). Information Transfer in a TEM Corrected for Spherical and Chromatic Aberration. *Microscopy and Microanalysis* **16**, 393–408.

HAIDER, MAX, ROSE, H., UHLEMANN, S., SCHWAN, E., KABIUS, B. & URBAN, K. (1998). A spherical-aberration-corrected 200kV transmission electron microscope. *Ultramicroscopy* **75**, 53–60.

HAIDER, MAXIMILIAN, UHLEMANN, S., SCHWAN, E., ROSE, H., KABIUS, B. & URBAN, K. (1998). Electron microscopy image enhanced. *Nature* **392**, 768–769.

HAILSTONE, R. K., DIFRANCESCO, A. G., LEONG, J. G., ALLSTON, T. D. & REED, K. J. (2009). A Study of Lattice Expansion in CeO_2 Nanoparticles by Transmission Electron Microscopy. *The Journal of Physical Chemistry C* **113**, 15155–15159.

HAN, W.-Q., WEN, W., HANSON, J. C., TENG, X., MARINKOVIC, N. & RODRIGUEZ, J. A. (2009). One-Dimensional Ceria as Catalyst for the Low-Temperature Water−Gas Shift Reaction. *The Journal of Physical Chemistry C* **113**, 21949–21955.

HAN, X., AMRANE, N., ZHANG, Z. & BENKRAOUDA, M. (2018). Unraveling the Negative Role of Oxygen-Vacancy Cluster in Ionic Conductivity in CeO_2: Hybrid Functional Study. *The Journal of Physical Chemistry C* **122**, 5871–5880.

HANSEN, T. W. & WAGNER, J. B. (2012). Environmental Transmission Electron Microscopy in an Aberration-Corrected Environment. *Microscopy and Microanalysis* **18**, 684–690.

HANSEN, T. W. & WAGNER, J. B. (eds.) (2016). *Controlled Atmosphere Transmission Electron Microscopy*. Springer International Publishing http://link.springer.com/10.1007/978-3-319-22988-1 (Accessed September 27, 2017).

HANSEN, T. W., WAGNER, J. B. & DUNIN-BORKOWSKI, R. E. (2010). Aberration corrected and monochromated environmental transmission electron microscopy: challenges and prospects for materials science. *Materials Science and Technology* **26**, 1338–1344.

HARI PRASAD, D., KIM, H.-R., PARK, J.-S., SON, J.-W., KIM, B.-K., LEE, H.-W. & LEE, J.-H. (2010). Superior sinterability of nano-crystalline gadolinium doped ceria powders synthesized by co-precipitation method. *Journal of Alloys and Compounds* **495**, 238–241.

HASHIMOTO, H., NAIKI, T., ETO, T. & FUJIWARA, K. (1968). High Temperature Gas Reaction Specimen Chamber for an Electron Microscope. *Japanese Journal of Applied Physics* **7**, 946–952.

HIGASHI, K., SONODA, K., ONO, H., SAMESHIMA, S. & HIRATA, Y. (1999). Synthesis and sintering of rare-earth-doped ceria powder by the oxalate coprecipitation method. *Journal of Materials Research* **14**, 957–967.

HIRANO, M. & INAGAKI, M. (2000). Preparation of monodispersed cerium(iv) oxide particles by thermal hydrolysis: influence of the presence of urea and Gd doping on their morphology and growth. *Journal of Materials Chemistry* **10**, 473–477.

HIRANO, M. & KATO, E. (2004). Hydrothermal Synthesis of Nanocrystalline Cerium(IV) Oxide Powders. *Journal of the American Ceramic Society* **82**, 786–788.

HIRSCH, P. B. (1977). *Electron microscopy of thin crystals*. Huntington, N.Y: R. E. Krieger Pub. Co.

HOBBS, L. W. (1979). Application of Transmission Electron Microscopy to Radiation Damage in Ceramics. *Journal of the American Ceramic Society* **62**, 267–278.

———— (1984). *Quantitative electron microscopy: proceedings of the Twenty Fifth Scottish Universities Summer School in Physics, Glasgow, August 1983; a NATO advanced study institute*. Chapman, J. N., Craven, A. J., Scottish Universities Summer School in Physics & NATO (Eds.). Edinburgh: SUSSP Publ.

HOFMANN, S., SHARMA, R., DUCATI, C., DU, G., MATTEVI, C., CEPEK, C., CANTORO, M., PISANA, S., PARVEZ, A., CERVANTES-SODI, F., FERRARI, A. C., DUNIN-BORKOWSKI, R., LIZZIT, S., PETACCIA, L., GOLDONI, A. & ROBERTSON, J. (2007). *In situ* Observations of Catalyst Dynamics during Surface-Bound Carbon Nanotube Nucleation. *Nano Letters* **7**, 602–608.

HOJO, H., MIZOGUCHI, T., OHTA, H., FINDLAY, S. D., SHIBATA, N., YAMAMOTO, T. & IKUHARA, Y. (2010). Atomic Structure of a CeO_2 Grain Boundary: The Role of Oxygen Vacancies. *Nano Letters* **10**, 4668–4672.

HOROWITZ, C. A. (2016). Paris Agreement. *International Legal Materials* **55**, 740–755.

HUANG, H., DAI, Q. & WANG, X. (2014). Morphology effect of Ru/CeO_2 catalysts for the catalytic combustion of chlorobenzene. *Applied Catalysis B: Environmental* **158–159**, 96–105.

HUANG, M. & FABRIS, S. (2008). CO Adsorption and Oxidation on Ceria Surfaces from DFT+U Calculations. *The Journal of Physical Chemistry C* **112**, 8643–8648.

HUANG, P. X., WU, F., ZHU, B. L., GAO, X. P., ZHU, H. Y., YAN, T. Y., HUANG, W. P., WU, S. H. & SONG, D. Y. (2005). CeO_2 Nanorods and Gold Nanocrystals Supported on CeO_2 Nanorods as Catalyst. *The Journal of Physical Chemistry B* **109**, 19169–19174.

HUANG, TA-JEN, LIN, H.-J. & YU, T.-C. (2005). A Comparison of Oxygen-vacancy Effect on Activity Behaviors of Carbon Dioxide and Steam Reforming of Methane over Supported Nickel Catalysts. *Catalysis Letters* **105**, 239–247.

HUANG, X. & BECK, M. J. (2014). Surface structure of catalytically-active ceria nanoparticles. *Computational Materials Science* **91**, 122–133.

HUANG, X. & REIMERT, R. (2013). Kinetics of steam reforming of ethane on Ni/YSZ (yttria-stabilised zirconia) catalyst. *Fuel* **106**, 380–387.

IGLESIAS-JUEZ, A. (2004). Metal–promoter interface in Pd/(Ce,Zr)O_x/Al_2O_3 catalysts: effect of thermal aging. *Journal of Catalysis* **221**, 148–161.

ISHIKAWA, R., OKUNISHI, E., SAWADA, H., KONDO, Y., HOSOKAWA, F. & ABE, E. (2011). Direct imaging of hydrogen-atom columns in a crystal by annular bright-field electron microscopy. *Nature Materials* **10**, 278–281.

ISHIKAWA, Y., TAKEDA, M., TSUKIMOTO, S., NAKAYAMA, K. S. & ASAO, N. (2016). Cerium Oxide Nanorods with Unprecedented Low-Temperature Oxygen Storage Capacity. *Advanced Materials* **28**, 1467–1471.

JACOBS, G., WILLIAMS, L., GRAHAM, U., THOMAS, G. A., SPARKS, D. & DAVIS, B. H. (2003). Low temperature water–gas shift: in situ DRIFTS-reaction study of ceria surface area on the evolution of formates on Pt/CeO_2 fuel processing catalysts for fuel cell applications. *Applied Catalysis A: General* **252**, 107–118.

JACOBSON, A. J. (2010). Materials for Solid Oxide Fuel Cells. *Chemistry of Materials* **22**, 660–674.

JI, Z., WANG, X., ZHANG, H., LIN, S., MENG, H., SUN, B., GEORGE, S., XIA, T., NEL, A. E. & ZINK, J. I. (2012). Designed Synthesis of CeO_2 Nanorods and Nanowires for Studying Toxicological Effects of High Aspect Ratio Nanomaterials. *ACS Nano* **6**, 5366–5380.

JIA, C. L., HOUBEN, L., THUST, A. & BARTHEL, J. (2010). On the benefit of the negative-spherical-aberration imaging technique for quantitative HRTEM. *Ultramicroscopy* **110**, 500–505.

JIA, C. L., MI, S. B., BARTHEL, J., WANG, D. W., DUNIN-BORKOWSKI, R. E., URBAN, K. W. & THUST, A. (2014). Determination of the 3D shape of a nanoscale crystal with atomic resolution from a single image. *Nature Materials* **13**, 1044–1049.

JIA, C.-L., LENTZEN, M. & URBAN, K. (2004). High-Resolution Transmission Electron Microscopy Using Negative Spherical Aberration. *Microscopy and Microanalysis* **10**, 174–184.

JINSCHEK, J. R. (2014). Advances in the environmental transmission electron microscope (ETEM) for nanoscale *In situ* studies of gas–solid interactions. *Chemical Communications* **50**, 2696.

JINSCHEK, J. R. & HELVEG, S. (2012). Image resolution and sensitivity in an environmental transmission electron microscope. *Micron* **43**, 1156–1168.

JOHNSTON-PECK, A. C., DUCHENE, J. S., ROBERTS, A. D., WEI, W. D. & HERZING, A. A. (2016). Dose-rate-dependent damage of cerium dioxide in the scanning transmission electron microscope. *Ultramicroscopy* **170**, 1–9.

DE JONGE, N., BIGELOW, W. C. & VEITH, G. M. (2010). Atmospheric Pressure Scanning Transmission Electron Microscopy. *Nano Letters* **10**, 1028–1031.

JUNG, D.-H., LEE, J.-H., KILIC, M. E. & SOON, A. (2018). Anisotropic vacancy-mediated phonon mode softening in Sm and Gd doped ceria. *Physical Chemistry Chemical Physics* **20**, 10048–10059.

KAMALADASA, R. J., SHARMA, A. A., LAI, Y.-T., CHEN, W., SALVADOR, P. A., BAIN, J. A., SKOWRONSKI, M. & PICARD, Y. N. (2015). *In Situ* TEM Imaging of Defect Dynamics under Electrical Bias in Resistive Switching Rutile-TiO_2. *Microscopy and Microanalysis* **21**, 140–153.

KAMIYA, M., SHIMADA, E., IKUMA, Y., KOMATSU, M. & HANEDA, H. (2000). Intrinsic and extrinsic oxygen diffusion and surface exchange reaction in cerium oxide. *Journal of the Electrochemical Society* **147**, 1222–1227.

KANG, H. S., SOHN, J. R., KANG, Y. C., JUNG, K. Y. & PARK, S. B. (2005). The characteristics of nano-sized Gd-doped CeO_2 particles prepared by spray pyrolysis. *Journal of Alloys and Compounds* **398**, 240–244.

KANT, K. M., ESPOSITO, V. & PRYDS, N. (2012). Strain induced ionic conductivity enhancement in epitaxial $Ce_{0.9}Gd_{0.1}O_{2-\delta}$ thin films. *Applied Physics Letters* **100**, 033105.

KHARTON, V. V., FIGUEIREDO, F. M., NAVARRO, L., NAUMOVICH, E. N., KOVALEVSKY, A. V., YAREMCHENKO, A. A., VISKUP, A. P., CARNEIRO, A., MARQUES, F. M. B. & FRADE, J. R. (2001). Ceria-based materials for solid oxide fuel cells. **36**, 1105–1117.

KHO, E. T., LOVELL, E., WONG, R. J., SCOTT, J. & AMAL, R. (2017). Manipulating ceria-titania binary oxide features and their impact as nickel catalyst supports for low temperature steam reforming of methane. *Applied Catalysis A: General* **530**, 111–124.

KILNER, J. A. & BURRIEL, M. (2014). Materials for Intermediate-Temperature Solid-Oxide Fuel Cells. *Annual Review of Materials Research* **44**, 365–393.

KILNER, J. A., DE SOUZA, R. A. & FULLARTON, I. C. (1996). Surface exchange of oxygen in mixed conducting perovskite oxides. *Solid State Ionics* **86**, 703–709.

KIMOTO, K., ASAKA, T., YU, X., NAGAI, T., MATSUI, Y. & ISHIZUKA, K. (2010). Local crystal structure analysis with several picometer precision using scanning transmission electron microscopy. *Ultramicroscopy* **110**, 778–782.

KISHIMOTO, H. (2004). Attempt of utilizing liquid fuels with Ni-ScSZ anode in SOFCs. *Solid State Ionics* **175**, 107–111.

KISHIMOTO, H., HORITA, T., YAMAJI, K., XIONG, Y., SAKAI, N., BRITO, M. E. & YOKOKAWA, H. (2005). Feasibility of n-Dodecane Fuel for Solid Oxide Fuel Cell with Ni-ScSZ Anode. *Journal of The Electrochemical Society* **152**, A532.

KLING, J., HANSEN, T. W. & WAGNER, J. B. (2016). Quantifying the growth of individual graphene layers by *In situ* environmental transmission electron microscopy. *Carbon* **99**, 261–266.

KNOLL, M. & RUSKA, E. (1932). Das Elektronenmikroskop. *Zeitschrift f*[illegible]*r Physik* **78**, 318–339.

KOH, A. L., LEE, S. C. & SINCLAIR, R. (2016). A Brief History of Controlled Atmosphere Transmission Electron Microscopy. In *Controlled Atmosphere Transmission Electron Microscopy*, Hansen, T. W. & Wagner, J. B. (Eds.), pp. 3–43. Cham: Springer International Publishing http://link.springer.com/10.1007/978-3-319-22988-1_1 (Accessed January 6, 2019).

KÖRNER, R., RICKEN, M., NÖLTING, J. & RIESS, I. (1989). Phase transformations in reduced ceria: Determination by thermal expansion measurements. *Journal of Solid State Chemistry* **78**, 136–147.

KRIVANEK, O. L., AHN, C. C. & KEENEY, R. B. (1987). Parallel detection electron spectrometer using quadrupole lenses. *Ultramicroscopy* **22**, 103–115.

KRIVANEK, O. L., CHISHOLM, M. F., MURFITT, M. F. & DELLBY, N. (2012). Scanning transmission electron microscopy: Albert Crewe's vision and beyond. *Ultramicroscopy* **123**, 90–98.

KRIVANEK, O. L., CHISHOLM, M. F., NICOLOSI, V., PENNYCOOK, T. J., CORBIN, G. J., DELLBY, N., MURFITT, M. F., OWN, C. S., SZILAGYI, Z. S., OXLEY, M. P., PANTELIDES, S. T. & PENNYCOOK, S. J. (2010). Atom-by-atom structural and chemical analysis by annular dark-field electron microscopy. *Nature* **464**, 571–574.

KRIVANEK, O. L., DELLBY, N. & LUPINI, A. R. (1999). Towards sub-Å electron beams. *Ultramicroscopy* **78**, 1–11.

KRIVANEK, O. L., DELLBY, N., SPENCE, A. J. & BROWN, L. M. (1998). Spherical aberration correction in dedicated STEM Electron Microscopy 1998. *Proceedings of ICEM 14, Cancun, Mexico* **1**, 55–56.

KRIVANEK, O. L., DELLBY, N., SPENCE, A. J., CAMPS, R. A. & BROWN, L. M. (1997). Aberration corretion in the STEM. *Inst. Phys. Conf. Ser.* **153**, 35–40.

KRIVANEK, O. L., LOVEJOY, T. C., DELLBY, N., AOKI, T., CARPENTER, R. W., REZ, P., SOIGNARD, E., ZHU, J., BATSON, P. E., LAGOS, M. J., EGERTON, R. F. & CROZIER, P. A. (2014). Vibrational spectroscopy in the electron microscope. *Nature* **514**, 209–212.

KRIVANEK, O. L., LOVEJOY, T. C., DELLBY, N. & CARPENTER, R. W. (2013). Monochromated STEM with a 30 meV-wide, atom-sized electron probe. *Microscopy* **62**, 3–21.

KRÖGER, F. A. & VINK, H. J. (1956). Relations between the Concentrations of Imperfections in Crystalline Solids. In *Solid State Physics*vol. 3, pp. 307–435. Elsevier https://linkinghub.elsevier.com/retrieve/pii/S0081194708601356 (Accessed January 25, 2019).

KUBACKA, A., MARTÍNEZ-ARIAS, A. & FERNÁNDEZ-GARCÍA, M. (2015). Role of the Interface in Base-Metal Ceria-Based Catalysts for Hydrogen Purification and Production Processes. *ChemCatChem* **7**, 3614–3624.

KUBOTA, J., HASHIMOTO, S., SHINDO, T., YASHIRO, K., MATSUI, T., YAMAJI, K., KISHIMOTO, H. & KAWADA, T. (2017). Self-modification of Ni Metal Surfaces with CeO_2 to Suppress Carbon Deposition at Solid Oxide Fuel Cell Anodes. *Fuel Cells* **17**, 402–406.

KULLGREN, J., HERMANSSON, K. & CASTLETON, C. (2012). Many competing ceria (110) oxygen vacancy structures: From small to large supercells. *The Journal of Chemical Physics* **137**, 044705.

KÜMMERLE, E. A. & HEGER, G. (1999). The structures of C–$Ce_2O_{3+\delta}$, Ce_7O_{12}, and $Ce_{11}O_{20}$. *Journal of Solid State Chemistry* **147**, 485–500.

KUWAUCHI, Y., TAKEDA, S., YOSHIDA, H., SUN, K., HARUTA, M. & KOHNO, H. (2013). Stepwise Displacement of Catalytically Active Gold Nanoparticles on Cerium Oxide. *Nano Letters* **13**, 3073–3077.

KWON, D.-H., KIM, K. M., JANG, J. H., JEON, J. M., LEE, M. H., KIM, G. H., LI, X.-S., PARK, G.-S., LEE, B., HAN, S., KIM, M. & HWANG, C. S. (2010). Atomic structure of conducting nanofilaments in TiO_2 resistive switching memory. *Nature Nanotechnology* **5**, 148–153.

LABERTY-ROBERT, C., LONG, J. W., LUCAS, E. M., PETTIGREW, K. A., STROUD, R. M., DOESCHER, M. S. & ROLISON, D. R. (2006). Sol−Gel-Derived Ceria Nanoarchitectures: Synthesis, Characterization, and Electrical Properties. *Chemistry of Materials* **18**, 50–58.

LANE, J. A. & KILNER, J. A. (2000). Oxygen surface exchange on gadolinia doped ceria. *Solid State Ionics* **136**, 927–932.

LAWRENCE, E. L. & CROZIER, P. A. (2018). Oxygen Transfer at Metal-Reducible Oxide Nanocatalyst Interfaces: Contrasting Carbon Growth from Ethane and Ethylene. *ACS Applied Nano Materials* **1**, 1360–1369.

LAWRENCE, N. J., BREWER, J. R., WANG, L., WU, T.-S., WELLS-KINGSBURY, J., IHRIG, M. M., WANG, G., SOO, Y.-L., MEI, W.-N. & CHEUNG, C. L. (2011). Defect Engineering in Cubic Cerium Oxide Nanostructures for Catalytic Oxidation. *Nano Letters* **11**, 2666–2671.

LEE, J. M., KIM, Y. G., LEE, S. J., KIM, H. S., YOON, S. P., NAM, S. W., YOON, S. D. & YUN, J. W. (2014). Carbon-tolerance effects of Sm0.2Ce0.8O2−δ modified Ni/YSZ anode for solid oxide fuel cells under methane fuel conditions. *Journal of Applied Electrochemistry* **44**, 581–588.

LEHWALD, S. & IBACH, H. (1979). Decomposition of hydrocarbons on flat and stepped Ni(111) surfaces. *Surface Science* **89**, 425–445.

LEI, Y., ITO, Y., BROWNING, N. D. & MAZANEC, T. J. (2002). Segregation Effects at Grain Boundaries in Fluorite-Structured Ceramics. *Journal of the American Ceramic Society* **85**, 2359–2363.

DE LEITENBURG, C., TROVARELLI, A., LLORCA, J., CAVANI, F. & BINI, G. (1996). The effect of doping CeO_2 with zirconium in the oxidation of isobutane. *Applied Catalysis A: General* **139**, 161–173.

LENG, Y., CHAN, S., JIANG, S. & KHOR, K. (2004). Low-temperature SOFC with thin film GDC electrolyte prepared in situ by solid-state reaction. *Solid State Ionics* **170**, 9–15.

LEVIN, B. D. A. (2017). Transmission Electron Microscopy of Vacuum Sensitive, Radiation Sensitive, and Structurally Delicate Materials.

LEVIN, B. D. A., PADGETT, E., CHEN, C.-C., SCOTT, M. C., XU, R., THEIS, W., JIANG, Y., YANG, Y., OPHUS, C., ZHANG, H., HA, D.-H., WANG, D., YU, Y., ABRUÑA, H. D., ROBINSON, R. D., ERCIUS, P., KOURKOUTIS, L. F., MIAO, J., MULLER, D. A. & HOVDEN, R. (2016). Nanomaterial datasets to advance tomography in scanning transmission electron microscopy. *Scientific Data* **3**, 160041.

LI, J., SHAN, Z. & MA, E. (2014). Elastic strain engineering for unprecedented materials properties. *MRS Bulletin* **39**, 108–114.

LI, P., CHEN, X., LI, Y. & SCHWANK, J. W. (2019). A review on oxygen storage capacity of CeO_2-based materials: Influence factors, measurement techniques, and applications in reactions related to catalytic automotive emissions control. *Catalysis Today* **327**, 90–115.

LI, Y., FU, Q. & FLYTZANI-STEPHANOPOULOS, M. (2000). Low-temperature water-gas shift reaction over Cu- and Ni-loaded cerium oxide catalysts. *Applied Catalysis B: Environmental* **27**, 179–191.

LI, Z.-P., MORI, T., AUCHTERLONIE, G. J., ZOU, J. & DRENNAN, J. (2011). Direct evidence of dopant segregation in Gd-doped ceria. *Applied Physics Letters* **98**, 093104.

LIN, K.-S. & CHOWDHURY, S. (2010). Synthesis, Characterization, and Application of 1-D Cerium Oxide Nanomaterials: A Review. *International Journal of Molecular Sciences* **11**, 3226–3251.

LIN, MING, FU, Z. Y., TAN, H. R., TAN, J. P. Y., NG, S. C. & TEO, E. (2012). Hydrothermal Synthesis of CeO_2 Nanocrystals: Ostwald Ripening or Oriented Attachment? *Crystal Growth & Design* **12**, 3296–3303.

LIN, M., YING TAN, J. P., BOOTHROYD, C., LOH, K. P., TOK, E. S. & FOO, Y.-L. (2006). Direct Observation of Single-Walled Carbon Nanotube Growth at the Atomistic Scale. *Nano Letters* **6**, 449–452.

LIN, XUFENG, XI, Y. & SUN, J. (2012). Unraveling the Reaction Mechanism for Nickel-Catalyzed Oxidative Dehydrogenation of Ethane by DFT: The C–H Bond Activation Step and Its Following Pathways. *The Journal of Physical Chemistry C* **116**, 3503–3516.

LIN, Y., WU, Z., WEN, J., DING, K., YANG, X., POEPPELMEIER, K. R. & MARKS, L. D. (2015). Adhesion and Atomic Structures of Gold on Ceria Nanostructures: The

Role of Surface Structure and Oxidation State of Ceria Supports. *Nano Letters* **15**, 5375–5381.

LIN, Y., WU, Z., WEN, J., POEPPELMEIER, K. R. & MARKS, L. D. (2014). Imaging the Atomic Surface Structures of CeO_2 Nanoparticles. *Nano Letters* **14**, 191–196.

LIU, J. J. (2011). Advanced Electron Microscopy of Metal-Support Interactions in Supported Metal Catalysts. *ChemCatChem* **3**, 934–948.

LIU, K., SONG, C. & SUBRAMANI, V. (eds.) (2010). *Hydrogen and syngas production and purification technologies*. Hoboken, N.J.: Wiley http://www.123library.org/book_details/?id=22465 (Accessed October 9, 2017).

LIU, L., CAO, Y., SUN, W., YAO, Z., LIU, B., GAO, F. & DONG, L. (2011). Morphology and nanosize effects of ceria from different precursors on the activity for NO reduction. *Catalysis Today* **175**, 48–54.

LIU, QIANLANG, MARCH, K. & CROZIER, P. A. (2017). Nanoscale probing of bandgap states on oxide particles using electron energy-loss spectroscopy. *Ultramicroscopy* **178**, 2–11.

LIU, X., YANG, H., HAN, L., LIU, W., ZHANG, C., ZHANG, X., WANG, S. & YANG, Y. (2013). Mesoporous-shelled CeO_2 hollow nanospheres synthesized by a one-pot hydrothermal route and their catalytic performance. *CrystEngComm* **15**, 7769.

LIU, X., ZHOU, K., WANG, L., WANG, B. & LI, Y. (2009). Oxygen Vacancy Clusters Promoting Reducibility and Activity of Ceria Nanorods. *Journal of the American Chemical Society* **131**, 3140–3141.

LIU, Z., GRINTER, D. C., LUSTEMBERG, P. G., NGUYEN-PHAN, T.-D., ZHOU, Y., LUO, S., WALUYO, I., CRUMLIN, E. J., STACCHIOLA, D. J., ZHOU, J., CARRASCO, J., BUSNENGO, H. F., GANDUGLIA-PIROVANO, M. V., SENANAYAKE, S. D. & RODRIGUEZ, J. A. (2016). Dry Reforming of Methane on a Highly-Active Ni-CeO_2 Catalyst: Effects of Metal-Support Interactions on C−H Bond Breaking. *Angewandte Chemie International Edition* **55**, 7455–7459.

LIU, ZONGYUAN, LUSTEMBERG, P., GUTIÉRREZ, R. A., CAREY, J. J., PALOMINO, R. M., VOROKHTA, M., GRINTER, D. C., RAMÍREZ, P. J., MATOLÍN, V., NOLAN, M., GANDUGLIA-PIROVANO, M. V., SENANAYAKE, S. D. & RODRIGUEZ, J. A. (2017). *In Situ* Investigation of Methane Dry Reforming on Metal/Ceria(111) Surfaces: Metal-Support Interactions and C−H Bond Activation at Low Temperature. *Angewandte Chemie International Edition* **56**, 13041–13046.

LU, X., ZHAI, T., CUI, H., SHI, J., XIE, S., HUANG, Y., LIANG, C. & TONG, Y. (2011). Redox cycles promoting photocatalytic hydrogen evolution of CeO_2 nanorods. *Journal of Materials Chemistry* **21**, 5569.

LUNDBERG, M., WANG, H.-J., BLENNOW, P. & MENON, M. (2011). Mesoporous high surface area $Ce_{0.9}Gd_{0.1}O_{1.95}$ synthesized by spray drying. *Ceramics International* **37**, 797–802.

LYKAKI, M., PACHATOURIDOU, E., ILIOPOULOU, E., CARABINEIRO, S. A. C. & KONSOLAKIS, M. (2017). Impact of the synthesis parameters on the solid state properties and the CO oxidation performance of ceria nanoparticles. *RSC Advances* **7**, 6160–6169.

MAI, H.-X., SUN, L.-D., ZHANG, Y.-W., SI, R., FENG, W., ZHANG, H.-P., LIU, H.-C. & YAN, C.-H. (2005). Shape-Selective Synthesis and Oxygen Storage Behavior of Ceria Nanopolyhedra, Nanorods, and Nanocubes. *The Journal of Physical Chemistry B* **109**, 24380–24385.

MANNING, P. S., SIRMAN, J. D. & KILNER, J. A. (1996). Oxygen self-diffusion and surface exchange studies of oxide electrolytes having the fluorite structure. *Solid State Ionics* **93**, 125–132.

MCINTOSH, S. & GORTE, R. J. (2004). Direct Hydrocarbon Solid Oxide Fuel Cells. *Chemical Reviews* **104**, 4845–4866.

MCKINLEY, W. A. & FESHBACH, H. (1948). The Coulomb Scattering of Relativistic Electrons by Nuclei. *Physical Review* **74**, 1759–1763.

MCMULLAN, G., FARUQI, A. R., CLARE, D. & HENDERSON, R. (2014). Comparison of optimal performance at 300keV of three direct electron detectors for use in low dose electron microscopy. *Ultramicroscopy* **147**, 156–163.

MCNAIR, H. M. & MILLER, J. M. (2011). *Basic Gas Chromatography*. New York, NY: John Wiley & Sons http://nbn-resolving.de/urn:nbn:de:101:1-201412084994 (Accessed December 28, 2018).

MELCHIONNA, M. & FORNASIERO, P. (2014). The role of ceria-based nanostructured materials in energy applications. *Materials Today* **17**, 349–357.

MIGANI, A., NEYMAN, K. M. & BROMLEY, S. T. (2012). Octahedrality versus tetrahedrality in stoichiometric ceria nanoparticles. *Chemical Communications* **48**, 4199.

MIGANI, A., VAYSSILOV, G. N., BROMLEY, S. T., ILLAS, F. & NEYMAN, K. M. (2010a). Dramatic reduction of the oxygen vacancy formation energy in ceria particles: a possible key to their remarkable reactivity at the nanoscale. *Journal of Materials Chemistry* **20**, 10535–10546.

———— (2010b). Greatly facilitated oxygen vacancy formation in ceria nanocrystallites. *Chemical Communications* **46**, 5936.

MILLER, B. K. & CROZIER, P. A. (2014). Analysis of Catalytic Gas Products Using Electron Energy-Loss Spectroscopy and Residual Gas Analysis for Operando Transmission Electron Microscopy. *Microscopy and Microanalysis* **20**, 815–824.

MILLER, E. L., PAPAGEORGOPOULOS, D., STETSON, N., RANDOLPH, K., PETERSON, D., CIERPIK-GOLD, K., WILSON, A., TREJOS, V., GOMEZ, J. C., RUSTAGI, N. & SATYAPAL, S. (2016). U.S. Department of Energy Hydrogen and Fuel Cells Program: Progress, Challenges and Future Directions. *MRS Advances* 1–17.

MINERVINI, L. (1999). Defect cluster formation in M_2O_3-doped CeO_2. *Solid State Ionics* **116**, 339–349.

MÖBUS, G., SAGHI, Z., SAYLE, D. C., BHATTA, U. M., STRINGFELLOW, A. & SAYLE, T. X. T. (2011). Dynamics of Polar Surfaces on Ceria Nanoparticles Observed *In Situ* with Single-Atom Resolution. *Advanced Functional Materials* **21**, 1971–1976.

MOGENSEN, M. (2000). Physical, chemical and electrochemical properties of pure and doped ceria. *Solid State Ionics* **129**, 63–94.

MOGENSEN, M., LINDEGAARD, T., HANSEN, U. R. & MOGENSEN, M. (1994). Physical Properties of Mixed Conductor Solid Oxide Fuel Cell Anodes of Doped CeO_2. *Journal of The Electrochemical Society* **141**, 2122.

MONTINI, T., MELCHIONNA, M., MONAI, M. & FORNASIERO, P. (2016). Fundamentals and Catalytic Applications of CeO_2-Based Materials. *Chemical Reviews* **116**, 5987–6041.

MUELLER, J. E., VAN DUIN, A. C. T. & GODDARD, W. A. (2010). Competing, Coverage-Dependent Decomposition Pathways for C_2H_y Species on Nickel (111). *The Journal of Physical Chemistry C* **114**, 20028–20041.

MUHICH, C. L. (2017). Re-Evaluating CeO_2 Expansion Upon Reduction: Noncounterpoised Forces, Not Ionic Radius Effects, Are the Cause. *The Journal of Physical Chemistry C* **121**, 8052–8059.

MULLINS, D. R., ALBRECHT, P. M. & CALAZA, F. (2013). Variations in Reactivity on Different Crystallographic Orientations of Cerium Oxide. *Topics in Catalysis* **56**, 1345–1362.

MURRAY, E. P., TSAI, T. & BARNETT, S. A. (1999). A direct-methane fuel cell with a ceria-based anode. *Nature* **400**, 649–651.

NAGAI, Y., DOHMAE, K., NISHIMURA, Y. F., KATO, H., HIRATA, H. & TAKAHASHI, N. (2013). Operando XAFS study of catalytic NO reduction over Cu/CeO_2: the effect of copper–ceria interaction under periodic operation. *Physical Chemistry Chemical Physics* **15**, 8461.

NAIK, I. K. & TIEN, T. Y. (1978). Small-polaron mobility in nonstoichiometric cerium dioxide. *Journal of Physics and Chemistry of Solids* **39**, 311–315.

NAMAI, Y., FUKUI, KEN-ICHI & IWASAWA, Y. (2003). Atom-Resolved Noncontact Atomic Force Microscopic Observations of CeO_2 (111) Surfaces with Different Oxidation States: Surface Structure and Behavior of Surface Oxygen Atoms. *The Journal of Physical Chemistry B* **107**, 11666–11673.

NAMAI, Y., FUKUI, KEN-ICHI & IWASAWA, Y. (2003). Atom-resolved noncontact atomic force microscopic and scanning tunneling microscopic observations of the structure and dynamic behavior of CeO_2(111) surfaces. *Catalysis Today* **85**, 79–91.

NIAKOLAS, D. K., ATHANASIOU, M., DRACOPOULOS, V., TSIAOUSSIS, I., BEBELIS, S. & NEOPHYTIDES, S. G. (2013). Study of the synergistic interaction between nickel, gold and molybdenum in novel modified NiO/GDC cermets, possible anode materials for CH_4 fueled SOFCs. *Applied Catalysis A: General* **456**, 223–232.

NIKOLAIDIS, P. & POULLIKKAS, A. (2017). A comparative overview of hydrogen production processes. *Renewable and Sustainable Energy Reviews* **67**, 597–611.

NILSSON PINGEL, T., JØRGENSEN, M., YANKOVICH, A. B., GRÖNBECK, H. & OLSSON, E. (2018). Influence of atomic site-specific strain on catalytic activity of supported nanoparticles. *Nature Communications* **9**. http://www.nature.com/articles/s41467-018-05055-1 (Accessed August 13, 2018).

NIU, G., ZOELLNER, M. H., SCHROEDER, T., SCHAEFER, A., JHANG, J.-H., ZIELASEK, V., BÄUMER, M., WILKENS, H., WOLLSCHLÄGER, J., OLBRICH, R., LAMMERS, C. & REICHLING, M. (2015). Controlling the physics and chemistry of binary and ternary praseodymium and cerium oxide systems. *Physical Chemistry Chemical Physics* **17**, 24513–24540.

NOLAN, M., FEARON, J. & WATSON, G. (2006). Oxygen vacancy formation and migration in ceria. *Solid State Ionics* **177**, 3069–3074.

NOLAN, M., GRIGOLEIT, S., SAYLE, D. C., PARKER, S. C. & WATSON, G. W. (2005). Density functional theory studies of the structure and electronic structure of pure and defective low index surfaces of ceria. *Surface Science* **576**, 217–229.

NOLAN, M., PARKER, S. C. & WATSON, G. W. (2005). The electronic structure of oxygen vacancy defects at the low index surfaces of ceria. *Surface Science* **595**, 223–232.

NOOTZ, G. (2012). *Fit 2D gaussian function to data*. https://www.mathworks.com/matlabcentral/fileexchange/37087-fit-2d-gaussian-function-to-data.

NOZAKI, T. & FUJIMOTO, K. (1994). Oxide ion transport for selective oxidative coupling of methane with new membrane reactor. *AIChE Journal* **40**, 870–877.

O'KEEFE, M. A. (2008). Seeing atoms with aberration-corrected sub-Ångström electron microscopy. *Ultramicroscopy* **108**, 196–209.

OKUNISHI, E., ISHIKAWA, I., SAWADA, H., HOSOKAWA, F., HORI, M. & KONDO, Y. (2009). Visualization of Light Elements at Ultrahigh Resolution by STEM Annular Bright Field Microscopy. *Microscopy and Microanalysis* **15**, 164–165.

OKUNISHI, E., SAWADA, H. & KONDO, Y. (2012). Experimental study of annular bright field (ABF) imaging using aberration-corrected scanning transmission electron microscopy (STEM). *Micron* **43**, 538–544.

OTSUKA, K., KOBAYASHI, S. & TAKENAKA, S. (2001). Catalytic decomposition of light alkanes, alkenes, and acetylene over Ni/SiO_2. *Applied Catalysis A: General* **210**, 371–379.

OU, D. R., MORI, T., YE, F., ZOU, J., AUCHTERLONIE, G. & DRENNAN, J. (2008). Oxygen-vacancy ordering in lanthanide-doped ceria: Dopant-type dependence and structure model. *Physical Review B* **77**. https://link.aps.org/doi/10.1103/PhysRevB.77.024108 (Accessed June 22, 2018).

OUYANG, M., BOLDRIN, P., MAHER, R. C., CHEN, X., LIU, X., COHEN, L. F. & BRANDON, N. P. (2019). A mechanistic study of the interactions between methane and nickel supported on doped ceria. *Applied Catalysis B: Environmental* **248**, 332–340.

ÖZER, N. (2001). Optical properties and electrochromic characterization of sol–gel deposited ceria films. *Solar Energy Materials and Solar Cells* **68**, 391–400.

PAHARI, S. K., SUTRADHAR, N., SINHAMAHAPATRA, A., PAL, P. & PANDA, A. B. (2011). Synthesis of nearly monodispersed metal oxide nanoparticles in water. *New Journal of Chemistry* **35**, 1460.

PAIER, J., PENSCHKE, C. & SAUER, J. (2013). Oxygen Defects and Surface Chemistry of Ceria: Quantum Chemical Studies Compared to Experiment. *Chemical Reviews* **113**, 3949–3985.

PAN, C., ZHANG, D. & SHI, L. (2008). CTAB assisted hydrothermal synthesis, controlled conversion and CO oxidation properties of CeO_2 nanoplates, nanotubes, and nanorods. *Journal of Solid State Chemistry* **181**, 1298–1306.

PAN, C.-J., TSAI, M.-C., SU, W.-N., RICK, J., AKALEWORK, N. G., AGEGNEHU, A. K., CHENG, S.-Y. & HWANG, B.-J. (2017). Tuning/exploiting Strong Metal-Support Interaction (SMSI) in Heterogeneous Catalysis. *Journal of the Taiwan Institute of Chemical Engineers* **74**, 154–186.

PAN, M. & CZARNIK, C. (2016). Image Detectors for Environmental Transmission Electron Microscopy (ETEM). In *Controlled Atmosphere Transmission Electron Microscopy*, Hansen, T. W. & Wagner, J. B. (Eds.), pp. 143–164. Cham: Springer International Publishing http://link.springer.com/10.1007/978-3-319-22988-1_5 (Accessed January 14, 2019).

PANLENER, R. J., BLUMENTHAL, R. N. & GARNIER, J. E. (1975). A thermodynamic study of nonstoichiometric cerium dioxide. *Journal of Physics and Chemistry of Solids* **36**, 1213–1222.

PARADIS, H., ANDERSSON, M., YUAN, J. & SUNDÉN, B. (2011). CFD Modeling: Different Kinetic Approaches for Internal Reforming Reactions in an Anode-Supported SOFC. *Journal of Fuel Cell Science and Technology* **8**, 031014.

PARK, J. L., BALIJEPALLI, S. K., ARGYLE, M. D. & STOWERS, K. J. (2018). Low Temperature Oxidative Dehydrogenation of Ethane by Ce-Modified NiNb Catalysts. *Industrial & Engineering Chemistry Research* **57**, 5234–5240.

PARK, S., VOHS, J. M. & GORTE, R. J. (2000). Direct oxidation of hydrocarbons in a solid-oxide fuel cell. *Nature* **404**, 265.

PEI, S., KLEEFISCH, M. S., KOBYLINSKI, T. P., FABER, J., UDOVICH, C. A., ZHANG-MCCOY, V., DABROWSKI, B., BALACHANDRAN, U., MIEVILLE, R. L. & POEPPEL, R. B. (1995). Failure mechanisms of ceramic membrane reactors in partial oxidation of methane to synthesis gas. *Catalysis Letters* **30**, 201–212.

PENNYCOOK, S. J. & NELLIST, P. D. (eds.) (2011). *Scanning transmission electron microscopy: imaging and analysis*. New York, NY: Springer.

PENNYCOOK, S. J., VARELA, M., HETHERINGTON, C. J. D. & KIRKLAND, A. I. (2006). Materials Advances through Aberration-Corrected Electron Microscopy. *MRS Bulletin* **31**, 36–43.

PERKINS, C. L., HENDERSON, M. A., PEDEN, C. H. F. & HERMAN, G. S. (2001). Self-diffusion in ceria. *Journal of Vacuum Science & Technology A: Vacuum, Surfaces, and Films* **19**, 1942–1946.

PERRICHON, V., LAACHIR, A., BERGERET, G., FRÉTY, R., TOURNAYAN, L. & TOURET, O. (1994). Reduction of cerias with different textures by hydrogen and their reoxidation by oxygen. *J. Chem. Soc., Faraday Trans.* **90**, 773–781.

PILLAI, M., LIN, Y., ZHU, H., KEE, R. J. & BARNETT, S. A. (2010). Stability and coking of direct-methane solid oxide fuel cells: Effect of CO_2 and air additions. *Journal of Power Sources* **195**, 271–279.

PLIMPTON, S. (1995). Fast Parallel Algorithms for Short-Range Molecular Dynamics. *Journal of Computational Physics* **117**, 1–19.

PLIMPTON, S., POLLOCK, R. & STEVENS, M. (1997). Particle-Mesh Ewald and rRESPA for Parallel Molecular Dynamics Simulations. In *PPSC*. Citeseer.

POOLE, C. F. (2012). *Gas chromatography*. 1st ed. Amsterdam ; Boston: Elsevier.

PUSHKAREV, V. V., KOVALCHUK, V. I. & D'ITRI, J. L. (2004). Probing Defect Sites on the CeO_2 Surface with Dioxygen. *The Journal of Physical Chemistry B* **108**, 5341–5348.

QI, G., YANG, R. T. & CHANG, R. (2004). MnO_x-CeO_2 mixed oxides prepared by co-precipitation for selective catalytic reduction of NO with NH_3 at low temperatures. *Applied Catalysis B: Environmental* **51**, 93–106.

QIAO, A., KALEVARU, V. N., RADNIK, J. & MARTIN, A. (2016). Oxidative dehydrogenation of ethane to ethylene over Ni–Nb–M–O catalysts: Effect of promoter metal and CO_2-admixture on the performance. *Catalysis Today* **264**, 144–151.

RAMÍREZ-CABRERA, E., ATKINSON, A. & CHADWICK, D. (2000). The influence of point defects on the resistance of ceria to carbon deposition in hydrocarbon catalysis. *Solid State Ionics* **136**, 825–831.

REIMER, L. & LÖDDING, B. (1984). Calculation and tabulation of mott cross-sections for large-angle electron scattering. *Scanning* **6**, 128–151.

RENUKA, N. K., PRAVEEN, A. K. & ANIZ, C. U. (2013). Ceria rhombic microplates: Synthesis, characterization and catalytic activity. *Microporous and Mesoporous Materials* **169**, 35–41.

RICKEN, M., NÖLTING, J. & RIESS, I. (1984). Specific heat and phase diagram of nonstoichiometric ceria (CeO2−x). *Journal of Solid State Chemistry* **54**, 89–99.

ROGELJ, J., SHINDELL, D., JIANG, K., FIFITA, S., FORSTER, P., GINZBURG, V., HANDA, C., KOBAYASHI, S., KRIEGLER, E., MUNDACA, L., SÉFÉRIAN, R., VILARIÑO, M. V., CALVIN, K., EMMERLING, J., FUSS, S., GILLETT, N., HE, C., HERTWICH, E., HÖGLUND-ISAKSSON, L., HUPPMANN, D., LUDERER, G., MEINSHAUSEN, M., MCCOLLUM, D. L., MILLAR, R., MEINSHAUSEN, M., POPP, A., RIAHI, K., RIBES, A., SAUNDERS, H., SCHÄDEL, C., SMITH, C., SMITH, P., TRUTNEVYTE, E., XIU, Y., ZHOU, W., ZICKFELD, K., FLATO, G., FUGLESTVEDT, J., MRABET, R. & SCHAEFFER, R. (2019). Mitigation Pathways Compatible with 1.5°C in the Context of Sustainable Development. 82.

ROSTRUP-NIELSEN, J. R. (1993). Production of synthesis gas. *Catalysis today* **18**, 305–324.

ROUTBORT, J. L., GORETTA, K. C., DE ARELLANO-LÓPEZ, A. R. & WOLFENSTINE, J. (1997). Creep of $Ce_{0.9}Gd_{0.1}O_{1.95}$. *Scripta Materialia* **38**, 315–320.

RUIZ PUIGDOLLERS, A., SCHLEXER, P., TOSONI, S. & PACCHIONI, G. (2017). Increasing Oxide Reducibility: The Role of Metal/Oxide Interfaces in the Formation of Oxygen Vacancies. *ACS Catalysis* **7**, 6493–6513.

RUIZ-TREJO, E., SIRMAN, J. D., BAIKOV, YU. M. & KILNER, J. A. (1998). Oxygen ion diffusivity, surface exchange and ionic conductivity in single crystal Gadolinia doped Ceria. *Solid State Ionics* **113–115**, 565–569.

RUPP, J. L. M., DROBEK, T., ROSSI, A. & GAUCKLER, L. J. (2007). Chemical Analysis of Spray Pyrolysis Gadolinia-Doped Ceria Electrolyte Thin Films for Solid Oxide Fuel Cells. *Chemistry of Materials* **19**, 1134–1142.

RUPP, J. L. M., FABBRI, E., MARROCCHELLI, D., HAN, J.-W., CHEN, D., TRAVERSA, E., TULLER, H. L. & YILDIZ, B. (2014). Scalable Oxygen-Ion Transport Kinetics in Metal-Oxide Films: Impact of Thermally Induced Lattice Compaction in Acceptor Doped Ceria Films. *Advanced Functional Materials* **24**, 1562–1574.

RUSHTON, M. J. D. & CHRONEOS, A. (2015). Impact of uniaxial strain and doping on oxygen diffusion in CeO_2. *Scientific Reports* **4**, 6068.

RUSKA, E. (1987). The development of the electron microscope and of electron microscopy. *Reviews of Modern Physics* **59**, 627–638.

RUSKIN, R. S., YU, Z. & GRIGORIEFF, N. (2013). Quantitative characterization of electron detectors for transmission electron microscopy. *Journal of Structural Biology* **184**, 385–393.

SADYKOV, V., USOLTSEV, V., YEREMEEV, N., MEZENTSEVA, N., PELIPENKO, V., KRIEGER, T., BELYAEV, V., SADOVSKAYA, E., MUZYKANTOV, V., FEDOROVA, YU., LUKASHEVICH, A., ISHCHENKO, A., SALANOV, A., OKHLUPIN, YU., UVAROV, N., SMORYGO, O., ARZHANNIKOV, A., KOROBEYNIKOV, M. & THUMM, MA. K. A. (2013). Functional nanoceramics for intermediate temperature solid oxide fuel cells and oxygen separation membranes. *Journal of the European Ceramic Society* **33**, 2241–2250.

SANNA, S., ESPOSITO, V., TEBANO, A., LICOCCIA, S., TRAVERSA, E. & BALESTRINO, G. (2010). Enhancement of Ionic Conductivity in Sm-Doped Ceria/Yttria-Stabilized Zirconia Heteroepitaxial Structures. *Small* **6**, 1863–1867.

SANTEN, R. A. VAN & NIEMANTSVERDRIET, J. W. (1995). *Chemical Kinetics and Catalysis*. New York: Plenum Press.

SATO, K. (2015). Grain-Boundary Structures Associated with Ionic Transport in Gd-Doped Ceria Nanostructured Electrolyte. *The Journal of Physical Chemistry C* **119**, 5734–5738.

SAWADA, H., TANISHIRO, Y., OHASHI, N., TOMITA, T., HOSOKAWA, F., KANEYAMA, T., KONDO, Y. & TAKAYANAGI, K. (2009). STEM imaging of 47-pm-separated atomic columns by a spherical aberration-corrected electron microscope with a 300-kV cold field emission gun. *Journal of Electron Microscopy* **58**, 357–361.

SAYLE, T. X. T., PARKER, S. C. & CATLOW, C. R. A. (1994). The role of oxygen vacancies on ceria surfaces in the oxidation of carbon monoxide. *Surface Science* **316**, 329–336.

SAYLE, T. X. T., PARKER, S. C. & SAYLE, D. C. (2004). Shape of CeO_2 nanoparticles using simulated amorphisation and recrystallisation. *Chemical Communications* 2438.

SCHÄDEL, B. T., DUISBERG, M. & DEUTSCHMANN, O. (2009). Steam reforming of methane, ethane, propane, butane, and natural gas over a rhodium-based catalyst. *Catalysis Today* **142**, 42–51.

SCHERZER, O. (1949). The Theoretical Resolution Limit of the Electron Microscope. *Journal of Applied Physics* **20**, 20–29.

SCHNEIDER, J. J., NAUMANN, M., SCHÄFER, C., BRANDNER, A., HOFMANN, H. J. & CLAUS, P. (2011). Template-assisted formation of microsized nanocrystalline CeO_2 tubes and their catalytic performance in the carboxylation of methanol. *Beilstein Journal of Nanotechnology* **2**, 776–784.

SCHWEIGER, S., PFENNINGER, R., BOWMAN, W. J., ASCHAUER, U. & RUPP, J. L. M. (2017). Designing Strained Interface Heterostructures for Memristive Devices. *Advanced Materials* **29**, 1605049.

SHARMA, R. & CROZIER, P. A. (2005). Environmental Transmission Electron Microscopy in Nanotechnology. In *Handbook of Microscopy for Nanotechnology*, Yao, N. & Wang, Z. L. (Eds.), pp. 531–565. Boston: Kluwer Academic Publishers http://link.springer.com/10.1007/1-4020-8006-9_17 (Accessed January 6, 2019).

SHARMA, R., CROZIER, P. A., KANG, Z. C. & EYRING, L. (2004). Observation of dynamic nanostructural and nanochemical changes in ceria-based catalysts during *In-situ* reduction. *Philosophical Magazine* **84**, 2731–2747.

SHARMA, R. & IQBAL, Z. (2004). *In situ* observations of carbon nanotube formation using environmental transmission electron microscopy. *Applied Physics Letters* **84**, 990.

SHARMA, R., REZ, P., TREACY, M. M. J. & STUART, S. J. (2005). *In situ* observation of the growth mechanisms of carbon nanotubes under diverse reaction conditions. *Microscopy* **54**, 231–237.

SHARMA, V., CROZIER, P. A., SHARMA, R. & ADAMS, J. B. (2012). Direct observation of hydrogen spillover in Ni-loaded Pr-doped ceria. *Catalysis Today* **180**, 2–8.

SHARMA, V., EBERHARDT, K. M., SHARMA, R., ADAMS, J. B. & CROZIER, P. A. (2010). A spray drying system for synthesis of rare-earth doped cerium oxide nanoparticles. *Chemical Physics Letters* **495**, 280–286.

SHIMIZU, K., KAWACHI, H. & SATSUMA, A. (2010). Study of active sites and mechanism for soot oxidation by silver-loaded ceria catalyst. *Applied Catalysis B: Environmental* **96**, 169–175.

SHOKO, E., SMITH, M. F. & MCKENZIE, R. H. (2011). Charge distribution and transport properties in reduced ceria phases: A review. *Journal of Physics and Chemistry of Solids* **72**, 1482–1494.

SINCLAIR, R. (2013). *In situ* high-resolution transmission electron microscopy of material reactions. *MRS Bulletin* **38**, 1065–1071.

SINCLAIR, R., LEE, S. C., SHI, Y. & CHUEH, W. C. (2017). Structure and chemistry of epitaxial ceria thin films on yttria-stabilized zirconia substrates, studied by high resolution electron microscopy. *Ultramicroscopy* **176**, 200–211.

SK, M. A., KOZLOV, S. M., LIM, K. H., MIGANI, A. & NEYMAN, K. M. (2014). Oxygen vacancies in self-assemblies of ceria nanoparticles. *J. Mater. Chem. A* **2**, 18329–18338.

SKORODUMOVA, N. V., BAUDIN, M. & HERMANSSON, K. (2004). Surface properties of CeO_2 from first principles. *Physical Review B* **69**. https://link.aps.org/doi/10.1103/PhysRevB.69.075401 (Accessed May 1, 2017).

SOLSONA, B., CONCEPCIÓN, P., HERNÁNDEZ, S., DEMICOL, B. & NIETO, J. M. L. (2012). Oxidative dehydrogenation of ethane over $NiO–CeO_2$ mixed oxides catalysts. *Catalysis Today* **180**, 51–58.

SOUENTIE, S., ATHANASIOU, M., NIAKOLAS, D. K., KATSAOUNIS, A., NEOPHYTIDES, S. G. & VAYENAS, C. G. (2013). Mathematical modeling of Ni/GDC and Au–Ni/GDC SOFC anodes performance under internal methane steam reforming conditions. *Journal of Catalysis* **306**, 116–128.

SPARKMAN, O. D., PENTON, Z. & KITSON, F. G. (2011). *Gas Chromatography and Mass Spectrometry: a Practical Guide.* Burlington: Elsevier Science http://public.eblib.com/choice/publicfullrecord.aspx?p=670206 (Accessed December 28, 2018).

SPENCE, J. C. H. & ZUO, J. M. (1988). Large dynamic range, parallel detection system for electron diffraction and imaging. *Review of Scientific Instruments* **59**, 2102–2105.

SPIECKER, E., GARBRECHT, M., JÄGER, W. & TILLMANN, K. (2010). Advantages of aberration correction for HRTEM investigation of complex layer compounds. *Journal of Microscopy* **237**, 341–346.

STACCHIOLA, D. J. (2015). Tuning the Properties of Copper-Based Catalysts Based on Molecular in Situ Studies of Model Systems. *Accounts of Chemical Research* **48**, 2151–2158.

STADELMANN, P. (2018). *JEMS, Electron Microscopy Software*. CIME-EPFL: Laussane, Switzerland.

STEELE, B. C. H. (1994). Oxygen transport and exchange in oxide ceramics. *Journal of Power Sources* **49**, 1–14.

STÖBER, W., FINK, A. & BOHN, E. (1968). Controlled growth of monodisperse silica spheres in the micron size range. *Journal of colloid and interface science* **26**, 62–69.

STOCKER, T. (ed.) (2014). *Climate change 2013: the physical science basis: Working Group I contribution to the Fifth assessment report of the Intergovernmental Panel on Climate Change*. New York: Cambridge University Press.

SUN, C., LI, H. & CHEN, L. (2012). Nanostructured ceria-based materials: synthesis, properties, and applications. *Energy & Environmental Science* **5**, 8475.

SUN, L., HUANG, X., WANG, L. & JANOTTI, A. (2017). Disentangling the role of small polarons and oxygen vacancies in CeO_2. *Physical Review B* **95**. http://link.aps.org/doi/10.1103/PhysRevB.95.245101 (Accessed July 19, 2017).

SUNARSO, J., BAUMANN, S., SERRA, J. M., MEULENBERG, W. A., LIU, S., LIN, Y. S. & DINIZ DA COSTA, J. C. (2008). Mixed ionic–electronic conducting (MIEC) ceramic-based membranes for oxygen separation. *Journal of Membrane Science* **320**, 13–41.

SUZUKI, M., YAGUCHI, T. & ZHANG, X. F. (2013). High-resolution environmental transmission electron microscopy: modeling and experimental verification. *Microscopy* **62**, 437–450.

TA, N., LIU, J. (JIMMY), CHENNA, S., CROZIER, P. A., LI, Y., CHEN, A. & SHEN, W. (2012). Stabilized Gold Nanoparticles on Ceria Nanorods by Strong Interfacial Anchoring. *Journal of the American Chemical Society* **134**, 20585–20588.

TA, N., LIU (JIMMY), J. & SHEN, W. (2013). Tuning the shape of ceria nanomaterials for catalytic applications. *Chinese Journal of Catalysis* **34**, 838–850.

TAHERI, M. L., STACH, E. A., ARSLAN, I., CROZIER, P. A., KABIUS, B. C., LAGRANGE, T., MINOR, A. M., TAKEDA, S., TANASE, M., WAGNER, J. B. & SHARMA, R. (2016). Current status and future directions for in situ transmission electron microscopy. *Ultramicroscopy* **170**, 86–95.

TAKEDA, S., KUWAUCHI, Y. & YOSHIDA, H. (2015). Environmental transmission electron microscopy for catalyst materials using a spherical aberration corrector. *Ultramicroscopy* **151**, 178–190.

TAKEDA, S. & YOSHIDA, H. (2013). Atomic-resolution environmental TEM for quantitative *in-situ* microscopy in materials science. *Microscopy* **62**, 193–203.

TAKENAKA, S., OGIHARA, H., YAMANAKA, I. & OTSUKA, K. (2001). Decomposition of methane over supported-Ni catalysts: effects of the supports on the catalytic lifetime. *Applied Catalysis A: General* **217**, 101–110.

TAKHT RAVANCHI, M., KAGHAZCHI, T. & KARGARI, A. (2009). Application of membrane separation processes in petrochemical industry: a review. *Desalination* **235**, 199–244.

TAN, J. P. Y., TAN, H. R., BOOTHROYD, C., FOO, Y. L., HE, C. B. & LIN, M. (2011). Three-Dimensional Structure of CeO_2 Nanocrystals. *The Journal of Physical Chemistry C* **115**, 3544–3551.

TANA, ZHANG, M., LI, J., LI, H., LI, Y. & SHEN, W. (2009). Morphology-dependent redox and catalytic properties of CeO_2 nanostructures: Nanowires, nanorods and nanoparticles. *Catalysis Today* **148**, 179–183.

TANAKA, I., OBA, F., TATSUMI, K., KUNISU, M., NAKANO, M. & ADACHI, H. (2002). Theoretical Formation Energy of Oxygen-Vacancies in Oxides. *MATERIALS TRANSACTIONS* **43**, 1426–1429.

TANG, W.-X. & GAO, P.-X. (2016). Nanostructured cerium oxide: preparation, characterization, and application in energy and environmental catalysis. *MRS Communications* **6**, 311–329.

TANG, X., ZHANG, B., LI, Y., XU, Y., XIN, Q. & SHEN, W. (2005). CuO/CeO_2 catalysts: Redox features and catalytic behaviors. *Applied Catalysis A: General* **288**, 116–125.

TAO, F. (FENG) & CROZIER, P. A. (2016). Atomic-Scale Observations of Catalyst Structures under Reaction Conditions and during Catalysis. *Chemical Reviews* **116**, 3487–3539.

TASKER, P. W. (1979). The stability of ionic crystal surfaces. *Journal of Physics C: Solid State Physics* **12**, 4977–4984.

TINOCO, M., FERNANDEZ-GARCIA, S., LOPEZ-HARO, M., HUNGRIA, A. B., CHEN, X., BLANCO, G., PEREZ-OMIL, J. A., COLLINS, S. E., OKUNO, H. & CALVINO, J. J. (2015). Critical Influence of Nanofaceting on the Preparation and Performance of Supported Gold Catalysts. *ACS Catalysis* **5**, 3504–3513.

TORRENTE-MURCIANO, L. & GARCIA-GARCIA, F. R. (2015). Effect of nanostructured support on the WGSR activity of Pt/CeO_2 catalysts. *Catalysis Communications* **71**, 1–6.

TORRENTE-MURCIANO, L., GILBANK, A., PUERTOLAS, B., GARCIA, T., SOLSONA, B. & CHADWICK, D. (2013). Shape-dependency activity of nanostructured CeO_2 in the total oxidation of polycyclic aromatic hydrocarbons. *Applied Catalysis B: Environmental* **132–133**, 116–122.

TROVARELLI, A. (1996). Catalytic Properties of Ceria and CeO_2-Containing Materials. *Catalysis Reviews* **38**, 439–520.

———— (ed.) (2002). *Catalysis by ceria and related materials*. London: Imperial College Press.

TROVARELLI, A. & LLORCA, J. (2017). Ceria Catalysts at Nanoscale: How Do Crystal Shapes Shape Catalysis? *ACS Catalysis* **7**, 4716–4735.

TSIPIS, E. V. & KHARTON, V. V. (2008). Electrode materials and reaction mechanisms in solid oxide fuel cells: a brief review: II. Electrochemical behavior vs. materials science aspects. *Journal of Solid State Electrochemistry* **12**, 1367–1391.

TSUNEKAWA, S., SAHARA, R., KAWAZOE, Y. & ISHIKAWA, K. (1999). Lattice relaxation of monosize CeO_{2-x} nanocrystalline particles. *Applied Surface Science* **152**, 53–56.

TSUNEKAWA, S., SIVAMOHAN, R., ITO, S., KASUYA, A. & FUKUDA, T. (1999). Structural study on monosize CeO_{2-x} nano-particles. *Nanostructured Materials* **11**, 141–147.

TULLER, H. L. & BISHOP, S. R. (2011). Point Defects in Oxides: Tailoring Materials Through Defect Engineering. *Annual Review of Materials Research* **41**, 369–398.

TULLER, H. L. & NOWICK, A. S. (1977). Small polaron electron transport in reduced CeO_2 single crystals. *Journal of Physics and Chemistry of Solids* **38**, 859–867.

UCHIYAMA, T., YOSHIDA, H., KUWAUCHI, Y., ICHIKAWA, S., SHIMADA, S., HARUTA, M. & TAKEDA, S. (2011). Systematic Morphology Changes of Gold Nanoparticles Supported on CeO_2 during CO Oxidation. *Angewandte Chemie International Edition* **50**, 10157–10160.

UHLEMANN, S. & HAIDER, M. (1998). Residual wave aberrations in the first spherical aberration corrected transmission electron microscope. *Ultramicroscopy* **72**, 109–119.

URBAN, K. W. (2008). Studying Atomic Structures by Aberration-Corrected Transmission Electron Microscopy. *Science* **321**, 506–510.

URBAN, K. W., JIA, C.-L., HOUBEN, L., LENTZEN, M., MI, S.-B. & TILLMANN, K. (2009). Negative spherical aberration ultrahigh-resolution imaging in corrected transmission electron microscopy. *Philosophical Transactions of the Royal Society A: Mathematical, Physical and Engineering Sciences* **367**, 3735–3753.

U.S. ENERGY INFORMATION ADMINISTRATION (2017). *International Energy Outlook 2017, DOE/EIA-0484 (2017).*

VANG, R. T., HONKALA, K., DAHL, S., VESTERGAARD, E. K., SCHNADT, J., LÆGSGAARD, E., CLAUSEN, B. S., NØRSKOV, J. K. & BESENBACHER, F. (2006). Ethylene dissociation on flat and stepped Ni(111): A combined STM and DFT study. *Surface Science* **600**, 66–77.

VENDELBO, S. B., ELKJÆR, C. F., FALSIG, H., PUSPITASARI, I., DONA, P., MELE, L., MORANA, B., NELISSEN, B. J., VAN RIJN, R., CREEMER, J. F., KOOYMAN, P. J. & HELVEG, S. (2014). Visualization of oscillatory behaviour of Pt nanoparticles catalysing CO oxidation. *Nature Materials* **13**, 884–890.

VENKATRAMAN, K., REZ, P., MARCH, K. & CROZIER, P. A. (2018). The influence of surfaces and interfaces on high spatial resolution vibrational EELS from SiO_2. *Microscopy* **67**, i14–i23.

VERANITISAGUL, C., KOONSAENG, N., LAOSIRIPOJANA, N. & LAOBUTHEE, A. (2012). Preparation of gadolinia doped ceria via metal complex decomposition method: Its application as catalyst for the steam reforming of ethane. *Journal of Industrial and Engineering Chemistry* **18**, 898–903.

VILLARS, P. & CALVERT, L. D. (1989). *Pearson's handbook of crystallographic data for intermetallic phases. Vol. 1*. Metals Park, Ohio: ASM International.

VOJVODIC, A., CALLE-VALLEJO, F., GUO, W., WANG, S., TOFTELUND, A., STUDT, F., MARTÍNEZ, J. I., SHEN, J., MAN, I. C., ROSSMEISL, J., BLIGAARD, T., NØRSKOV, J. K. & ABILD-PEDERSEN, F. (2011). On the behavior of Brønsted-Evans-Polanyi relations for transition metal oxides. *The Journal of Chemical Physics* **134**, 244509.

WACHSMAN, E. D. & CLITES, T. L. (2002). Stable Mixed-Conducting Bilayer Membranes for Direct Conversion of Methane to Syngas. *Journal of The Electrochemical Society* **149**, A242.

WACHSMAN, E. D. & LEE, K. T. (2011). Lowering the Temperature of Solid Oxide Fuel Cells. *Science* **334**, 935–939.

WAGNER, J. B., CAVALCA, F., DAMSGAARD, C. D., DUCHSTEIN, L. D. L. & HANSEN, T. W. (2012). Exploring the environmental transmission electron microscope. *Micron* **43**, 1169–1175.

WANG, B., XI, X. & CORMACK, A. N. (2014). Chemical Strain and Point Defect Configurations in Reduced Ceria. *Chemistry of Materials* **26**, 3687–3692.

WANG, F., KISHIMOTO, H., ISHIYAMA, T., BAGARINAO, K. D.-, YAMAJI, K., HORITA, T. & YOKOKAWA, H. (2017). Modification of Ni-YSZ Surface with High Carbon Tolerance Using GDC Nanoparticles. *ECS Transactions* **78**, 1457–1461.

WANG, GONGHUA, WANG, L., FEI, X., ZHOU, Y., SABIRIANOV, R. F., MEI, W. N. & CHEUNG, C. L. (2013). Probing the bifunctional catalytic activity of ceria nanorods towards the cyanosilylation reaction. *Catalysis Science & Technology* **3**, 2602.

WANG, LEI, MERKLE, R., MASTRIKOV, Y. A., KOTOMIN, E. A. & MAIER, J. (2012). Oxygen exchange kinetics on solid oxide fuel cell cathode materials—general trends and their mechanistic interpretation. *Journal of Materials Research* **27**, 2000–2008.

WANG, R., CROZIER, P. A. & SHARMA, R. (2009). Structural Transformation in Ceria Nanoparticles during Redox Processes. *The Journal of Physical Chemistry C* **113**, 5700–5704.

WANG, R, XU, H., LIU, X., GE, Q. & LI, W. (2006). Role of redox couples of $Rh_0/Rh_{\delta+}$ and Ce^{4+}/Ce^{3+} in CH_4/CO_2 reforming over $Rh–CeO_2/Al_2O_3$ catalyst. *Applied Catalysis A: General* **305**, 204–210.

WANG, SHENGPING, ZHAO, L., WANG, W., ZHAO, Y., ZHANG, G., MA, X. & GONG, J. (2013). Morphology control of ceria nanocrystals for catalytic conversion of CO_2 with methanol. *Nanoscale* **5**, 5582.

WANG, W., HOWE, J. Y., LI, Y., QIU, X., JOY, D. C., PARANTHAMAN, M. P., DOKTYCZ, M. J. & GU, B. (2010). A surfactant and template-free route for synthesizing ceria nanocrystals with tunable morphologies. *Journal of Materials Chemistry* **20**, 7776.

WANG, WEI, JIANG, S. P., TOK, A. I. Y. & LUO, L. (2006). GDC-impregnated Ni anodes for direct utilization of methane in solid oxide fuel cells. *Journal of Power Sources* **159**, 68–72.

WANG, XUE, JIANG, Z., ZHENG, B., XIE, Z. & ZHENG, L. (2012). Synthesis and shape-dependent catalytic properties of CeO_2 nanocubes and truncated octahedra. *CrystEngComm* **14**, 7579.

WANG, Z. L. & FENG, X. (2003). Polyhedral Shapes of CeO_2 Nanoparticles. *The Journal of Physical Chemistry B* **107**, 13563–13566.

WEN, K., LV, W. & HE, W. (2015). Interfacial lattice-strain effects on improving the overall performance of micro-solid oxide fuel cells. *Journal of Materials Chemistry A* **3**, 20031–20050.

WILLIAMS, D. B. & CARTER, C. B. (2009). *Transmission electron microscopy: a textbook for materials science*. 2. ed. New York: Springer.

WU, Q., ZHANG, F., XIAO, P., TAO, H., WANG, X., HU, Z. & LÜ, Y. (2008). Great Influence of Anions for Controllable Synthesis of CeO_2 Nanostructures: From Nanorods to Nanocubes. *The Journal of Physical Chemistry C* **112**, 17076–17080.

WU, Z., LI, M., HOWE, J., MEYER, H. M. & OVERBURY, S. H. (2010). Probing Defect Sites on CeO_2 Nanocrystals with Well-Defined Surface Planes by Raman Spectroscopy and O_2 Adsorption†. *Langmuir* **26**, 16595–16606.

WU, Z., LI, M., MULLINS, D. R. & OVERBURY, S. H. (2012). Probing the Surface Sites of CeO_2 Nanocrystals with Well-Defined Surface Planes via Methanol Adsorption and Desorption. *ACS Catalysis* **2**, 2224–2234.

WU, Z., LI, M. & OVERBURY, S. H. (2012). On the structure dependence of CO oxidation over CeO_2 nanocrystals with well-defined surface planes. *Journal of Catalysis* **285**, 61–73.

WU, Z. & OVERBURY, S. H. (2015). *Catalysis by materials with well-defined structures*. Amsterdam: Elsevier Ltd.

YAGUCHI, T., SUZUKI, M., WATABE, A., NAGAKUBO, Y., UEDA, K. & KAMINO, T. (2011). Development of a high temperature-atmospheric pressure environmental cell for high-resolution TEM. *Journal of Electron Microscopy* **60**, 217–225.

YAN, L., YU, R., CHEN, J. & XING, X. (2008). Template-Free Hydrothermal Synthesis of CeO_2 Nano-octahedrons and Nanorods: Investigation of the Morphology Evolution. *Crystal Growth & Design* **8**, 1474–1477.

YANG, C., YU, X., HEIßLER, S., NEFEDOV, A., COLUSSI, S., LLORCA, J., TROVARELLI, A., WANG, Y. & WÖLL, C. (2017). Surface Faceting and Reconstruction of Ceria Nanoparticles. *Angewandte Chemie International Edition* **56**, 375–379.

YANG, S. & GAO, L. (2006). Controlled Synthesis and Self-Assembly of CeO_2 Nanocubes. *Journal of the American Chemical Society* **128**, 9330–9331.

YANG, W., WANG, H., ZHU, X. & LIN, L. (2005). Development and Application of Oxygen Permeable Membrane in Selective Oxidation of Light Alkanes. *Topics in Catalysis* **35**, 155–167.

YANG, Y., LÜ, W., YAO, Y., SUN, J., GU, C., GU, L., WANG, Y., DUAN, X. & YU, R. (2014). *In situ* TEM Observation of Resistance Switching in Titanate Based

Device. *Scientific Reports* **4**. http://www.nature.com/articles/srep03890 (Accessed October 3, 2016).

YANG, Z., HAN, D., MA, D., LIANG, H., LIU, L. & YANG, Y. (2010). Fabrication of Monodisperse CeO_2 Hollow Spheres Assembled by Nano-octahedra. *Crystal Growth & Design* **10**, 291–295.

YANG, Z., YANG, Y., LIANG, H. & LIU, L. (2009). Hydrothermal synthesis of monodisperse CeO_2 nanocubes. *Materials Letters* **63**, 1774–1777.

YANG, Z., ZHOU, K., LIU, X., TIAN, Q., LU, D. & YANG, S. (2007). Single-crystalline ceria nanocubes: size-controlled synthesis, characterization and redox property. *Nanotechnology* **18**, 185606.

YANKOVICH, A. B., BERKELS, B., DAHMEN, W., BINEV, P., SANCHEZ, S. I., BRADLEY, S. A., LI, A., SZLUFARSKA, I. & VOYLES, P. M. (2014). Picometre-precision analysis of scanning transmission electron microscopy images of platinum nanocatalysts. *Nature Communications* **5**. http://www.nature.com/articles/ncomms5155 (Accessed August 13, 2018).

YILDIZ, B. (2014). "Stretching" the energy landscape of oxides—Effects on electrocatalysis and diffusion. *MRS Bulletin* **39**, 147–156.

YIN, L., WANG, Y., PANG, G., KOLTYPIN, Y. & GEDANKEN, A. (2002). Sonochemical Synthesis of Cerium Oxide Nanoparticles—Effect of Additives and Quantum Size Effect. *Journal of Colloid and Interface Science* **246**, 78–84.

YOSHIDA, H., KUWAUCHI, Y., JINSCHEK, J. R., SUN, K., TANAKA, S., KOHYAMA, M., SHIMADA, S., HARUTA, M. & TAKEDA, S. (2012). Visualizing Gas Molecules Interacting with Supported Nanoparticulate Catalysts at Reaction Conditions. *Science* **335**, 317–319.

YU, R., YAN, L., ZHENG, P., CHEN, J. & XING, X. (2008). Controlled Synthesis of CeO_2 Flower-Like and Well-Aligned Nanorod Hierarchical Architectures by a Phosphate-Assisted Hydrothermal Route. *The Journal of Physical Chemistry C* **112**, 19896–19900.

YUAN, Q., DUAN, H.-H., LI, L.-L., SUN, L.-D., ZHANG, Y.-W. & YAN, C.-H. (2009). Controlled synthesis and assembly of ceria-based nanomaterials. *Journal of Colloid and Interface Science* **335**, 151–167.

ZENG, Y., LIN, Y. S. & SWARTZ, S. L. (1998). Perovskite-type ceramic membrane: synthesis, oxygen permeation and membrane reactor performance for oxidative coupling of methane. *Journal of Membrane Science* **150**, 87–98.

ZHA, S. (2004). Ni-$Ce_{0.9}Gd_{0.1}O_{1.95}$ anode for GDC electrolyte-based low-temperature SOFCs. *Solid State Ionics* **166**, 241–250.

ZHAN, Z. & BARNETT, S. A. (2005). An Octane-Fueled Solid Oxide Fuel Cell. *Science* **308**, 844–847.

ZHANG, CHUNJUAN, GRASS, M. E., YU, Y., GASKELL, K. J., DECALUWE, S. C., CHANG, R., JACKSON, G. S., HUSSAIN, Z., BLUHM, H., EICHHORN, B. W. & LIU, Z. (2012). Multielement Activity Mapping and Potential Mapping in Solid Oxide Electrochemical Cells through the use of *operando* XPS. *ACS Catalysis* **2**, 2297–2304.

ZHANG, DENGSONG, DU, X., SHI, L. & GAO, R. (2012). Shape-controlled synthesis and catalytic application of ceria nanomaterials. *Dalton Transactions* **41**, 14455.

ZHANG, F.-L., LI, L.-C. & TIAN, A.-M. (2009). Ethane adsorption and decomposition on Ni (111) surface. *Acta Physico-Chimica Sinica* **25**, 1883–1889.

ZHANG, J., KUMAGAI, H., YAMAMURA, K., OHARA, S., TAKAMI, S., MORIKAWA, A., SHINJOH, H., KANEKO, K., ADSCHIRI, T. & SUDA, A. (2011). Extra-Low-Temperature Oxygen Storage Capacity of CeO_2 Nanocrystals with Cubic Facets. *Nano Letters* **11**, 361–364.

ZHANG, J., OHARA, S., UMETSU, M., NAKA, T., HATAKEYAMA, Y. & ADSCHIRI, T. (2007). Colloidal Ceria Nanocrystals: A Tailor-Made Crystal Morphology in Supercritical Water. *Advanced Materials* **19**, 203–206.

ZHANG, LINGLING, XU, N., LI, X., WANG, S., HUANG, K., HARRIS, W. H. & CHIU, W. K. S. (2012). High CO_2 permeation flux enabled by highly interconnected three-dimensional ionic channels in selective CO_2 separation membranes. *Energy & Environmental Science* **5**, 8310.

ZHANG, MANLI, CHEN, Y., QIU, C., FAN, X., CHEN, C. & WANG, Z. (2014). Synthesis and atomic-scale characterization of CeO_2 nano-octahedrons. *Physica E: Low-dimensional Systems and Nanostructures* **64**, 218–223.

ZHANG, S., CHEN, C., CARGNELLO, M., FORNASIERO, P., GORTE, R. J., GRAHAM, G. W. & PAN, X. (2015). Dynamic structural evolution of supported palladium–ceria core–shell catalysts revealed by *in situ* electron microscopy. *Nature Communications* **6**. http://www.nature.com/articles/ncomms8778 (Accessed January 14, 2019).

ZHANG, SEN, ZHANG, X., JIANG, G., ZHU, H., GUO, S., SU, D., LU, G. & SUN, S. (2014). Tuning Nanoparticle Structure and Surface Strain for Catalysis Optimization. *Journal of the American Chemical Society* **136**, 7734–7739.

ZHANG, T. & AMIRIDIS, M. D. (1998). Hydrogen production via the direct cracking of methane over silica-supported nickel catalysts. *Applied Catalysis A: General* **167**, 161–172.

ZHANG, X., YOU, R., LI, D., CAO, T. & HUANG, W. (2017). Reaction Sensitivity of Ceria Morphology Effect on Ni/CeO_2 Catalysis in Propane Oxidation Reactions. *ACS Applied Materials & Interfaces* **9**, 35897–35907.

ZHANG, Y., BALS, S. & VAN TENDELOO, G. (2018). Understanding CeO_2-Based Nanostructures through Advanced Electron Microscopy in 2D and 3D. *Particle & Particle Systems Characterization* 1800287.

ZHOU, K., WANG, X., SUN, X., PENG, Q. & LI, Y. (2005). Enhanced catalytic activity of ceria nanorods from well-defined reactive crystal planes. *Journal of Catalysis* **229**, 206–212.

ZHOU, X., ZHEN, J., LIU, L., LI, X., ZHANG, N. & SUN, K. (2012). Enhanced sulfur and carbon coking tolerance of novel co-doped ceria based anode for solid oxide fuel cells. *Journal of Power Sources* **201**, 128–135.

ZHOU, X.-D. & HUEBNER, W. (2001). Size-induced lattice relaxation in CeO_2 nanoparticles. *Applied Physics Letters* **79**, 3512–3514.

ZHOU, Y., PHILLIPS, R. J. & SWITZER, J. A. (1995). Electrochemical Synthesis and Sintering of Nanocrystalline Cerium(IV) Oxide Powders. *Journal of the American Ceramic Society* **78**, 981–985.

ZHU, Y. & BROWNING, N. D. (2017). The Role of Gas in Determining Image Quality and Resolution During *In Situ* Scanning Transmission Electron Microscopy Experiments. *ChemCatChem* **9**, 3478–3485.

ZINKEVICH, M., DJUROVIC, D. & ALDINGER, F. (2006). Thermodynamic modelling of the cerium–oxygen system. *Solid State Ionics* **177**, 989–1001.

ZUO, J. M. & SPENCE, J. C. H. (2017). *Advanced transmission electron microscopy: imaging and diffraction in nanoscience*. New York: Springer.